

Chemistry in Cryogenic Matrices:  
Solvation of Aryl(trifluoromethyl)carbenes and  
Astrochemistry in Ammonia Ices

**Dissertation**

To obtain the degree of  
Doctor of natural science (Dr. rer. nat.)

by

**Yetsedaw Andargie Tsegaw**

from Gondar, Ethiopia

RUHR  
UNIVERSITÄT  
BOCHUM

**RUB**

Bochum 2018



Dedicated to my parents.



This work was carried out from October 2014 to February 2018 at the Department of Organic Chemistry II of the Ruhr-Universität Bochum under the supervision of Prof. Dr. Wolfram Sander. Part of the work reported in this thesis was performed in collaboration with Dr. Sándor Góbi, Dr. Marko Förstel, Dr. Pavlo Maksyutenko and Prof. Dr. Ralf I. Kaiser (Department of Chemistry, University of Hawaii at Manoa) with Niklas Tötsch and Prof. Dr. Elsa Sanchez-Garcia (Max-Planck-Institut für Kohlenforschung).

First Referee: Prof. Dr. Wolfram Sander

Second Referee: Prof. Dr. Patrick Nürnberger

Day of submission: 25/07/2018

Day of disputation: 26/09/2018

## Publications

**Y. A. Tsegaw**, W. Sander, R.I. Kaiser, Electron Paramagnetic Resonance Spectroscopic Study on Nonequilibrium Reaction Pathways in the Photolysis of Solid Nitromethane ( $\text{CH}_3\text{NO}_2$ ) and D3-Nitromethane ( $\text{CD}_3\text{NO}_2$ ), *J. Phys. Chem. A*, **2016**, 120, 1577.

M. Förstel, **Y. A. Tsegaw**, P. Maksyutenko, A.M. Mebel, W. Sander, R.I. Kaiser, On the Formation of  $\text{N}_3\text{H}_3$  Isomers in Irradiated Ammonia Bearing Ices: Triazene ( $\text{H}_2\text{NNNH}$ ) or Triimide ( $\text{HNHNNH}$ ), *ChemPhysChem*, **2016**, 17, 2726.

**Y. A. Tsegaw**, P. E. Kadam, N. Tötsch, E. Sanchez-Garcia, W. Sander, Is Magnetic Bistability of Carbenes a General Phenomenon? Isolation of Simple Aryl(trifluoromethyl)carbenes in Both Their Singlet and Triplet States, *J. Am. Chem. Soc.*, **2017**, 139, 12310.

**Y. A. Tsegaw**, S. Gobi, M. Förstel, P. Maksyutenko, W. Sander, R.I. Kaiser, Formation of Hydroxylamine in Low-temperature Interstellar Model Ices, *J. Phys. Chem. A*, **2017**, 121, 7477.

A. Mardyukov, **Y. A. Tsegaw**, W. Sander and P. R. Schreiner, The Phenylselenyl Radical and its Reaction with Molecular Oxygen, *Phys. Chem. Chem. Phys.*, **2017**, 19, 27384.

**Y. A. Tsegaw**, D. Grote and W. Sander, Matrix Isolation and Spectroscopic Characterization of Quartet Dehydroarylnitrenes, manuscript in preparation.

**Y. A. Tsegaw**, P. E. Kadam, L. H. Song, E. Mendez-Vega and W. Sander, Activation of Ammonia by Aryl(trifluoromethyl)carbenes, manuscript in preparation.

**Y. A. Tsegaw**, P. E. Kadam, E. Mendez-Vega and W. Sander, Spin-selective Hydrogenation of Aryl(trifluoromethyl)carbenes, manuscript in preparation.

## **Scientific Meetings**

Graduate School Solvation Science Workshop, RUB, 10/2014 (Poster).

Gordon Research Conference, Physical Organic Chemistry, Holderness School, New Hampshire, USA, 06/2015 (Poster).

Graduate School Solvation Science Workshop Area A, RUB, 10/2015 (Poster).

Graduate School Solvation Science Autumn Workshop, RUB, 10/2016 (Poster).

International Symposium on Reactive Intermediates and Unusual Molecules (ISRIUM 17), Sorrento, Italy, 07/2017 (Poster).

## **International Internship**

From 09/2015 to 10/2015 in the research group of Prof. Dr. Ralf I. Kaiser at the Department of Chemistry and W. M. Keck Research Laboratory in Astrochemistry, University of Hawaii at Manoa, Hawaii, USA.

*“If you can't fly then run, if you can't run then walk, if you can't walk then crawl, but whatever you do you have to keep moving forward.”*

Dr. Martin Luther King Jr.

## Table of contents

<b>Summary</b> .....	<b>1</b>
<b>1. General introduction</b> .....	<b>6</b>
Why chemistry at cryogenic temperatures? .....	6
Carbenes .....	6
Nitrenes .....	10
Astrochemistry in ammonia ice .....	11
Laboratory ammonia ice.....	13
Matrix isolation.....	14
EPR spectroscopy .....	16
Zeeman splitting.....	16
Hyperfine splitting.....	17
Zero field splitting .....	19
<b>2. Photochemistry of aryl(trifluoromethyl)carbenes</b> .....	<b>23</b>
Introduction .....	23
Results and discussion .....	25
EPR spectroscopy.....	25
UV-vis spectroscopy.....	28
IR spectroscopy .....	30
Conclusion .....	33
<b>3. Bistable aryl(trifluoromethyl)carbenes</b> .....	<b>34</b>
Introduction .....	34
Results and discussion .....	35
<i>p</i> -Tolyl(trifluoromethyl)carbene .....	35
EPR spectroscopy.....	36
IR spectroscopy .....	37
UV-vis spectroscopy.....	44
DFT calculations .....	47
Reaction of <i>p</i> -tolyl(trifluoromethyl)carbene in argon matrices doped with 1% of water.....	49
DFT calculations .....	51
Reaction of <i>p</i> -tolyl(trifluoromethyl)carbene in LDA water ice.....	53
UV-vis spectroscopy.....	53
IR spectroscopy .....	54
<i>p</i> -Fluorophenyl(trifluoromethyl)carbene .....	55
EPR spectroscopy.....	56
IR spectroscopy .....	57
UV-vis spectroscopy.....	59
Reaction of <i>p</i> -fluorophenyl(trifluoromethyl)carbene in argon matrices doped with 1% of water....	60
DFT calculations .....	62
Fluorenyl(trifluoromethyl)carbene.....	64
EPR spectroscopy.....	65

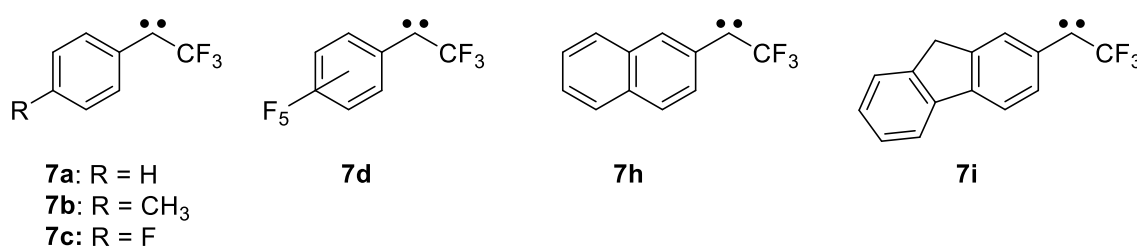
	IR spectroscopy .....	66
	UV-vis spectroscopy.....	67
	DFT calculations .....	68
	Conclusion .....	69
<b>4.</b>	<b>Activation of ammonia by aryl(trifluoromethyl)carbenes .....</b>	<b>70</b>
	Introduction .....	70
	Results and discussion .....	71
	Reaction of <i>p</i> -tolyl(trifluoromethyl)carbene in argon matrices doped with 1% of ammonia.....	71
	EPR spectroscopy.....	72
	UV-vis spectroscopy.....	75
	IR spectroscopy .....	75
	DFT calculations .....	80
	Kinetics .....	81
	Reaction of <i>p</i> -fluorophenyl(trifluoromethyl)carbene in argon matrices doped with 1% of ammonia .....	83
	Reaction of aryl(trifluoromethyl)carbenes in LDA ammonia ice.....	85
	UV-vis spectroscopy.....	85
	IR spectroscopy .....	87
	Conclusion .....	89
<b>5.</b>	<b>Spin-selective hydrogenation of aryl(trifluoromethyl)carbenes .....</b>	<b>91</b>
	Introduction .....	91
	Results and discussion .....	92
	IR spectroscopy .....	92
	UV-vis spectroscopy.....	99
	EPR spectroscopy.....	100
	DFT calculations .....	101
	Conclusion .....	103
<b>6.</b>	<b>Dehydroarylnitrenes .....</b>	<b>105</b>
	Introduction .....	105
	Results and discussion .....	107
	Photochemistry of iodobiphenylazides and terphenylazide .....	107
	IR spectroscopy .....	107
	UV-vis spectroscopy.....	108
	EPR spectroscopy.....	109
	Photochemistry of idonaphthylazides .....	112
	IR spectroscopy .....	112
	UV-vis spectroscopy.....	114
	EPR spectroscopy.....	117
	Conclusion .....	119
<b>7.</b>	<b>Formation of hydroxylamine in interstellar model ices.....</b>	<b>120</b>
	Introduction .....	120

Results and discussion .....	122
IR spectroscopy .....	122
Qualitative analysis .....	122
Deconvolution.....	126
Quantitative analysis, mass balances .....	129
Quantitative analysis, reaction pathways .....	132
PI-ReTOF mass spectroscopy .....	136
Astrochemical implications.....	138
<b>8. Formation of triazene in ammonia bearing ices.....</b>	<b>140</b>
Introduction .....	140
Results and discussion .....	141
Detection .....	142
Isomer identification.....	144
Reaction pathways.....	145
Conclusion .....	146
<b>9. EPR study on the photolysis of solid nitromethane .....</b>	<b>148</b>
Introduction .....	148
Results and discussion .....	149
Individual EPR spectra.....	150
Atomic hydrogen (H) and deuterium (D).....	150
Methyl (CH <sub>3</sub> ) and D3-methyl (CD <sub>3</sub> ) radicals.....	151
Nitromethyl (CH <sub>2</sub> NO <sub>2</sub> ) and D2-nitromethyl (CD <sub>2</sub> NO <sub>2</sub> ) radicals .....	153
Methoxy (CH <sub>3</sub> O) and D3-methoxy (CD <sub>3</sub> O) radicals .....	154
Nitrogen dioxide (NO <sub>2</sub> ).....	155
Nitrogen monoxide (NO).....	157
Simulation of the experimental EPR spectra .....	158
Conclusion .....	160
<b>Experimental section .....</b>	<b>161</b>
Synthesis .....	161
Matrix isolation .....	164
Ammonia bearing ices .....	165
Calculations.....	166
<b>References.....</b>	<b>167</b>
<b>Acknowledgments .....</b>	<b>179</b>
<b>Appendix.....</b>	<b>181</b>

## Summary

- **Aryl(trifluoromethyl)carbenes**

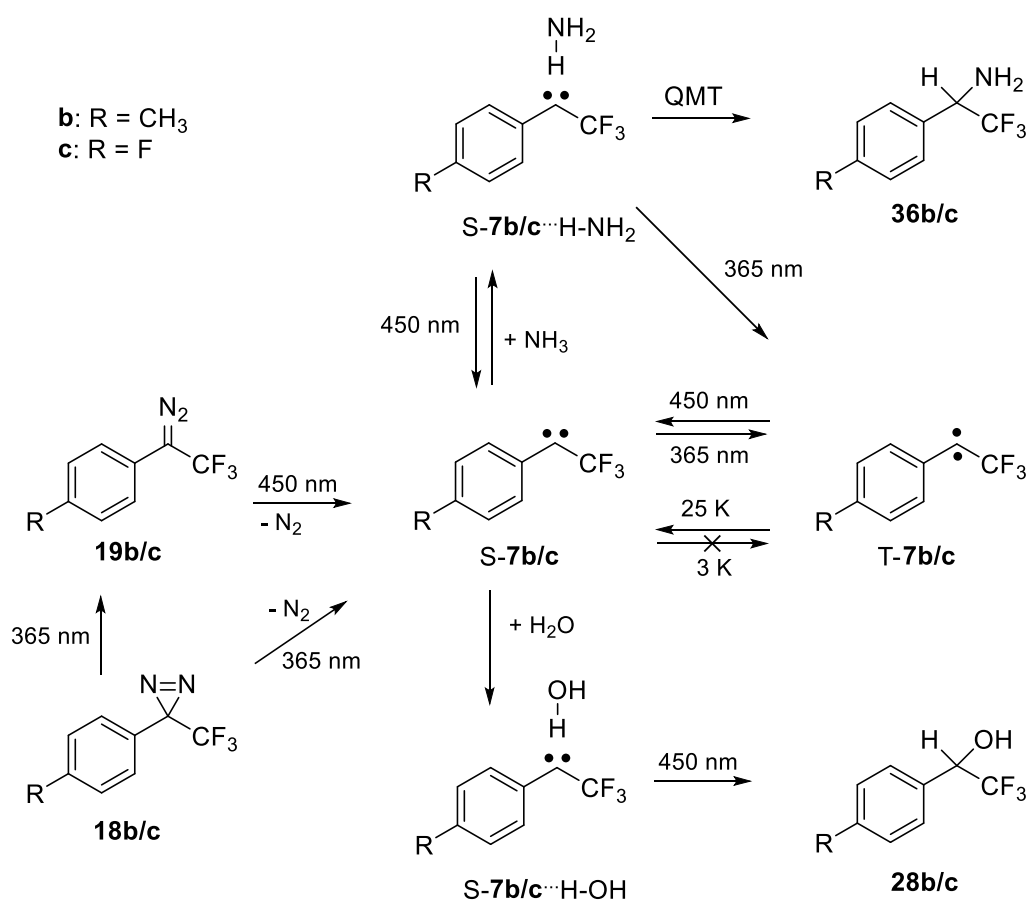
A detailed analysis of the chemistry of several aryl(trifluoromethyl)carbenes **7** was carried out by using the matrix isolation technique and quantum chemical calculations (Scheme I). This study shows that the photochemical rearrangement of **7a** to cycloheptatetraene **21a** takes place upon visible light ( $\lambda = 450$  nm) irradiation, in contrast to the parent phenylcarbene **6**, which occurs by UV irradiation. On the other hand, carbenes **7b-7i** are found to be stable under both UV and visible light irradiations.



**Scheme I.** Aryl(trifluoromethyl)carbenes investigated in this study.

At cryogenic temperatures, carbenes are generally produced in their thermodynamically most stable electronic ground state, which can be either singlet or triplet, but its excited spin state could not be detected as the inter system crossing (ISC) is too fast under these conditions. In contrast to this general belief, with our experiments we show that **7b** can be isolated in both its lowest singlet (**S-7b**) and triplet (**T-7b**) states at low temperatures of 3 K. At temperatures below 10 K, both spin states coexist indefinitely and can be interconverted by irradiation into the absorption maxima of **S-7b** in the UV or **T-7b** in the visible range, respectively. Annealing at higher temperatures (> 20 K) leads to an increase of **S-7b**, which is not reversible by cooling back to lower temperatures (3 K) (Scheme II). An alternative way to generate the singlet carbene **S-7b** is the reaction of the triplet carbene **T-7b** with water molecules by annealing of water-doped matrices at 25 K. This results in the irreversible formation of a hydrogen-bonded complex between the singlet carbene and water (**S-7b**···H–OH). These findings are further supported by DFT calculations at the B2PLYP-GD3BJ/aug-cc-pVTZ level of theory, which predict a S – T gap of –0.4 kcal/mol for carbene **7b**, whereas in the complex with water the gap is –6.5 kcal/mol in favour of the singlet. Similar chemistry was observed for the analogues carbenes **7c** and **7i**. Controlling the magnetic and chemical properties of carbenes by using light of different wavelengths might be of fundamental importance for the understanding of carbene

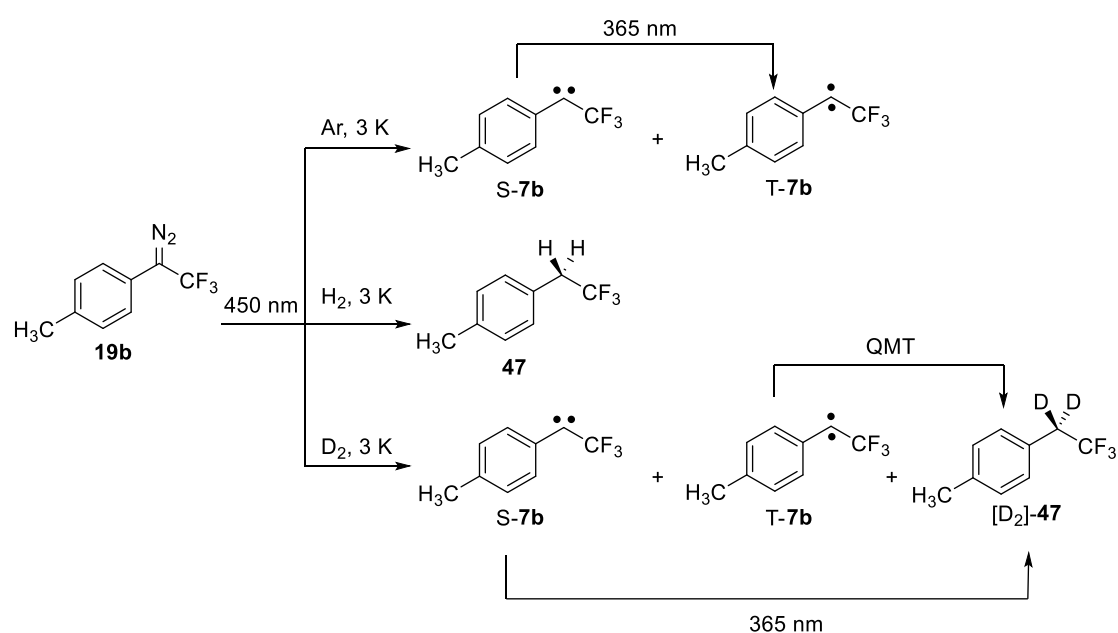
reactions as well as for the development of applications such as optically switchable organic magnetic materials.



**Scheme II.** Synthesis and reactions of aryl(trifluoromethyl)carbenes **7b** and **7c** with water and ammonia.

In a similar manner, singlet carbene **S-7b** was prepared upon the reaction of the triplet carbene **T-7b** with ammonia molecules by annealing of ammonia-doped matrices at 25 K. This results in the formation of a hydrogen-bonded complex (**S-7b**···**H-NH<sub>2</sub>**). Once formed, this complex is only metastable even at cryogenic temperatures and rearranges to form the formal N–H insertion product **36b**. The reaction rate ( $2.5 \pm 0.5 \times 10^{-5} \text{ s}^{-1}$ ) was found to be independent of temperature between 3 and 20 K, strongly indicating a tunneling reaction. Similarly, **S-7b**···**D-ND<sub>2</sub>** was prepared in argon doped with 1% of **ND<sub>3</sub>**. However, **S-7b**···**D-ND<sub>2</sub>** was found to be stable under our experimental conditions at 3 K, indicating a very huge kinetic isotope effect (KIE) as expected for a tunneling reaction. In addition, the reaction between carbene **7c** and ammonia was investigated. The principal results are identical to carbene **7b**. Finally, the carbenes presented here are also generated in amorphous water and ammonia ices at cryogenic temperatures to explore the stability of the carbenes in a reactive, Lewis-basic medium.

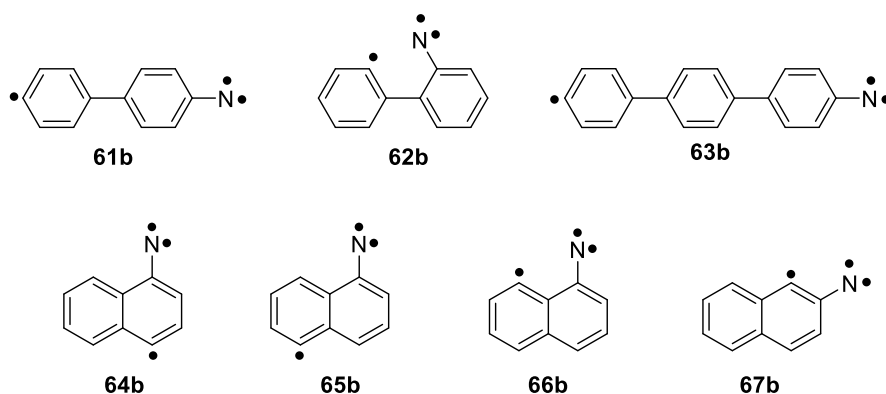
The spin-selective reactivity of **7b** was also studied in solid H<sub>2</sub> and D<sub>2</sub> matrices. Both singlet (**S-7b**) and triplet (**T-7b**) states are not observed in solid H<sub>2</sub>, but they are detected in solid D<sub>2</sub> at 3 K for few hours (**T-7b**) and over 48 hours (**S-7b**) under our experimental conditions. In both matrices, the final product is the insertion product **47** (Scheme III). In a similar manner, the reaction between carbene **7a** and hydrogen was investigated. The principal results are identical to carbene **7b**. These suggests that hydrogenation of carbenes **7a** and **7b** to form the H<sub>2</sub>-insertion product is assisted by QMT at cryogenic temperatures.



**Scheme III.** Photochemistry of **19b** in solid Ar, H<sub>2</sub> and D<sub>2</sub> matrices.

- **Dehydroarylnitrenes**

In addition to aryl(trifluoromethyl)carbenes, the photochemistry of iodinatedbiphenylazides (**61**, **62**), terphenylazide (**63**) and naphthylazides (**64-67**) was carried out by using the matrix isolation technique and quantum chemical calculations. The primary photoproducts are the corresponding nitrenes (**61a-67a**). These nitrenes are highly photolabile and rearranges to the corresponding ketenimine and azirine compounds, in analogy to the photochemistry of the parent arylnitrene molecules (without the iodine group). Despite these competing rearrangements, however, prolonged irradiation ( $\lambda = 254$  nm) of nitrenes **61a**, **62a**, **63a**, **65a** and **67a** produced the corresponding quartet species, which was detected by EPR spectroscopy but the yield was too low to be detected with IR and UV-vis spectroscopy (Scheme IV). In general, the obtained ZFS parameters D and E of the quartet species are linearly related to the spin density at their nitrene and radical centers, respectively.



**Scheme IV.** Dehydroarylnitrenes investigated in this work.

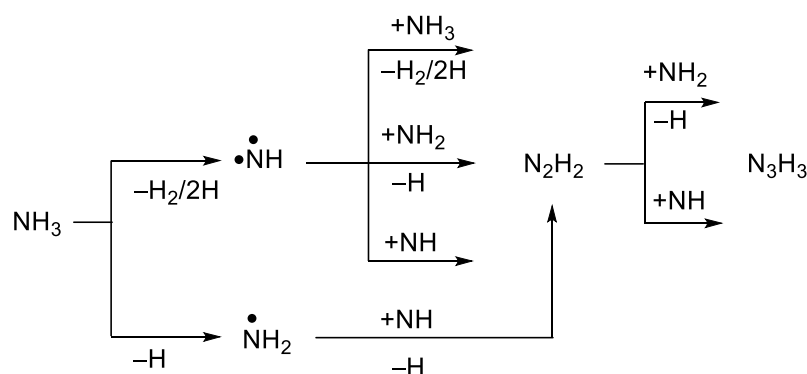
- **Astrochemistry in ammonia ices**

As the number of molecules detected in space increases and the identified molecules grow in complexity, one of the main goals in astrochemistry today is to find a link between astrochemistry and astrobiology. Although not yet detected, hydroxylamine ( $\text{NH}_2\text{OH}$ ) is considered as a potential precursor for the formation of biorelevant molecules like amino acids in the interstellar medium (ISM). During my internship at University of Hawaii, we aimed to prepare  $\text{NH}_2\text{OH}$  under interstellar relevant conditions. In detail, we irradiated binary ice mixtures of ammonia ( $\text{NH}_3$ ) and oxygen ( $\text{O}_2$ ) ices at astrophysically relevant temperatures of 5.5 K with energetic electrons to mimic the energy transfer process that occur in the track of galactic cosmic-rays (GCRs). With our experiments, we proved the synthesis of hydroxylamine ( $\text{NH}_2\text{OH}$ ), water ( $\text{H}_2\text{O}$ ), hydrogen peroxide ( $\text{H}_2\text{O}_2$ ), nitrosyl hydride ( $\text{HNO}$ ) and a series of nitrogen oxides ( $\text{NO}$ ,  $(\text{NO})_2$ ,  $\text{N}_2\text{O}_2$ ,  $\text{N}_2\text{O}$ ,  $\text{NO}_2$ ,  $\text{N}_2\text{O}_3$ ) under these conditions. We also conducted an isotope-labeled experiment examining the electron-irradiated D3-ammonia–oxygen ( $\text{ND}_3\text{--O}_2$ ) ices, which confirmed our findings. Infrared spectroscopic analysis complemented by temperature programmed desorption (TPD) studies utilizing highly sensitive reflectron time-of-flight mass spectrometry coupled with pulsed photoionization (PI-ReTOF-MS) at photoionization energies of 10.49 eV was used to analyze our data. In summary, our study provides clear, concise evidence of the formation of hydroxylamine by irradiation of interstellar analog ices and can help explain the question how potential precursors to complex biorelevant molecules may be formed in the ISM.



**Scheme V:** Formation of hydroxylamine ( $\text{NH}_2\text{OH}$ ) in low temperature interstellar model ices.

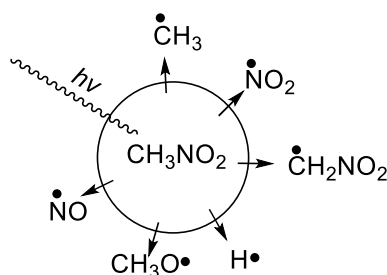
The second project at University of Hawaii was targeting to synthesize the highly elusive fundamental triazene ( $\text{N}_3\text{H}_3$ ) molecule. Triazenes, a class of compounds with  $\text{R}_1\text{R}_2\text{N}-\text{N}=\text{N}-$  moiety, is a potential key intermediate in hydrogen–nitrogen chemistry ranging from polymer synthesis to anticancer drugs. With our study, we report the first experimental detection of  $\text{N}_3\text{H}_3$ ,  $\text{N}_3\text{D}_3$ ,  $^{15}\text{N}_2\text{NH}_3$  and  $^{15}\text{NN}_2\text{H}_3$  in the gas phase after it sublimates from energetically processed ammonia bearing starting materials ( $\text{NH}_3$ ,  $\text{ND}_3$ ,  $\text{NH}_3:\text{N}_2$  and  $\text{NH}_3:^{15}\text{N}_2$  ices). This study also suggests that the most likely formation pathway of  $\text{N}_3\text{H}_3$  is via the diimide ( $\text{N}_2\text{H}_2$ ) (Scheme VI).



**Scheme VI.** Principal reaction pathways towards the formation of  $\text{N}_3\text{H}_3$ .

- **Nitromethane**

Nitromethane ( $\text{CH}_3\text{NO}_2$ ) is an important polar solvent with many applications in industry and synthesis. At the same time, it is the simplest organic nitro compound. The decomposition of nitromethane leading to highly reactive radicals is therefore an important issue for many applications. To investigate this, the photolysis of nitromethane at discrete wavelength between 266 nm and 121 nm has been studied in detail in the neat compound at cryogenic temperatures as well as in argon and neon matrices, and a number of reaction intermediates and products with unpaired electrons were identified for the first time (Scheme VII).



**Scheme VII.** Compilation of the photodecomposition of nitromethane detected by EPR spectroscopy.

## 1. General introduction

### Why chemistry at cryogenic temperatures?

The goal of this work and physical organic chemistry at large is to understand the reaction mechanisms that involve in chemical processes. As such, many chemical reactions, particularly those initiated photochemically, generates short-lived, highly reactive species that undergo further reactions very rapidly, and thus their concentration is too low to be detected under ordinary techniques. As a result, the chemical and physical characterization of these species are usually performed at extremely low (cryogenic) temperatures. The IUPAC definition of "cryogenic" states that "*low temperature processes, apparatus, etc.; usually applied to systems operated at the temperature of liquid nitrogen, helium or other condensed gas which boils at a very low temperature.*" Under cryogenic conditions, atoms, radicals and molecules are cooled down and thus there is negligible thermal/kinetic energy available for diffusion and chemical reactions. By combining with matrix isolation technique, which is mainly used in this work, the fundamental aspects of chemical structure and reactivity of what is known as "reactive intermediate" can then be obtained and characterized spectroscopically in detail, with the same degree as is possible to study stable molecules.

The area of low temperature chemistry covers all fields of chemistry, from synthesis, characterization and identification of reactive organic molecules to the chemical modification of ices by energetic irradiations relevant to interstellar processes. Many fundamental aspects of reactions, for example, tunneling reactions can be studied at cryogenic temperatures. Several books and reviews have been devoted to this emerging field of chemistry.<sup>[1-4]</sup>

### Carbenes

Carbenes are neutral divalent carbon species, which play a prominent role not only in synthetic chemistry, reaction mechanisms and materials-related practical applications, but also in astrochemistry, atmospheric chemistry as well as photoaffinity labelling.<sup>[5-11]</sup> It possess two non-bonding electrons that occupy two orbitals, an in-plane hybridized  $\sigma$ -orbital and out-of-plane  $\pi$  orbital,<sup>[12]</sup> and therefore can have two spin states depending on the distribution of the electrons. If the two electrons occupy separate orbitals with parallel spins, then the spin state of the system is  $S = \frac{1}{2} + \frac{1}{2} = 1$  and the multiplicity is  $m_s = 2S + 1 = 3$ , often referred to as a triplet state. On the other hand, if we have opposing spins either in the same (closed-shell) or

in a separate (open-shell) orbitals,  $S = \frac{1}{2} + (-\frac{1}{2}) = 0$  and  $m_s = 1$ , gives rise to a singlet state. The energy difference between the lowest lying singlet state (closed-shell) and triplet state is referred to as “singlet-triplet splitting” ( $\Delta E_{ST}$ ).

Geometrically, carbenes can be either linear or bent (Figure 1).<sup>[13-14]</sup> If the carbene is linear, the two nonbonding electrons would occupy the two degenerate  $p_x$  and  $p_y$  orbitals according to the Hund’s rule, and thus the ground spin state of the carbene should be a triplet. In a bent structure, however, the carbene adopts a  $sp^2$ -hybridization and therefore, breaks the degeneracy of the orbitals by stabilizing the  $p_x$  orbital which in turn gains additional  $s$  character. The resulting orbital is often referred to as  $\sigma$  orbital. On the other hand, the  $p_y$  orbital will not be significantly perturbed as a result of bending, classified as  $\pi$  orbital. The distribution of the two non-bonding electrons into  $\sigma$  and the  $\pi$  orbitals determines the ground state spin multiplicity of carbenes, and corresponds to the lowest sum of orbital energies and electron-electron repulsion. If the energy gap between  $\sigma$  and  $\pi$  orbital is large, then the unpaired electrons occupy the lower energy  $\sigma$  orbital, giving a singlet state. However, if the spacing is small, the electron-electron Coulombic repulsion is larger than the energy required to promote an electron from  $\sigma$  to  $\pi$  orbital, resulting in a triplet state. Accordingly, the chemistry of carbenes depends on ground spin multiplicity and the  $\Delta E_{ST}$  energy gap, which can be rationalized in terms of the electronic, steric and hyperconjugation properties of the substituents.<sup>[15]</sup>

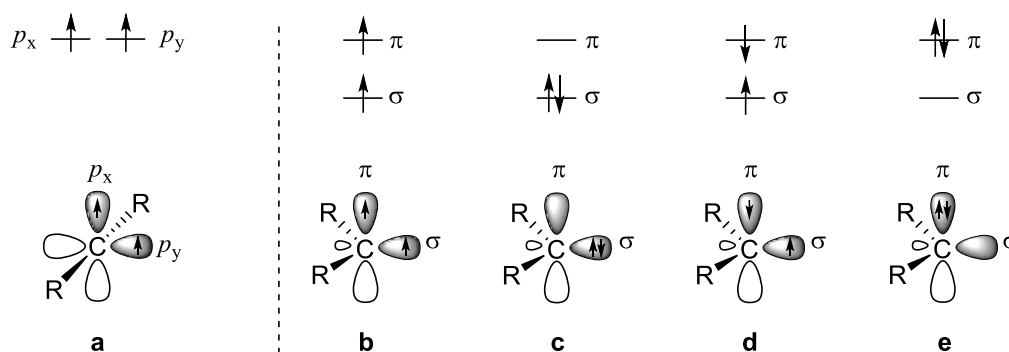
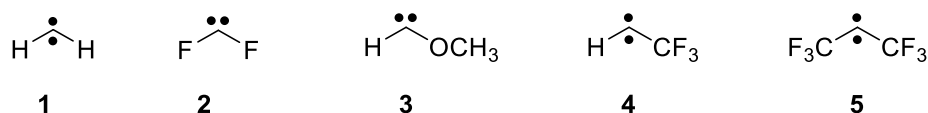


**Figure 1.** Schematic depiction of the electronic configurations of carbenes in a linear structure with the carbon  $sp$ -hybridized (left) and in a bent structure with the carbon  $sp^2$ -hybridized (right). a) Triplet state,  $p_x^1 p_y^1$ . b) Triplet state,  $\sigma^1 \pi^1$ . c) Closed-shell singlet state,  $\sigma^2$ . d) Open-shell singlet state,  $\sigma^1 \pi^1$ . e) Closed-shell singlet state,  $\pi^2$ .

The simplest carbenes, methylene **1** and difluoromethylene **2**, have been investigated in great detail both experimentally and theoretically.<sup>[16-18]</sup> EPR experiments determined that **1** is a triplet ground state carbene with a bond angle of H–C–H around  $136^\circ$ .<sup>[19]</sup> This suggested that the geometry of methylene is bent with the carbon atom  $sp^2$ -hybridized. Noteworthy, compared to the triplet state, the singlet state should have a smaller angle, since this geometry increases

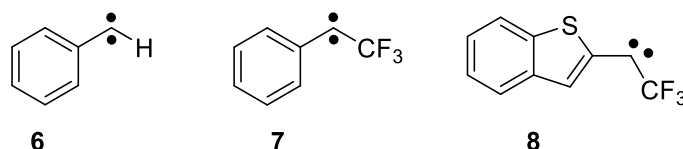
the s character in the  $\sigma$  orbital, and thus minimizing the electron-electron repulsion.<sup>[12]</sup> Further, using far-infrared laser magnetic resonance spectroscopy<sup>[20]</sup> and negative ion photoelectron spectroscopy (NIPES),<sup>[21]</sup> the  $\Delta E_{ST}$  of **1** was determined experimentally to be 9.05 kcal/mol. In contrast, in difluoromethylene **2**, the singlet state was found to be  $-54 \pm 3$  kcal/mol below the triplet state according to NIPES measurements.<sup>[22]</sup> Thus, the substituents determine the ground state spin multiplicity and  $\Delta E_{ST}$  of the carbenes. The stabilization of the singlet state in carbene **2** can be rationalized by the  $\pi$  donor ability and inductive electron withdrawal effect of the fluorine atoms which, respectively, raises the  $\pi$  and lowers the  $\sigma$  orbital energies, and stabilizes the singlet state. For the same reason, carbene **3** is found in a singlet ground state.<sup>[23]</sup> Moreover, this effect has led to several room temperature stable singlet carbenes.<sup>[24-25]</sup>



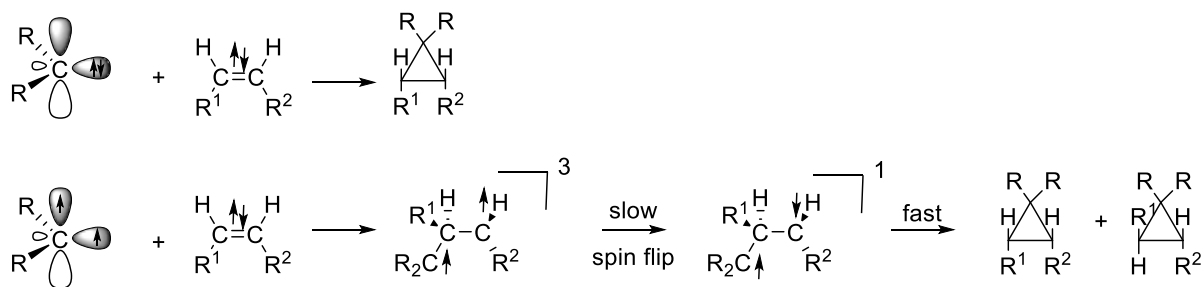
Given that  $\pi$  donor substituents stabilize the singlet state, common analogy suggests that the strongly electron withdrawing  $\text{CF}_3$  group should have the opposite effect, destabilizing the singlet carbene relative to the triplet. However, this assumption does not hold for the spin state of reported carbenes, where the  $\text{CF}_3$  group attached adjacent to the carbene carbon. In 1985, calculations by Dixon suggested that the  $\text{CF}_3$  group could affect  $\Delta E_{ST}$  in a manner similar to hydrogen.<sup>[26]</sup> Later, calculation by O’Gara and Dailey at the QCISD(T)/6-311(2D,2P)//MP2-(FC)/6-31G\*\* level of theory predicted  $\Delta E_{ST}$  of 10.8 and 8.5 kcal/mol for carbenes **1** and **4**, respectively, suggesting that the  $\text{CF}_3$  group either stabilizing the singlet or destabilizing the triplet.<sup>[27]</sup> Note that, since a  $\text{CF}_3$  group is considerably larger than H, steric effects are also expected to disfavor smaller angle of singlet  $\text{CF}_3$  carbenes. Despite of this effect, however, Nemirowski and Schreiner reported that **5** has a  $\Delta E_{ST}$  gap of 1 kcal/mol lower than that of carbene **1** at the CCSD(T)/cc-pVDZ level of theory.<sup>[28]</sup>

More recently, calculation and experimental works showed that substitution of a hydrogen atom by a  $\text{CF}_3$  group stabilizes the singlet state of carbenes relative to triplet by a small amount. Calculations by Song and Sheridan at the B3LYP/6-31+G(d,p) level of theory predicted a S – T gap of 11.1 and 4.0 kcal/mol for carbenes **4** and **7**, compared with 12.4 and 5.4 kcal/mol for carbenes **1** and **6**, respectively.<sup>[29]</sup> By employing natural bond analysis, Sheridan concluded that this energy lowering is due to rehybridization of the carbenic carbon, induced by the strong inductive electron-withdrawing effect of the  $\text{CF}_3$  group. Moreover, adding  $\pi$  donor substituents

to the  $\text{CF}_3$  carbene increases the  $\sigma$ - $\pi$  energy gap further. Accordingly, the low temperature spectroscopy and chemical reactivity of **8** was found to be consistent with a singlet ground state carbenes.<sup>[30]</sup> Finally, because of the strength and the electron deficient nature of the C-F bond, carbenes such as **7** and **8** are expected to not show 1,2-fluorine migrations thereby stabilizing the carbene center kinetically, adding advantage to exploring these carbenes while information on the hydrocarbon counterparts are difficult to obtain.<sup>[31]</sup>



Due to the different geometries and electron configurations, one method to determine the carbene multiplicity is based on reactivity.<sup>[32-33]</sup> The triplet state has two electrons in the  $\sigma$  and  $\pi$  orbitals, and therefore displays similar reactivity as radicals. On the other hand, the singlet state has a pair of electrons in one of the  $\sigma$  (or  $\pi$  orbital), leaving the other orbital empty. Thus, triplet carbenes undergo stepwise radical-type abstraction reactions, whereas singlet carbenes are likely to react in concerted reactions. For instance, singlet carbenes react with alkenes in a single step to form cyclopropanes with retained stereochemistry, whereas triplet carbenes cannot form a covalent bond with the two unpaired electrons simultaneously, since it is a spin-forbidden process. Instead, the reaction proceeds in two steps via a radical pair intermediate followed by spin flipping yielding a mixture of cis- and trans cyclopropane (Scheme 1). Thus, a comparison of the stereochemistry of the starting alkene and the cyclopropane product can be used as one of the experimental tests to determine the spin state of the reacting carbene, known as the Skell-Woodworth rule.<sup>[34]</sup> Alternatively, the reactions with alcohols has been used to determine the spin-selectivity chemistry of carbenes: triplet carbenes undergo insertion into C-H bonds whereas singlet carbenes insert into the O-H bonds of alcohols.<sup>[35-36]</sup>



**Scheme 1.** Addition of singlet and triplet carbenes to alkenes.

## Nitrenes

Nitrenes are a neutral monovalent nitrogen species containing six valence electrons.<sup>[37-38]</sup> Nitrene play a great role in multiple applications for example as a potential candidate for building organic magnets.<sup>[39-40]</sup> Moreover, aryl azides, commonly used for generating aryl nitrenes, have applications in organic synthesis,<sup>[41]</sup> in the formation of electrically conducting polymers<sup>[42]</sup> and as photoaffinity labelling for identifying biological receptors.<sup>[8]</sup> A nitrene is equivalent to a carbene with a  $sp$ -hybridized nitrogen atom. It possesses four nonbonding electrons that are distributed into two  $p$  orbitals. Depending on the distribution of the electrons, nitrene can exist in triplet, open-shell singlet or closed-shell singlet ground-states (Figure 2).<sup>[43]</sup> Therefore, in analogy to carbenes, the chemistry of nitrenes depends on the energy separation between the frontier orbitals that can be rationalized in terms of the effect of the substituents.

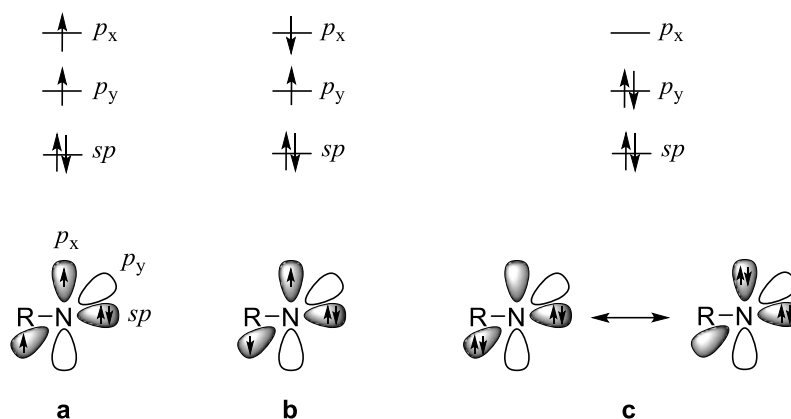
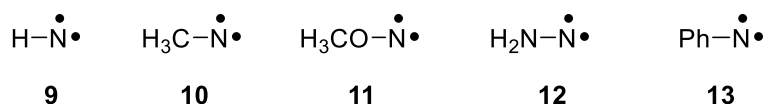


**Figure 2.** Schematic depiction of common electronic configurations of nitrenes. a) Triplet state. b) Open-shell singlet state. c) Closed-shell singlet state.

The simplest nitrene, imidogen **9** has been studied in detail both experimentally and theoretically. The ground state of **9** is a triplet as examined with EPR spectroscopy.<sup>[44]</sup> The  $\Delta E_{ST}$  gap of **9** was determined experimentally by NIPES to 36 kcal/mol,<sup>[45]</sup> a value much larger than the  $\Delta E_{ST}$  separation of the isoelectronic carbene **1** (9.05 kcal/mol)<sup>[21]</sup> determined using the same technique. This huge  $\Delta E_{ST}$  difference can be explained in two ways. First, the two non-bonding electrons in **9** occupy the energetically degenerate  $p$  orbitals, whereas in **1** the non-bonding electrons are in a non-degenerate  $\sigma$  and  $\pi$  orbitals. Thus, the electron-electron Coulombic repulsion in **9** is severe relative to **1** and greatly favors the triplet state. Second, the zero field splitting (ZFS) parameter  $D$  reported for carbene **1** and nitrene **9** are 0.6881 and 1.86  $\text{cm}^{-1}$ , respectively.<sup>[19, 44]</sup> In other words, as we will see it in the EPR section, these experiments demonstrated that the distance between the two non-bonding electrons in **9** is relatively smaller

than **1**, which implies that the singlet state of **9** suffers more electron-electron repulsion compared to **1**. For the same reasons, the  $\Delta E_{ST}$  gap of phenylnitrene **13** determined experimentally by NIPES to 14.8 kcal/mol<sup>[46]</sup> is much higher than the  $\Delta E_{ST}$  of 2–3 kcal/mol obtained for phenylcarbene **6** in various solvents.<sup>[47]</sup>



In analogy to carbenes, substituents affect the singlet-triplet separation of nitrenes both sterically as well as electronically. However, because of the very large  $\Delta E_{ST}$  of the parent nitrene **9**, strong electron donating groups such as NH<sub>2</sub> are required to switch the spin state of nitrenes, explaining the reason why most of the reported nitrenes in literatures have a triplet ground state.<sup>[48]</sup> The singlet-triplet energy separation of **12** is –17 kcal/mol compared with 31 and 10 kcal/mol for **10** and **11**, respectively.<sup>[43]</sup>

Similar to the chemistry of carbenes, the chemical reactivity of nitrenes depends on their spin multiplicity. For example, singlet nitrenes undergo insertion into the aryl C–H bonds in a concerted approach, whereas triplet nitrenes insert into the alkyl C–H bonds in a two-step process through abstraction-recombination mechanisms.<sup>[43]</sup> Compared to carbenes, the  $\Delta E_{ST}$  gaps in nitrenes are bigger, which results in a more rapid intersystem crossing (ISC) in carbenes relative to nitrenes.<sup>[49]</sup> Thus, the rate of the reaction in nitrenes and carbenes differs extremely under different conditions. For example, compared with phenylcarbene **6**, phenylnitrene **13** rapidly undergoes ring expansion in solution at ambient temperatures.<sup>[49]</sup> For the same reason, in solution phase, **7** produces stable products upon reaction with different functional groups such as alcohols and alkenes,<sup>[35-36]</sup> whereas **13** forms polymeric tar that has no application in synthetic chemistry.<sup>[50]</sup>

### Astrochemistry in ammonia ice

Fundamental questions concerning the beginning of life on our planet and its existence elsewhere in the Universe has been a prime focus of investigations for scientists working in chemistry, astronomy and physics. The interdisciplinary science that deals with the chemical origin and fate of life in our Solar System and beyond is known as astrochemistry.<sup>[51-53]</sup> It uses techniques from astronomical observations to laboratory studies and chemical modelling aimed

at exploring the formation, destruction and excitation of molecules in astrochemical environments.

Prior to the detection of ammonia in 1968,<sup>[54]</sup> scientists thought that the space between stars, also known as interstellar medium (ISM), is too hostile for organic species to be formed. This paradigm of thought is mainly due to extreme conditions: temperature ( $\sim 10$  K to  $10^6$  K), pressure ( $\sim 10^{-13}$  torr) and density ( $\sim 10^{-4}$  to  $10^8$  particles per  $\text{cm}^3$ ) as well as energetic irradiations (e.g., galactic cosmic ray particles  $E_{\text{max}} \sim 10^{20}$  eV) occurring in the ISM.<sup>[55]</sup> Accordingly, it seemed impossible to support chemistry, and space was thought to be a void for many years. However, the detection of almost 180 molecules in the colder and denser interstellar regions over the past 50 years (not counting isotopologues) showed that in fact the ISM is host to a rich chemistry.<sup>[56-58]</sup> Majority of the species detected so far are organic molecules such as simple aromatic hydrocarbons (glycoaldehyde<sup>[59]</sup> and acetamide<sup>[60]</sup>) as well as polycyclic aromatic hydrocarbons (PAHs)<sup>[61]</sup> and fullerene.<sup>[62]</sup> Therefore, one of the main goals of astrochemistry today is to link these molecules to (pre)biotic species.

In this context, nitrogen-containing compounds have been shown to be important. Of the molecules identified in the ISM so far, about one third contain nitrogen atoms. Icy grain mantles within molecular clouds are potential reservoirs of molecules such as ammonia ( $\text{NH}_3$ ) and therefore are worth considering in some detail hereafter.<sup>[63]</sup> Solid ammonia has been observed in the ices surrounding low- and high-mass young stellar objects (YSOs)<sup>[64-66]</sup> as well as in recent comets<sup>[67]</sup> with abundances of a few percent with respect to water. In addition,  $\text{H}_2\text{O}$ ,  $\text{CO}$  and  $\text{CO}_2$  ices have been detected in large quantity in the ISM.<sup>[68]</sup> In general, these species are known to be common during the cold and dense stages of stars formation and are subject to irradiation by energetic particles trapped in planetary magnetospheres. Thus,  $\text{NH}_3$ , along with compounds containing O and C, is a key molecule in the formation of simple amino acids possibly leading to life in the cold icy grains.<sup>[69]</sup> It is worth to mention that in our own Milky Way galaxy, Sagittarius B2 is a perfect target in the search of amino acids. These biorelevant molecules produced can be delivered to young planets including our own planet Earth, which is subject to a long debate.<sup>[70]</sup>

Since the average temperature in the interstellar clouds is below 20 K, all species except He,  $\text{H}_2$  and Ne tend to freeze on the surface of dust ice mantles and remain there for long periods of time. Thus, ammonia may be produced in ISM via barrierless successive hydrogenations of nitrogen atoms on the surface of these ice mantles ( $\text{N} + 3\text{H} \rightarrow \text{NH}_3$ ). This reaction was observed

in laboratory experiments under conditions similar to astrochemical environments.<sup>[71]</sup> Alternatively, NH<sub>3</sub> can also be synthesized by dissociative combination mechanisms (NH<sub>4</sub><sup>+</sup> + e<sup>-</sup> → NH<sub>3</sub> + H).<sup>[72]</sup>

### Laboratory ammonia ice

The ammonia molecule has been subject of investigations in different laboratories for its countless applications, in particular its solid state received considerable astrochemical interest.<sup>[73-74]</sup> At room temperature and regular pressure, ammonia is found in gaseous state, but at temperatures below 240 K it liquidifies. At temperatures below its melting point (195.4 K), ammonia shows a series of solid phase transitions. Under low pressure (ultrahigh vacuum) conditions, ammonia solidifies completely at temperatures below 80 K. The solid state of ammonia can be classified into two main groups, (i) an amorphous phase and (ii) a cubic crystalline phase.<sup>[75]</sup> The phase transition of the amorphous structure of ammonia to the crystalline phase is observed at 57 K.<sup>[75]</sup> Amorphous ammonia ice can be prepared by condensing ammonia directly on a cold substrate in an ultrahigh vacuum chamber at 5 K, to mimicking the conditions of astrochemical environments (Figure 3). This ice is characterized by its broad IR bands at 1077 (ν<sub>2</sub>), 1624 (ν<sub>4</sub>), 3211 (ν<sub>1</sub>) and 3369 (ν<sub>3</sub>) cm<sup>-1</sup>. On the other hand, cubic crystalline solid ammonia can be prepared either by condensing ammonia vapor directly at temperature above 57 K or by annealing the amorphous to temperatures above 57 K. The IR absorption spectrum of the cubic phase are sharper than those of the amorphous phase.<sup>[75]</sup> These observations are similar to the features observed for the phase differences of water ice.<sup>[76]</sup> However, the phase transition of water ice from amorphous to crystalline is observed at 120 K, a much higher temperature than that of the phase transition in ammonia, and is explained by stronger intermolecular interactions. The hydrogen bond in solid ammonia is much weaker (3.1 kcal/mol) compared to that of water (5.1 kcal/mol), since the nitrogen atom has only one available lone-pair of electrons interacting with three hydrogen atoms of neighboring ammonia molecules.<sup>[77]</sup> Finally, laboratory investigations on the radiolysis of ammonia ice under conditions similar to ISM have been reported.<sup>[78]</sup> The synthesis of N<sub>2</sub>, H<sub>2</sub>, NH<sub>2</sub>, N<sub>2</sub>H<sub>2</sub>, N<sub>2</sub>H<sub>4</sub>, N<sub>3</sub>H<sub>5</sub> and HN<sub>3</sub> was evident using FTIR and time-of-flight (TOF) mass spectroscopy.

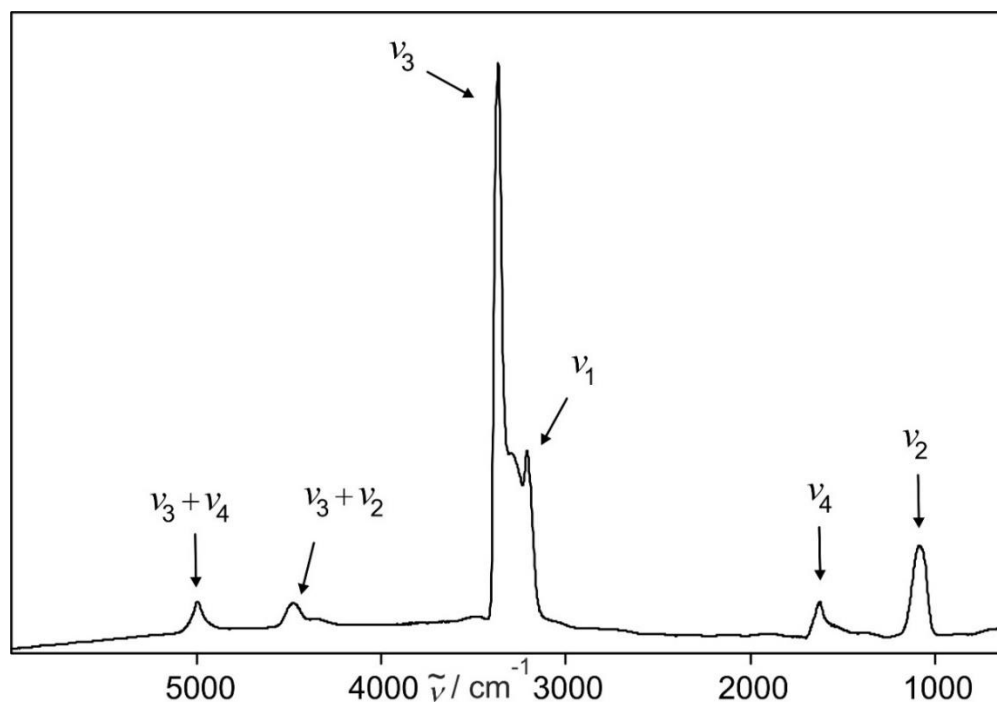


**Figure 3.** IR spectrum of amorphous ammonia ice at 5 K.

## Matrix isolation

As already discussed in the previous sections, the generation and characterization of reactive intermediates using conventional techniques is a challenge for physical organic chemists as they are short lived and highly reactive species. In general, there are two techniques used to overcome this barrier: ultrafast spectroscopy<sup>[79]</sup> and matrix isolation spectroscopy.<sup>[80]</sup> Since the later technique was mainly used for the work of this thesis, details of the method are given below.

The matrix isolation was invented by Pimentel and his co-workers in 1954 to study free radicals and other unstable species.<sup>[81]</sup> In the same year, Norman and Porter independently reported the isolation of atoms and radicals trapped in organic glasses at a temperature of liquid nitrogen.<sup>[82]</sup> Since then, matrix isolation has been broadly used to investigate unstable species such as carbenes, nitrenes, radicals and astrochemical interest compounds at extreme conditions. The method is based on capturing reactive species embedded in unreactive host materials at extremely low temperatures. Briefly, a precursor of the molecule of interest is deposited along with excess of host gas (1:1000), such as argon, neon, nitrogen<sup>[80]</sup> or even water,<sup>[83]</sup> ammonia<sup>[74]</sup> or hydrogen<sup>[84]</sup> onto a cold spectroscopic window and can be converted efficiently to the desired reactive species. The conversion can be achieved in several ways, e.g. by photolysis and pyrolysis.<sup>[81]</sup> The resulting reactive species is isolated in the rigid matrix, and hence

diffusion and intermolecular interactions suppressed. In this way, the fingerprint of the targeted species can be detected using various instrumental techniques such as IR, UV–vis and EPR spectroscopy.

Another application of matrix isolation technique is to study bimolecular chemistry such as weakly bound systems, e.g, hydrogen-bonded complexes, by co-deposition of more than one substrate on the cold spectroscopic window. After the desired reactive species is generated, annealing the matrix to one third of the sublimation point of the host material, e.g. 25 K for argon, allows diffusion of molecules present in the matrix. The interaction of these molecules can then be studied spectroscopically. The reaction of oxygen with phenylcarbene<sup>[85]</sup> or the interaction of water with diphenyl carbene<sup>[86]</sup> are good examples of cryochemical reactions of unstable species studied by matrix isolation techniques. Photochemically induced reactions by irradiation at a suitable wavelength can also be studied using the matrix isolation techniques.<sup>[87]</sup>

To sum up the application of low temperature chemistry combined with matrix isolation techniques, the IR spectrum of ammonia in the gas phase, in the solid phase and in argon matrix are depicted together in Figure 4, as a simplified example. Generally, the IR spectroscopy provides vibrational and rotational information of molecules. However, due to the rigidity of host materials at cryogenic temperatures, the rotation of molecules is highly inhibited, and also only the lowest possible electronic and vibrational states are populated. This results a very fine structure for the matrix-isolated IR spectrum of ammonia in contrast to its spectrum in the gas phase. The spectral differences between with and without a host gas at low temperatures is due to the formation of ammonia aggregates, discussed in the previous section.

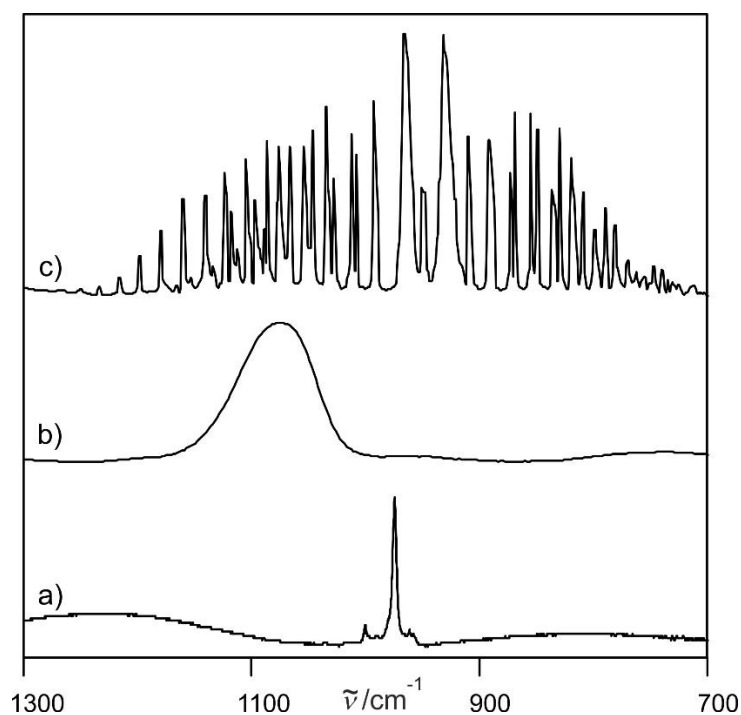


**Figure 4.** IR spectrum of ammonia (a) in argon matrix at 3 K, (b) without argon matrix at 3 K and (c)<sup>[88]</sup> in the gas phase. Note that the small peak in (a) at  $1000.7\text{ cm}^{-1}$  is due to ammonia aggregates.

## EPR spectroscopy

The basic principle shared by all spectroscopic techniques is based on the fact that each atom and molecule has discrete states, each with a corresponding energy. As a result, spectroscopy measures the energy difference that occurred under the influence of electromagnetic radiation. One of these spectroscopic techniques, electron magnetic resonance (EPR) also known as electron spin resonance (ESR), is concerned with the interaction between molecules with at least one unpaired electron ( $S > 0$ ) and an external magnetic field ( $B$ ).<sup>[89]</sup>

## Zeeman splitting

The simplest EPR active system with a single unpaired electron ( $S = 1/2$ ) can exist in one of the two spin quantum number ( $m_s$ ) values,  $+1/2$  and  $-1/2$ . In the absence of the external magnetic field, these two states are energetically degenerate. However, when an external magnetic field is applied, the energy of the  $-1/2$  state decreases whereas the energy of the  $+1/2$  state increases linearly as a function of the strength of the applied magnetic field. This energy splitting is called Zeeman splitting (Figure 5). Mathematically, the electron-Zeeman splitting is defined by  $\Delta E = g_e \mu_B B$ , where  $g_e$  is the factor of electron, describing the magnetic environment of

electron (the free electron  $g$ -value is 2.0023), and  $\mu_B$  is the magnetic moment of a spinning electron called Bohr magneton and it is a constant ( $9.27 \times 10^{-24} \text{ J.T}^{-1}$ ).

The Zeeman splitting energy difference can be matched to the energy of irradiation ( $h\nu = \Delta E = g_e \cdot \mu_B \cdot B$ ), a relation known as the resonance condition, where  $h$  is Planck's constant ( $6.626 \times 10^{-34} \text{ J.s}$ ) and  $\nu$  is the microwave frequency. Accordingly, the EPR experiment can be conducted in two ways; either the magnetic field is held constant and the frequency is varied, or the frequency is kept constant and the magnetic field is varied. For technical reasons, most EPR spectrometers use the latter case.<sup>[89]</sup> For example, the so called X-band EPR spectroscopy which is used in this work, operates at a constant microwave frequency of 9.5 GHz while the magnetic field varies from 20 to 10,000 G. Therefore, as described above, the basis of EPR spectroscopy is the existence of the two Zeeman levels and the possibility of inducing transition from the lower level to the upper level which corresponds to absorption of a radiation in the microwave region.

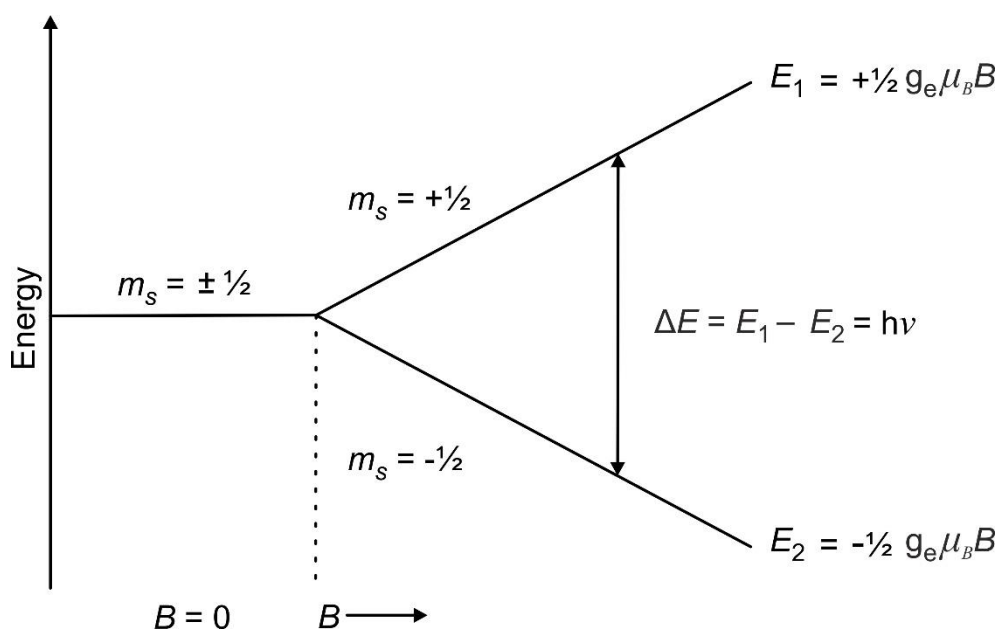


**Figure 5.** Electron-Zeeman splitting as a function of the strength of the magnetic field,  $B$ .

### Hyperfine splitting

In addition to the interaction of electrons with the applied magnetic field, the electron is also very sensitive to its local surroundings. Thus, the interaction between the electron spin and the nucleus spin is called hyperfine interaction. This effect is perhaps one of the most important chemical information that can be obtained about a species by EPR spectroscopy, which allows to identify for example, the identity and number of atoms that make up a molecule or complex.<sup>[90]</sup>

In general, the interaction of the electron spin and  $n$  equivalent spin of a nucleus, described by the spin quantum number  $I$ , produces  $2nI + 1$  number of lines. In many cases, however, the electron can interact with several inequivalent nuclei, which give rise to a more complex spectrum with  $(2n_1I_1) (2n_2I_2) \dots (2n_nI_n)$  number of lines, as shown for some examples below.

A hydrogen atom consists of one proton and one electron. In the presence of the magnetic field, the two energy levels of the electron are aligned with the field ( $m_s = -1/2$ ) or opposing the field ( $m_s = +1/2$ ). These two levels are further split into two levels by interaction with the nuclear spin of the hydrogen atom ( $m_I = \pm 1/2$ ), giving a total of four sublevels. This produces two spectral lines, governed by the EPR selection rules, i.e.,  $\Delta m_I = 0$  and  $\Delta m_s = \pm 1$  (Figure 6). Alternatively, the number of lines in the hydrogen spectrum can also be predicted by the  $2nI + 1$  rule, resulting  $(2 \times 1 \times 1/2) + 1 = 2$  peaks. These predictions agree with experimental findings, which are discussed in the next chapters. The same rules can also be applied to the deuterium atom, which has  $m_s = \pm 1/2$  and  $m_I = \pm 1$ , and thus gives rise to 3 spectral lines.<sup>[91]</sup>

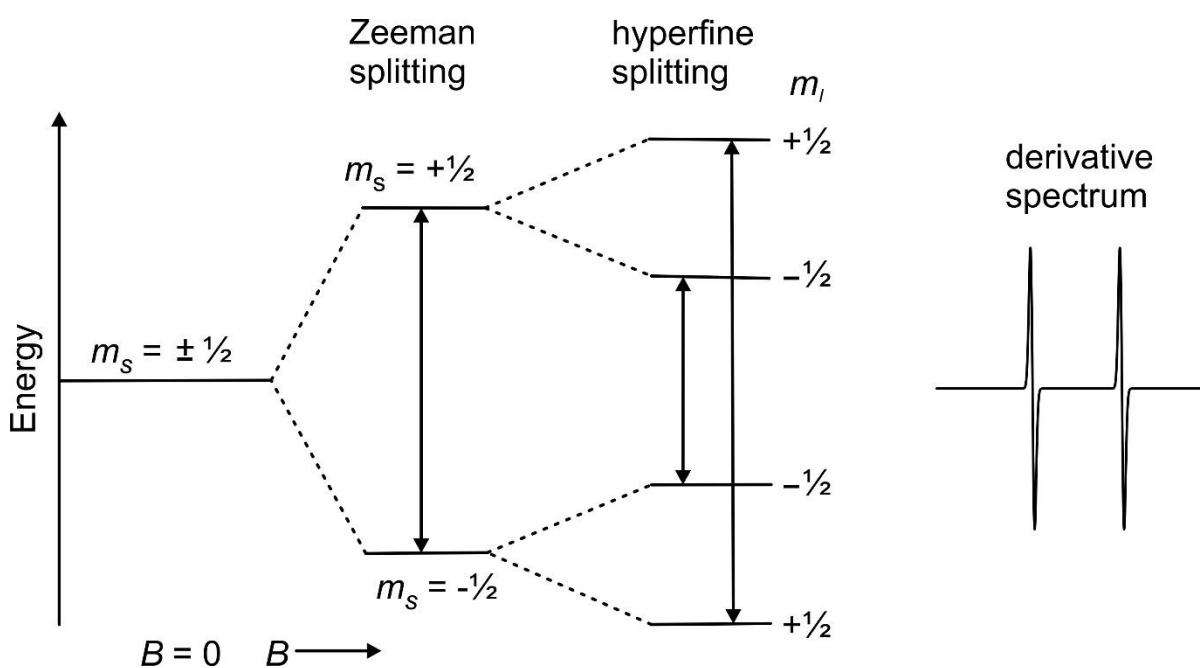


**Figure 6.** Energy level diagram showing the effect of applied field,  $B$ , on the spin energy states  $m_s = \pm 1/2$  and further splitting due to interaction of electron with nuclear spins  $m_I = \pm 1/2$  in hydrogen atom. The actual spectrum of a hydrogen atom is also included in the right side of the figure.

Similarly to the hydrogen atom, methyl radical consists of one electron on the carbon atom and three neighboring hydrogen nuclei. Thus, in the presence of the magnetic field, the electron on the carbon atom splits into two levels, and each level splits further into four sublevels by interacting with the nuclear spin of three hydrogen atoms ( $m_I = \pm 3/2$ ), giving a total of 8

sublevels (Figure 7). This produces four spectral lines obeying to the EPR selection rules. Alternatively, the  $2nI+1$  rule also indicates 4 peaks for  $\text{CH}_3$  radical. Using the same rules, the isotopologues  $^{13}\text{CH}_3$  and  $\text{CD}_3$  radicals should have 8 and 7 lines, respectively.<sup>[92]</sup>

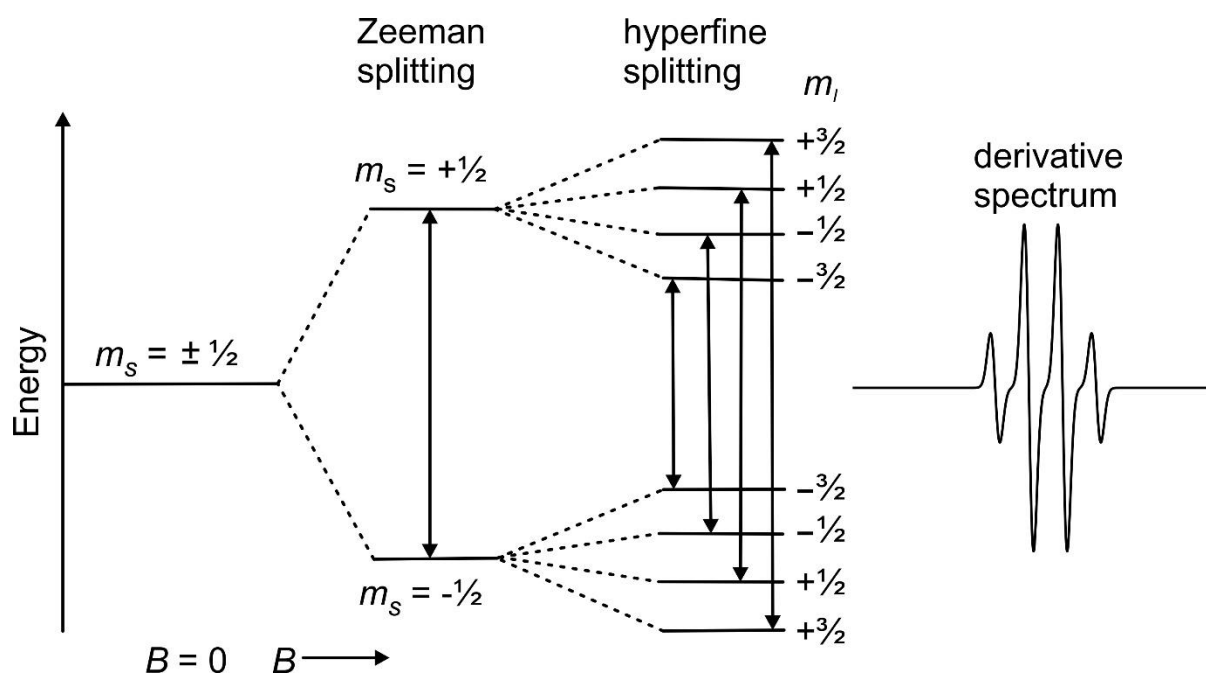


**Figure 7.** Energy level diagram showing the effect of applied field,  $B$ , on the spin energy states  $m_s = \pm 1/2$  and further splitting due to interaction of electron with nuclear spins  $m_I = \pm 3/2$  in methyl radical. The actual spectrum of a methyl radical is also included in the right side of the figure.

### Zero field splitting

So far, we considered the spin systems with one unpaired electron ( $S = 1/2$ ). When more than one electron ( $S > 1/2$ ) is present, e.g., in high-spin systems, we also have to take into account electron spin dipolar interactions. Because of the presence of more than one unpaired electron at small distances, splitting of spin levels occur even in the absence of magnetic field, referred to as zero field splitting (ZFS).<sup>[89]</sup> ZFS can be characterized by two parameters,  $D$  and  $E$ , which are the axial and rhombic components of the magnetic anisotropy, respectively.<sup>[93]</sup> Details are given below for the case of carbenes.

As discussed before, a carbene comprises two unpaired electrons, which can be found in singlet ( $S = 0$ ) or triplet ( $S = 1$ ) state, depending on the alignment of the electrons. There is no EPR transition for the singlet state since the electrons are paired. On the other hand, there are three spin levels in a triplet state ( $m_s = +1, 0, -1$ ), between which two EPR transitions are allowed ( $|0\rangle \rightarrow |+1\rangle$  and  $|0\rangle \rightarrow |-1\rangle$ ), which gives rise to an EPR spectrum.<sup>[93]</sup>

However, the energy of the three spin levels of the triplet state are dependent on the magnetic moment of the electrons, which is connected to the rotation of the molecule in the  $x$ ,  $y$ , and  $z$  directions.<sup>[94]</sup> This behavior is depicted in Figure 8.<sup>[95]</sup>  $T_X$  represents a ZF state in which the two electrons are spinning in the  $YZ$  plane and the components of the spin angular momentum along  $x$  is zero. Likewise  $T_Y$  represents the magnetic moment of a triplet state in which the spin is quantized in the  $XZ$  plane with no spin angular momentum along the direction of  $y$ -axis, and for  $T_Z$  the spin is restricted to the  $XY$  plane with a zero component along the  $z$ -axis.

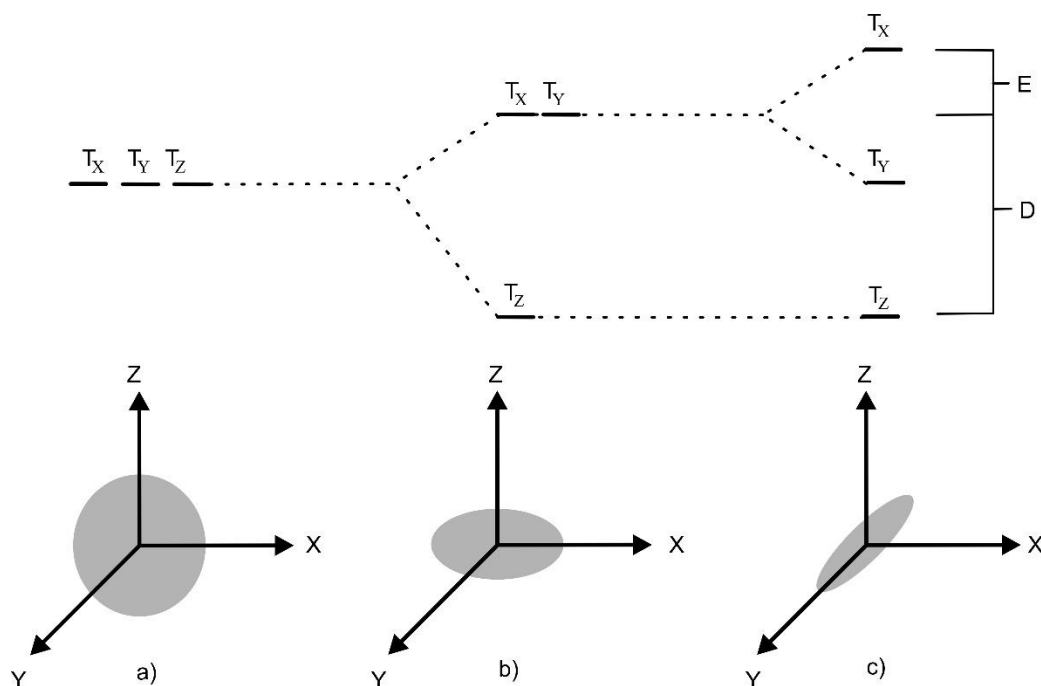


**Figure 8.** Energy states as a function of electron distribution:<sup>[95]</sup> (a) spherical symmetry with the electron evenly distributed, (b) axial symmetry with the electron flattened along  $z$ -axis and (c) anisotropy symmetry with the electron spin interaction flattened along  $z$ -axis and elongated along  $x$ -axis.

Therefore, the quantization of the spins in triplet state is dependent on the geometry of the molecule. In a spherical geometry, the average distance of the two parallel spins in the three different planes is the same, and thus  $T_X$ ,  $T_Y$  and  $T_Z$  are energetically degenerate, i.e., the electrons can move nowhere to minimize the repulsive dipole-dipole interactions and the energy is the same everywhere. If, however, the electron distribution in one direction is perturbed, the average distance between the unpaired electrons in the different planes is not anymore equal. This produces repulsive interaction between the closer electrons, and thus three-fold degeneracy is removed and gives rise to a ZFS. For instance, if symmetry is lost along the  $z$ -axis, the two electrons will be closer to the  $YZ$  and  $XZ$  planes, but further apart in the  $XY$  plane resulting in the state splitting depicted in Figure 8b. Hence, in these cases,  $T_X$  and  $T_Y$  are higher in energy than  $T_Z$ .

The energetic difference of these levels caused by the distribution of electron can be characterized in terms of the ZFS parameters, D and E. In general, D is defined as the distance between  $T_z$  and the center between  $T_x$  and  $T_y$ , whereas E is defined as half the distance between  $T_x$  and  $T_y$ . Thus, when the molecule is spherical both D and E is zero, since  $T_x$ ,  $T_y$  and  $T_z$  are energetically degenerate as we have shown above. On the other hand, when the molecular orbitals are not spherically distributed, for example in the case of planar molecules, D will have a non-zero value but E can have a zero or non-zero value depending on the magnetic dipole interaction along the x and y axes. In a simplified model for a triplet system, D is  $\propto (r^2 - 3z^2)/r^5 \approx (1/r^3)$  and E is  $\propto ((y^2 - x^2)/r^5)$ , where r is the distance between the two spins.<sup>[96]</sup> Thus, a higher D value means stronger spin interaction of the unpaired electrons. Noteworthy, for aromatic carbenes, the more the electrons are delocalized within the aromatic system, the smaller the D value will be. On the other hand, E describes the bond angle at the carbene center and the larger the bond angle, the smaller E value will be. Therefore, the ZFS parameters D and E contain chemical information about the species being studied by EPR spectroscopy.

So far we have discussed for triplet systems in the absence of a magnetic field. In the presence of a field, the triplet spin levels (+1, 0, -1) will undergo Zeeman splitting. Note that only those levels will be affected that have the field aligned parallel (or anti-parallel) to them, otherwise the energy remains the same. For instance, if the field is aligned perpendicular to the z-axis, the electrons whose spin vectors are in the XY plane will be at the same energy, but those in the YZ or XZ planes will either be stabilized or destabilized depending on their alignment, with or against the field. This gives rise to two signals, denoted to as  $z_1$  and  $z_2$ , for the two EPR allowed transitions ( $|0\rangle \rightarrow |+1\rangle$  and  $|0\rangle \rightarrow |-1\rangle$ ). Likewise, there will be additional transitions  $x_1$ ,  $x_2$  and  $y_1$ ,  $y_2$ , for orientations where the magnetic field is parallel to x and y-axes, respectively. Thus, in total 6 transitions are expected for a triplet species.<sup>[97]</sup> However, usually not all of these transitions are accessible as the zero field splitting is already large and the application of external magnetic field will further split the levels, so that some transitions are not observable in the given microwave region.<sup>[93]</sup> For example, the so called X-band EPR spectroscopy operates at a microwave frequency of 9.5 GHz, does not allow to detect the  $x_1$  and  $y_1$  transitions of all triplet carbenes investigated in this work due to their large D values, as shown in Figure 9 for the case of phenyl(trifluoromethyl)carbene **7**.

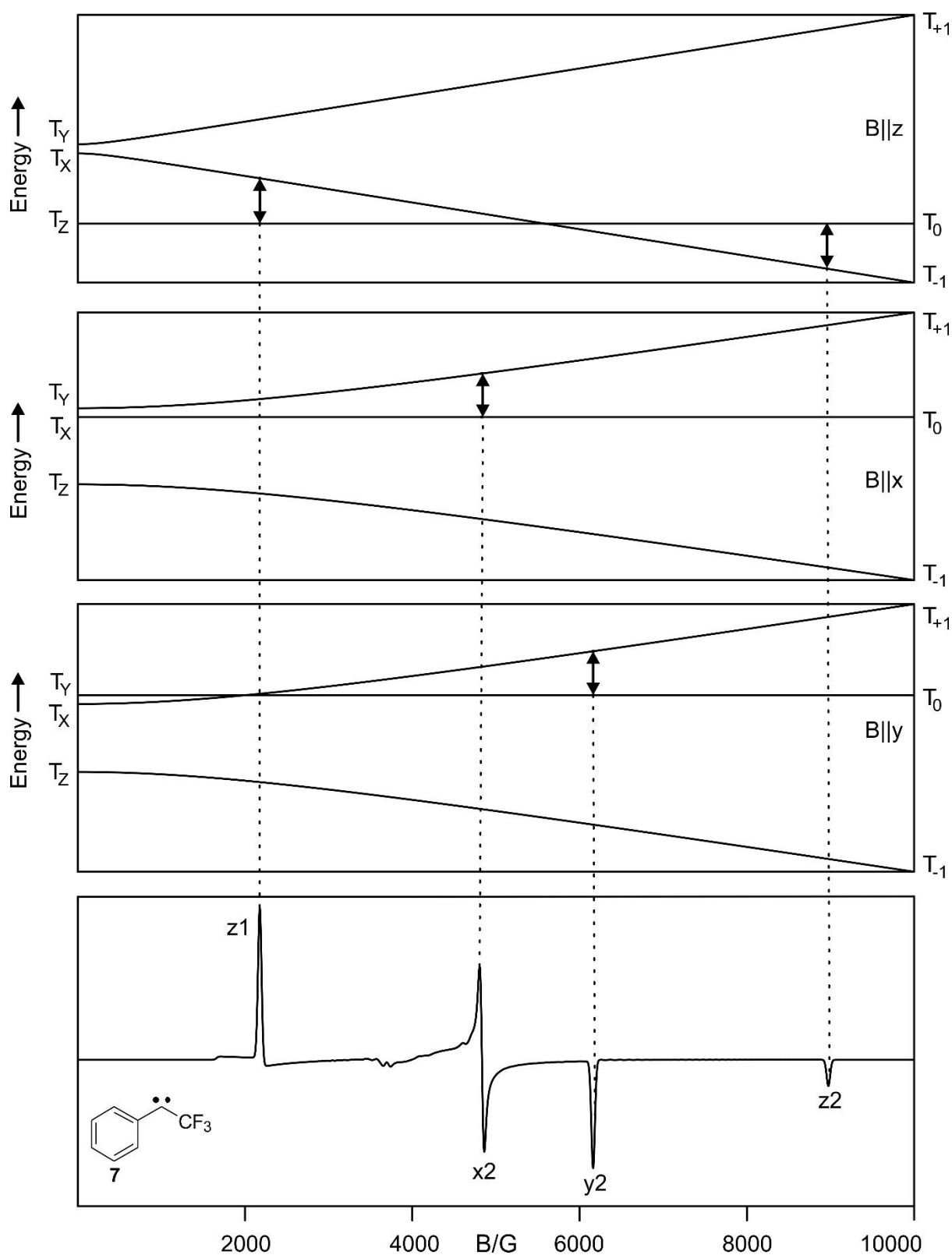
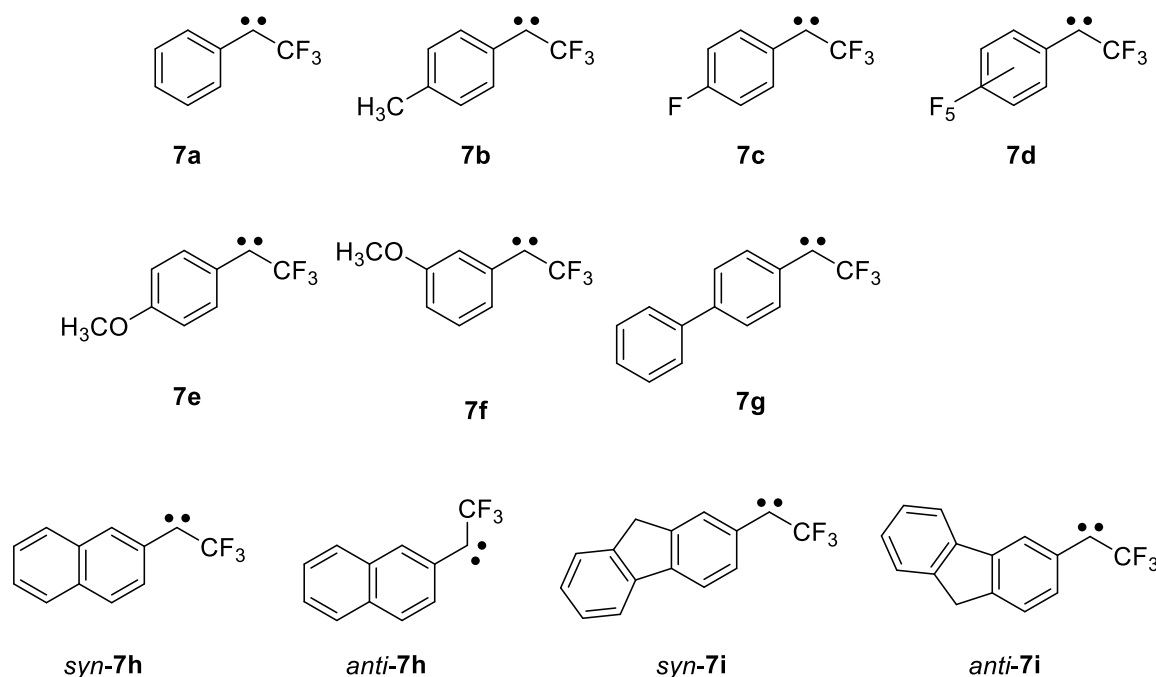


**Figure 9.** The three sublevels of triplet carbene **7** with the external field  $B$  parallel to  $z$ ,  $x$  and  $y$ -axis, respectively, calculated using the ZFS parameters of  $|D/hc| = 0.523 \text{ cm}^{-1}$  and  $|E/hc| = 0.032 \text{ cm}^{-1}$  ( $g = 2.003$ ,  $\nu = 9.5 \text{ GHz}$ ).

## 2. Photochemistry of aryl(trifluoromethyl)carbenes

### Introduction

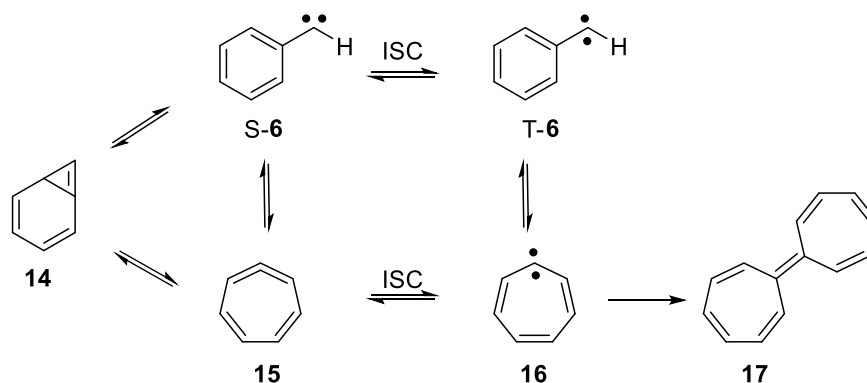
Aryl(trifluoromethyl)diazirine and the corresponding diazo compounds, are commonly used in photoaffinity labeling and cross-linking applications, e.g., for identifying the binding sites of biological receptors and are ideal precursors for generating aryl(trifluoromethyl)carbenes **7**.<sup>[8-11]</sup> Surprisingly, however, little is known about these carbenes and their photochemistry and spin-dependent reactivity has not been reported. Therefore, a set of CF<sub>3</sub> carbenes **7a-7i** (Scheme 2) were synthesized and characterized using matrix isolation IR, EPR and UV-vis techniques as well as quantum chemical calculations. The results are presented in three chapters. First the photochemistry of these carbenes is discussed (Chapter 2), followed by the effect of substituents on the singlet-triplet gaps resulting in energetically degenerate spin state (Chapter 3). Finally, the spin-dependent reactivity of these species with small molecules was investigated (Chapters 3-5).



**Scheme 2.** Aryl(trifluoromethyl)carbenes investigated at cryogenic temperatures.

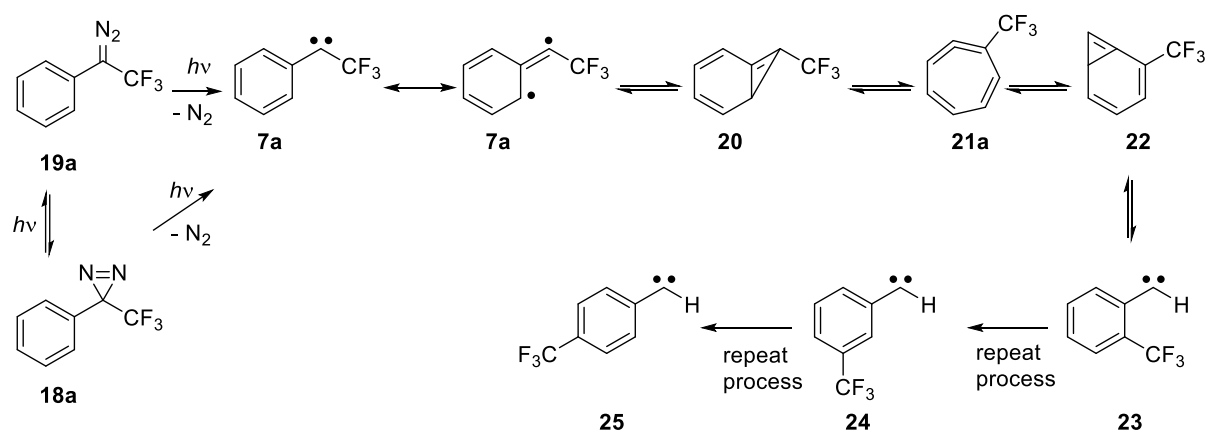
The photo- and thermochemistry of the analogues phenylcarbene **6** have been studied extensively.<sup>[98-99]</sup> The mechanism of the phenylcarbene rearrangements to different products such as cycloheptatetraene **15**, cycloheptatrienyldiene **16** and heptafulvalene **17** are well understood (Scheme 3). In general, such carbene-carbene rearrangements are a common

phenomenon for aryl carbenes.<sup>[100-103]</sup> Thus, it is expected that the photochemistry of phenyl(trifluoromethyl)carbenes **7** bears similar reactions, although the presence of the  $\alpha$ -fluorine might inhibit rearrangements of **7**.<sup>[31]</sup>



**Scheme 3.** Phenylcarbene rearrangements. <sup>[98-99]</sup>

In previous studies, phenyl(trifluoromethyl)carbene **7a** has been generated photolytically in low temperature matrices as well as in supersonic jet flash pyrolysis. Thus the EPR spectrum,<sup>[104]</sup> IR spectrum,<sup>[105-106]</sup> TOF-mass spectrum and femtosecond dynamics of **7a** are documented.<sup>[107]</sup> Very recently, Blanch and Wentrup reported a detailed study of the photochemistry of **7a** formed by either broad-band UV photolysis and flash vacuum thermolysis (FVT) of the diazirine precursor **18a** in argon matrix.<sup>[104]</sup> The authors observed the photochemical carbene-carbene rearrangement from **7a** to **23–25** and suggested that this process occurred on the singlet energy surface (Scheme 4). Additionally, the processes were found to be wavelength dependent. However, (trifluoromethyl)cycloheptatetraene **21a**, the main intermediate in the carbene-carbene rearrangement of **7a** to **23–25**, was not detected photochemically.



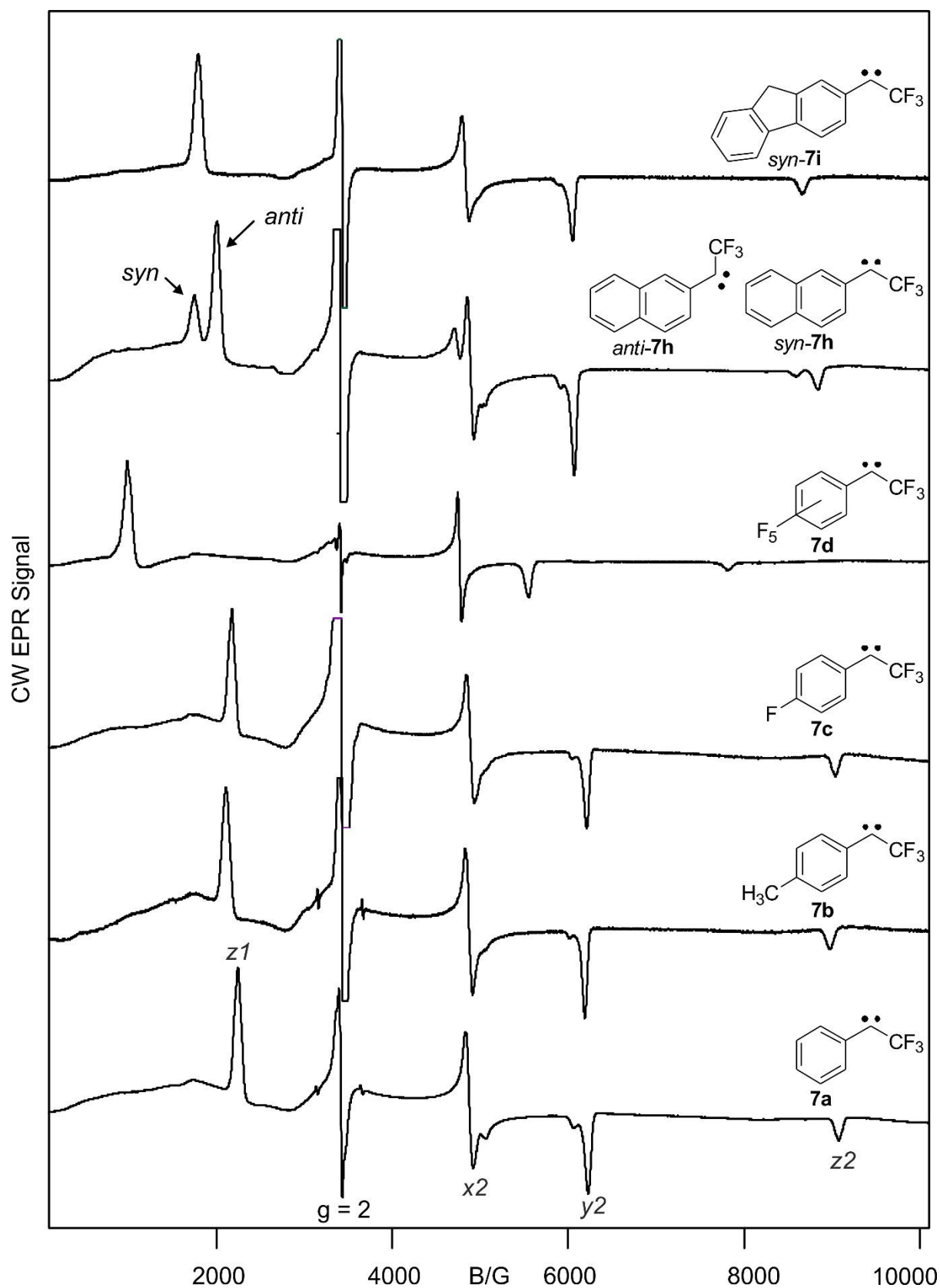
**Scheme 4.** Phenyl(trifluoromethyl)carbene rearrangements. <sup>[104]</sup>

## Results and discussion

### EPR spectroscopy

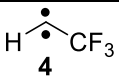
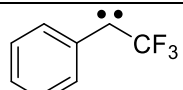
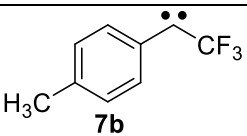
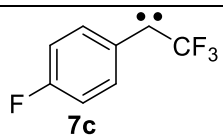
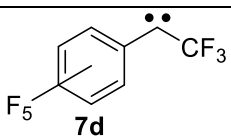
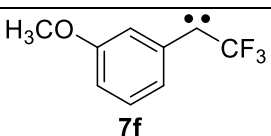
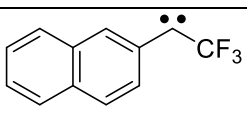
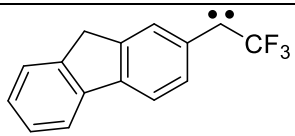
Figure 10 shows the X-band EPR spectra of carbenes **7a-7i** after several hours of visible light ( $\lambda = 450$  nm) irradiation of the corresponding diazo precursors isolated in argon matrix at 4 K. The zero-field splitting (ZFS) parameters of these species (**7a-7i**) are compiled in Table 1. The ZFS parameters obtained for carbene **7a** of  $|D/hc| = 0.527$   $\text{cm}^{-1}$  and  $|E/hc| = 0.032$   $\text{cm}^{-1}$  are in agreement with literature values.<sup>[104]</sup> Likewise, ZFS parameters  $|D/hc| = 0.522$   $\text{cm}^{-1}$  and  $|E/hc| = 0.031$   $\text{cm}^{-1}$  obtained for carbene **7b** are similar to the values reported for **7b** in an organic glass at 77 K.<sup>[108]</sup> The D values are almost identical, whereas the E value in argon is slightly larger than that recorded in the organic glass, which might reflect small differences in the conformation of **7b** generated in different matrices. This values are also comparable to the ZFS parameters obtained for carbene **7c**, which are  $|D/hc| = 0.532$   $\text{cm}^{-1}$  and  $|E/hc| = 0.032$   $\text{cm}^{-1}$ . ZFS parameters of  $|D/hc| = 0.415$   $\text{cm}^{-1}$  and  $|E/hc| = 0.021$   $\text{cm}^{-1}$  are documented for carbene **7d**. As expected, two sets of triplet signals with different ZFS parameters are obtained for carbene **7h**, ascribed to the *syn*- and *anti*-stereoisomers. Briefly, the observed splitting is due to the different electron density distribution at the C-1 and C-3 positions, which has been reported similarly for 2-naphthylcarbene.<sup>[109]</sup> The major signals assigned to *anti*-**7h** has  $|D/hc| = 0.509$   $\text{cm}^{-1}$  and  $|E/hc| = 0.028$   $\text{cm}^{-1}$  whereas the weaker signal assigned to the *syn*-**7h** has  $|D/hc| = 0.487$   $\text{cm}^{-1}$  and  $|E/hc| = 0.028$   $\text{cm}^{-1}$ . Finally, for carbene **7i** ZFS parameters of  $|D/hc| = 0.488$   $\text{cm}^{-1}$  and  $|E/hc| = 0.031$   $\text{cm}^{-1}$  are obtained. For comparison,  $|D/hc|$  and  $|E/hc|$  values for triplet carbenes **4** (0.712 and 0.021)  $\text{cm}^{-1}$  and <sup>[110]</sup> **7f** (0.519 and 0.030)  $\text{cm}^{-1}$ ,<sup>[111]</sup> respectively, were reported in literatures. In contrary, carbenes **7e** and **8** are reported to be EPR inactive.<sup>[30, 111]</sup>

The parameters listed above can be interpreted based on the electronic and steric effects of the substituents. The D values are found to decrease on going from methylene- **4** to phenyl- **7a** to naphthyl- **7h** to fluorenyl- **7i** substituted (trifluoromethyl)carbenes, which can be rationalized in terms of the increase in spin delocalization into the aromatic systems. Note that there are only small changes of the E/D values of carbenes **7a-7i**, which indicates that the central bond angle of these carbenes is not affected significantly by the substituents, in agreement with calculated values ranging between  $136^\circ$ – $138^\circ$  as we will be discussed in the next sections.



**Figure 10.** X-band CW EPR spectra of aryl(trifluoromethyl)carbenes isolated in argon matrices at 4 K. The ZFS parameters of these carbenes are compiled in Table 1. All carbenes were generated with 450 nm irradiation of the corresponding diazo precursors.

**Table 1.** Zero-field splitting parameters for alkyl- and aryl(trifluoromethyl)carbenes in argon matrices at 4 K.

Carbenes	D/hc	E/hc	E/D	Reference
	(cm <sup>-1</sup> )			
 <b>4</b>	0.712	0.021	0.029	[110]
 <b>7a</b>	0.527	0.032	0.061	This work
 <b>7b</b>	0.522	0.031	0.059	This work
 <b>7c</b>	0.532	0.032	0.060	This work
 <b>7d</b>	0.415	0.021	0.051	This work
 <b>7f</b>	0.519	0.030	0.058	[111]
 <b>7h</b>	( <i>syn</i> -) 0.487 ( <i>anti</i> -) 0.509	0.028 0.028	0.057 0.055	This work
 <b>7i</b>	0.488	0.030	0.061	This work

Finally, there is also a linearly correlation found between the experimentally obtained D values of CF<sub>3</sub> carbenes and the calculated spin density ( $\rho$ ) on the carbenic carbon at the B3LYP/EPR-III level of theory. Carbene **4** bears the highest spin density (1.90) and shows the highest D value (0.712) of the carbenes presented in Table 1. The  $\rho$  of **7a** (1.47), **7b** (1.43), **7c** (1.48), **7d** (1.41) and **7f** (1.44) are also calculated employing the same level of theory.

### UV–vis spectroscopy

Similar experiments were carried out using UV–vis detection. Figure 11 shows the UV–vis spectra of carbenes **7a**, **7b**, **7c**, **7h**, **7i** after several hours of visible light ( $\lambda = 450$  nm) irradiation of the corresponding diazo precursors matrix-isolated in argon at 8 K (**7a** was generated by 254 nm irradiation, see IR section). The UV–vis spectrum of carbene **7a** shows a strong absorption band at 248 nm and a weak broad band ranging from 400 to 450 nm. Similarly, carbenes **7b** and **7c** feature a slightly red shifted strong band at 257 and 252 nm, respectively, and weak absorption bands from 400 to 450 nm. Shifts are more pronounced as the  $\pi$  system increases, carbenes **7h** and **7i** show strong UV–vis absorption bands at 281 and 322 nm, respectively, and several weak band in the visible region up to 600 nm.

Therefore, irradiation into these absorption bands is expected to give significant changes in their spectra, which will be discussed in detail in the next chapters. For instance, prolonged irradiation of carbene **7a** with a visible light ( $\lambda = 450$  nm) results in a bleaching of the carbene bands and formation of a broad weak band in the UV region, which is assigned to (trifluoromethyl)cycloheptatetraene **16** based on the results of IR measurements (see IR section).

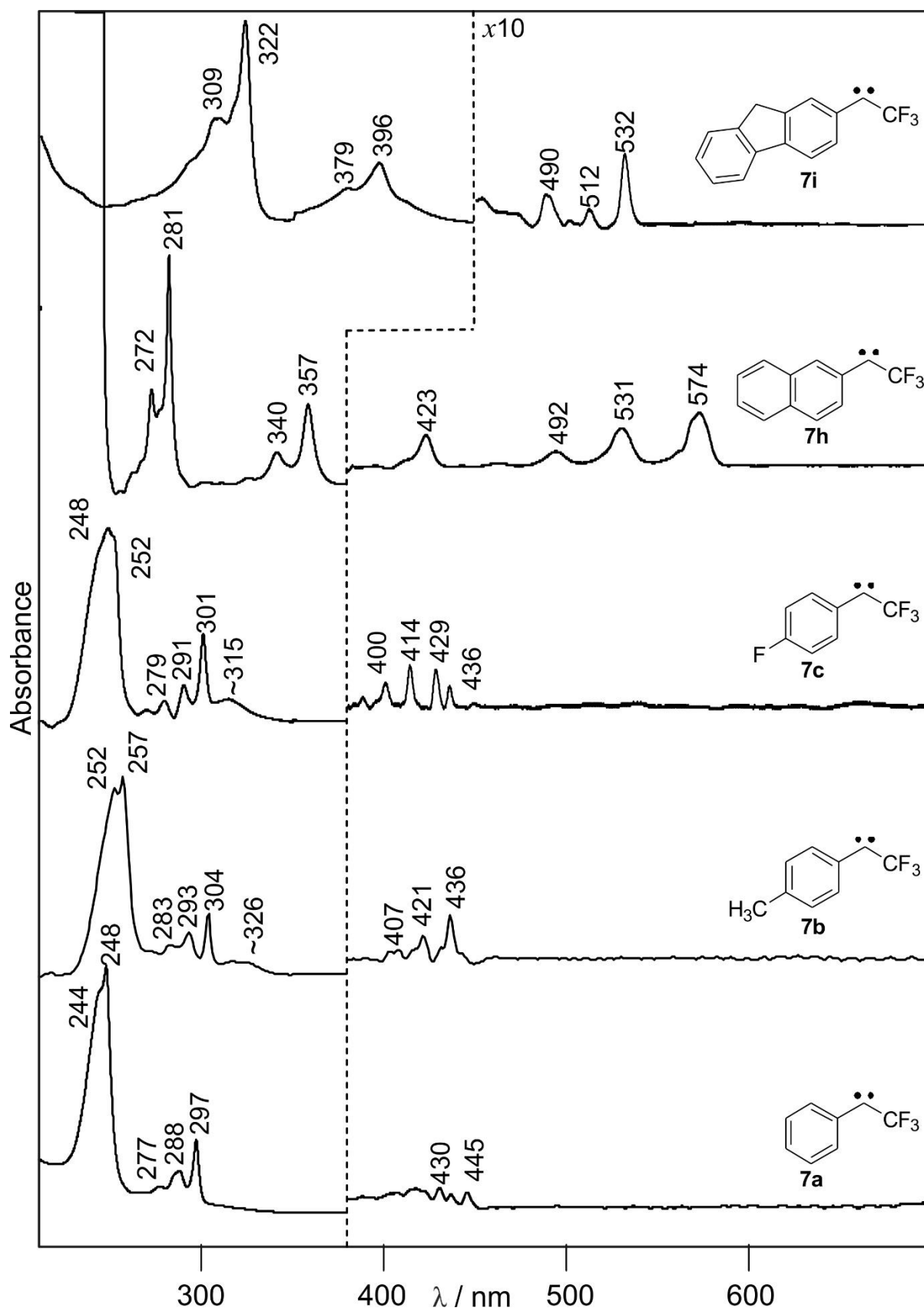


**Figure 11.** UV-vis spectra of aryl(trifluoromethyl)carbenes matrix-isolated in argon at 8 K. All carbenes were generated by 450 nm irradiation of the corresponding diazo precursors, except **7a**, which was generated by 254 nm irradiation (see details in IR spectroscopy section).

## IR spectroscopy

In analogy to the EPR and UV–vis experiments, IR experiments were carried out to explore the photochemistry of aryl(trifluoromethyl)carbenes towards UV and visible light irradiations. Carbene **7a** can be generated upon short time UV ( $\lambda = 254$  nm) or visible light ( $\lambda = 450$  nm) photolysis of the phenyl(trifluoromethyl)diazomethane **19a** isolated in argon matrix at 3 K. The obtained spectrum is found to be in agreement with the values reported in literatures.<sup>[105-106]</sup> However, in contrast to the data in literature, prolonged irradiation of carbene **7a** with visible light results in carbene-carbene rearrangement to (trifluoromethyl)cycloheptatetraene **21a** (Figure 12).

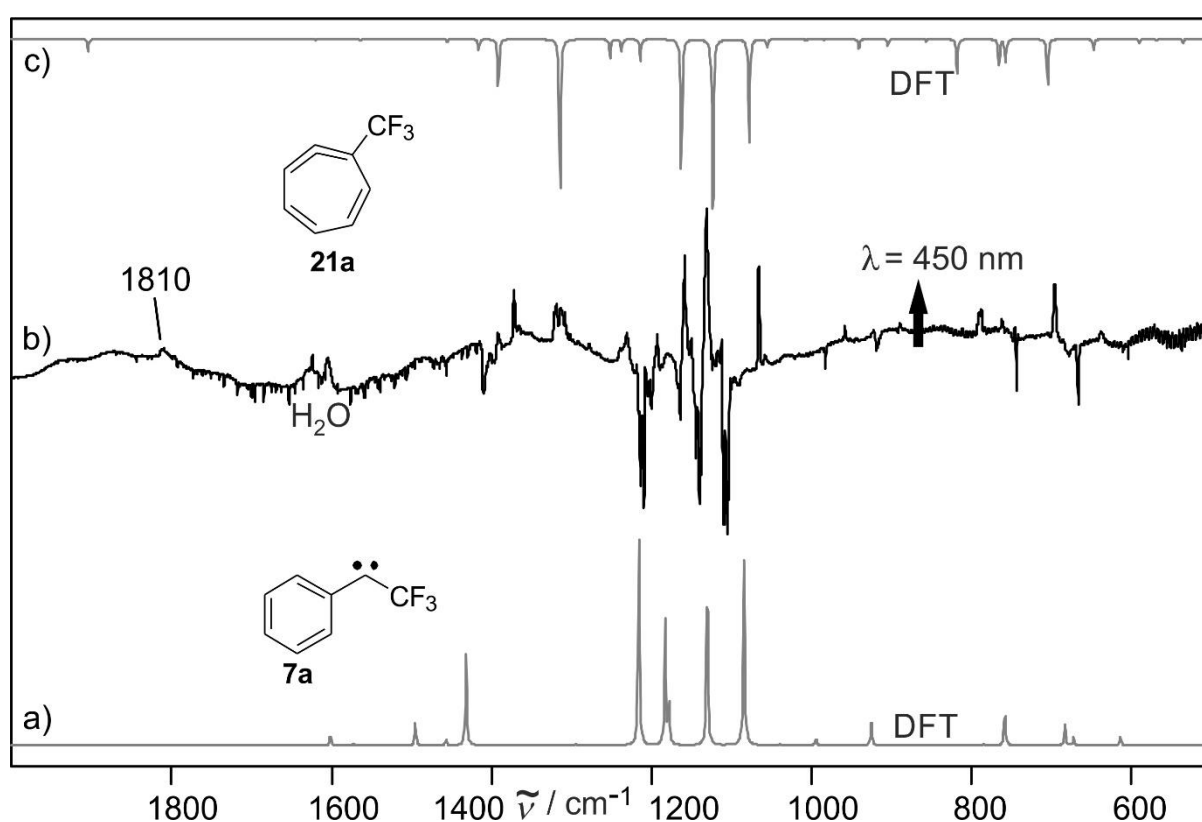


**Figure 12.** IR spectra showing the rearrangement of **7a** to cycloheptatetraene **21a**. a) IR spectrum of **7a** calculated at the B3LYP/6-311++G(d,p) level of theory. b) Difference IR spectrum showing the **7a** to **21a** rearrangement with prolonged 450 nm irradiation. c) IR spectrum of **21a** calculated at the B3LYP/6-311++G(d,p) level of theory.

This is also found in contrary to carbenes **7b-7h**, which are rather photochemically stable toward prolonged irradiation ( $\lambda = 450$  nm). For instance, the rearrangement of carbene **7b** to the corresponding *p*-methyl(trifluoromethyl)cycloheptatetraene **21b** is only achieved with the intense, highly monochromatic light of an OPO laser system in the range between 435 and 444 nm (Figure 13). Both the singlet and triplet states of **7b** (to be discussed in Chapter 3) decrease in intensity to give **21b**. On the other hand, even prolonged irradiation of **7b** with the

low-intensity LED light source with a maximum emission at 450 nm does not result in the rearrangement to **21b**.

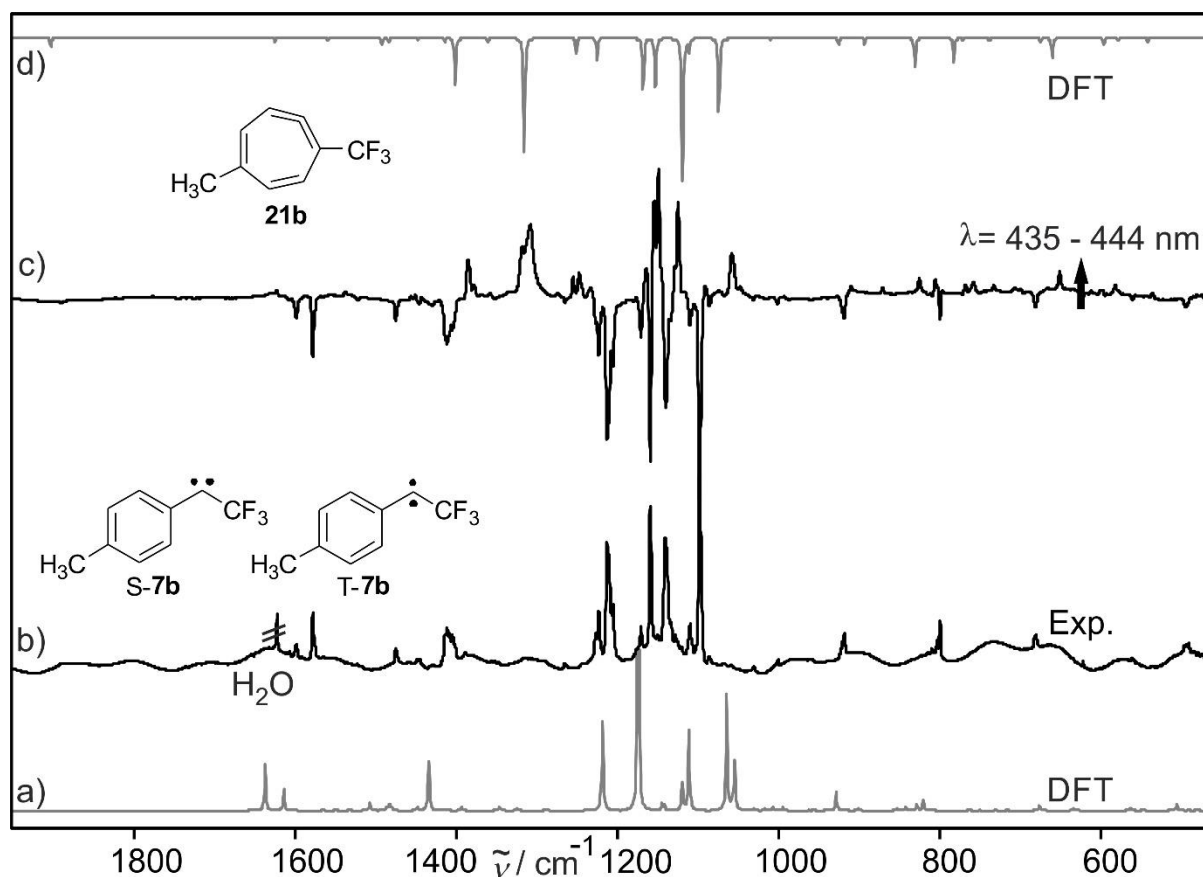


**Figure 13.** IR spectra showing the rearrangement of **S-7b** and **T-7b** to cycloheptatetraene **21b**. a) IR spectrum of **S-7b** and **T-7b** calculated at the B3LYP/6-311++G(d,p) level of theory. Equal contributions of the **S-7b** and **T-7b** were used to simulate the IR spectrum. b) IR Spectrum after 20 hours of 450 nm irradiation of **19b** at 3 K. c) Difference IR spectrum showing the rearrangement of **S-7b** and **T-7b** to **21b** after 60 minutes of 435-444 nm OPO laser irradiation of the same matrix. d) IR spectrum of **21b** calculated at the B3LYP/6-311G++ level of theory.

Thus, special attention is paid to explore the photochemistry of carbene **7a** in more detail. In order to have better understanding of the photochemistry, the UV-vis and IR spectra of **7a** were recorded in the same matrix at 3 K (Figure 14). These experiments allow to correlate changes in band intensities in the UV-vis and IR regions and confirm the band assignments. Upon 30 minutes of irradiation of phenyl(trifluoromethyl)diazomethane **19a** with  $\lambda = 254$  nm, a series of absorptions stretching from 244 to 450 nm is produced in the UV-vis spectrum. By comparison with the reported IR spectrum, the IR signals of **7a** were assigned.<sup>[105-106]</sup> Noteworthy, overnight irradiation of **7a** with  $\lambda = 254$  nm did not lead to any changes in the spectra, which is in contrast to the high photolability of carbene **6**. However, prolonged irradiation of **7a** with  $\lambda = 450$  nm results in significant changes in both, the IR and UV-vis spectrum. While the UV-vis bands of **7a** decreased in intensity, a new broad band at 310 nm

increases in the UV-vis spectrum as well as a characteristic band at  $1810\text{ cm}^{-1}$  in the IR spectrum. The new species is assigned to the carbene-carbene rearrangement product **21a** based on calculations at the B3LYP/6-311++G(d,p) level of theory.

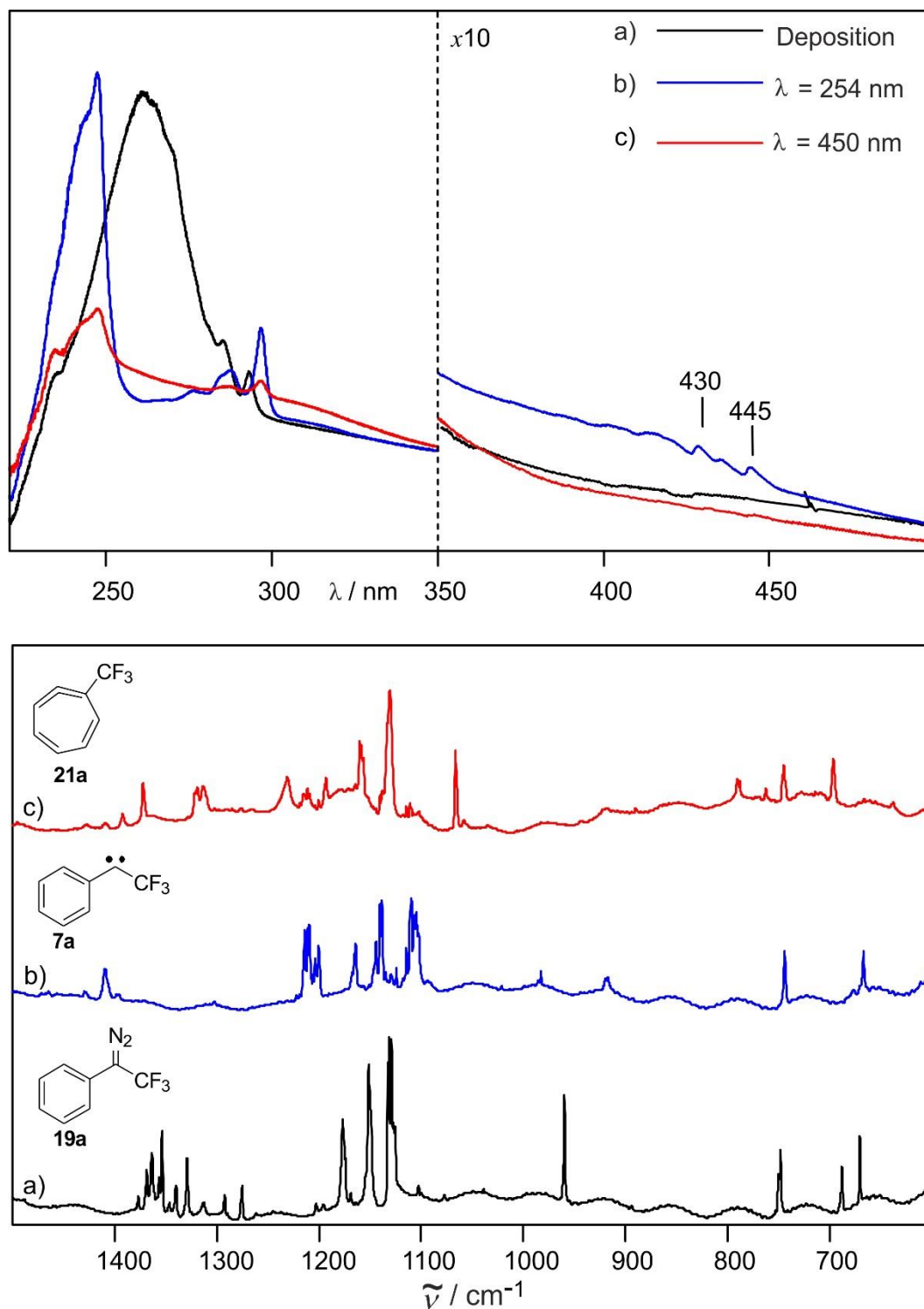


**Figure 14.** UV-vis (top) and IR (bottom) spectra recorded from the same argon matrix at 3 K showing the photochemical reaction of **7a**. (a) Phenyl(trifluoromethyl)diazomethane **19a** (black line). (b) Spectra of **7a** obtained after 15 hrs of irradiation of **19a** with  $\lambda = 254\text{ nm}$  (blue line). (c) Spectra of **21a** obtained after overnight irradiation of **7a** with  $\lambda = 450\text{ nm}$  (red line).

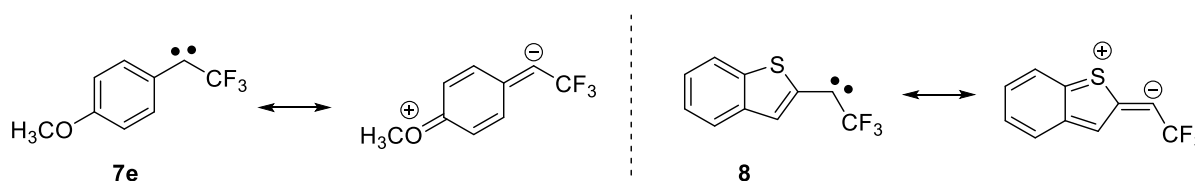
## Conclusion

In summary, the photochemistry of several aryl(trifluoromethyl)carbenes was investigated by low temperature EPR, IR and UV-vis spectroscopy. The experiments show that phenyl(trifluoromethyl)carbene **7a** is photostable under UV irradiation, in contrast to phenylcarbene **6**, which is highly photolabile toward rearrangement to cycloheptatetraene **15**. This might be due to the presence of the  $\alpha$ -fluorine atom in **7a**, which stabilizes the carbene kinetically. However, carbene **7a** could also be efficiently converted to **21a** upon prolonged visible light ( $\lambda = 450$  nm) irradiation. In addition, rearrangement of **21a** to **7a** is found to not be reversible. Finally, carbenes **7b-7i** are found stable under both UV and visible light irradiation, and thus may have applications in photoaffinity labeling.

### 3. Bistable aryl(trifluoromethyl)carbenes

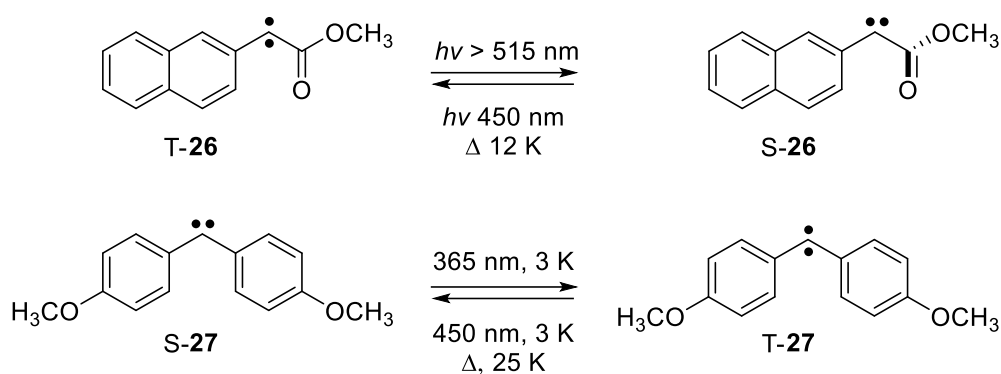
#### Introduction

As we discussed before, the chemistry of carbenes is dependent on the energy gap between the  $\sigma$  and  $\pi$  orbitals, which can be tuned by electronic and steric effects of the substituents at the carbene center. In general,  $\sigma$ -accepting and  $\pi$ -donating substituents such as O, N, or halogens stabilize the singlet states whereas most alkyl and aryl substituents lead to triplet state carbenes.<sup>[15]</sup> A similar effect is observed for substitutions in aryl(trifluoromethyl)carbenes reported in literatures: **7a**,<sup>[104]</sup> **7b**,<sup>[108]</sup> **7f**,<sup>[111]</sup> **7g**<sup>[112]</sup> and **7i**<sup>[113]</sup> are triplet ground state carbenes in contrast to **7e**<sup>[111]</sup> and **8**,<sup>[30]</sup> which have been reported to exist as singlet ground state carbenes. The stabilization of the singlet state of **7e** and **8** can be rationalized by  $\pi$ -electron donation from the substituent as shown via resonance structure (Scheme 5).



**Scheme 5.** Singlet aryl(trifluoromethyl)carbenes stabilized by substituents.

At cryogenic temperatures, carbenes are generally produced in their thermodynamically most stable electronic ground state, which can be either singlet or triplet, but its excited spin state could not be detected as the inter system crossing (ISC) is too fast under these conditions.<sup>[13]</sup> However, carbenes **26** and **27** have been reported to be exceptions to this general belief where both the ground state and excited state coexist for a period of hours at low temperatures.<sup>[114-118]</sup> Moreover, depending on temperature and irradiation conditions, matrices containing mainly the triplet or singlet states of carbenes **26** and **27** can be generated (Scheme 6). These two carbenes are of importance to probe spin-specific reactions of carbenes in a single experiment. A disadvantage of carbenes **26** and **27** for studying the magnetic bistability, however, is that both carbenes form several energetically close lying conformers, and in addition **26** shows secondary photochemistry, which results in complex product mixtures and complicates the interpretation of the spectra. We therefore were searching for structurally simple, photostable arylcarbenes with nearly degenerate singlet and triplet states that would allow us to matrix-isolate both spin states. In this regard, aryl(trifluoromethyl)carbenes are selected as a feasible candidate to fulfill these requirements for the reasons described below.



**Scheme 6.** Magnetically bistable carbenes **26** and **27**.

Phenyl(trifluoromethyl)carbene **7a** is found to be photostable compared to its counterpart phenylcarbene **6**, which is highly photolabile towards carbene-carbene rearrangements, as discussed in the previous chapter. In addition, the trifluoromethyl group stabilizes the singlet state by a small amount ( $\Delta E_{\text{ST}}$  (**6**) = 5.4 kcal/mol, (**7a**) = 4.0 kcal/mol).<sup>[29]</sup> The S–T gap in **7a** is still too large to expect magnetic bistability, but it can be further lowered by electron-donating substituent in the para-position of the phenyl ring. In addition, as mentioned before, **7** are of special interest since they found wide applications in photoaffinity labeling.<sup>[8–11]</sup>

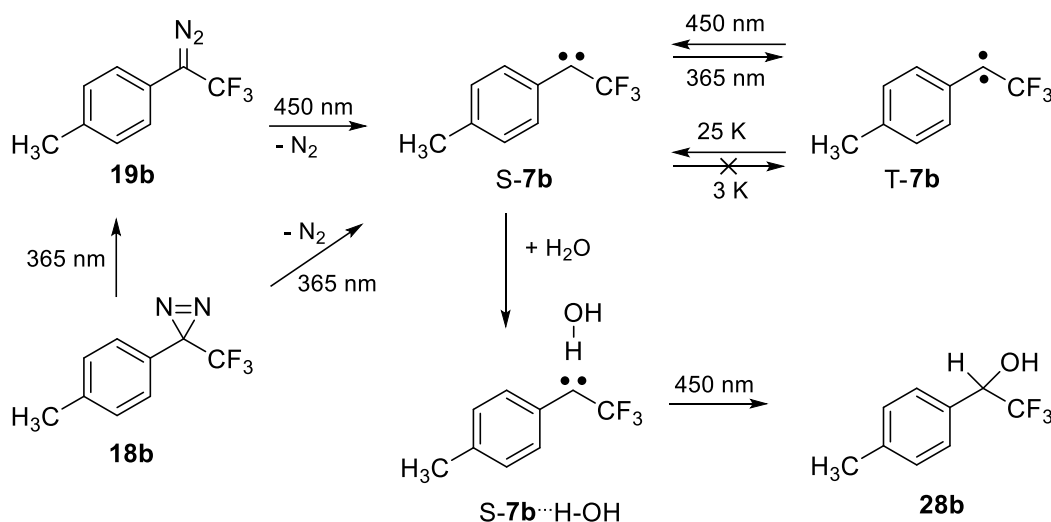
In the light of this premise, preliminary studies for *p*-tolyl(trifluoromethyl)carbene **7b** using matrix isolation EPR spectroscopy was investigated (Chapter 2). A typical triplet EPR spectrum could be recorded with ZFS parameters of  $|D/hc| = 0.5219$  and  $|E/hc| = 0.0304\ \text{cm}^{-1}$ , which suggests that **7b** either has a triplet ground state or such a small S–T energy gap that the excited triplet state is thermally populated even at 4 K. Similarly, from laser flash photolysis studies in the presence of various quenchers, Platz and co-workers estimated the S–T gap of carbene **7b** to be 0.5 – 1.5 kcal/mol.<sup>[108]</sup> Therefore, carbene **7b** is selected as the structurally simple carbene to investigate magnetic bistability of carbenes with such small S–T gap. The related *p*-fluorophenyl (trifluoromethyl)carbene **7c** and fluorenyl(trifluoromethyl)carbene **7h** are also investigated to answer the question whether or not magnetic bistability is a general phenomenon in carbenes with small S–T gaps utilizing the matrix isolation techniques.

## Results and discussion

### *p*-Tolyl(trifluoromethyl)carbene

Carbene **7b** was generated by either UV ( $\lambda = 365\ \text{nm}$ ) photolysis of *p*-tolyl (trifluoromethyl)diazirine **18b** or by visible light ( $\lambda = 450\ \text{nm}$ ) photolysis of *p*-tolyl

(trifluoromethyl)diazomethane **19b** in neon, argon, xenon or nitrogen matrices at 3 – 8 K, utilizing the matrix isolation IR, UV–vis, and EPR spectroscopy techniques. Photolysis of **18b** produced small amounts of **19b**, otherwise, the same products were obtained from both precursors (Scheme 7).



**Scheme 7.** Synthesis and chemistry of carbene **7b**.

### EPR spectroscopy

Photolysis of **19b** in argon matrix at 4 K results in the formation of T-**7b** with an EPR spectrum typical of a triplet carbene with ZFS parameters  $|D/hc| = 0.5219$  and  $|E/hc| = 0.0304$   $\text{cm}^{-1}$  (Figure 15). In an attempt to measure the Curie-Weiss behavior and thus to determine the ground state of **7b**, the matrix was stepwise annealed for 10 min at temperatures of 8, 12, 16, 20, and 25 K. An EPR spectrum was recorded at each of these temperatures, and before increasing the temperature to the next higher level, the matrix was cooled back to 4 K to record a second EPR spectrum (Figure 15, inset). These experiments clearly demonstrate an irreversible loss of T-**7b** at each temperature step, summing to more than 30% loss after warming to 25 K. While keeping the matrix at 4 K for several hours did not result in any increase of the signals of T-**7b**, several minutes UV irradiation (365 nm) resulted in a partial signal recovery. In these experiments, we took care that **19b** was completely photolyzed, and therefore remaining **19b** was not the precursor of T-**7b** under these conditions. Subsequent annealing again irreversibly reduced the amount of T-**7b**, and this behavior was reproducible in repeated annealing/irradiation cycles. These experiments indicate that T-**7b** thermally

rearranges to an EPR-silent product, which upon UV irradiation rearranges back to T-**7b**. It is tempting to assign this EPR-silent product to the singlet state S-**7b**.

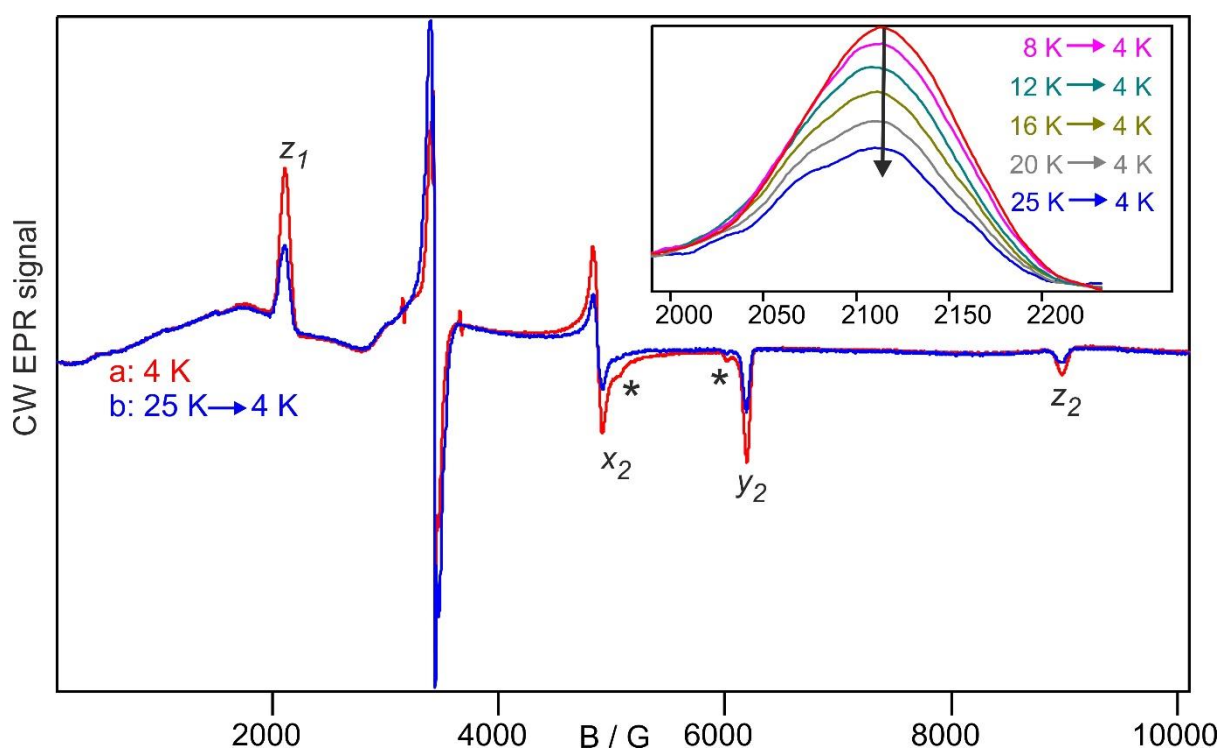


**Figure 15.** X-band CW EPR spectra of an argon matrix showing the thermal behavior of T-**7b** after warming from 4 to 25 K and cooling back to 4 K. (a) Argon matrix at 4 K showing the spectrum of T-**7b** (read line; ZFS parameters  $|D/hc| = 0.5219 \text{ cm}^{-1}$  and  $|E/hc| = 0.0304 \text{ cm}^{-1}$ ). (b) After subsequent annealing at 25 K for 10 min and cooling back to 4 K, 36 % of the signal intensity is lost (blue line). Inset shows the loss of the T-**7b** signal at the  $z_1$  canonical position after cooling back from 8, 12, 16, 20 and 25 K to 4 K. The bands marked with an asterisk are assigned to products of carbene-carbene rearrangements.

## IR spectroscopy

This assumption was confirmed by following the thermal and photochemical S–T interconversion of **7b** using IR spectroscopy. Visible light irradiation ( $\lambda = 450 \text{ nm}$ ) of matrix-isolated **19b** results in the complete photolysis of the diazo precursor and formation of a major product assigned to T-**7b** and a minor product assigned to S-**7b** with characteristic absorptions at  $1578.8$  and  $1599.5 \text{ cm}^{-1}$ , respectively (Figures 16 and 17, Tables 2 and 3). Annealing at 25 K or prolonged 450 nm irradiation leads to an increase of the bands of the minor component S-**7b**. Further UV irradiation ( $\lambda = 365 \text{ nm}$ ) results in the almost complete bleaching of all IR bands of S-**7b** and concurrently in an increase of the absorptions of the major product T-**7b**. This assignment was confirmed by comparing the experimental IR spectra to calculations at the B2PLYP-GD3BJ/ aug-cc-pVTZ level of theory, which nicely reproduce the experimental data (Figure 17).

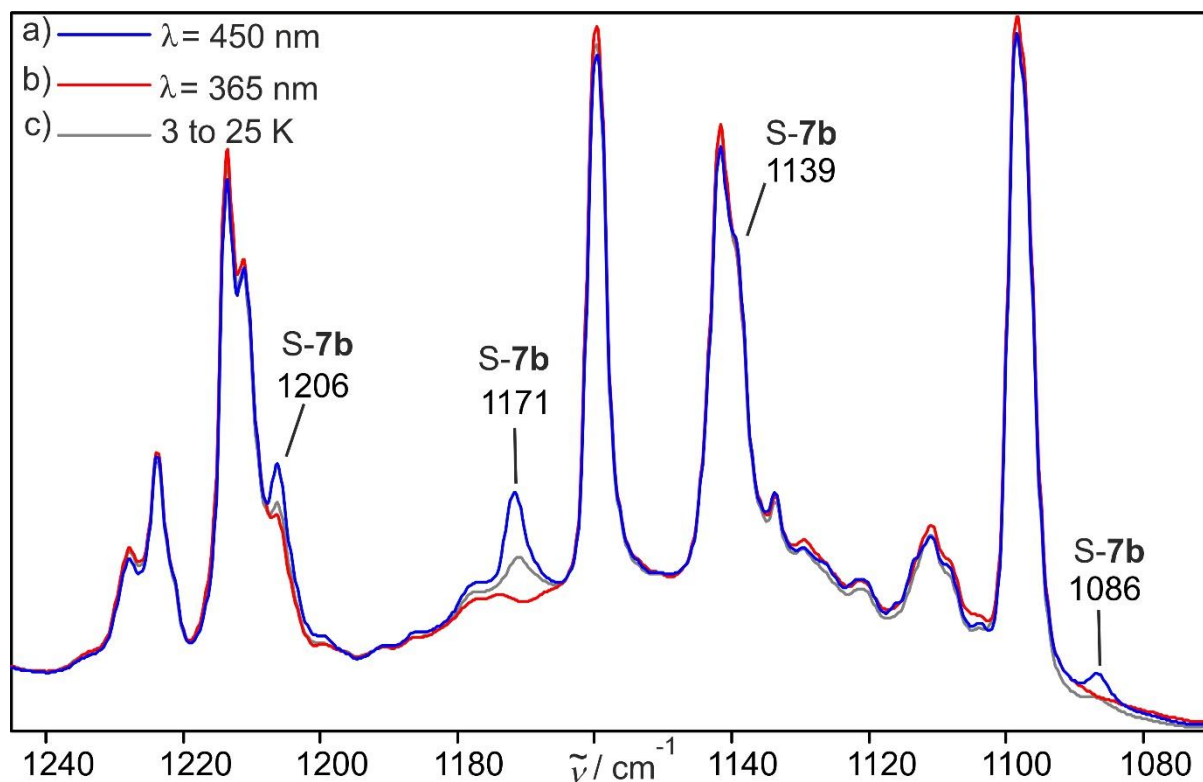


**Figure 16.** IR spectra showing the thermal and photochemical interconversion of S-7b and T-7b in argon matrix. a) IR spectrum after 15 hours of 450 nm irradiation of **19b** at 3 K (blue line). b) IR spectrum at 3 K showing changes after 60 min of 365 nm irradiation of the same matrix. Bands assigned to S-7b are disappearing and bands pointing upward, assigned to T-7b are increasing (red line). c) IR spectrum showing changes of the same matrix after subsequent annealing at 25 K for 15 min and cooling back to 3 K. Bands assigned to T-7b are decreasing and bands pointing upward, assigned to S-7b are reappearing (gray line). Note that bands of S-7b are assigned with arrows whereas all the rest unassigned bands are of T-7b.

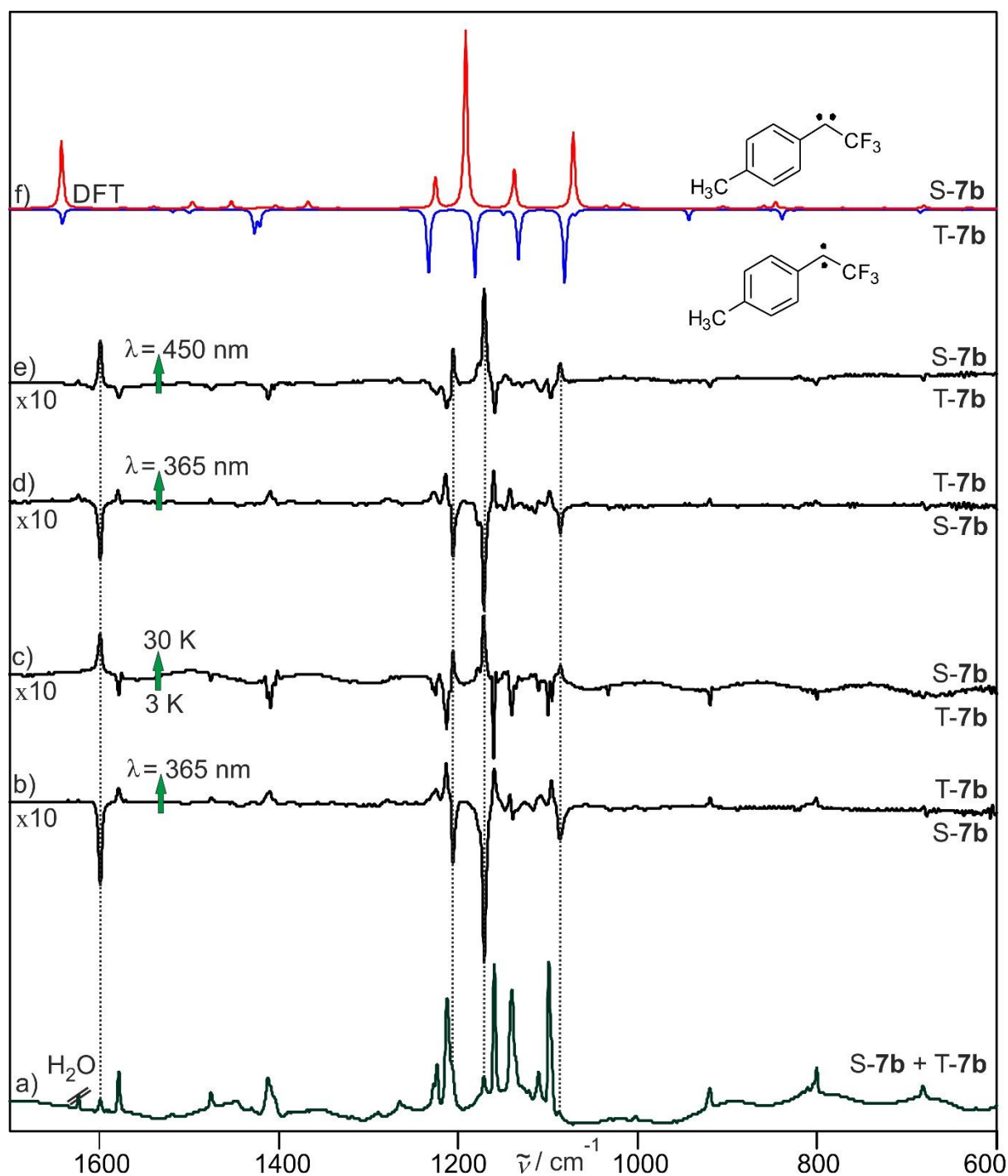


**Figure 17.** IR spectra showing the interconversion of **S-7b** and **T-7b** in argon matrix. (a) IR spectrum after several hours of 450 nm irradiation of **19b** at 3 K (dark green). (b) Difference IR spectrum at 3 K showing changes after 60 min of 365 nm irradiation of the same matrix. Bands pointing downward, assigned to **S-7b**, are disappearing, and bands pointing upward, assigned to **T-7b** are appearing. (c) Difference IR spectrum of the same matrix after 10 min annealing to 30 K and cooling back to 3 K. Bands pointing downward, assigned to **T-7b**, are disappearing, and bands pointing upward, assigned to **S-7b**, are appearing. (d) Difference IR spectrum at 3 K showing changes after 60 min of 365 nm irradiation of the same matrix. Bands pointing downward, assigned to **S-7b**, are disappearing, and bands pointing upward, assigned to **T-7b** are appearing. (e) Difference IR spectrum at 3 K showing changes after 60 min of 450 nm irradiation of the same matrix. Bands pointing downward, assigned to **T-7b**, are disappearing, and bands pointing upward, assigned to **S-7b**, are appearing. (f) Superimposed IR spectrum showing the interconversion of **T-7b** (blue) to **S-7b** (red) calculated at the B2PLYP-GD3BJ/aug-cc-pVTZ level of theory. Equal contributions of **S-7b** and **T-7b** were used to simulate the IR spectra.

The highest yield of **S-7b** of approximately 20% was obtained in a nitrogen matrix, whereas in solid argon only 13% yield was obtained after 450 nm irradiation and annealing at 25 K. Further 450 nm irradiation or annealing did not increase yield of **S-7b**. The interconversion between **T-7b** and **S-7b** was reproducible in several 450 nm/365 nm irradiation cycles (Figures 17 and 18). At 3 K and in the absence of irradiation, **T-7b** and **S-7b** coexist without noticeable changes in their spectra even after several days.

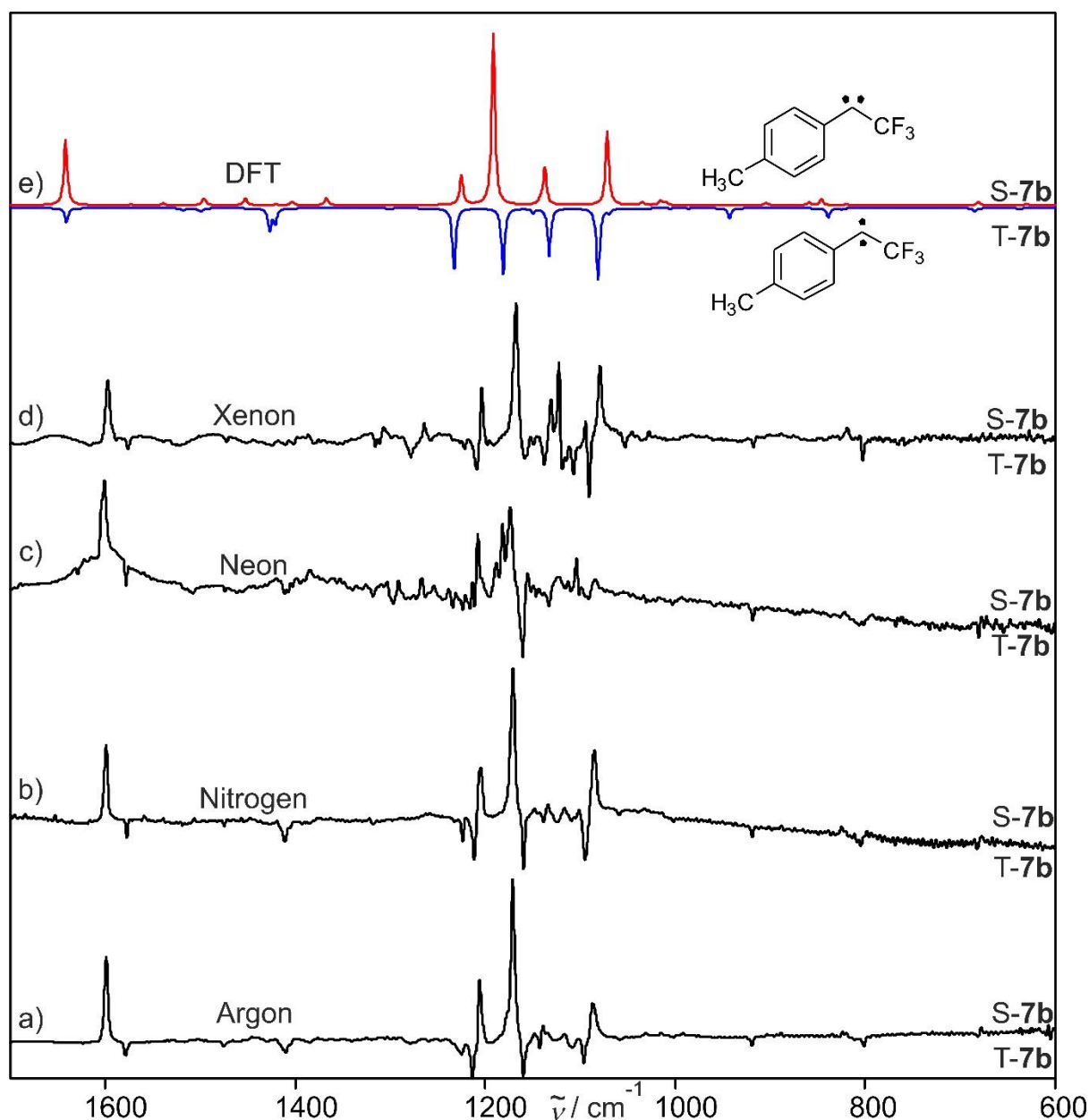


**Figure 18.** IR spectra showing the photochemical interconversion of **S-7b** and **T-7b** in several matrices at 3 K. a) In argon matrix, b) nitrogen matrix, c) neon matrix and d) xenon matrix. Difference IR spectra at 3 K showing changes after app. 60 min of 450 nm irradiation of a matrix containing **T-7b**. Bands pointing downward, assigned to **T-7b**, are disappearing, and bands pointing upward, assigned to **S-7b**, are appearing. Superimposed spectrum showing the interconversion of **T-7b** (blue) to **S-7b** (red) calculated at the B2PLYP-GD3BJ/aug-cc-pVTZ level of theory. Equal contributions of **S-7b** and **T-7b** were used to simulate the IR spectra.

This observations is reproducible when we used *p*-tolyl(trifluoromethyl)diazirine **18b** as a precursor to generate carbene **7b** in argon matrix at 3 K. However, **18b** is found to be stable upon visible light irradiation ( $\lambda = 450$  nm). Thus, upon short irradiation of **18b** with UV light ( $\lambda = 365$  nm), carbene T-**7b** is obtained along with trace amounts of the diazo compound **19b**. Note that, as described above, UV light irradiation efficiently converted S-**7b** to T-**7b**. Therefore, subsequent annealing at higher temperatures or follow up irradiation with visible light is required to generate S-**7b** from precursor **18b** (Figure 19). For the same reason, only signals of T-**7b** could be detected after 308 laser irradiation of **19b** in argon matrix at 3 K (Figure A1).

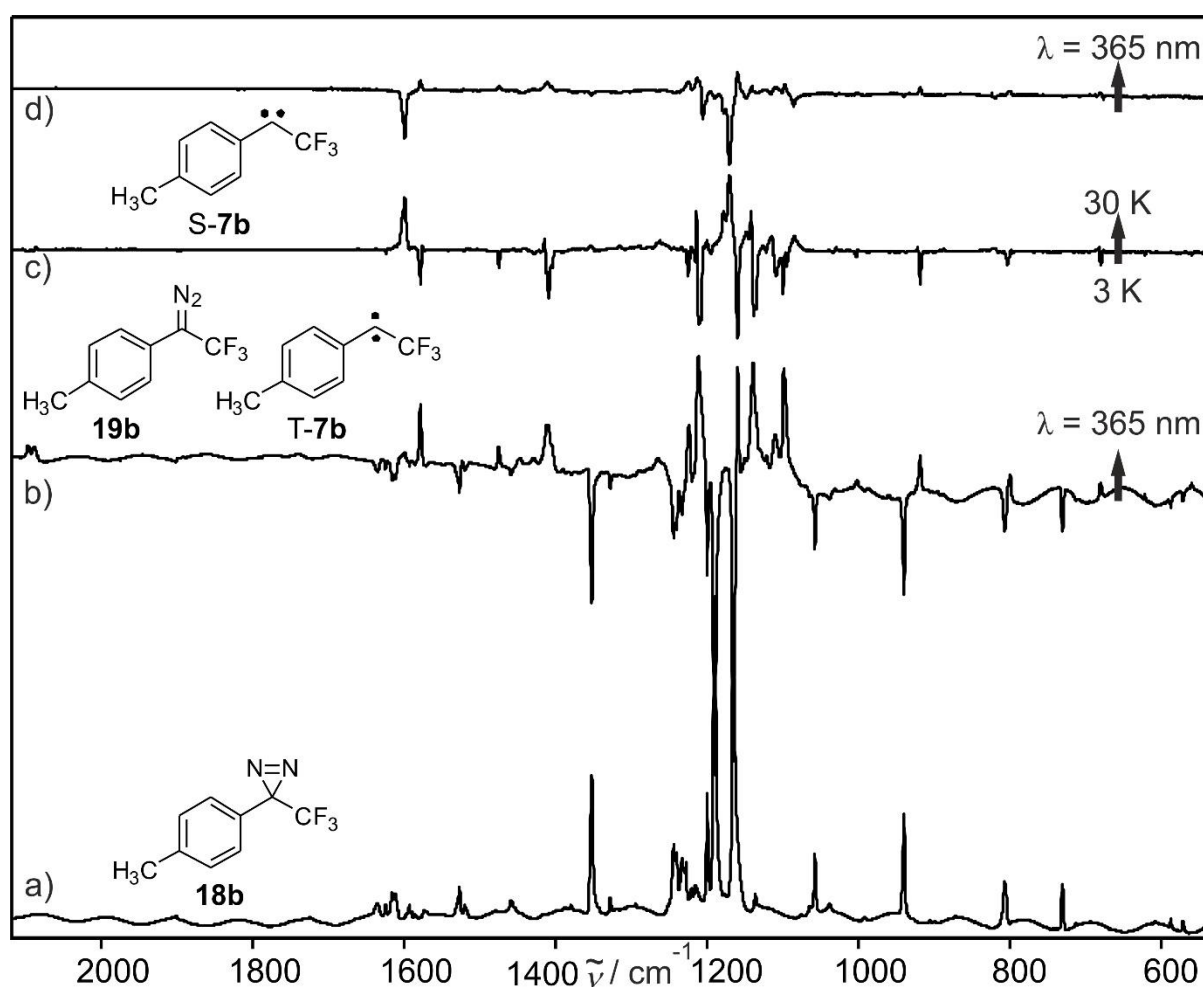


**Figure 19.** IR spectra showing interconversion of S-**7b** and T-**7b** by irradiation and annealing in argon matrix. a) IR spectrum of *p*-tolyl(trifluoromethyl)diazirine **18b** matrix-isolated in argon at 3 K. b) Difference IR spectrum at 3 K showing changes after 60 min of 365 nm irradiation of the same matrix. Bands pointing downward, assigned to **18b**, are disappearing, and bands pointing upward, assigned to T-**7b** and traces of **19b** are appearing. c) Difference IR spectrum showing changes after subsequent 30 min annealing at 30 K and cooling back to 3 K. Bands pointing downward, assigned to T-**7b**, are disappearing, and bands pointing upward, assigned to S-**7b**, are appearing. d) IR spectrum of the same matrix after 25 min irradiation with  $\lambda = 365$  nm at 3 K. The bands of S-**7b** decreases, whereas those of T-**7b** increase during irradiation.

**Table 2.** IR spectroscopic data of **S-7b**.

Mode	Calculated <sup>a</sup> v/cm <sup>-1</sup> (I <sub>abs</sub> )	Argon <sup>b</sup> v/cm <sup>-1</sup> (I <sub>rel</sub> )	Nitrogen <sup>b</sup> v/cm <sup>-1</sup> (I <sub>rel</sub> )	Neon <sup>b</sup> v/cm <sup>-1</sup> (I <sub>rel</sub> )	Xenon <sup>b</sup> v/cm <sup>-1</sup> (I <sub>rel</sub> )	Assignment <sup>c</sup>
29	1071.6 (278.7)	1086.7(32)	1085.8 (38)	1084.2(23)	1079.1(37)	C-CF <sub>3</sub> bend (out of plane)
30	1137.4 (139.3)	1139.2 (39)	1136.8(36)	1134.3(32)	1130.2(35)	C-CF <sub>3</sub> bend (in plane)
32	1191.5 (645.0)	1171.7(100)	1170.6(100)	1173.7(100)	1167.0(100)	C-C-C str. (carbene center)
33	1225.3 (115.5)	1206.4(44)	1205.4(53)	1207.9(49)	1203.3(32)	C-H def. (in plane)
44	1642.1 (247.8)	1599.5 (43)	1599.8(40)	1601.4(60)	1597.3(41)	C=C str. Ring

<sup>a</sup> Calculated at the B2PLYP-GD3BJ/aug-cc-pVTZ level of theory. <sup>b</sup> Matrices at 3 K. <sup>c</sup> Tentative assignment.

**Table 3.** IR spectroscopic data of **T-7b**.

Mode	Calculated <sup>a</sup> v/cm <sup>-1</sup> (I <sub>abs</sub> )	Argon <sup>b</sup> v/cm <sup>-1</sup> (I <sub>rel</sub> )	Nitrogen <sup>b</sup> v/cm <sup>-1</sup> (I <sub>rel</sub> )	Neon <sup>b</sup> v/cm <sup>-1</sup> (I <sub>rel</sub> )	Xenon <sup>b</sup> v/cm <sup>-1</sup> (I <sub>rel</sub> )	Assignment <sup>c</sup>
13	510.7 (14.4)	492.1 (1)	496.1 (6)	493.1(5)	491.5(5)	Ring def.
14	566.5 (4.9)	561.6 (1)	560.4 (2)	560.1 (1)	559.1(2)	Ring def.
16	637.6 (3.5)	622.7 (1)	622.2 (1)	622.9 (1)	622.8(1)	Ring def.
17	684.4 (13.0)	681.4 (9)	680.8 (7)	682.5 (12)	678.8(10)	C-CF <sub>3</sub> bend
21	838.8 (36.3)	799.9 (19)	803.9 (18)	802.6 (36)	801.3(34)	Ring def.
23	942.7 (39.5)	919.5 (15)	918.9 (13)	918.9 (21)	917.1(23)	Ring def.
27	1030.2 (2.7)	1001.3 (3)	1001.3 (2)	1003.1 (5)	1001.3(4)	Ring def.
28	1069.4 (15.5)	1099.2 (81)	1096.1 (100)	1102.7 (67)	1092.4(100)	C-CH <sub>3</sub> bend
29	1081.2 (272.5)	1110.9 (16)	1110.6 (15)	1112.1 (55)	1107.6(60)	C-CF <sub>3</sub> bend
30	1132.7 (182.1)	1140.5 (100)	1138.6 (92)	1147.1 (98)	1133.9(99)	C-CF <sub>3</sub> bend
31	1149.6 (17.2)	1159.8 (66)	1160.2 (61)	1161.3 (88)	1156.2(100)	C-H bend
32	1181.2 (251.3)	1213.9 (52)	1212.1 (33)	1214.8 (100)	1198-1206(85)	C-C-C str.
33	1232.8 (230.4)	1223.7 (32)	1223.9 (26)	1224.8 (53)	1220-1230 (57)	C-H bend
35	1300.9 (2.98)	1266.5 (15)	1266.1 (5)	1265.7 (26)	1262.9(30)	Ring def.
37	1421.1 (55.3)	1404-1410 (59)	1405-1412 (49)	1404-1408 (75)	1400-1415(69)	C-C-C str.
38	1427.1 (83.8)	1447.8 (5)	1447.8(4)			
40	1498.9 (10.8)	1458 (3)			1454.1(4)	C-CH <sub>3</sub> bend
42	1518.0 (11.0)	1475.8 (8)	1447.8(6)	1475.5(10)	1471.1(12)	C-H bend
44	1641.2 (53.1)	1578.8 (22)	1578.2 (18)	1579.6(24)	1574.8(33)	C=C str.

<sup>a</sup> Calculated at the B2PLYP-GD3BJ/aug-cc-pVTZ level of theory. <sup>b</sup> Matrices at 3 K. <sup>c</sup> Tentative assignment.

From our experiments, the rate constants for the thermal conversion of **T-7b** to **S-7b** can also be obtained using the stretched exponential approach of Wildman and Siebrand, which can be described by equation (E1).<sup>[119]</sup>

$$[A]_t = [A]_0 e^{(-kt)^\beta} + c \quad \text{with } 0 < \beta < 1 \quad (\text{E1})$$

Where  $[A]_0$  represents the initial IR integrated intensity,  $[A]_t$  represents the integrated IR intensity at time  $t$ (s),  $k$  is rate constant with units of time ( $\text{s}^{-1}$ ),  $\beta$  is a parameter for superposition of exponential decays,  $c$  is a constant and  $t$  is the elapsed time. The results are compiled in Table 4 and Figure 20. The dispersive kinetics and the distribution of rate constants perceived in our experiments can be explained by matrix effects. Noteworthy, the matrix effect is also responsible for the observed temperature dependent S – T interconversion of carbene **7b**. At 3 K, the rare gas matrices are very rigid, and thus kinetic and thermal energies are highly inhibited. Whereas at higher temperature the matrices loses its rigidity (above 20 K in argon and 30 K in xenon) and thus allows the changes in the C-C-C bond angle which is required for the spin switching of carbene **7b**, which results in equilibrium populations of spin states observed in our experiments.

**Table 4.** Rate constants (as fitted to E1 with  $\beta = 0.75$ ) for the thermal rearrangement of T-**7b** to S-**7b**.

T(K)	Matrix	K / $10^{-4} \text{ s}^{-1}$	$t_{\text{final}}$ / h
25	Argon	1.3 <sup>a</sup>	7.6
30	Argon	1.6 <sup>a</sup>	1.9
40	Xenon	1.9 <sup>b</sup>	1.2
50	Xenon	2.5 <sup>b</sup>	3.7

<sup>a</sup> Values obtained by global fitting of the increasing intensities of the IR peaks of S-**7b** at 1171.7 and 1599.5  $\text{cm}^{-1}$  as well as the decreasing intensity of the IR peaks of T-**7b** at 1159.8 and 1578.8  $\text{cm}^{-1}$ . <sup>b</sup> Due to scattering of points, only the IR peak of T-**7b** at 1159.8  $\text{cm}^{-1}$  was used to fit E1.

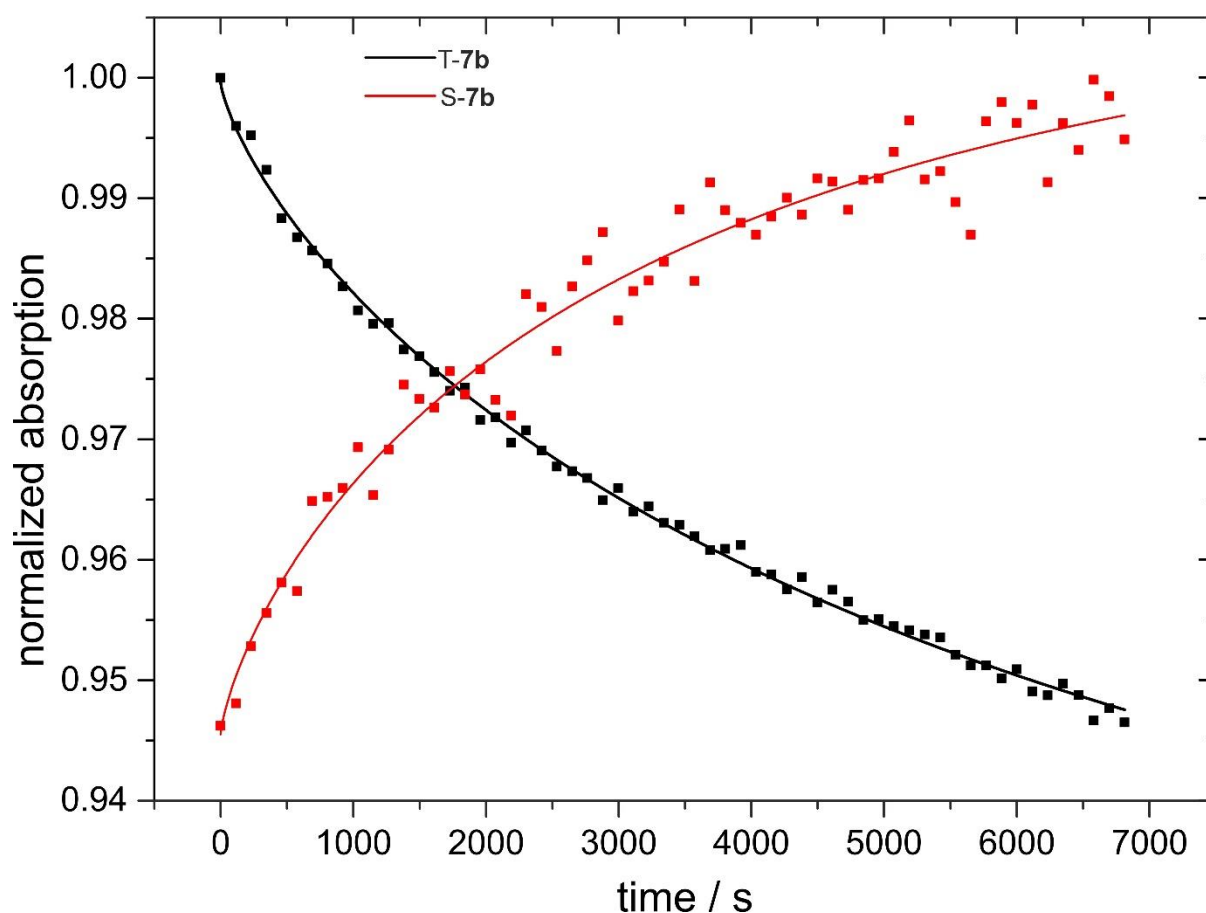


**Figure 20.** Simultaneous fit of the increasing intensities of the IR peaks of the S-**7b** at  $1171.7\text{ cm}^{-1}$  as well as the decreasing intensity of the IR peaks of T-**7b** at  $1159.8\text{ cm}^{-1}$  to E1 as recorded in argon matrix at 30 K.

### UV-vis spectroscopy

The singlet and triplet state of **7b** are easily distinguished in their UV-vis spectra. Visible light photolysis ( $\lambda = 450\text{ nm}$ ) of **19b** produces the UV-vis spectrum shown in Figure 21 with a series of absorptions stretching from 250 to 450 nm. A broad band with  $\lambda_{\text{max}} = 326\text{ nm}$  completely disappears after 365 nm irradiation and reappears after 450 nm irradiation, and thus is assigned to S-**7b**. The triplet carbene T-**7b** shows an absorption with a pronounced progression at  $\lambda_{\text{max}} = 436\text{ nm}$ , and irradiation into this band results in the rearrangement of T-**7b** to S-**7b**. To confirm the assignment of the UV-vis absorptions of the two states of **7b**, we recorded UV-vis and IR spectra from the same matrix (Figures 21). These experiments allow us to correlate changes in band intensities in the UV-vis and the IR region and confirm the band assignments.

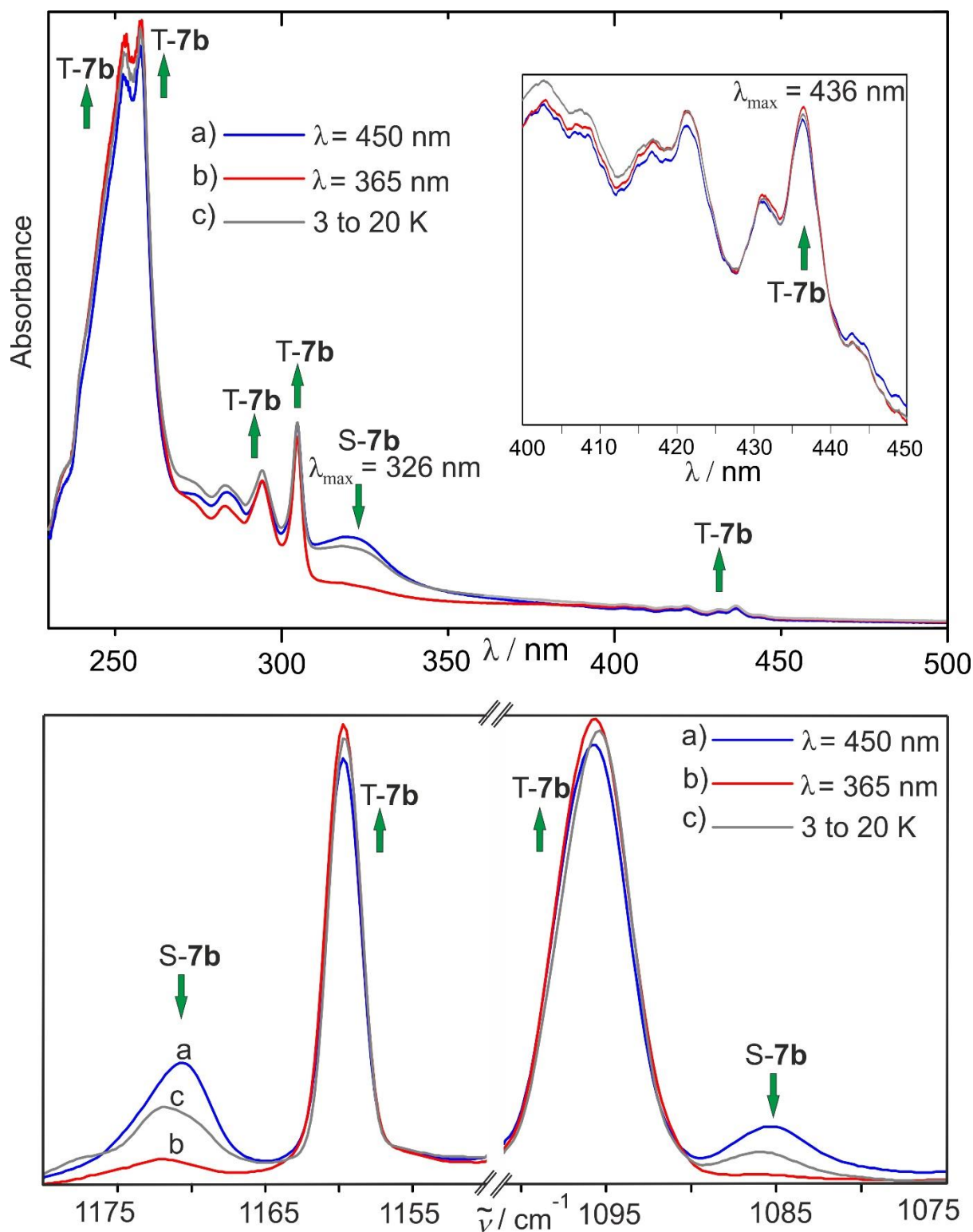


**Figure 21.** UV-vis (top) and IR (bottom) spectra recorded from the same nitrogen matrix showing the S-T interconversion of **7b**. (a) T-7b and S-7b obtained after several hours of 450 nm irradiation of **19b** at 3 K (blue line). (b) Spectra obtained after 60 min irradiation with  $\lambda = 365 \text{ nm}$  at 3 K (red line). (c) Spectra obtained after subsequent annealing for 30 min at 20 K and cooling back to 3 K (gray line). The weak band of T-7b in the visible region of the UV-vis spectrum is shown in the inset.

In summary, both singlet and triplet states of carbene **7b** are observed in our experiments. Since we obtained singlet at annealing temperatures and that of the triplet can also be populated

quantitatively, an open question is that what is the ground spin state of **7b**? If we assume that the S – T gap of **7b** is zero, then we should have a 75% of triplet and 25% of singlet population due to the three-fold degeneracy of the triplet. Accordingly, from the observed maximum yield of 20% of S-**7b**, we estimate  $\Delta E_{ST} = 0.014$  kcal/mol under the assumption of a Boltzmann distribution between the spin states in our experiments (E2 to E8). However, the matrix effects as described before, could have both thermodynamic and kinetic influence on the coexistence and distribution of the triplet and singlet states of carbene **7b**. Thus, instead of having a well-defined value as in the gas phase,<sup>[118]</sup> we expect a distribution of S – T splitting values on the order of 1–2 kcal/mol in rare gas matrices at 3 K. We assume that this results in equilibrium populations of the singlet and triplet states under specific thermal and photochemical conditions, observed in our experiments.

According to the Boltzmann distribution, the probability  $p_j$  of a state  $j$  is given by

$$p_j = g_j \frac{e^{-\beta E_j}}{Z} \quad (\text{E2})$$

where  $g_j$  is the degeneracy of the state,  $E_j$  its energy,  $Z$  the partition function of the system and  $\beta = \frac{1}{kT}$  with the Boltzmann constant  $k = 1.38065 \times 10^{-23} \text{ J/K} = 0.001987 \text{ kcal mol}^{-1} \text{ K}^{-1}$  and temperature  $T$ . The probability ratio of two states  $j$  and  $i$  is given by

$$\frac{p_j}{p_i} = \frac{g_j}{g_i} e^{-\beta(E_j - E_i)} \quad (\text{E3})$$

$$\ln\left(\frac{p_j}{p_i}\right) = \ln\left(\frac{g_j}{g_i}\right) - \beta(E_j - E_i) \quad (\text{E4})$$

$$(E_j - E_i) = \frac{1}{-\beta} \left[ \ln\left(\frac{p_j}{p_i}\right) - \ln\left(\frac{g_j}{g_i}\right) \right] \quad (\text{E5})$$

The S – T gap of **7b** can then be estimated via

$$\Delta E_{ST} = \frac{1}{-\beta} \left[ \ln\left(\frac{p_S}{p_T}\right) - \ln\left(\frac{g_S}{g_T}\right) \right] \quad (\text{E6})$$

$$\Delta E_{ST} = \frac{1}{-0.001987 \text{ kcal mol}^{-1} \text{ K}^{-1} (25 \text{ K})} \left[ \ln\left(\frac{0.2}{0.8}\right) - \ln\left(\frac{1}{3}\right) \right] \quad (\text{E7})$$

$$\Delta E_{ST} = 0.014 \text{ kcal/mol} \quad (\text{E8})$$

**DFT calculations** (Provided by Niklas Tötsch and Prof. Dr. Elsa Sanchez Garcia)

The experimentally observed spin state degeneracy of carbene **7b** is supported by calculations. There are only very few accurate experimental gas-phase data available on the S–T energy gaps of carbenes.<sup>[20-22, 120-121]</sup> CCSD(T) calculations with large basis sets are often used as “gold standard” for calculating  $\Delta E_{ST}$  of carbenes<sup>[122]</sup> and for calibrating less expensive DFT results. Here, our calculations of the S–T splitting of **7b** at the CCSD(T)/cc-pV(D/T)Z//B97D-GD3/def2-TZVP level of theory result in  $\Delta E_{ST} = 0.0$  kcal/mol (excluding ZPVE), thus predicting degeneracy of the spin states in the gas phase. We tested several density functionals (Table 5) and found that B2PLYP-GD3BJ predicts  $\Delta E_{ST} = -0.4$  kcal/mol (the zero point vibrational energy (ZPVE) correction is 0.03 kcal/mol at this level of theory) in excellent agreement with the CCSD(T) result. Thus, unless otherwise specified, we are using this functional for discussing the structures, energies, and spectra of **7b**. Furthermore, B3LYP-GD3BJ/aug-cc-pVTZ calculations gave a S–T gap of 2.6 kcal/mol. However, it is reported that B3LYP overestimates the S–T gap of carbenes but can be empirically corrected by subtracting the error of the S–T gap of methylene ( $\Delta E_{ST,CH_2}$ ). The  $\Delta E_{ST,CH_2}$  equals 1.9 kcal/mol (including ZPVE) at the B3LYP-GD3BJ/aug-cc-pVTZ level of theory. This results in a B3LYP-GD3BJ S–T gap of 0.7 kcal/mol, closer to those calculated at the B2PLYP-GD3BJ and CCSD(T) levels.

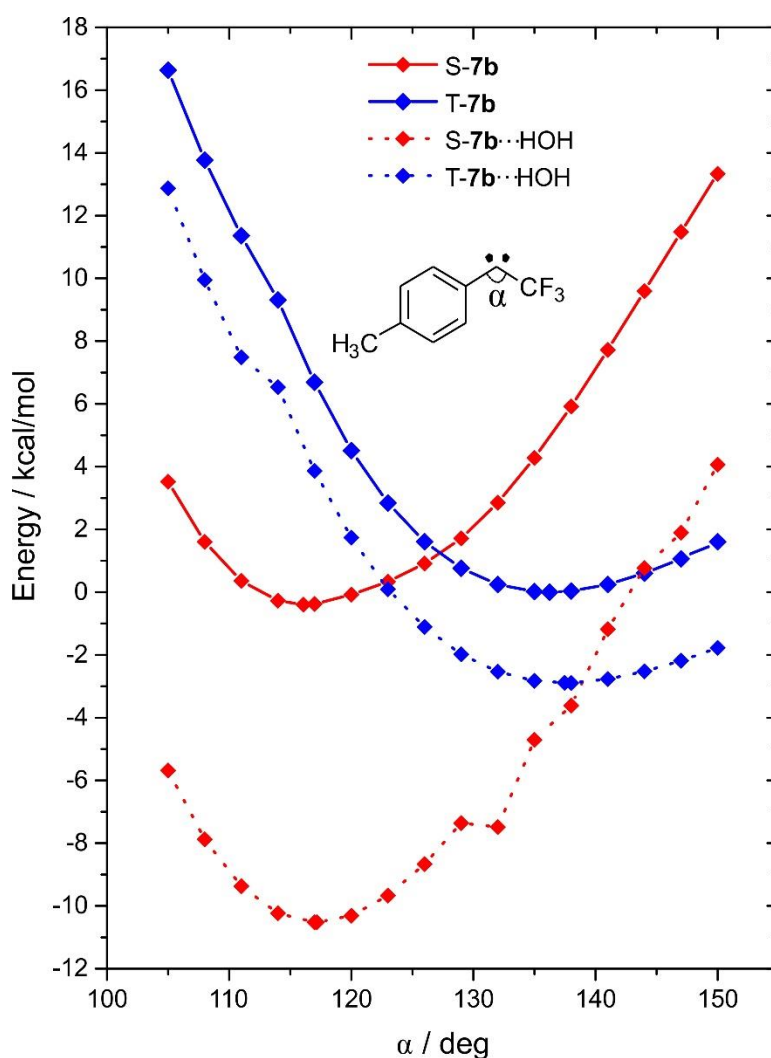
**Table 5.** S–T gaps of **7b** (kcal/mol) calculated with several density functionals. All structures were optimized using the aug-cc-pVTZ basis set.

Method	Gap	ZPVE	Gap + ZPVE
B2PLYP-GD3BJ	-0.4	0.0	-0.4
B3LYP-GD3BJ	2.3	0.3	2.6
BLYP-GD3BJ	0.8	0.2	1.0
M06-GD3	2.7	0.3	3.0
B97D-GD3	4.2	0.2	4.4

While the adiabatic S–T gap is very small, the vertical gaps of S-**7b** and T-**7b** are –8.7 and 8.5 kcal/mol at their respective minimum geometries. The relaxed one-dimensional scan of S-**7b** and T-**7b** shows an intersection at a carbene C–C–C bond angle of 127°, the triplet minimum at 135° and the singlet minimum at 115° (Figure 22), otherwise, the structures of S-**7b** and T-**7b** are very similar (Table 6).

**Table 6.** Comparison of the structures of **S-7b** and **T-7b** optimized using different density functionals and the aug-cc-pVTZ basis set.

Functional	Multiplicity	RMSD / Å	carbene angle / degree
B2PLYP-GD3BJ	S	0.000	115.3
B3LYP-GD3BJ		0.034	116.1
BLYP-GD3BJ		0.096	117.1
M06-GD3		0.031	115.9
B97D-GD3		0.021	115.8
B2PLYP-GD3BJ	T	0.000	134.8
B3LYP-GD3BJ		0.036	136.2
BLYP-GD3BJ		0.061	137.6
M06-GD3		0.016	135.6
B97D-GD3		0.042	137.8

**Figure 22.** Relaxed one dimensional scan of the C-C-C carbene angles of **7b** and the water complexes **7b···H-OH** calculated at the B3LYP-GD3BJ/aug-cc-pVTZ level of theory. Adiabatic energy differences are empirically corrected using the B2PLYP-GD3BJ results (see details in the reference).<sup>[123]</sup> Solid lines represent **7b** and dotted lines **7b···H-OH**. The irregularity at 132° in the scan of **S-7b···H-OH** is caused by the rotation of the CF<sub>3</sub> group. Please note that vertical excitations cannot be extrapolated from this figure.

### Reaction of *p*-tolyl(trifluoromethyl)carbene in argon matrices doped with 1% of water

Previous studies demonstrated that the spin state of triplet ground state carbenes such as diphenylcarbene **29** [86] or fluorenylidene **30** [124] is switched from triplet to singlet upon formation of hydrogen bonds with methanol or water under the conditions of matrix isolation. In a similar experiment and thus to probe the thermal and photochemical spin switching of carbene **7b**, **19b** was photolyzed ( $\lambda = 450$  nm) in argon matrices doped with 0.5 – 1% of water at 3K.

Similar to the photolysis in argon in the absence of water, mixtures T-**7b** as major and S-**7b** as minor constituent were formed. Annealing at 25 K for several minutes allowed the diffusion of water molecules which can be easily followed in the IR spectra by observing the formation of water dimers and oligomers.<sup>[86]</sup> Simultaneously, all IR bands assigned to T-**7b** decrease in intensity, and singlet carbene S-**7b** is formed. However, in comparison to S-**7b** obtained in the absence of water, all IR bands of the singlet carbene are blue-shifted by 3 – 9  $\text{cm}^{-1}$  (Table 7). This is a clear indication that the water complex S-**7b**···H–OH and not the free singlet carbene is the preferred product under these conditions. A further proof for the water complex S-**7b**···H–OH is its 450 nm photochemistry, which rapidly leads to the insertion product, *p*-tolyl(trifluoromethyl)ethanol **28b** (Figure 23). In contrast, as described above, 450 nm irradiation of mixtures of T-**7b** and S-**7b** leads to an increase of S-**7b** and not to the destruction of the singlet carbene.

**Table 7.** Experimental and calculated vibrational frequencies and shifts of the S-**7b**···H–OH complex.

Calculated <sup>a</sup>			Experimental			Assignment <sup>e</sup>
S- <b>7b</b>	S- <b>7b</b> ···H–OH	Shift <sup>b</sup>	Argon <sup>c</sup>	Ar/H <sub>2</sub> O <sup>d</sup>	Shift <sup>b</sup>	
$\nu/\text{cm}^{-1}$ ( $I_{\text{abs}}$ )	$\nu/\text{cm}^{-1}$ ( $I_{\text{abs}}$ )		$\nu/\text{cm}^{-1}$ ( $I_{\text{rel}}$ )	$\nu/\text{cm}^{-1}$ ( $I_{\text{rel}}$ )		
1071.6 (278.7)	1070.8 (278.6)	-0.8	1086.7 (32)	1095.3 (40)	+8.6	C-CF <sub>3</sub> bend (out of plane)
1137.4 (139.3)	1131.2 (191.3)	-6.2	1139.2 (39)	1147.5 (50)	+8.3	C-CF <sub>3</sub> bend (in plane)
1191.5 (645.0)	1192.8 (656.8)	+1.3	1171.7 (100)	1178.6 (100)	+6.9	C-C-C str. (carbene center)
1225.3 (115.5)	1230.5 (49.4)	+5.2	1206.4 (44)	1211.1 (86)	+4.7	C-H def. (in plane)
1642.1 (247.8)	1648.9 (290.3)	+6.8	1599.5 (43)	1602.2 (75)	+2.7	C=C str. Ring

<sup>a</sup> Calculated at the B2PLYP-GD3BJ (S-**7b**) or B2PLYP-GD3BJ//B3LYP/aug-cc-pVTZ (S-**7b**···H–OH) level of theory. <sup>b</sup> Frequency shift relative to the monomers ( $\text{cm}^{-1}$ ). <sup>c</sup> In argon matrix at 3 K. <sup>d</sup> In argon matrix doped with 1% of H<sub>2</sub>O at 3 K. <sup>e</sup> Tentative assignment.

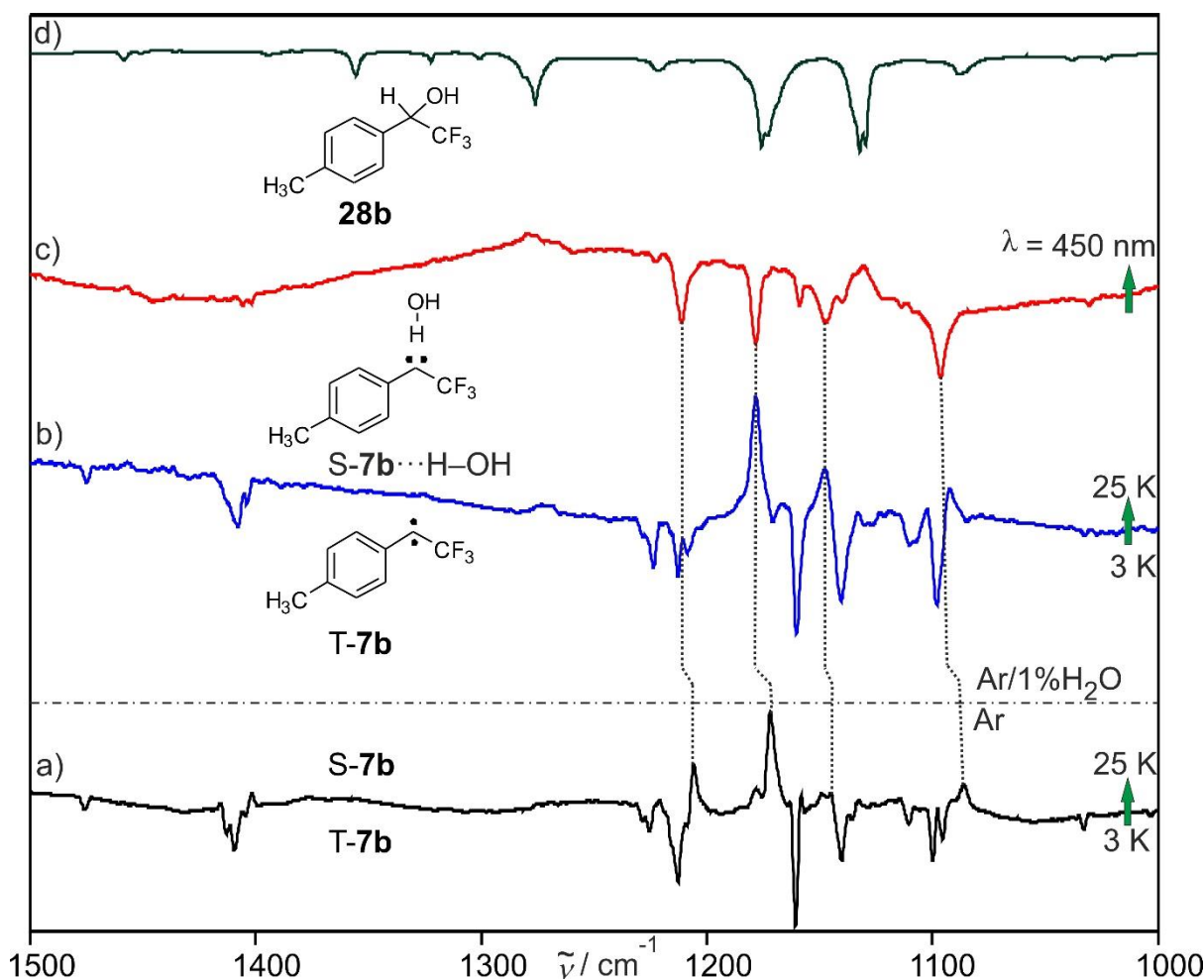
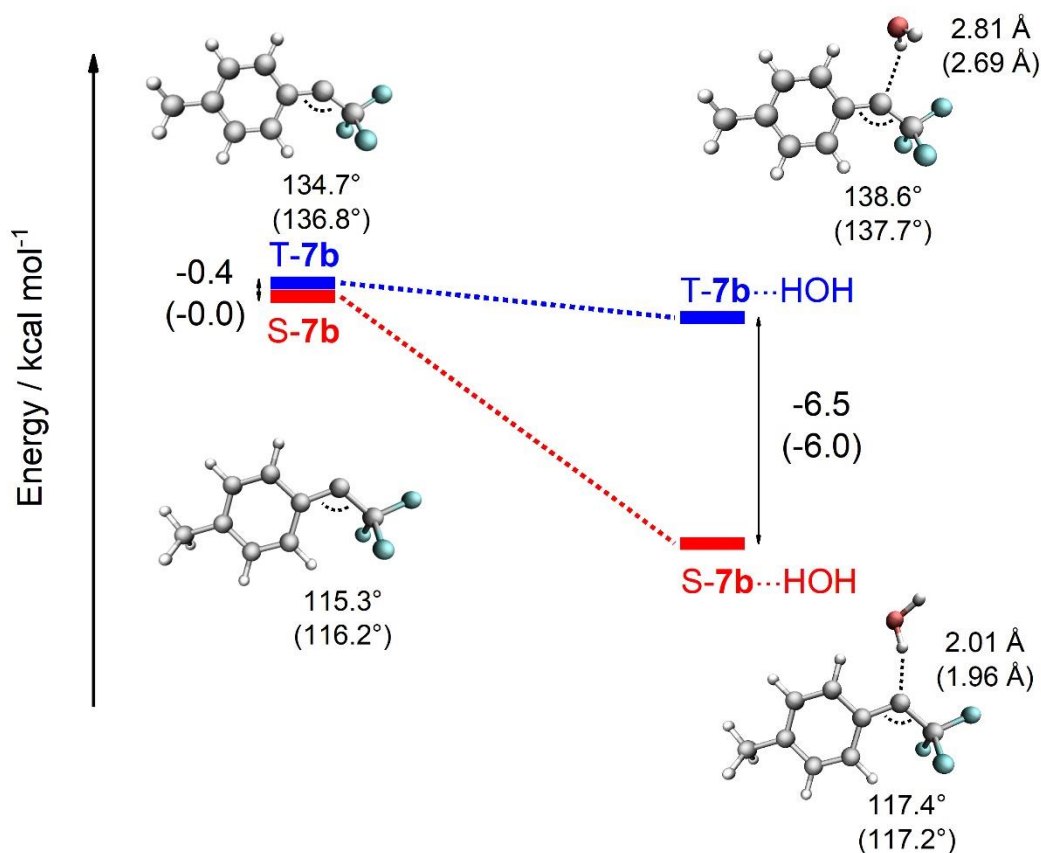


**Figure 23.** IR spectra of the water complex  $S-7b \cdots H-OH$  matrix-isolated in argon. (a) Difference IR spectrum showing changes of an argon matrix (without water) containing  $T-7b$  and  $S-7b$  at 3 K after annealing for 10 min at 25 K (black line). Bands pointing downward, assigned to  $T-7b$ , are disappearing, and bands pointing upward, assigned to  $S-7b$ , are appearing. Intensity divided by 5. (b) Difference IR spectrum of a similar experiment in argon doped with 1% of water (blue line). Bands pointing downward are disappearing and assigned to  $T-7b$ , bands pointing upward are appearing and assigned to  $S-7b \cdots H-OH$ . (c) Difference IR spectrum of the same matrix showing changes after 3 h irradiation ( $\lambda = 450$ ) (red line). Bands pointing downward are assigned to  $S-7b \cdots H-OH$ , and bands pointing upward are assigned to *p*-tolyl(trifluoromethyl)ethanol **28b**. (d) Reference spectrum of **28b**, matrix-isolated in argon at 3 K.

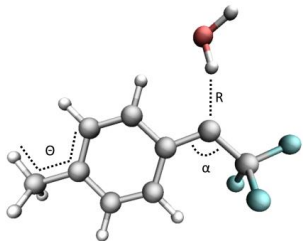
It has been showed in literatures that the water complexes of diphenylcarbene ( $S-29 \cdots H-OH$ )<sup>[86]</sup> and fluorenylidene ( $S-30 \cdots H-OH$ )<sup>[124]</sup> are only meta-stable at low temperatures as 3 K and rearrange to give the corresponding OH insertion product via quantum chemical tunneling. Under the same conditions, however, thermal rearrangement of the water complex  $S-7b \cdots H-OH$  is found at least 3 orders of magnitude slower compared to  $S-29 \cdots H-OH$  and  $S-30 \cdots H-OH$ , rationalized by the higher barrier for the OH insertion of the water complex of **7b** compared to that of **29** and **30** (see calculations below).

**DFT calculations** (Provided by Niklas Tötsch and Prof. Dr. Elsa Sanchez Garcia)

The experimental findings were supported by DFT calculations at the B2PLYP-GD3BJ/aug-cc-pVTZ level of theory. As expected, upon interaction with a single molecule of water, the singlet state is stabilized by 8.2 kcal/mol, whereas the triplet is only weakly stabilized by 2.0 kcal/mol. This is enlightened by the strength of the hydrogen bond complexes formed between the two spin states of **7b** and water. Accordingly, the bond distance between the carbene center and hydrogen of water is different for the two spin states: 2.01 Å in **S-7b**⋯H–OH compared to 2.81 Å in **T-7b**⋯H–OH (Figure 24). In summary, the calculation prevails **S-7b** is thermodynamically more stable than **T-7b** upon water addition in excellent agreement with the experimental results. Additional information on comparing the structures of **S-7b**⋯H–OH and **T-7b**⋯H–OH at various level of theory are compiled in Table 8. Compared to the free carbene, the dihedral angle  $\theta$  of the methyl group differs for singlet and triplet water complexes: close to 0° for singlet states but almost 90° for triplets.



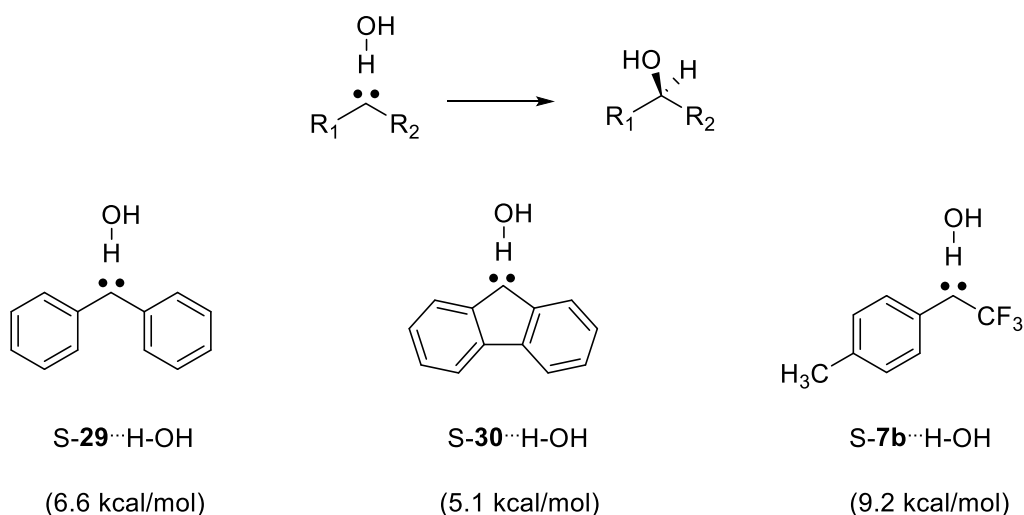
**Figure 24.** Relative energies of **S-7b**, **T-7b** and their most stable complexes with water. Calculations performed at the B2PLYP-GD3BJ/aug-cc-pVTZ and CCSD(T)/cc-pV(D/T)Z//B97D-GD3/def2-TZVP (in parenthesis) levels of theory. DFT values are ZPVE corrected.

**Table 8.** Structures of S-**7b**···H–OH optimized at different levels of theory.


Fucctionals	Multiplicity	$\alpha$	R	$\theta$	Gap	ZPVE
B3LYP	S	117.38	2.01	-1.67	-3.9	1.4
	T	138.62	2.81	83.07		
B3LYP-GD3	S	117.00	1.98	-1.69	-4.8	1.4
	T	137.34	2.55	84.78		
B3LYP-GD3BJ <sup>a</sup>	S	117.38	2.01	-1.67	-4.9	1.4
	T	138.62	2.81	83.07		
B2PLYP-GD3BJ <sup>a</sup>	S	117.38	2.01	-1.67	-7.6	1.1
	T	138.62	2.81	83.07		
B97D-GD3/def2-TZVP	S	117.23	1.96	-0.88	-0.7	0.9
	T	137.69	2.69	86.39		

<sup>a</sup> single point calculations on B3LYP optimized geometries. <sup>b</sup> Internal coordinates are given in the figure. Singlet-triplet energy gap (kcal/mol), R(Å),  $\alpha$  and  $\theta$  is given in degrees.

The calculations also allow us to rationalize the higher thermal stability of the water complex of the singlet state of **7b** compared to that of diphenylcarbene **29** and fluorenylidene **30**. While the barriers for the OH insertion of S-**29**···H–OH and S-**30**···H–OH are reported as 6.6 and 5.1 kcal/mol,<sup>[86, 125]</sup> respectively, at the B3LYP-D3/6-311++G(d,p) level of theory, that of S-**7b**···H–OH is predicted to 9.2 kcal/mol at the same level and to 10.0 kcal/mol at the CCSD(T)/cc-pV(D/T)Z//B97D-GD3/def2-TZVP level of theory (Scheme 8), and thus considerably higher. This explains the observed higher thermal stability of S-**7b**···H–OH compared to S-**29**···H–OH and S-**30**···H–OH at 3 K.



**Scheme 8.** Activation barriers ( $E_a$ ) for the OH insertion reactions of carbene–water complexes calculated at the B3LYP-D3/6-311++G(d,p) level of theory.<sup>[86, 125]</sup>

### Reaction of *p*-tolyl(trifluoromethyl)carbene in LDA water ice

Very recently reactive aromatic cationic species such as the benzhydryl<sup>[125]</sup> and fluorenyl<sup>[124]</sup> cations were generated in low density amorphous (LDA) water ices by protonation of the corresponding carbenes **29** and **30**, respectively. Thus, it was tempting to check the stability of carbene **7b** in a more polar medium. However, since the proton affinity of **7b** is much lower than **29** and **30**, we expect that the protonation of **7b** may not happen. The calculated proton affinity values of **7b**, **29** and **30** at the B3LYP-D3/def2TZVP level of theory, respectively, are 256, 274 and 273 kcal/mol.

### UV–vis spectroscopy

The UV–vis spectrum of **19b** in LDA ice is depicted in Figure 25. The deposition was carried out similar to the procedures described in literatures.<sup>[124–125]</sup> Visible light (450 nm) photolysis of the matrix produces the UV–vis spectrum shown in Figure 25. Under these conditions, T-**7b** is not detected at any time with short/long irradiation, suggesting the rapid reactivity of T-**7b** with the surrounding water molecule. A broad band with  $\lambda = 326$  nm could be detected upon short irradiation of **19b** assigned to the complex S-**7b**···H–OH and/or traces of S-**7b**. However, in contrast to the experiments in argon doped with 1% of water, which shows rearrangement to the insertion product through visible light photolysis, the band at 326 nm is found stable at 8 K for several hours. Upon prolonged irradiation, small but distinct bands are observed in the UV region of below 300 nm, assigned to the insertion product. Under these conditions no other

band is detected that could be assigned to the cationic species, explained by the predicted lower probability of protonation of carbene **7b**.

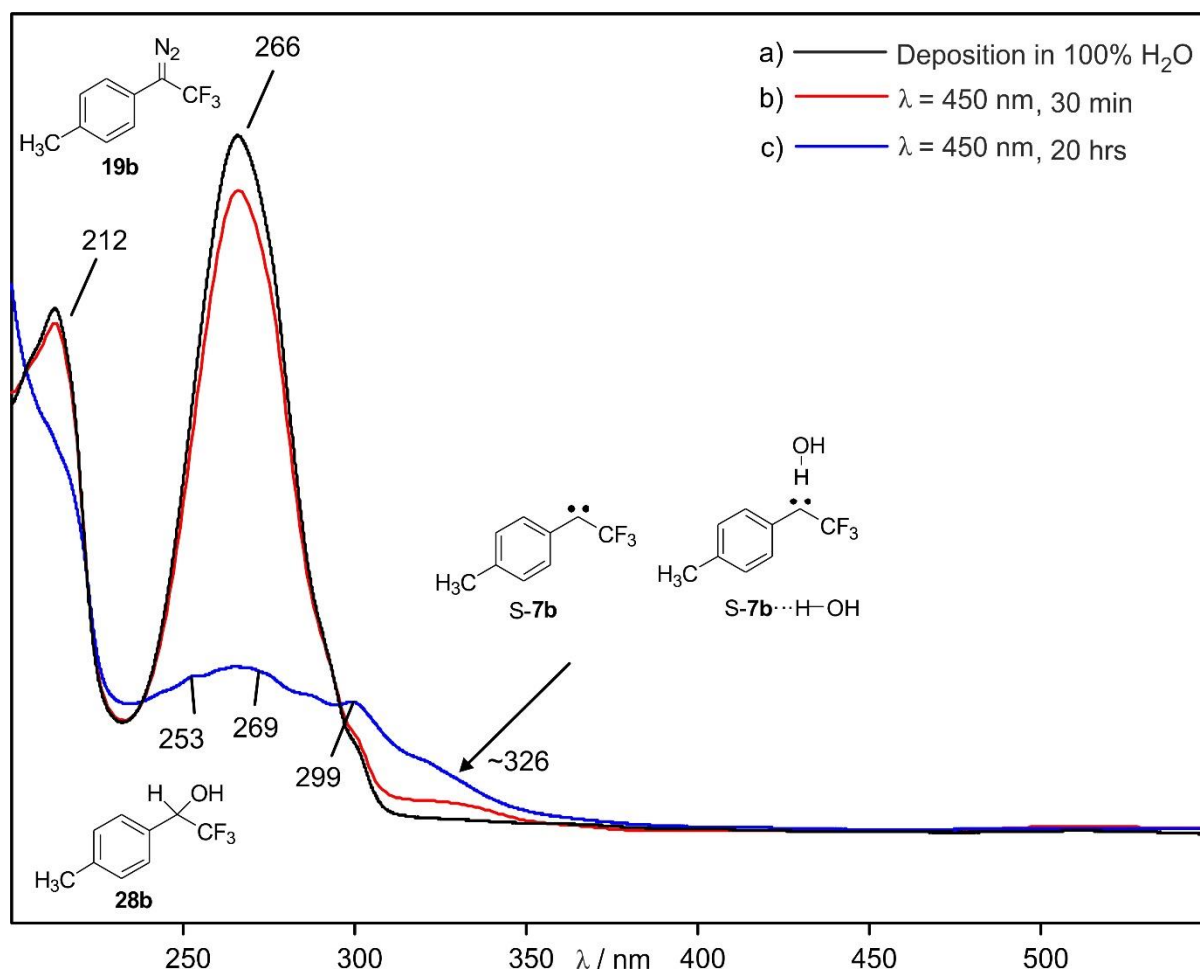


**Figure 25.** Photochemistry of *p*-tolyl(trifluoromethyl)diazomethane **19b** in LDA water ice. a) **19b** in LDA ice at 8 K. b) UV-vis spectrum of the same matrix after 30 minutes of 450 nm irradiation showing the formation of **S-7b** $\cdots$ **H-OH** and/or traces of **S-7b**. c) UV-vis spectrum of the same matrix after several hours of 450 nm irradiation showing the formation of the formal O-H insertion product **28b**.

### IR spectroscopy

To confirm these assignments, we also monitored the photolysis of **19b** in LDA ice at 3 K by IR spectroscopy (Figure 26). The IR spectrum of **19b** in LDA ice is similar to that in argon matrices, with the only exception that the spectrum in water ice shows broader line widths and less fine structure than in argon. The IR bands of **19b** decrease upon several hours of irradiation with visible light, and a new species appears with characteristic IR absorptions at 1132, 1180, and  $1266\text{ cm}^{-1}$ , assigned to the formal OH insertion product *p*-tolyl(trifluoromethyl)ethanol **28b**. The IR spectrum obtained after complete photolysis is found in good agreement with the authenticated matrix-isolated spectrum of **28b** in solid argon at 3 K. Under these conditions

neither T-**7b** nor cationic species is detected, matching well with the results obtained by UV-vis spectroscopy.

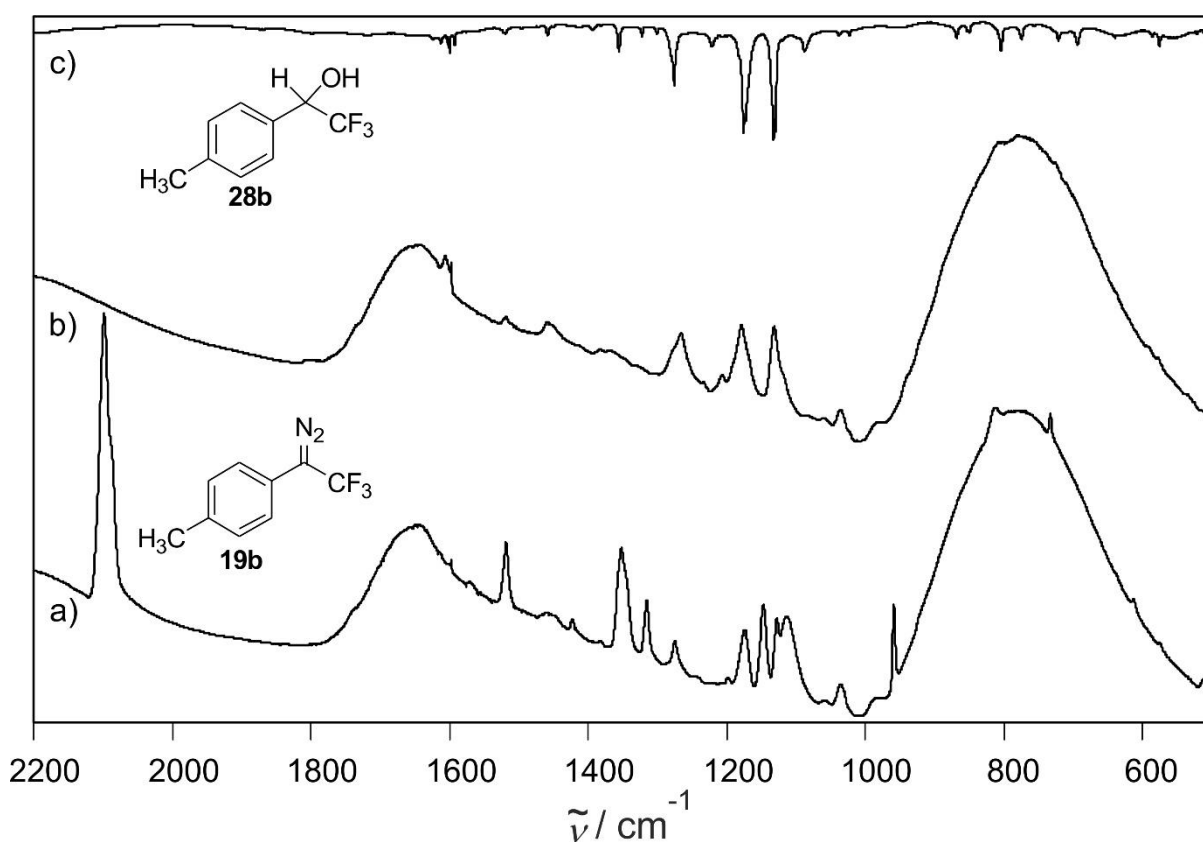
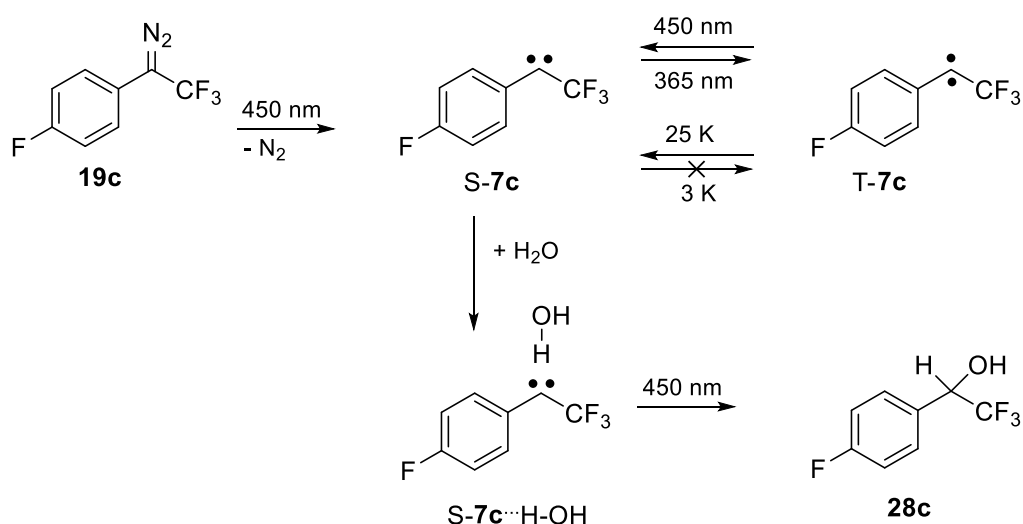


**Figure 26.** Photochemistry of *p*-tolyl(trifluoromethyl)diazomethane (**19b**) in LDA water ice. a) **19b** in LDA ice at 8 K. b) IR spectrum of the same matrix after several hours of 450 nm irradiation showing the formation of *p*-tolyl(trifluoromethyl)ethanol (**28b**). c) Reference spectrum of **28b** in argon matrix at 3 K.

### *p*-Fluorophenyl(trifluoromethyl)carbene

To shed light on the magnetic bistability behavior of carbene **7b**, we perform similar experiments with equally structurally simple analogues carbene **7c**. The principal results are the same for the two carbenes: triplet state (T-**7c**) as major constituent and singlet state (S-**7c**) as minor constituent coexist indefinitely in argon matrix at temperature below 10 K, and can be interconverted by irradiation into the absorption maxima of singlet species in the UV or triplet species in the visible range, respectively. The main results of **7c** is summarized in Scheme 9.



**Scheme 9.** Synthesis and chemistry of carbene **7c**.

### EPR spectroscopy

The X-band EPR spectrum of **7c** obtained after several hours irradiation ( $\lambda = 450$ ) of the *p*-fluorophenyl(trifluoromethyl)diazomethane (**19c**) in solid argon at 4 K shows a pattern characteristic of a typical triplet carbene with  $|D/hc| = 0.532 \text{ cm}^{-1}$  and  $|E/hc| = 0.032 \text{ cm}^{-1}$  (Figure 27). In an attempt to measure the Curie-Weiss behavior and thus to determine the ground state of **7c**, the matrix was annealed for 10 minutes each at various higher temperatures in the range between 5 and 25 K. When we cooled back the matrix to 4 K, triplet intensity signal could not be recovered, indicates the irreversible reaction of **T-7c** to an EPR-silent singlet species. Interestingly if we do further irradiation ( $\lambda = 365 \text{ nm}$ ) at 4 K, we could partially recovered the triplet signals. In these experiments, we took care that **19c** was completely photolyzed, and therefore remaining **19c** was not the precursor of **T-7c** under these conditions. Subsequent annealing at higher temperatures again irreversibly reduced the signal of **T-7c**. This behavior was reproducible in repeated annealing/irradiation cycles. In summary, annealing of the matrix containing **T-7c** and irradiation with visible light ( $\lambda = 450$ ) results in the formation of an EPR-silent species, which in turn can be restored by UV irradiation ( $\lambda = 365$ ). In the light of the chemistry of **7b** discussed before, this EPR-silent singlet species is assigned to **S-7c**.

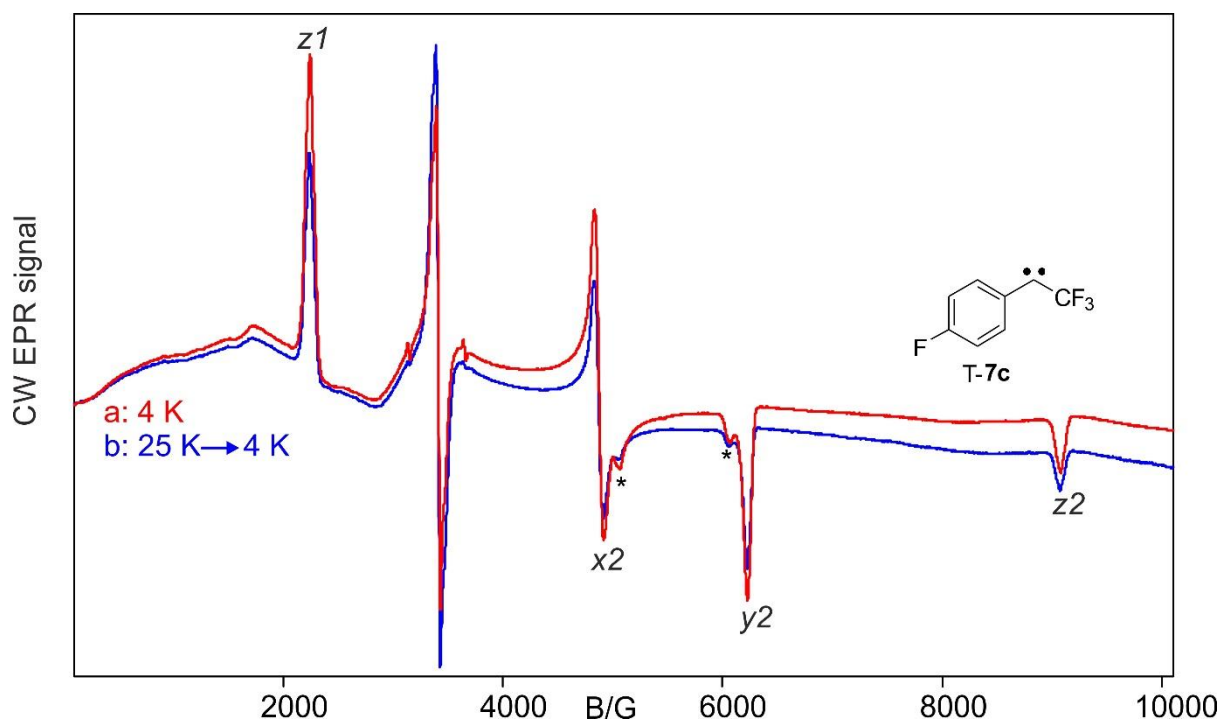


**Figure 27.** X-band CW EPR spectra of an argon matrix showing the thermal behavior of T-7c after warming from 4 to 25 K and cooling back to 4 K. (a) Argon matrix at 4 K showing the spectrum of T-7c (read line; ZFS parameters  $|D/hc| = 0.532 \text{ cm}^{-1}$  and  $|E/hc| = 0.032 \text{ cm}^{-1}$ ). (b) After subsequent annealing at 25 K for 10 min and cooling back to 4 K, 28% of the signal intensity is lost (blue line). The bands marked with an asterisk are assigned to products of carbene-carbene rearrangements.

## IR spectroscopy

To confirm this assignments, we utilized a complementary IR spectroscopy. Several hours irradiation ( $\lambda = 450 \text{ nm}$ ) of *p*-fluorophenyl(trifluoromethyl)diazomethane (**19c**) in argon matrix at 3 K resulted in a disappearance of all IR absorptions of the diazo compound and formation of a complex spectrum (Figure 28). In the light of the results of **7b** discussed previously, the newly formed species are assigned to triplet (82%) and singlet (18%) carbene **7c**. Subsequent irradiation with UV light ( $\lambda = 365 \text{ nm}$ ) of the same matrix resulted in an increase of the IR absorption bands of the T-**7c** and a completely bleaching out of the bands assigned to S-**7c**. However, annealing of the same matrix at 25 K and irradiation with visible light ( $\lambda = 450 \text{ nm}$ ) partially recovered the signals of S-**7c** and concurrently in a decrease of bands of T-**7c**. This assignment was confirmed further by comparing the experimental IR spectra to calculations at the B2PLYP-GD3BJ/aug-cc-pVTZ levels of theory, which nicely reproduce the experimental data (Figure 28, Tables 9 and 10).

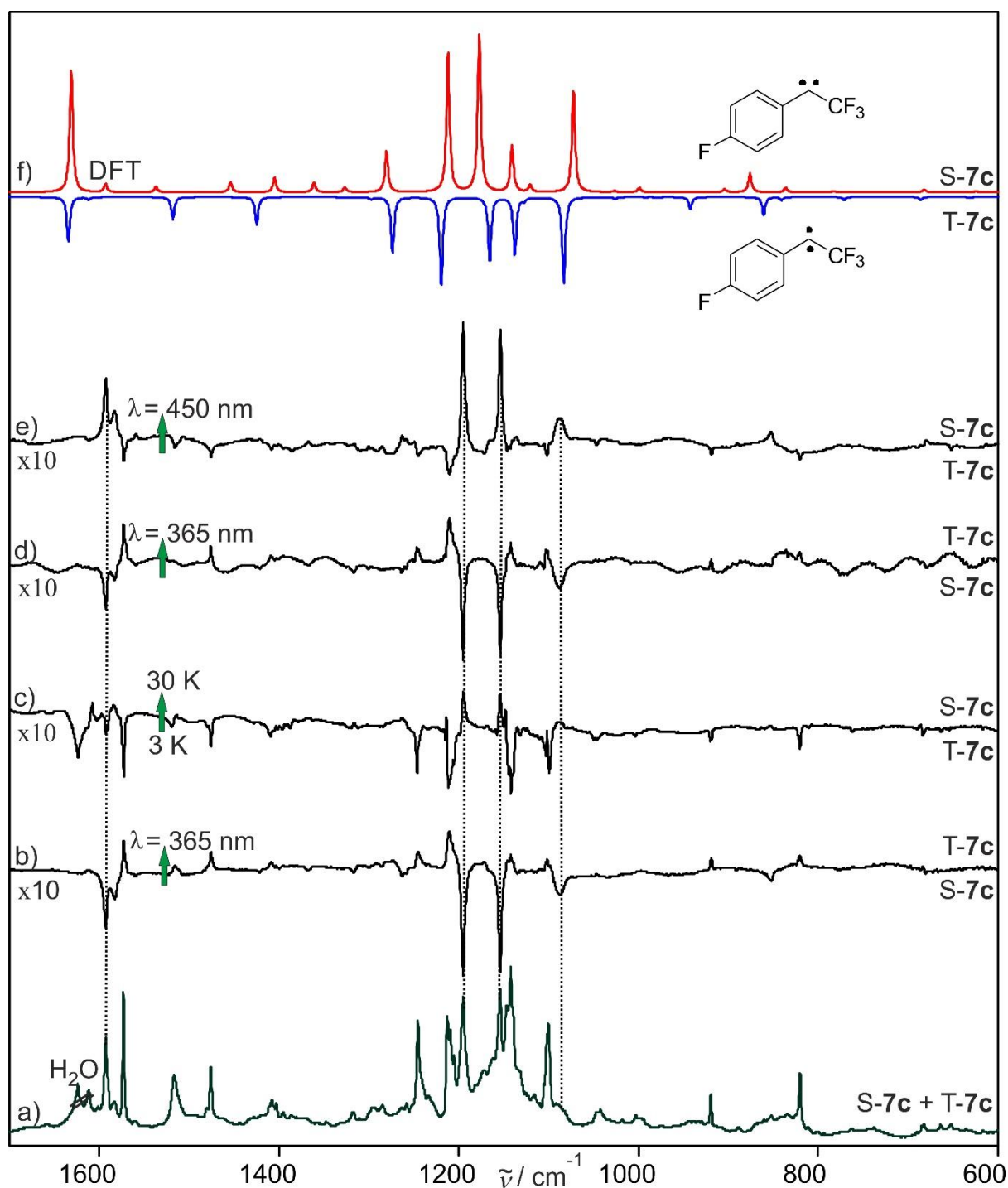


**Figure 28.** IR spectra showing the interconversion of S-7c and T-7c in argon matrix. (a) IR spectrum after several hours of 450 nm irradiation of **19c** at 3 K (dark green). (b) Difference IR spectrum at 3 K showing changes after 60 min of 365 nm irradiation of the same matrix. Bands pointing downward, assigned to S-7c, are disappearing, and bands pointing upward, assigned to T-7c are appearing. (c) Difference IR spectrum of the same matrix after 10 min annealing to 30 K and cooling back to 3 K. Bands pointing downward, assigned to T-7c, are disappearing, and bands pointing upward, assigned to S-7c, are appearing. (d) Difference IR spectrum at 3 K showing changes after 60 min of 365 nm irradiation of the same matrix. Bands pointing downward, assigned to S-7c, are disappearing, and bands pointing upward, assigned to T-7c are appearing. (e) Difference IR spectrum at 3 K showing changes after 60 min of 450 nm irradiation of the same matrix. Bands pointing downward, assigned to T-7c, are disappearing, and bands pointing upward, assigned to S-7c, are appearing. (f) Superimposed IR spectrum showing the interconversion of T-7c (blue) to S-7c (red) calculated at the B2PLYP-GD3BJ/aug-cc-pVTZ level of theory. Equal contributions of S-7c and T-7c were used to simulate the IR spectra.

**Table 9.** IR spectroscopic data of **S-7c**.

Mode	Calculated <sup>a</sup>	Argon <sup>b</sup>	Assignment <sup>c</sup>
	$\nu/\text{cm}^{-1}$ ( $I_{\text{abs}}$ )	$\nu/\text{cm}^{-1}$ ( $I_{\text{rel}}$ )	
26	1072.4 (277.9)	1087.6 (35)	C-CF <sub>3</sub> bend (out of plane)
28	1141.0 (127.9)	1140.2 (11)	C-CF <sub>3</sub> bend (in plane)
29	1177.3 (436.3)	1154.3 (100)	C-C-C str. (carbene center)
30	1212.1 (381.7)	1195.5 (88)	C-H def. (in plane)
31	1280.6 (111.8)	1263.5 (13)	Ring def. (in plane)
38	1631.6 (334.5)	1593.5 (64)	C=C str. Ring

<sup>a</sup> Calculated at the B2PLYP-GD3BJ/aug-cc-pVTZ level of theory. <sup>b</sup> Matrix at 3 K. <sup>c</sup> Tentative assignment.

**Table 10.** IR spectroscopic data of **T-7c**.

Mode	Calculated <sup>a</sup>	Argon <sup>b</sup>	Assignment <sup>c</sup>
	$\nu/\text{cm}^{-1}$ ( $I_{\text{abs}}$ )	$\nu/\text{cm}^{-1}$ ( $I_{\text{rel}}$ )	
12	521.2 (15.6)	500.3 (3)	Ring def.
13	565.4 (20.0)	561.1 (7)	Ring def.
15	631.2 (2.8)	616.8 (1)	Ring def.
16	685.9 (9.6)	684.9 (4)	C-CF <sub>3</sub> bend
18	771.3 (9.1)	763.1 (3)	C-CF <sub>3</sub> bend
21	860.0 (56.0)	820.1 (23)	Ring def.
22	942.3 (38.1)	919.8 (10)	Ring def.
26	1083.2 (272.6)	1099.9 (59)	C-CF <sub>3</sub> bend
27	1127.5 (11.5)	1131.5 (4)	Ring def.
28	1137.8 (181.1)	1142.1 (100)	C-CF <sub>3</sub> bend
29	1165.7 (200.6)	1205.2 (37)	C-H bend
30	1219.7 (275.6)	1213.2 (47)	C-C-C str.
31	1273.9 (176.3)	1245.6 (41)	C-F bend
34	1425.1 (87.4)	1408.8 (21)	C-C-C str.
36	1518.5 (70.1)	1476.4 (29)	C-H bend
38	1634.9 (140.0)	1573.4 (42)	C=C str.

<sup>a</sup> Calculated at the B2PLYP-GD3BJ/aug-cc-pVTZ level of theory. <sup>b</sup> Matrices at 3 K. <sup>c</sup> Tentative assignment.

### UV–vis spectroscopy

The UV–vis experiments demonstrate that *p*-fluorophenyl(trifluoromethyl)diazomethane (**19c**) in argon matrix shows a strong absorption band at 252 nm and a weak broad band in the region of 450 nm. Upon several hours irradiation of **19c** in the visible region ( $\lambda = 450$ ) produces the UV–vis spectrum shown in Figure 29 with a series of absorptions ranging from 250 to 450 nm.

A broad band with  $\lambda_{\max} = 313$  nm completely disappears after 365 nm irradiation and reappears after 450 nm irradiation, and thus is assigned to S-7c. The triplet carbene T-7c shows an absorption with a pronounced progression with  $\lambda_{\max} = 430$  nm, and irradiation into this band results in the rearrangement of T-7c to S-7c. Subsequent irradiation with UV light ( $\lambda = 365$  nm) results in an increase of the bands of the triplet T-7c and a completely bleaching out the band of S-7c, whereas annealing at 25 K resulted in recovering of the band of S-7c and a decrease of the triplet T-7c bands. This behavior was reproducible in repeated annealing/irradiation cycles.

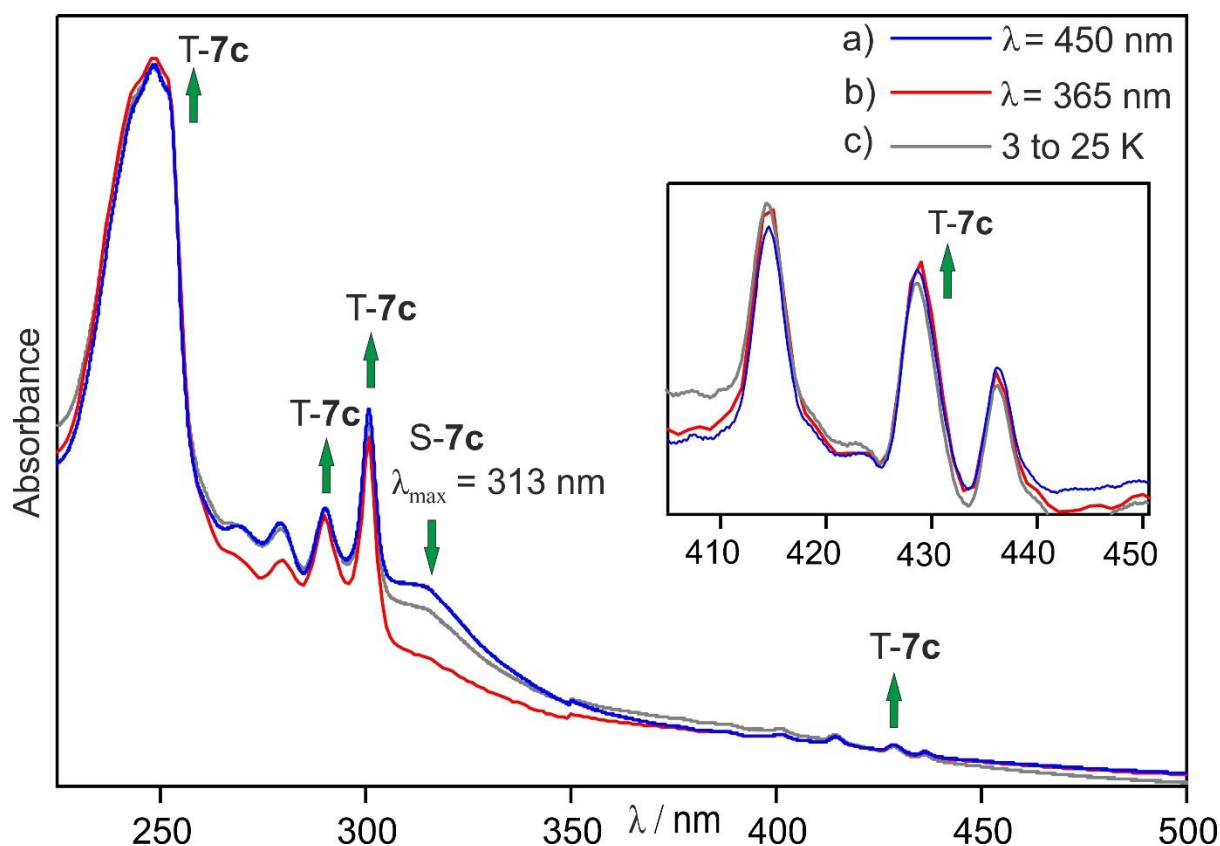


**Figure 29.** UV-vis showing the S-T interconversion of 7c in argon matrix at 8 K. (a) T-7c and S-7c obtained after several hours of 450 nm irradiation of 19c at 8 K (blue line). (b) Spectra obtained after 60 min irradiation with  $\lambda = 365$  nm at 8 K (red line). (c) Spectra obtained after subsequent annealing for 30 min at 25 K and cooling back to 8 K (gray line). The weak band of T-7c in the visible region of the UV-vis spectrum is shown in the inset. Note that the triplet signal in the region of 250 nm is saturated and might not show the real changes.

### Reaction of p-fluorophenyl(trifluoromethyl)carbene in argon matrices doped with 1% of water

Similar to experiments with the reaction of 7b and water described before, the reaction of 7c and water is also investigated. Both the singlet state S-7c and triplet state T-7c are present in the matrix after photolysis of 19c in solid argon doped with 1% of water at 3 K. To allow the

diffusion of species in solid argon, even of small molecules such as water, it's necessary to anneal the matrix at temperatures above 20 K for several minutes. The higher temperatures causes softening of the matrix and possibly bimolecular interactions of species present in the matrices.<sup>[86]</sup> However, as we discussed in the previous sections, T-7c was partially converted to S-7c by annealing the matrix to higher temperatures in the absence of water. Thus, in the presence of water, we expect interaction of water with both S-7c and T-7c. Here, the more polar S-7c is expected to interact strongly with water under formation of strong hydrogen bonded complex S-7c···H-OH, whereas the weakly interacting T-7c with water complex will also rapidly convert to S-7c···H-OH complex similar to previous finding in the literatures.<sup>[86]</sup> Consequently, several new IR bands are appearing during warming the matrices containing carbene 7c and water from 3 to 25 K, concurrently all bands of T-7c are decreased in intensity. In light of the experiments of carbene 7b, this new bands are assigned to S-7c···H-OH (Table 11, Figure 30). Note that these bands are observed only if both the carbene and water are present in the matrix. As expected, the IR spectrum of S-7c in the complex is only slightly disturbed upon complexation with water, very similar to the chemistry of carbene 7b described previously. A further proof for the water complex S-7c···H-OH is its 450 nm photochemistry, which rapidly leads to the insertion product, p-fluorophenyl(trifluoromethyl)ethanol 28c (Figure 30).

**Table 11.** Experimental and calculated vibrational frequencies and shifts of the S-7c···H-OH complex.

Calculated <sup>a</sup>			Experimental				Assignment <sup>e</sup>
S-7c	S-7c···H-OH	Shift <sup>b</sup>	Argon <sup>c</sup>	Ar/H <sub>2</sub> O <sup>d</sup>	Shift <sup>b</sup>		
v/cm <sup>-1</sup> (I <sub>abs</sub> )	v/cm <sup>-1</sup> (I <sub>abs</sub> )		v/cm <sup>-1</sup> (I <sub>rel</sub> )	v/cm <sup>-1</sup> (I <sub>rel</sub> )			
1053.8 (273.2)	1066.1 (278.1)	+12.3	1087.6 (35)	1095.4 (20)	+7.8	C-CF <sub>3</sub> bend (out of plane)	
1123.1 (129.8)	1130.9 (153.4)	+7.8	1140.2 (11)	1147.4 (45)	+7.2	C-CF <sub>3</sub> bend (in plane)	
1175.0 (687.3)	1181.7 (731.2)	+6.7	1154.3 (100)	1160.6 (100)	+6.3	C-C-C str. (carbene center)	
1203.8 (117.0)	1210.7 (87.0)	+6.9	1195.5 (88)	1203.8 (90)	+7.7	C-H def. (in plane)	
1278.9 (92.0)	1294.6 (81.4)	+15.7	1263.5 (13)	1269.3 (11)	+5.8	Ring def.(in plane)	
1630.3 (314.3)	1634.0 (341.2)	+3.7	1593.5 (64)	1590.2 (60)	-3.3	C=C str. Ring	

<sup>a</sup> Calculated at the B3LYP-D3/def2-TZVP level of theory. <sup>b</sup> Frequency shift relative to the monomers (cm<sup>-1</sup>). <sup>c</sup> In argon matrix at 3 K. <sup>d</sup> In argon matrix doped with 1% H<sub>2</sub>O at 3 K. <sup>e</sup> Tentative assignment.

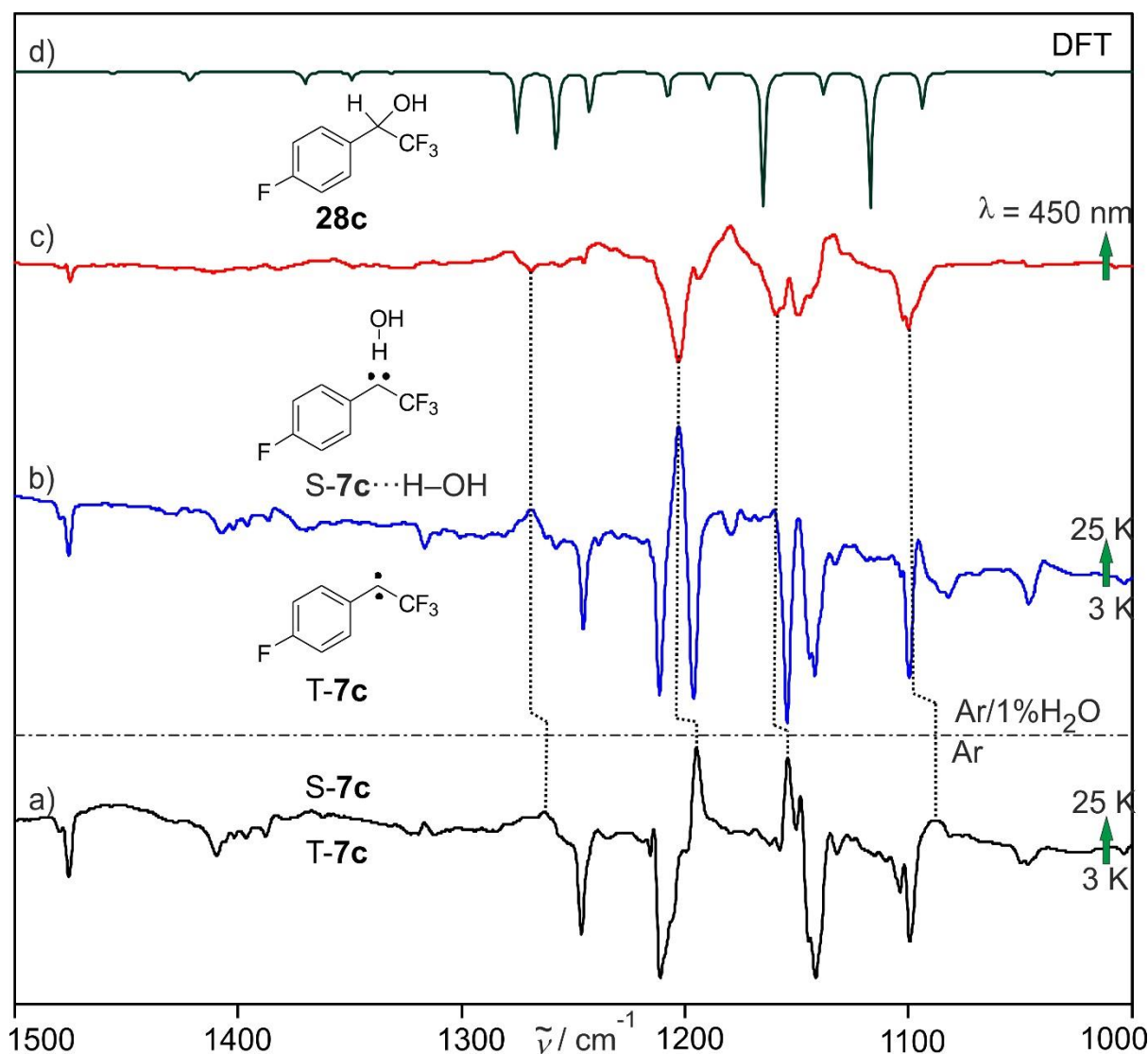


**Figure 30.** IR spectra of the water complex  $S-7c \cdots H-OH$  matrix-isolated in argon. (a) Difference IR spectrum showing changes of an argon matrix (without water) containing  $T-7c$  and  $S-7c$  at 3 K after annealing for 10 min at 25 K (black line). Bands pointing downward, assigned to  $T-7c$ , are disappearing, and bands pointing upward, assigned to  $S-7c$ , are appearing. Intensity divided by 5. (b) Difference IR spectrum of a similar experiment in argon doped with 1% of water (blue line). Bands pointing downward are disappearing and assigned to  $T-7c$  and  $S-7c$ , bands pointing upward are appearing and assigned to  $S-7c \cdots H-OH$ . (c) Difference IR spectrum of the same matrix showing changes after 3 h irradiation ( $\lambda = 450$ ) (blue line). Bands pointing downward are assigned to  $S-7c \cdots H-OH$ , and bands pointing upward are assigned to *p*-tolyl(trifluoromethyl)ethanol (**28c**). (d) IR spectrum of **28c** calculated at the B3LYP-D3/def2-TZVP level of theory.

### DFT calculations

These results were corroborated with DFT calculations at the B2PLYP-GD3BJ/aug-cc-pVTZ level of theory. The calculation predicts  $\Delta E_{ST}$  of  $-0.63$  kcal/mol (the ZPVE correction is 0.07 kcal/mol) for carbene **7c** in excellent agreement with the experimental results, and also comparable to the computed results of carbene **7b** of  $\Delta E_{ST} = -0.40$  kcal/mol (the ZPVE correction is 0.03 kcal/mol) at the same level of theory. The single-triplet energy gap of carbene **7c** calculated at the CCSD(T)/aug-cc-pVDZ//B3LYP-D3/def2-TZVP level of theory also

result in  $\Delta E_{ST} = 0.0$  kcal/mol, thus predicting degeneracy of the spin states in the gas phase. **S-7c** and **T-7c** are structurally the same, with the only exception that they differ on their C-C-C bond angle. However, the complexes **S-7c**···H–OH and **T-7c**···H–OH differ geometrically because the carbene-water interaction is dependent on the electronic state. As expected, introduction of a water molecule results in a stabilization of the singlet state of 9.1 kcal/mol, whereas the triplet is only stabilized by 3.7 kcal/mol upon water addition calculated at the B3LYP-D3/def2-TZVP level of theory.

**Table 12.** Singlet-triplet gaps of carbenes **7b** and **7c** (kcal/mol) calculated at different level of theories.

Method	<b>7b</b>	<b>7c</b>
B3LYP-D3/def2-TZVP	2.4	2.1
B3LYP-D3/def2-TZVP + ZPVE	2.8	2.6
CCSD(T)/cc-PVDZ//B3LYP-D3/def2-TZVP	2.7	2.2
CCSD(T)/cc-PVTZ//B3LYP-D3/def2-TZVP	0.8	0.2
CCSD(T)/aug-cc-PVDZ//B3LYP-D3/def2-TZVP	0.1	0.0
CCSD(T)/aug-cc-PVTZ//B3LYP-D3/def2-TZVP	–	–0.6
B2PLYP-GD3BJ/aug-cc-pVTZ	–0.4	–0.6
B2PLYP-GD3BJ/aug-cc-pVTZ + ZPVE	–0.4	–0.6

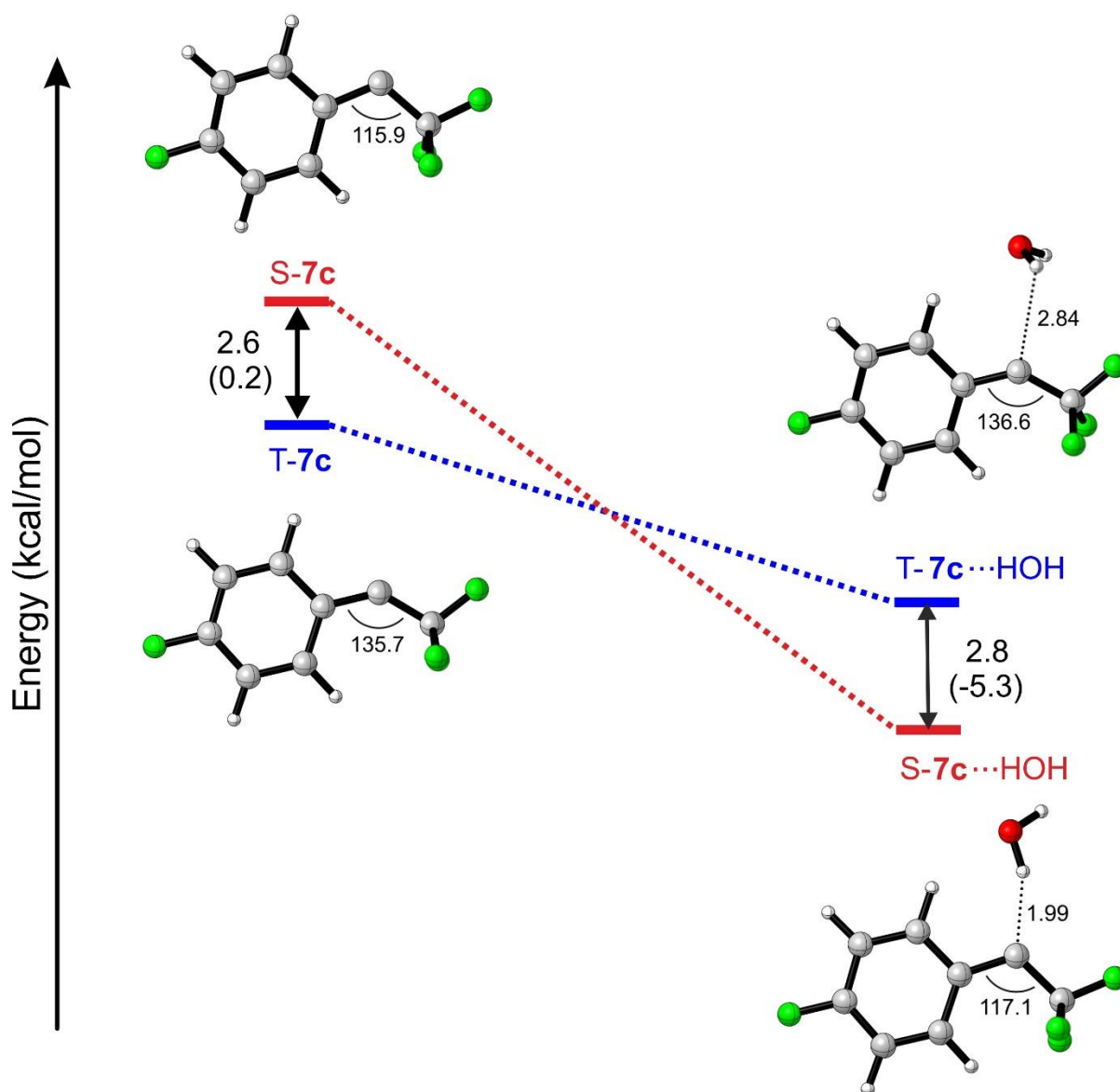
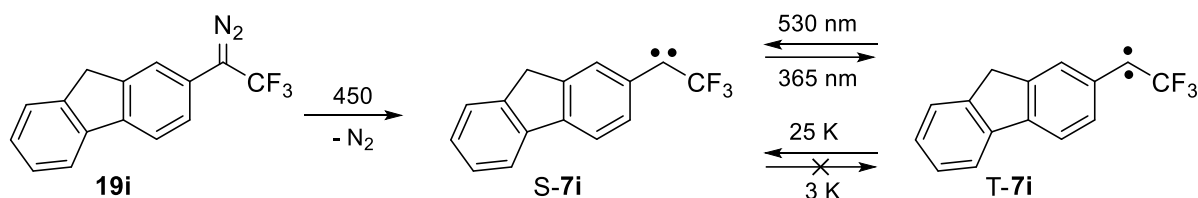


**Figure 31.** Relative energies of S-7c, T-7c and their most stable complexes with water. Calculations performed at the B3LYP-D3/def2-TZVP and CCSD(T)/cc-pVTZ//B3LYP-D3/def2-TZVP (in parenthesis) levels of theory. DFT values are ZPVE corrected.

### Fluorenyl(trifluoromethyl)carbene

Under the same conditions to carbenes **7b** and **7c** described before, the related fluorenyl(trifluoromethyl)carbene **7i** is also investigated to answer the question whether or not magnetic bistability is a general phenomenon in carbenes with small S –T gaps. Previously, **7i** was studied by Platz *et al.* using ultrafast time resolved absorption spectroscopy.<sup>[113]</sup> In acetonitrile the singlet carbene S-**7i** was characterized as a transient species with an initial absorption maximum at 427 nm that shifts to 432 nm after vibrational cooling. On the other hand, as we already discussed in Chapter 2, carbene **7i** produced a typical triplet carbene EPR spectrum with ZFS parameters  $|D/hc| = 0.4880$  and  $|E/hc| = 0.0305 \text{ cm}^{-1}$ , which suggests that

**7i** either has a triplet ground state or such a small S–T gap that the excited triplet state is thermally populated even at 4 K. In the light of this premise, the bistable magnetic behavior of carbene **7i** is investigated using the matrix isolation techniques and characterized by EPR, UV–vis and IR spectroscopy. The main finding is summarized in Scheme 10.



**Scheme 10.** Synthesis and chemistry of carbene **7i**.

### EPR spectroscopy

The EPR experiments demonstrated that carbene **T-7i** is generated upon visible light ( $\lambda = 450\text{ nm}$ ) irradiation of fluorenyl(trifluoromethyl)diazomethane **19i** in argon matrix at 4 K. The ZFS parameters obtained are  $|D/hc| = 0.4880\text{ cm}^{-1}$  and  $|E/hc| = 0.0305\text{ cm}^{-1}$ . In order to determine the ground spin state of **7c**, a temperature-dependent EPR experiment was carried out and a linear Curie-Weiss behavior was observed in the range between 6 and 30 K. An EPR spectrum was recorded at each of these temperatures, and before the temperature was increased to the next higher level, the matrix was cooled back to 4 K to record a second EPR spectrum (Figure 32, inset). These experiments clearly demonstrate an irreversible loss of **T-7i** at each temperature step: at 10 K the loss was 12 %, at 14 K 23 %, at 18 K 38 %, at 22 K 50 %, at 26 K 60 % and at 30 K 65 %. Interestingly, subsequent irradiation of the same matrix with  $\lambda = 365\text{ nm}$  partially recovered signals of **T-7i**, while irradiation with  $\lambda = 530\text{ nm}$  leads to a loss of the signal again. Note that, in these experiments, we took care that **19i** was completely photolyzed, and therefore remaining **19i** was not the precursor of **T-7i** under these conditions. Thus, the experiments demonstrated the EPR silent species formed after annealing can be converted back to **T-7i** upon irradiation with UV light, and on the other hand **T-7i** can be partially transformed back to the EPR silent species upon irradiation with visible light. This behavior was reproducible in repeated annealing/irradiation cycles. Based on the experimental observations of carbenes **7b** and **7c** discussed before, it is tempting to assign this EPR silent species to **S-7i**.

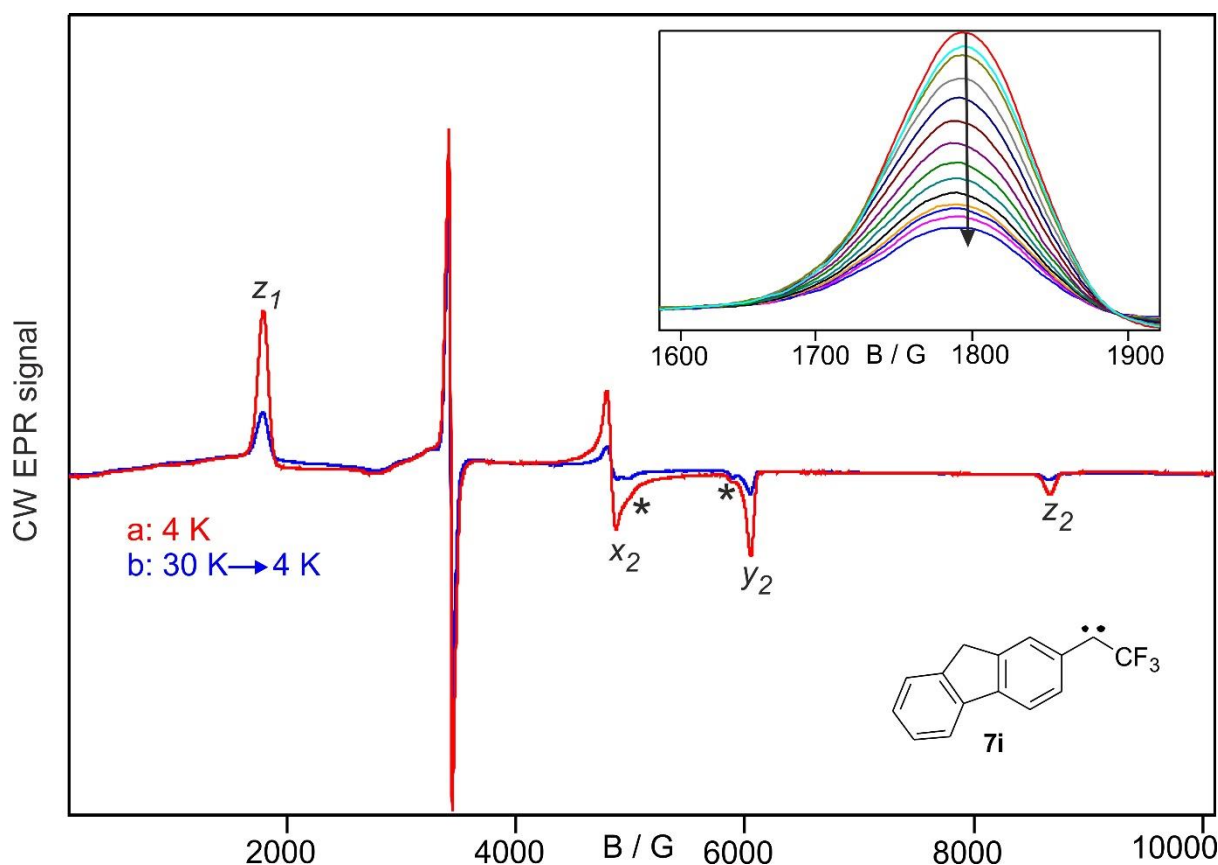


**Figure 32.** X-band CW EPR spectra of an argon matrix showing the thermal behavior of T-**7i** after warming from 4 to 30 K and cooling back to 4 K. a) Argon matrix at 4 K showing the spectrum of T-**7i** (red line) with ZFS parameters  $|D/hc| = 0.4880$  and  $|E/hc| = 0.0305$  cm<sup>-1</sup>. b) After subsequent annealing at 30 K for 10 min and cooling back to 4 K, 65 % of the signal intensity is lost (blue line). Inset shows the loss of the T-**7i** signal at the  $z_1$  canonical position after cooling back from 6, 8, 10, 12, 14, 16, 18, 20, 22, 24, 26, 28 and 30 K to 4 K. The bands marked with an asterisk are assigned to products of carbene-carbene rearrangements.

## IR spectroscopy

A complementary IR detection technique was utilized to investigate the singlet-triplet switching of carbene **7i**. **7i** is generated upon visible light ( $\lambda = 450$  nm) irradiation of **19i** in argon matrix at 4 K. Comparison of the experimental spectrum with DFT calculations at the (U)B3LYP-D3/def2-TZVP level of theory shows, the formation of T-**7i** and S-**7i**, and their two conformers. Annealing of such matrix for 10 minutes at higher temperatures in the range between 10 and 30 K results in a substantial change in the IR spectrum: bands of conformers of T-**7i** decreased in intensity and concurrently an increase of the absorptions of conformers of S-**7i**. When we keep the matrix at 3 K for several hours, it did not result in any interconversion of T-**7i** and S-**7i**. However, several minutes of UV irradiation ( $\lambda = 365$  nm) resulted in partial conversion of S-**7i** to T-**7i**, whereas upon irradiation with visible light ( $\lambda = 530$  nm) leads to conversion of T-**7i** to S-**7i**. Therefore, similar to the results obtained using EPR analysis described previously, here the IR experiments revealed that annealing of the matrix containing

conformers of **T-7i** and irradiation with visible light results in the formation of **S-7i**, which in turn can be restored by UV irradiation (Figure 33).

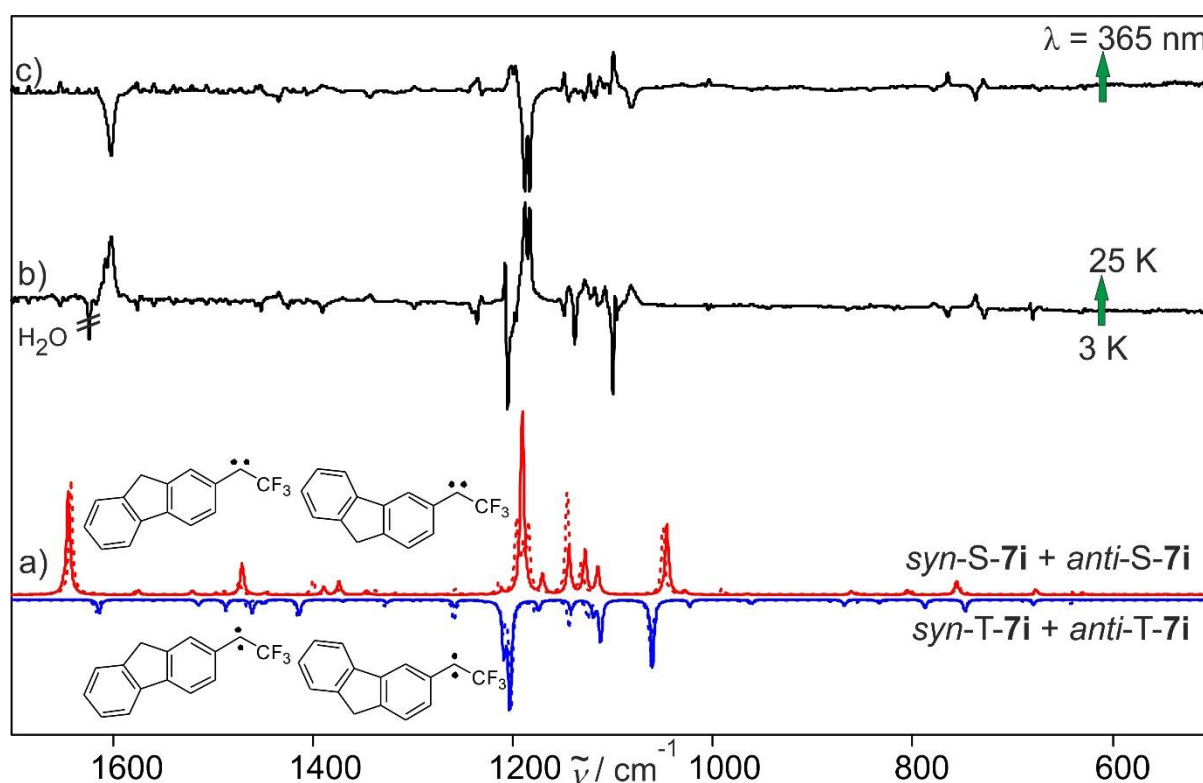


**Figure 33.** IR spectra showing the thermal interconversion of **T-7i** to **S-7i**. a) Superimposed spectrum showing the interconversion of **T-7i** (blue line) and **S-7i** (red line) calculated at the (U)B3LYP-D3/def2-TZVP level of theory (solid lines: *anti-T-7i* and *anti-S-7i*; dotted lines: *syn-T-7i* and *syn-S-7i*). Equal contributions of the two conformers, *syn* and *anti*, were used to simulate the IR spectrum. b) Difference spectrum at 3 K showing changes after 10 min annealing of an argon matrix containing both **T-7i** and **S-7i** at 25 K. Bands pointing downward, assigned to **T-7i**, are disappearing, and bands pointing upward, assigned to **S-7i**, are appearing. The S/T ratio is increased from about 41:59 to 63:37 due to annealing. c) Difference spectrum at 3 K showing changes after 10 min of 365 nm irradiation of the same matrix. Bands pointing downward, assigned to **S-7i**, are disappearing, and bands pointing upward, assigned to **T-7i**, are appearing. UV photolysis slightly changed the S/T ratio from 63:37 to 52:48.

### UV-vis spectroscopy

Similar experiments as described above were conducted with UV-vis spectroscopy (Figure 34). The UV-vis spectrum of **19i** in argon matrix shows a strong absorption band at 300 nm. Irradiation of **19i** with 365 nm produces strong broad bands at 322 and 396 nm and weak bands in the regions of 532 nm. A broad band with  $\lambda_{\text{max}} = 396$  nm increases in intensity after annealing at higher temperatures and decreases after 365 nm irradiation, and thus is assigned to **S-7i**. The triplet species **T-7i** shows absorption at 532 nm, and thus irradiation into this band results in the rearrangement of **T-7i** to **S-7i**. These observations are matching well with the EPR and IR analysis discussed before.

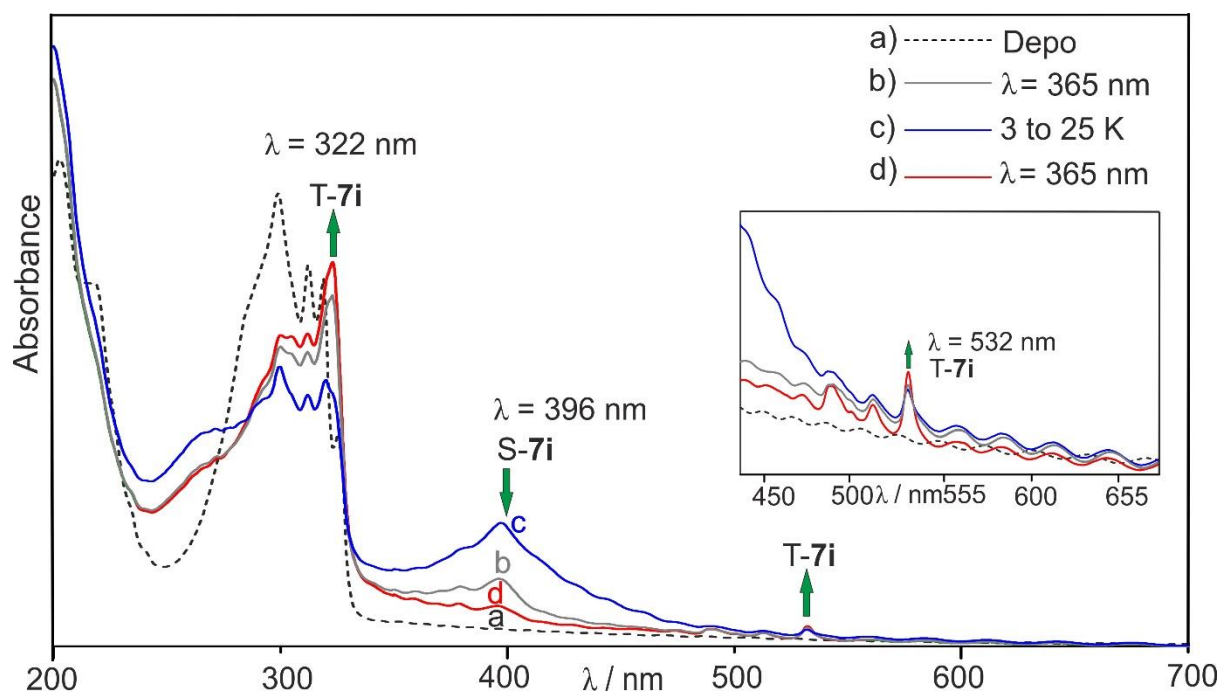
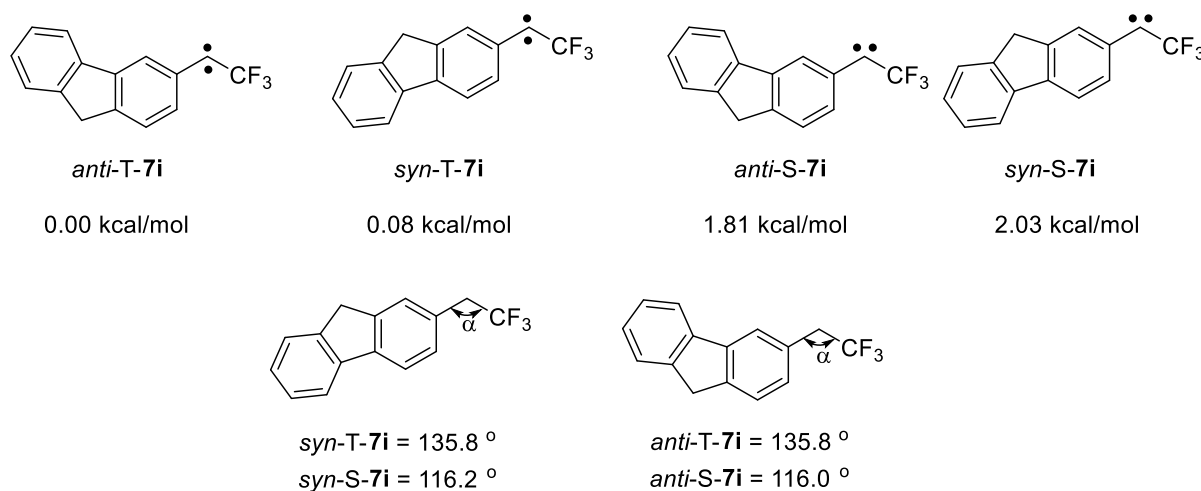


**Figure 34.** UV-vis spectra showing interconversion of T-7i, and S-7i by irradiation and annealing. a) UV-vis spectrum of **19i** isolated in argon matrix at 8 K (dotted line). b) UV-vis spectrum obtained after several hours of 365 nm irradiation of **19i** at 8 K (gray line). c) UV-vis spectrum of the same matrix after 10 min annealing to 25 K and cooling back to 8 K (blue line). d) UV-vis spectrum after subsequent 60 min irradiation with  $\lambda = 365$  nm (red line). The band of S-7i decreases, whereas those of T-7i increase during irradiation (indicated by green arrows). The weak band of T-7i in the visible region of the spectrum is shown in the inset.

### DFT calculations

The experimental results were supported by calculations at the (U)B3LYP-D3/def2-TZVP level of theory. As discussed before for carbenes **7b** and **7c**, the singlet and triplet states of carbenes mainly differ on their C-C-C bond angle at the carbene center. In addition, there are conformational changes that has to be considered for carbene **7i**, namely *sys* and *anti*, due to the CF<sub>3</sub> orientations (Scheme 11). The triplet state T-7i is estimated to be 1.81 – 2.03 kcal/mol more stable than S-7i. This is in qualitative agreement with the experiments indicating that the singlet state is slightly more stable than the triplet state.



**Scheme 11.** C–C–C bond angles at the carbene center and singlet–triplet splitting of **7i** calculated at the B3LYP-D3/def2-TZVP level of theory.

## Conclusion

In summary, the thermal and photochemical interconversion between the singlet and triplet states of aryl(trifluoromethyl)carbenes **7b**, **7c** and **7i** have been investigated in solid argon by EPR, IR and UV-vis spectroscopy as well as by quantum mechanical calculations.

These experiments demonstrated that carbenes **7b**, **7c** and **7i** could be isolated both in their lowest singlet and triplet states. At temperatures below 10 K, both spin states coexist indefinitely and can be interconverted by irradiation into the absorption maxima of singlets in the UV or triplets in the visible range, respectively. On the other hand, at temperatures above 10 K, it was shown a partial conversion of triplet to singlet states of **7b**, **7c** and **7i**; however, the reversed thermal interconversion of singlets into triplets is not observed, similar to **S-27**, which thermally does not rearrange to **T-27**.<sup>[118]</sup> According to our calculations, the singlet and triplet states of these carbenes are energetically nearly degenerate in the gas phase, in agreement with our experimental results. These results lead us to conclude magnetic bistability of carbenes is a general phenomenon that only depends on the S–T gap rather than the nature of the carbene.

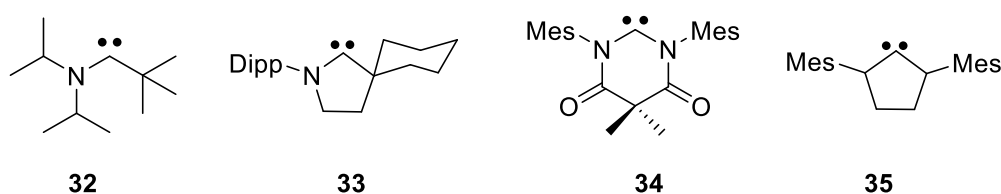
Parts of chapters 2 and 3 were "Reprinted (adapted) with permission from *J. Am. Chem. Soc.*, **2017**, 139 (35), pp 12310–12316. Copyright 2018 American Chemical Society."

## 4. Activation of ammonia by aryl(trifluoromethyl)carbenes

### Introduction

Since the hydrogenation of ethylene was reported by Sabatier and Senderens in 1897, catalytic transformation of inexpensive small molecules ( $\text{H}_2$ ,  $\text{NH}_3$ , etc) into useful compounds has received considerable interest from the scientific community.<sup>[126-128]</sup> However, the key role in these processes almost exclusively taken by transition metal-based catalysts, for which abundance, expense and toxicity are significant issues.<sup>[129]</sup> For some molecules like ammonia, the metal-based activation remains challenging since instead of cleavage of the strong N–H bond (~107 kcal/mol) of ammonia the formation of stable amine Werner-like adducts through binding via the nitrogen lone pair occurs.<sup>[130-131]</sup> Consequently, activation of ammonia by metal free methods has been a prime focus of investigation for the last few years.

Stable singlet amino carbenes which possess a pair of electrons in the  $\sigma$  orbital and an accessible empty  $\pi$  orbital, resembles to some extent the electron structure of transition metals. Recently, it has been shown that these carbenes can activate small molecules similar to transition metal complexes.<sup>[132]</sup> Moreover, while the metal center act as electrophile towards ammonia, the carbene behaves primarily as nucleophiles, thus in contrast to metals no formation of the Werner-like adducts is observed. These results were reported in a pioneering work by Bertrand *et al.* showing the potential of (alkyl)(amino) carbenes such as **32** and **33** for activating ammonia under ambient conditions.<sup>[133]</sup> Later, Bielawski *et al.* documented similar reactivity of ammonia with carbenes such as **34** and **35** with a nearly quantitatively yield.<sup>[134-135]</sup> Alternatively, catalysts based on main elements like P,<sup>[136]</sup> Si,<sup>[137]</sup> Ge,<sup>[138]</sup> or Sn<sup>[139]</sup> capable of ammonia activation have also been reported recently.



**Scheme 12.** Stable carbenes known to activate ammonia. Dipp = 2,6-diisopropylphenyl, Mes = 2,4,6-trimethylphenyl.

Generally, the mechanism of the insertion of carbenes into the N–H bond of amines is not well understood. Bethell *et al.* studied the reaction of diphenylcarbene **29** with amines in solution, and pointed out the involvement of an intermediate before formation of the formal N–H

insertion product.<sup>[140]</sup> Zupancic *et al.* documented similar reactivity of amines with fluorenylidene **30**.<sup>[141]</sup> Both authors assigned the intermediate to ylide, since they did not observe a kinetic isotopic effect in their reaction. It is noteworthy to mention that the authors did not observe formation of an ylide derived from primary amines by LFP, although they assign the ylide derived from tertiary amines. These results were supported in a theoretical work by Pople *et al.*, who calculated the potential energy surface for the reaction of methylene with ammonia to form an ylide without an activation barrier.<sup>[142]</sup>

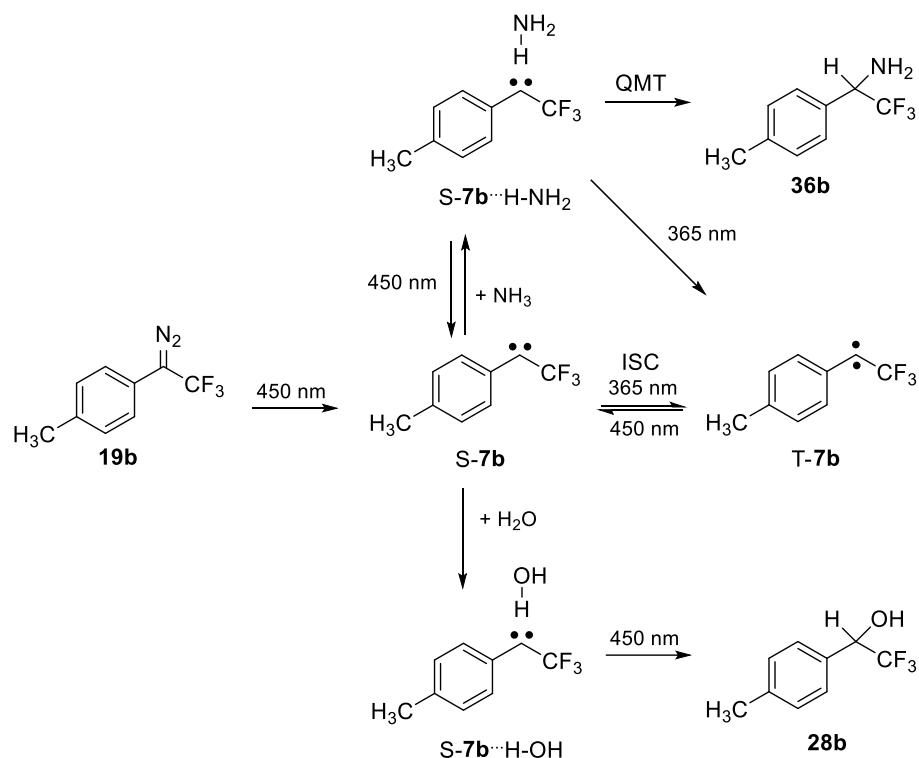
An alternative pathway for the reaction between carbenes and solvent molecules in two step-processes via formation of a hydrogen-bonded complex have recently been reported in a series of experiments by our group.<sup>[125, 143-144]</sup> The conclusion from these studies is that the highly polar singlet carbenes are stabilized by hydrogen bonding with the solvent molecules giving a hydrogen-bonded complex as an intermediate. In some cases, this complex is only metastable even at cryogenic temperatures and rearrange to form the formal X–H insertion product via quantum mechanical tunneling (QMT).

In the previous chapters, carbenes **7b** and **7c** were shown to be easily generated by visible-light photolysis (450 nm) of **19b** and **19c**, respectively, under the conditions of matrix isolation in rare gases, and are stable towards prolonged irradiations. Under these conditions, **7b** and **7c** are isolated in a mixture of their lowest singlet and triplet states. We have also described the formation of S-**7b**···H–OH and S-**7c**···H–OH in argon matrices doped with 1% water molecules. Because of its fundamental importance, here, we report similar experiments of the reaction of carbenes **7b** and **7c** in argon/xenon matrices doped with 1% ammonia (NH<sub>3</sub>/ND<sub>3</sub>). In addition, the carbenes presented here are generated in amorphous ammonia ices at cryogenic temperatures to explore the stability of the carbenes in a reactive, Lewis-basic medium.

## Results and discussion

### Reaction of *p*-tolyl(trifluoromethyl)carbene in argon matrices doped with 1% of ammonia

To study the reaction of carbene **7b** with ammonia, the experiments of the reaction of **7b** with water were used as reference (see details in Chapter 3).<sup>[125, 143-144]</sup> The main findings of the experiments with ammonia and water are compiled in Scheme 13.



**Scheme 13.** Synthesis and reactions of *p*-tolyl(trifluoromethyl)carbene **7b** with water and ammonia.

### EPR spectroscopy

Visible-light irradiation of matrix-isolated **19b** in argon doped with 1% of  $\text{NH}_3$  at 4 K results in the EPR spectrum of **T-7b** with ZFS parameters  $|D/hc| = 0.5259 \text{ cm}^{-1}$  and  $|E/hc| = 0.0304 \text{ cm}^{-1}$  (Figure 35). In addition, well-defined signals in the radical regions are observed, which are assigned to the  $\text{NH}_2$  radicals based on its characteristics hyperfine coupling pattern that was previously reported in literatures (Figure 35 inset, and Figure A2 in the Appendix).<sup>[145]</sup> To allow the diffusion of ammonia, the matrix was annealed at 25 K for 10 minutes and cooled back to 4 K. A loss of 52% of the triplet signal is observed and no other paramagnetic species are formed, suggesting the formation of the EPR silent hydrogen-bonded complex between the singlet carbene **S-7b** and ammonia (**S-7b**... $\text{H-NH}_2$ ). When the matrix is kept in the dark for several hours at 4 K, a new paramagnetic species centered at 3425 G (Figure 36) is formed, while no change in the signals of the triplet carbene is observed. This new species is assigned to the triplet radical-pair **37**, and small *D* and *E* values of  $0.0310 \text{ cm}^{-1}$  and  $0.0002 \text{ cm}^{-1}$  respectively, are obtained, which are a typical for radical-pairs.<sup>[125]</sup> As expected for radical-pairs, subsequent warming of the matrix at 25 K results in the disappearance of this new species, attributed to recombination as a result of the higher mobility of **37** at higher

temperatures. To explain the source of this radical-pair signal we proposed the pathways presented in Scheme 14.

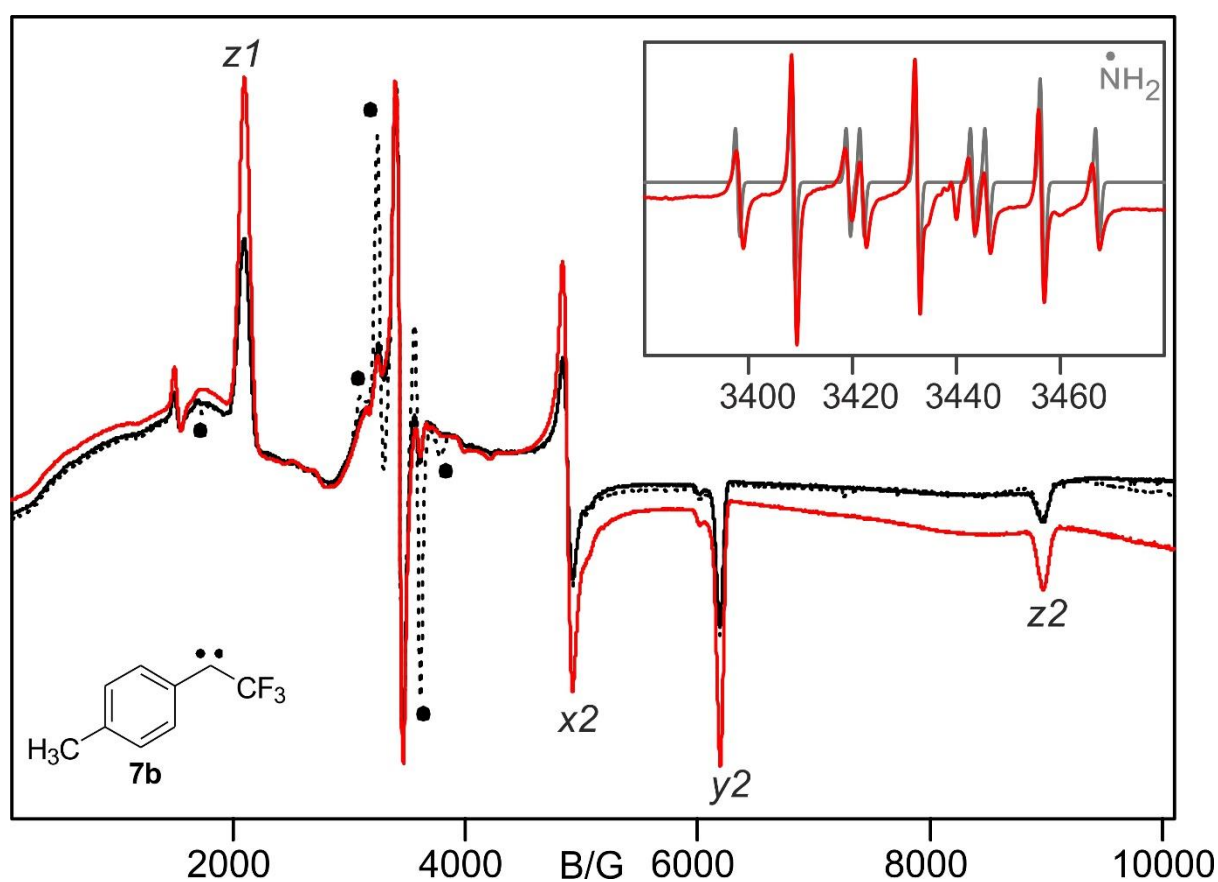


**Figure 35.** X-band CW EPR spectra showing the reaction of carbene **7b** with ammonia. Red line: Spectrum of **7b** in argon doped with 1% of NH<sub>3</sub> at 4 K. Solid black line: Spectrum of the same matrix after annealing to 25 K for 10 min and cooling back to 4 K. Dashed black line: Spectrum obtained after keeping the same matrix at 4 K for 16 hrs. Bands marked with black dots are assigned to the radical pair (see expanded region in Figure 36). Inset shows the radical region together with a simulated spectrum of NH<sub>2</sub> radical ( $\mu = 9.6280$  GHz;  $g_{iso} = 2.004$ ;  $A_1 = 67.3$ ,  $A_2 = 29.6$  and  $A_3 = 30.2$  MHz) (see Figure A2 in the Appendix for details).

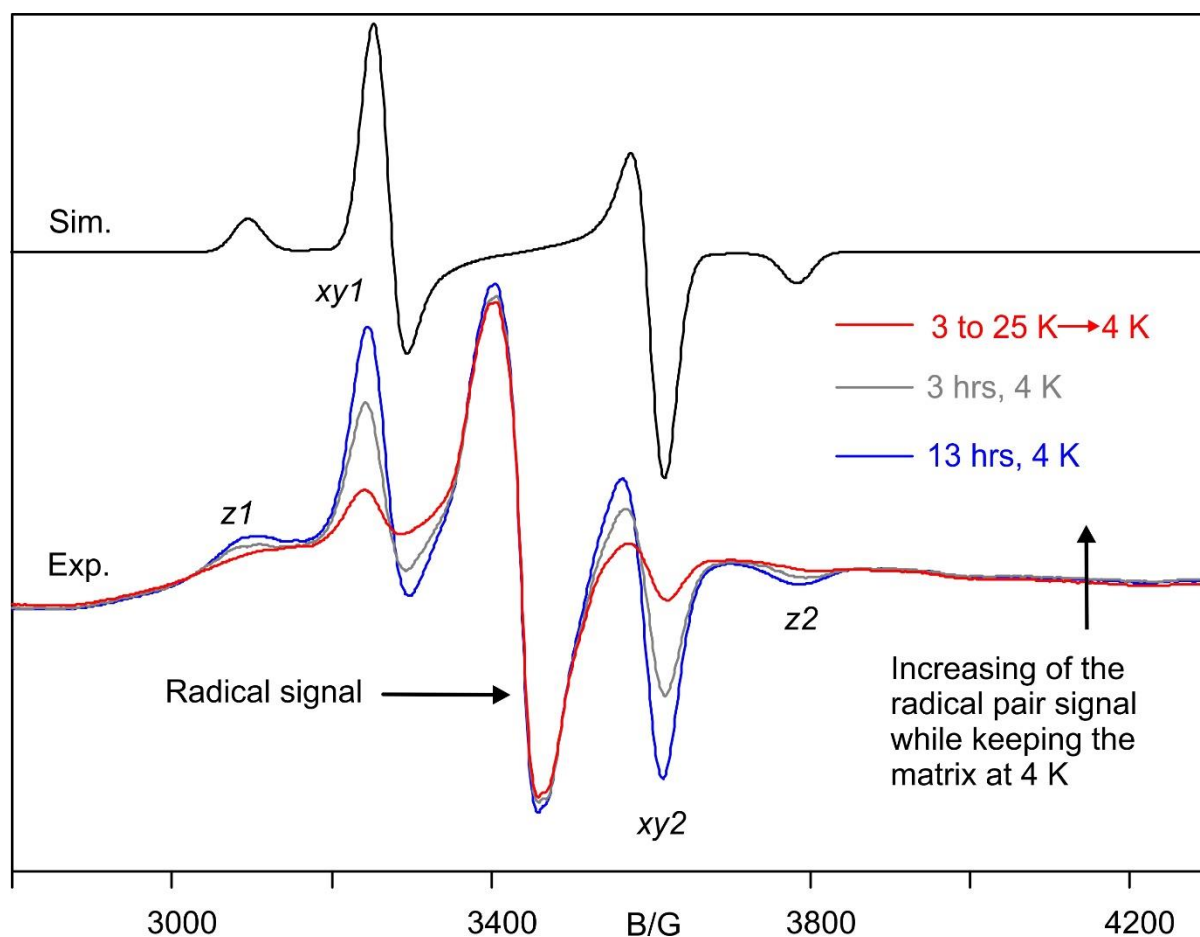
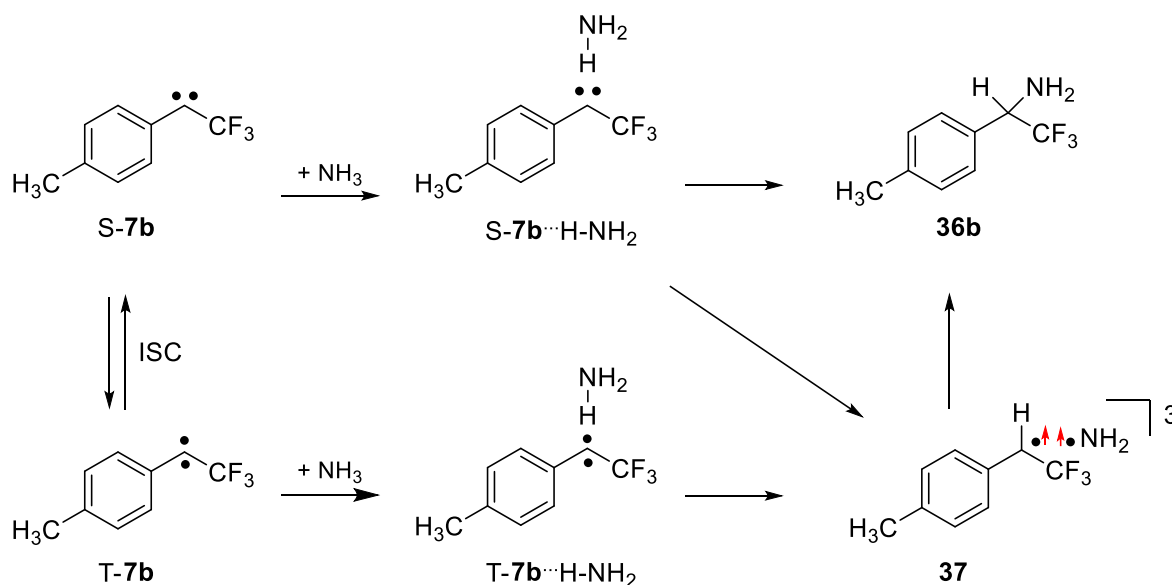


**Figure 36.** X-band CW EPR spectra showing the increasing of the radical-pair signal **37** after keeping the carbene-ammonia matrix in darkness at 4 K. Red line: Spectrum obtained after warming a matrix containing carbene **T-7b** and ammonia from 4 to 25 K for 10 minutes and cooled down to 4 K. Green line: Spectrum obtained after keeping the same matrix at 4 K for 3 hrs. Blue line: Spectrum obtained after keeping the same matrix at 4 K for 13 hrs. Black line: Simulated spectrum with  $|D/hc| = 0.0310 \text{ cm}^{-1}$  and  $|E/hc| = 0.0002 \text{ cm}^{-1}$ .



**Scheme 14.** Proposed mechanism of reaction of **7b** with ammonia.

## UV-vis spectroscopy

As described in Chapter 3, T-**7b** and S-**7b** can easily be distinguished based on their UV-vis spectra, which shows a series of absorptions stretching from 250 to 450 nm in rare gas matrices at 8 K. The UV-vis spectrum of **7b** in argon matrix with 1% NH<sub>3</sub> at 3 K also show the formation of triplet and singlet state with characteristics absorptions at 304 and 326 nm, respectively. A broad band at  $\lambda = 326$  nm increases upon warming of the matrices to 25 K, but decreases when keeping the matrix in darkness at 8 K for several hours, and thus assigned to S-**7b**···H-NH<sub>2</sub> complex (Figure 37). This assignment is in good agreement with the observation from IR and EPR experiments. However, the radical-pair **37** observed by EPR and the formal insertion product **36b** are not detected under these conditions, which might be overlaid by intense signals of unreacted T-**7b** or the yield might not be high enough to be detected with UV-vis spectroscopy.

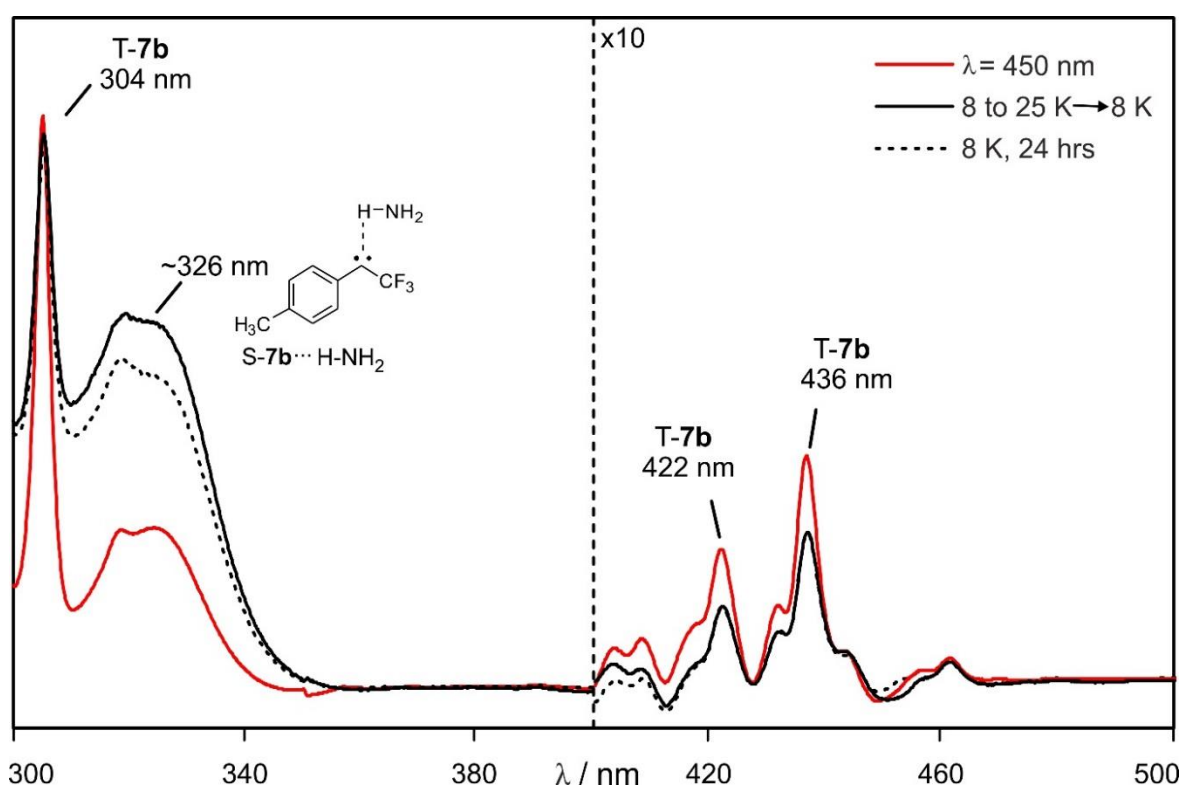


**Figure 37.** UV-vis spectra showing the reaction of carbene **7b** with ammonia. Red line: Spectrum of **7b** in argon doped with 1% of NH<sub>3</sub> at 8 K. Solid black line: Spectrum of the same matrix after annealing to 25 K for 10 min and cooling back to 4 K. Dashed black line: Spectrum obtained after keeping the same matrix at 8 K for 24 hrs.

## IR spectroscopy

To gain more insight into the mechanism of the reaction between carbene **7b** and ammonia, similar experiments were performed using IR spectroscopy. Visible-light irradiation of **19b** in

argon doped with 1% of NH<sub>3</sub> resulted in the formation of T-**7b** and S-**7b** with characteristics IR absorptions at 1160 and 1172 cm<sup>-1</sup>, respectively (Figures 38–40). In addition, very strong bands of NH<sub>3</sub> are observed with characteristics absorptions at 972 ( $\nu_2$ ), 1631 ( $\nu_4$ ), 3436 ( $\nu_1$ ) and 3436 ( $\nu_3$ ) cm<sup>-1</sup>. Annealing at 25 K for 10 min allows the NH<sub>3</sub> to diffuse in the argon matrices, which can be easily followed in the IR spectra by observing its dimers and higher aggregates (Figure 39).<sup>[146]</sup> Additionally, all IR bands assigned to T-**7b** decrease in intensity, while a set of bands at 1089, 1141, 1173, 1208 and 1600 cm<sup>-1</sup> increases, which is assigned to the ammonia complex S-**7b**···H–NH<sub>2</sub>. The assignment of the new bands to S-**7b**···H–NH<sub>2</sub> is based on the IR absorptions of the free singlet carbene S-**7b** and comparison to signals of the water complex S-**7b**···H–OH (see details in Chapter 3). Compared to S-**7b**, the IR bands of the S-**7b**···H–NH<sub>2</sub> complex are blue-shifted by 0.5 – 2 cm<sup>-1</sup>, as expected for a hydrogen-bonded complex between the singlet carbene and ammonia. The S-**7b**···H–NH<sub>2</sub> complexes is only metastable and reacts to the NH<sub>2</sub> insertion product in darkness at cryogenic temperatures (Table 13 and Figure 39, see Kinetics section). However, in contrast to the photochemistry of S-**7b**···H–OH described before, which resulted in the formation of the formal OH insertion product, photolysis of the S-**7b**···H–NH<sub>2</sub> breaks the complex and giving back the free triplet/singlet carbenes, depending on the light source used for the photolysis. These results suggest that, compared to water, the weaker Lewis-acid ammonia forms a weaker hydrogen-bonded complex with strongly basic carbene S-**7b**.

**Table 13.** Experimental and calculated vibrational frequencies and shifts of the S-**7b**···H–OH and S-**7b**···H–NH<sub>2</sub> complexes.

Calculated <sup>[a]</sup> v/cm <sup>-1</sup> (I <sub>abs</sub> )	S- <b>7b</b> <sup>[b]</sup> v/cm <sup>-1</sup> (I <sub>rel</sub> )	S- <b>7b</b> ···H–OH <sup>[c]</sup> v/cm <sup>-1</sup> (I <sub>rel</sub> )	Shift <sup>[d]</sup>	S- <b>7b</b> ···H–NH <sub>2</sub> <sup>[e]</sup> v/cm <sup>-1</sup> (I <sub>rel</sub> )	Shift <sup>[d]</sup>	Assignment <sup>[f]</sup>
1052.9 (259.7)	1086.7 (32)	1095.3 (40)	+8.6 (+13.4)	1088.7 (60)	+2.0 (+1.7)	C–CF <sub>3</sub> bend
1120.2 (142.7)	1139.2 (39)	1147.5 (50)	+8.3 (+9.1)	1140.5 (40)	+1.4 (+1.8)	C–CF <sub>3</sub> bend
1179.6 (719.6)	1171.7 (100)	1178.6 (100)	+6.9 (+6.7)	1173.2 (100)	+1.5 (+0.5)	C–C–C str.
1227.8 (18.8)	1206.4 (44)	1211.1 (86)	+4.7 (+3.2)	1207.5 (80)	+1.1 (+3.1)	C–H def.
1640.3 (245.9)	1599.5 (43)	1602.2 (75)	+2.7 (+3.4)	1599.9 (72)	+0.4 (+2.2)	C=C str.

[a] Calculated at the B3LYP-D3/def2-TZVP level of theory. [b] In argon matrix at 3 K. [c] In argon matrix doped with 1% of H<sub>2</sub>O at 3 K. [d] Frequency shift relative to the monomers (values within parenthesis refer to the calculated shifts). [e] In argon matrix doped with 1% of NH<sub>3</sub> at 3 K. [f] Tentative assignment.

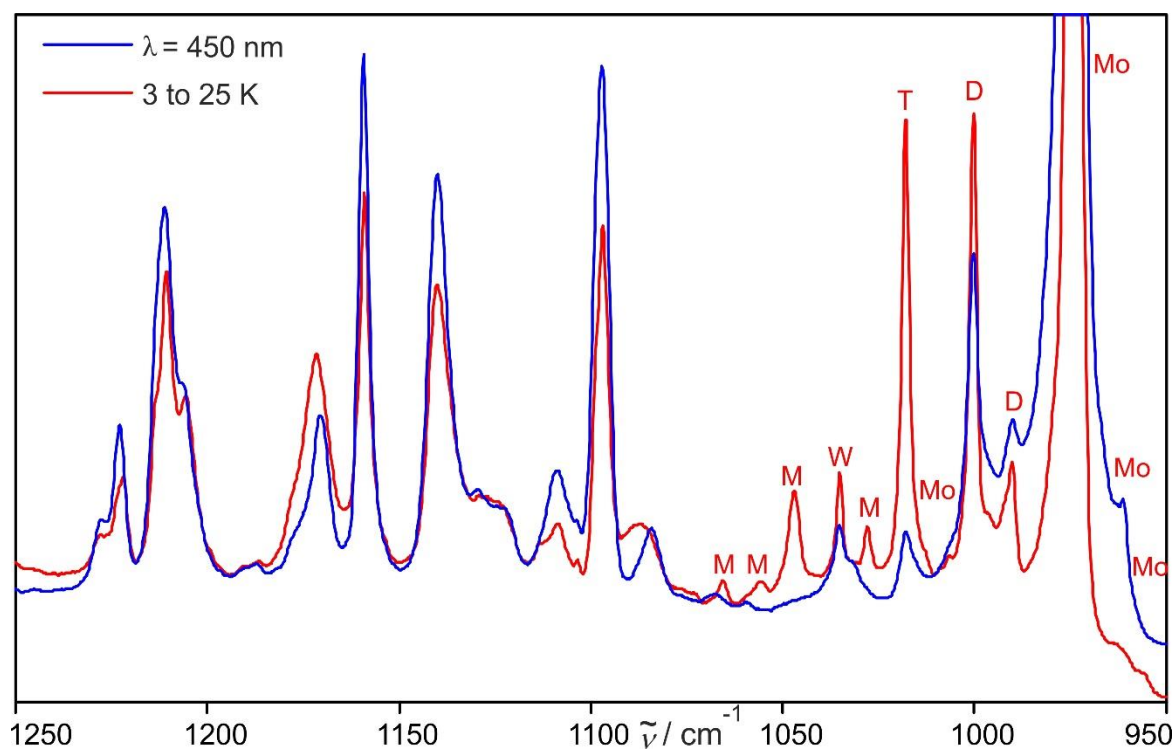


**Figure 38.** IR spectra of the ammonia complex  $S-7b \cdots H-NH_2$  matrix-isolated in argon at 3 K. (a) IR spectrum of  $S-7b$  obtained after photolysis ( $\lambda = 450$  nm) of  $19b$  in argon doped with 1% ammonia (blue line). (b) IR spectrum of the same matrix showing changes after 10 min annealing to 25 K and cooled back to 3 K (red line). Bands of  $S-7b \cdots H-NH_2$ , ammonia dimers (D), trimers (T), multimer (M) are appearing whereas bands of  $T-7b$  and ammonia monomer (Mo) are decreasing.

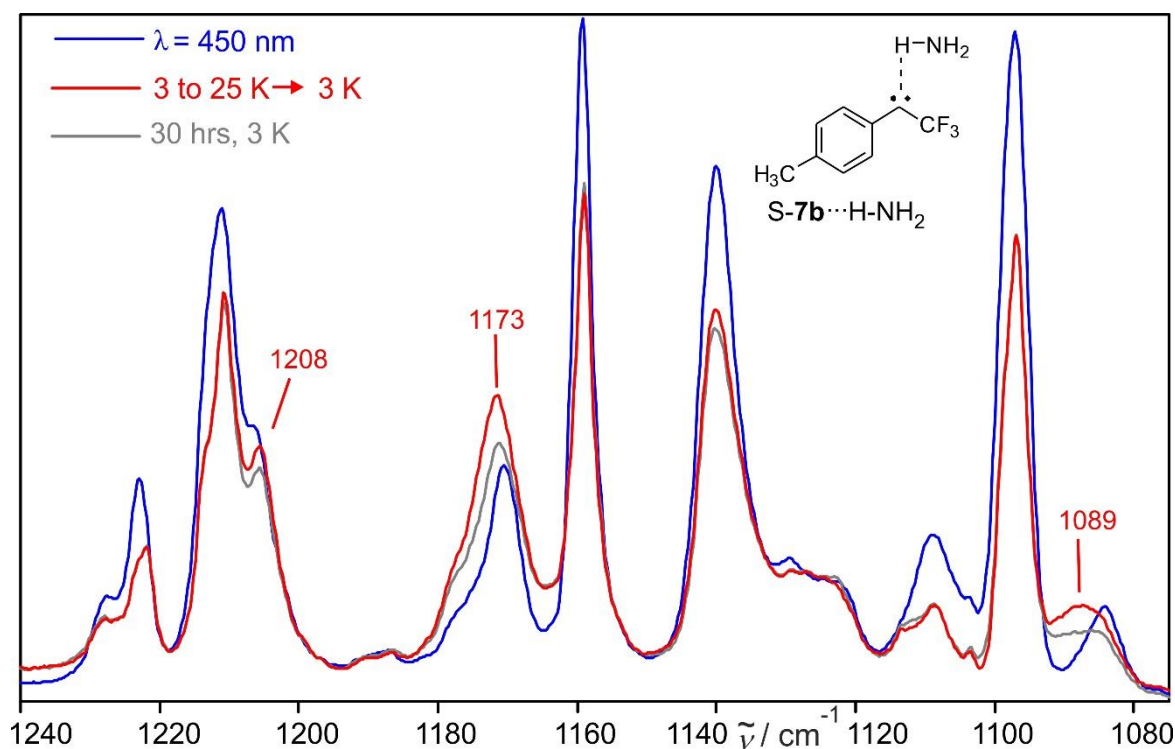


**Figure 39.** IR spectra showing the formation and destruction of the ammonia complex  $S-7b \cdots H-NH_2$ . (a) IR spectrum of  $S-7b$  obtained after photolysis ( $\lambda = 450$  nm) of  $19b$  in argon doped with 1% ammonia (blue line). (b) IR spectrum of the same matrix showing changes after 10 min annealing to 25 K and cooled back to 3 K (red line). (c) IR spectrum of the same matrix showing changes after keeping the matrix at 3 K for 30 hours (gray line).

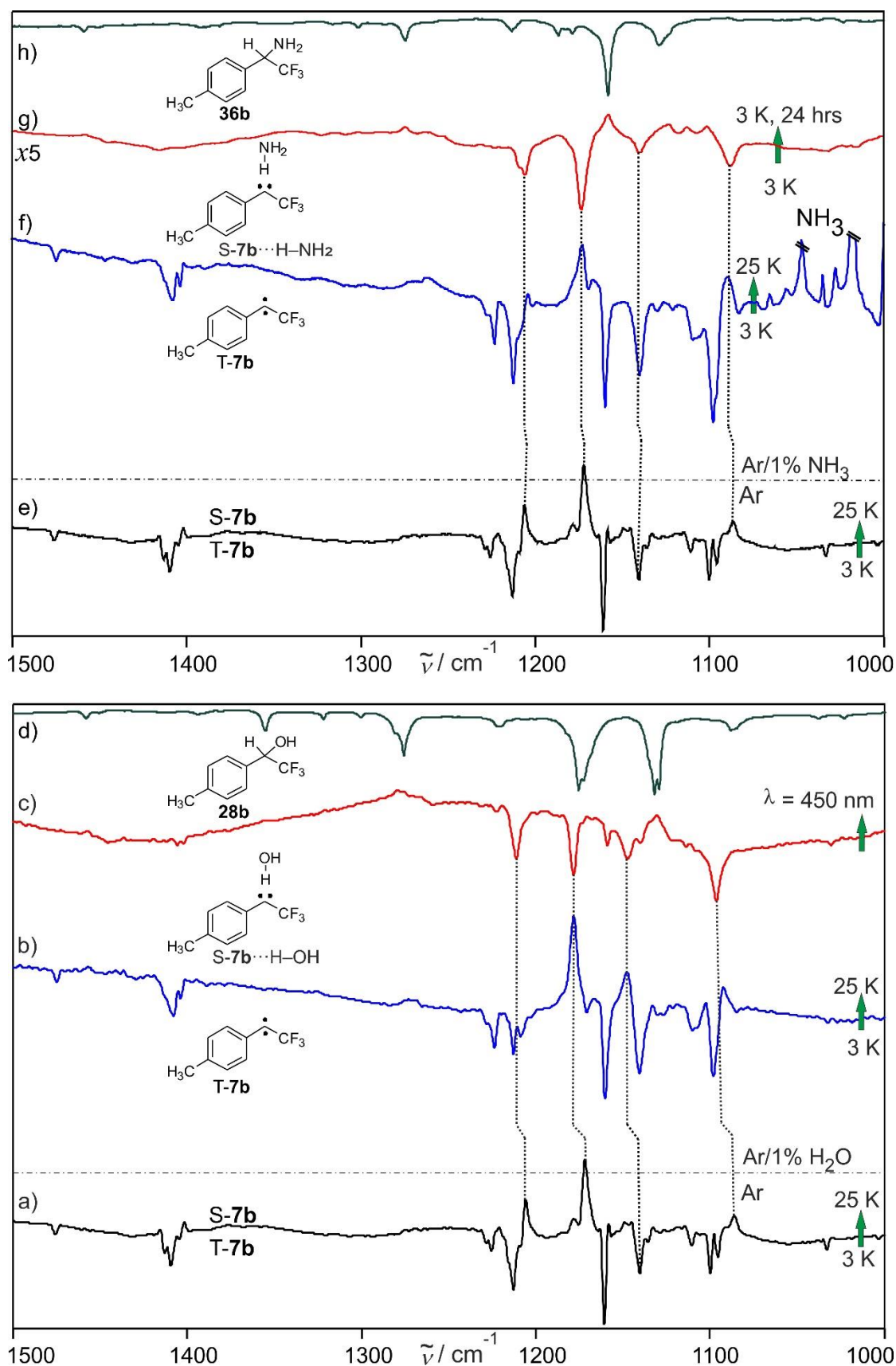


**Figure 40.** IR spectra of the water complex  $S-7b \cdots H-OH$  and ammonia complex  $S-7b \cdots H-NH_2$  matrix-isolated in argon. (a) Difference IR spectrum showing changes of an argon matrix (without water) containing  $T-7b$  and  $S-7b$  at 3 K after annealing for 10 min at 25 K (black line). Bands pointing downward, assigned to  $T-7b$  are disappearing, and bands pointing upward, assigned to  $S-7b$  are appearing. (b) Difference IR spectrum of a similar

experiment in argon doped with 1% of water (blue line). Bands pointing downward are disappearing and assigned to **T-7b**, bands pointing upward are appearing and assigned to **S-7b**···H-OH. (c) Difference IR spectrum of the same matrix showing changes after 3 h irradiation ( $\lambda = 450$ ) (blue line). Bands pointing downward are assigned to **S-7b**···HOH, and bands pointing upward are assigned to *p*-tolyl(trifluoromethyl)ethanol **28b**. (d) Reference spectrum of **28b** matrix-isolated in argon at 3 K. (e) Difference IR spectrum showing changes of an argon matrix (without ammonia) containing **T-7b** and **S-7b** at 3 K after annealing for 10 min at 25 K (black line). Bands pointing downward, assigned to **T-7b**, are disappearing, and bands pointing upward, assigned to **S-7b**, are appearing. (f) Difference IR spectrum of a similar experiment in argon doped with 1% of ammonia (blue line). Bands pointing downward are disappearing and assigned to **T-7b**, bands pointing upward are appearing and assigned to **S-7b**···H-NH<sub>2</sub>. (g) IR spectrum of the same matrix showing changes after keeping the matrix at 3 K for 24 hours. Bands pointing downward are assigned to **S-7b**···HNH<sub>2</sub>, and bands pointing upward are assigned to *p*-tolyl(trifluoromethyl)ethanamine **36b**. (h) Reference spectrum of **36b** matrix-isolated in argon at 3 K.

In similar experiments, **S-7b**···D-ND<sub>2</sub> was observed upon annealing of an argon matrix doped with 1% of ND<sub>3</sub> containing the carbene at 25 K (Figure 41). However, in contrast to **S-7b**···H-NH<sub>2</sub>, **S-7b**···D-ND<sub>2</sub> is stable at 3 K and does not give to the ND<sub>3</sub> insertion product. This isotope effect indicates that the insertion reaction is assisted by QMT, and furthermore allows to rule out the formation of ylide **39c** as an intermediate under our experimental conditions (Scheme 15).

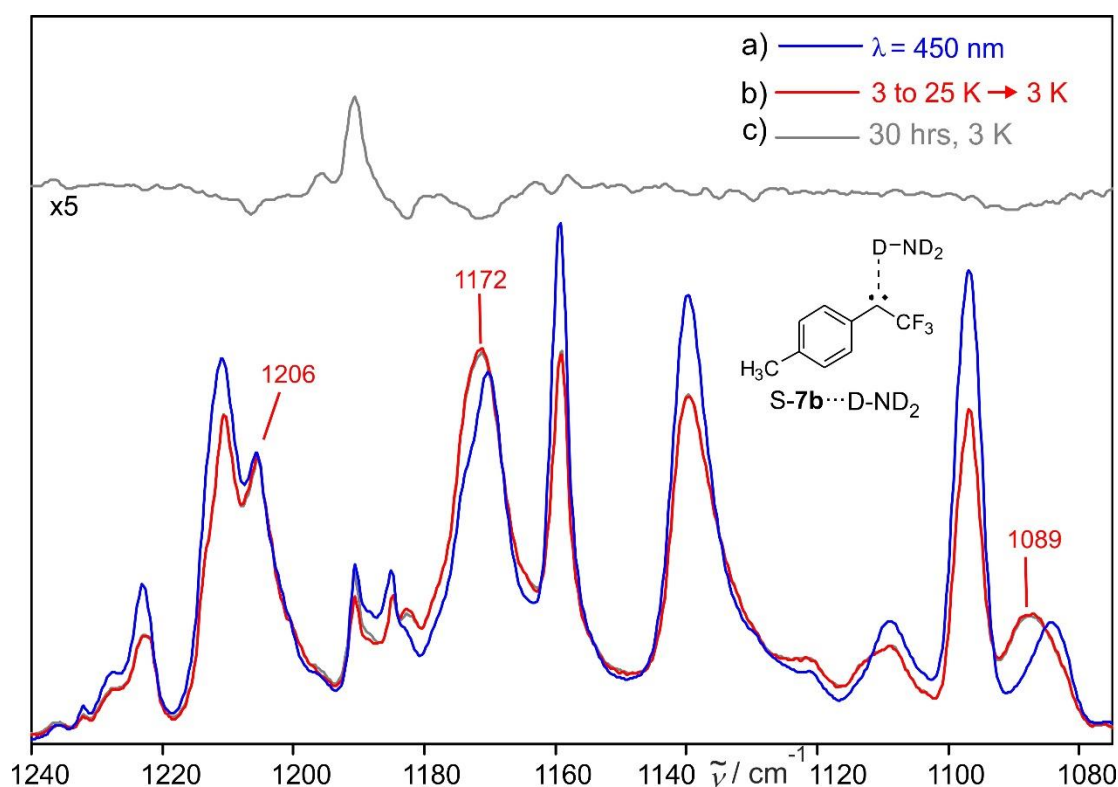
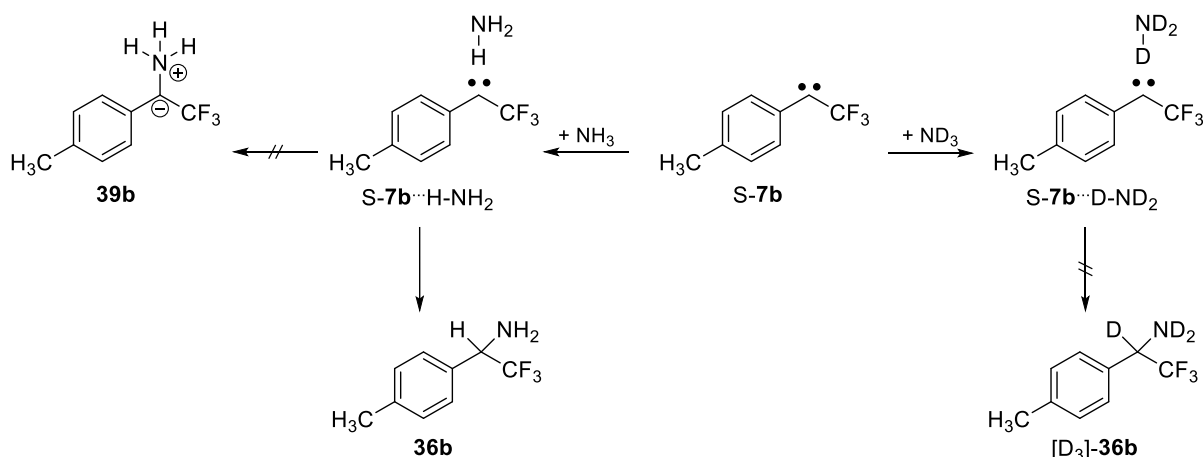


**Figure 41.** IR spectra of the ammonia complex **S-7b**···D-ND<sub>2</sub> matrix-isolated in argon at 3 K. (a) IR spectrum of **S-7b** obtained after photolysis ( $\lambda = 450$  nm) of **19b** in argon doped with 1% D<sub>3</sub>-ammonia (blue line). (b) IR spectrum of the same matrix showing changes after 10 min annealing to 25 K (red line). Bands assigned to **S-7b**···DND<sub>2</sub> are increasing whereas those bands assigned to **T-7b** are decreasing due to annealing. (c) IR spectrum of the same matrix showing no changes after keeping the matrix at 3 K for 30 hours. The difference spectrum is shown on top of the spectra to show that the complex is stable at 3 K for several hours. The band in the region of 1190 cm<sup>-1</sup> belongs to ND<sub>3</sub> ( $\nu_4$ ).



**Scheme 15.** Reaction of *p*-tolyl(trifluoromethyl)carbene **7b** with  $\text{NH}_3$  and  $\text{ND}_3$ .

### DFT calculations

To gain more insight into the mechanism of the reaction between **7b** and ammonia, we perform DFT calculations at the B3LYP-D3/6-311++G(d,p) level of theory as well as CCSD(T)/cc-pVDZ//B3LYP-D3/6-311++G(d,p) (Figure 42). The strongly basic, highly polar singlet carbene S-**7b** is stabilized by hydrogen bonding with Lewis acidic solvents, whereas T-**7b** is much less polar, and thus only weakly interacts with these solvents. Compared with water, ammonia is a weaker Lewis acid, and therefore is expected to interact weakly with S-**7b**. This is confirmed by DFT calculations: S-**7b** is stabilized by hydrogen bonding with ammonia by  $-5.3$  kcal/mol compared to water by  $-9.1$  kcal/mol at the same level of theory. On the other hand T-**7b** forms a weak van der Waals complex with both ammonia and water, stabilized by  $-3.3$  and  $-3.4$  kcal/mol, respectively. These values are close to the stabilization energy of S-**7b** ( $-7.0$ ) and T-**7b** ( $-4.2$ ) by ammonia calculated at the CCSD(T)/cc-pVDZ//B3LYP-D3/6-311++G(d,p) level of theory (Figure 42). In summary, computational studies in the gas phase predicts that a single molecule of water and ammonia stabilizes S-**7b** to make it thermodynamically more stable than T-**7b**, in an excellent agreement with the experimental results.

The DFT calculations could also be used to rationalize the thermal stability of the water and ammonia complexes with **7b**. The intrinsic reaction coordinate (IRC) of the rearrangement of the water complex S-**7b** $\cdots\text{H-OH}$  to the formal insertion product **28b** shows a concerted reaction with activation barrier of  $9.2$  kcal/mol, explaining the higher thermal stability of S-**7b** $\cdots\text{H-OH}$ . With the same approach, unfortunately, all our efforts to find the transition state (TS) that connects the singlet ammonia complex S-**7b** $\cdots\text{H-NH}_2$  and the insertion product **36b**

is not materialized. Note that, we are able to find the TS for other carbene-ammonia complexes, it is only a problem for CF<sub>3</sub> carbenes **7a-7c**. Surprisingly, if we insert strong electron donating group in the para position for CF<sub>3</sub> carbenes, for example for *p*-methoxyphenyl (trifluoromethyl)carbene **7e**, we are able to get the TS connecting the complex and the insertion product. Thus, high level calculation might be required to rationalize the thermal reactivity of S-**7b**···H-NH<sub>2</sub>.

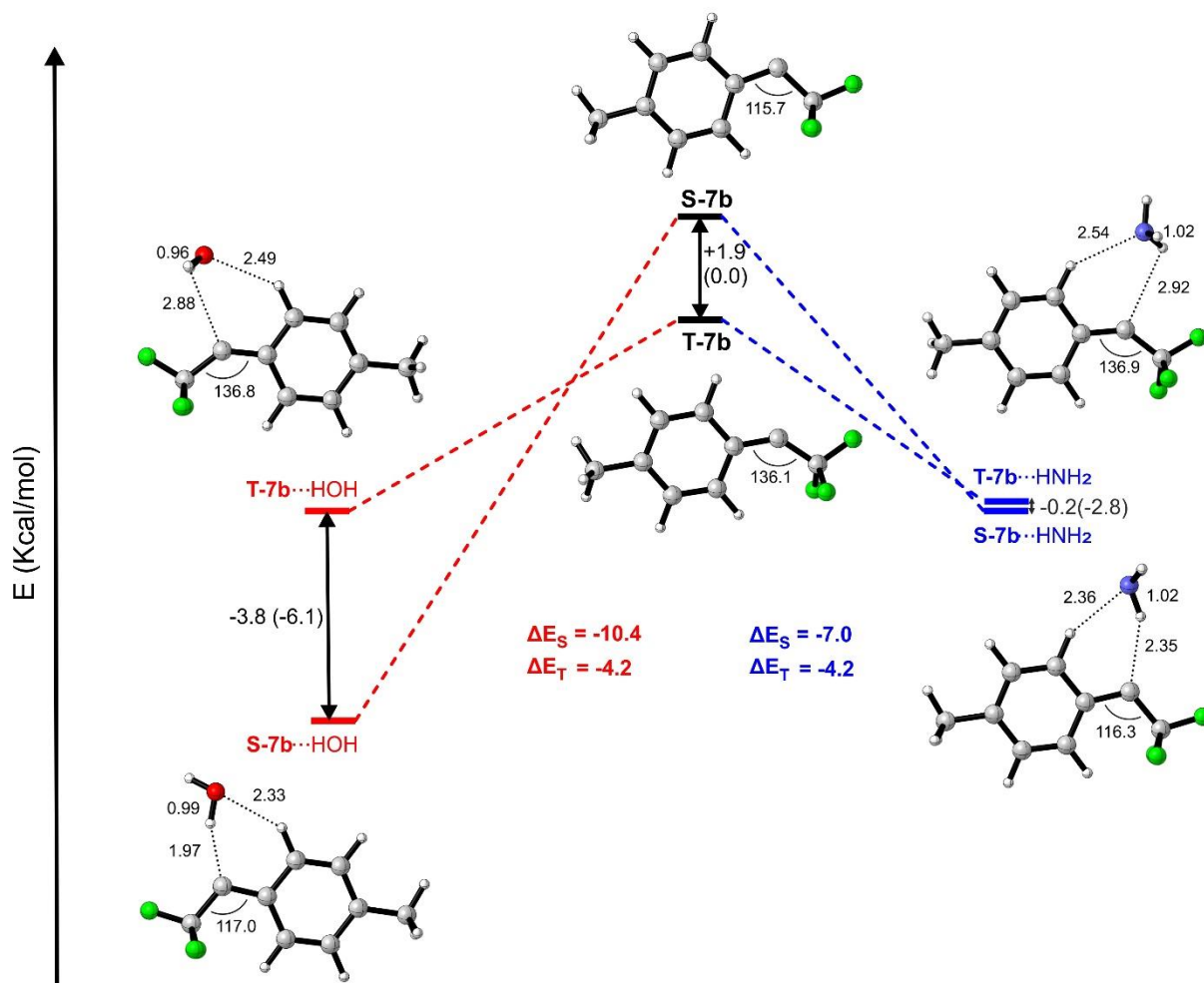


**Figure 42.** Relative energies of S-**7b**, T-**7b** and their most stable complexes with water (red) and ammonia (blue). Calculations performed at the B3LYP-D3/6-311++G(d,p) and CCSD(T)/cc-pVDZ//B3LYP-D3/6-311++G(d,p) (in parenthesis) levels of theory. DFT values are ZPVE corrected.  $\Delta E_S$  and  $\Delta E_T$  refers to the binding energies for singlet and triplet complexes, respectively. The bond angles at the carbene center (in degree) and the C···H-X distances (in Å) are also shown in the figure.

## Kinetics

The results of EPR, UV-vis and IR demonstrated that the insertion of carbenes into N-H bond of ammonia proceeds in two step process via forming a strong hydrogen-bonded complex (S-**7b**···H-NH<sub>2</sub>). Once formed, this complex is metastable and rearranged slowly to the formal

N–H insertion product **36b** even at low temperatures of 3 K. In general, reactions that occur at such low temperatures must have a very small activation barrier. However, as mentioned above, a transition state that connects **S-7b**···H–NH<sub>2</sub> and **36b** was not found, and thus a theoretical value of the activation barrier of this rearrangement is not obtained. Nevertheless, the fact that the reaction could not proceed instantaneously at 3 K suggested the activation energy (*E<sub>a</sub>*) is a few kcal/mol. Thus, this rearrangement is likely to involve QMT, as there is not enough thermal energy available to proceed the reaction at such low temperatures at 3 K.

To explain this, experiments at 3, 8 and 12 K in argon as well as at 20 K in xenon doped ammonia matrices were carried out. Assuming a pseudo first order reaction (E1), a reaction rate of  $2.5 \pm 0.5 \times 10^{-5} \text{ s}^{-1}$  was found for the rearrangement of **S-7b**···H–NH<sub>2</sub> to **36b** between 3 and 20 K (Table 14 and Figure 43). Hence, the rearrangement is independent of temperature in this range, strongly indicating a tunneling reaction. On the other hand, **S-7b**···D–ND<sub>2</sub> is stable under our experimental conditions at 3 K, indicating a very large kinetic isotope effect (KIE) as expected for a tunneling reaction. Compared to the water complex, for which a very slow reaction is observed, the tunneling rate in the ammonia complex is at least 3 orders of magnitude faster (Table 14). This is presumably due to the higher barrier for the OH insertion product of **S-7b**···H–OH (9.2 kcal at the B3LYP-D3/6-311++g(d,p) level of theory) compared to that of **S-7b**···H–NH<sub>2</sub> (not known).

**Table 14.** Rate constants as fitted to E1 (with  $\beta = 0.75$ ) for the insertion of aryl(trifluoromethyl)carbenes into NH<sub>3</sub>, ND<sub>3</sub> and H<sub>2</sub>O under different experimental conditions.

Carbene	Host	Temperature (K)	Time (h)	Cutoff filter (cm <sup>-1</sup> )	k (×10 <sup>-5</sup> )
<b>7b</b>	Ar/NH <sub>3</sub>	3	30	-	2.3 ± 0.1
	Ar/NH <sub>3</sub>	3	24	4000	2.5 ± 0.1
	Ar/NH <sub>3</sub>	3	70	4000	2.2 ± 0.1
	Ar/NH <sub>3</sub>	3	26	1600	2.7 ± 0.1
	Ar/NH <sub>3</sub>	8	51	-	2.5 ± 0.2
	Ar/NH <sub>3</sub>	12	32	-	3.0 ± 0.1
	Xe/NH <sub>3</sub>	20	45	-	2.9 ± 0.1
	Ar/ND <sub>3</sub>	3	30	-	No reaction
	Ar/H <sub>2</sub> O	3	76	-	0.0084 ± 1
<b>7c</b>	Ar/NH <sub>3</sub>	3	30	-	3.4 ± 0.1
	Ar/ND <sub>3</sub>	3	20	-	No reaction
	Ar/H <sub>2</sub> O	3	50	-	0.019 ± 1

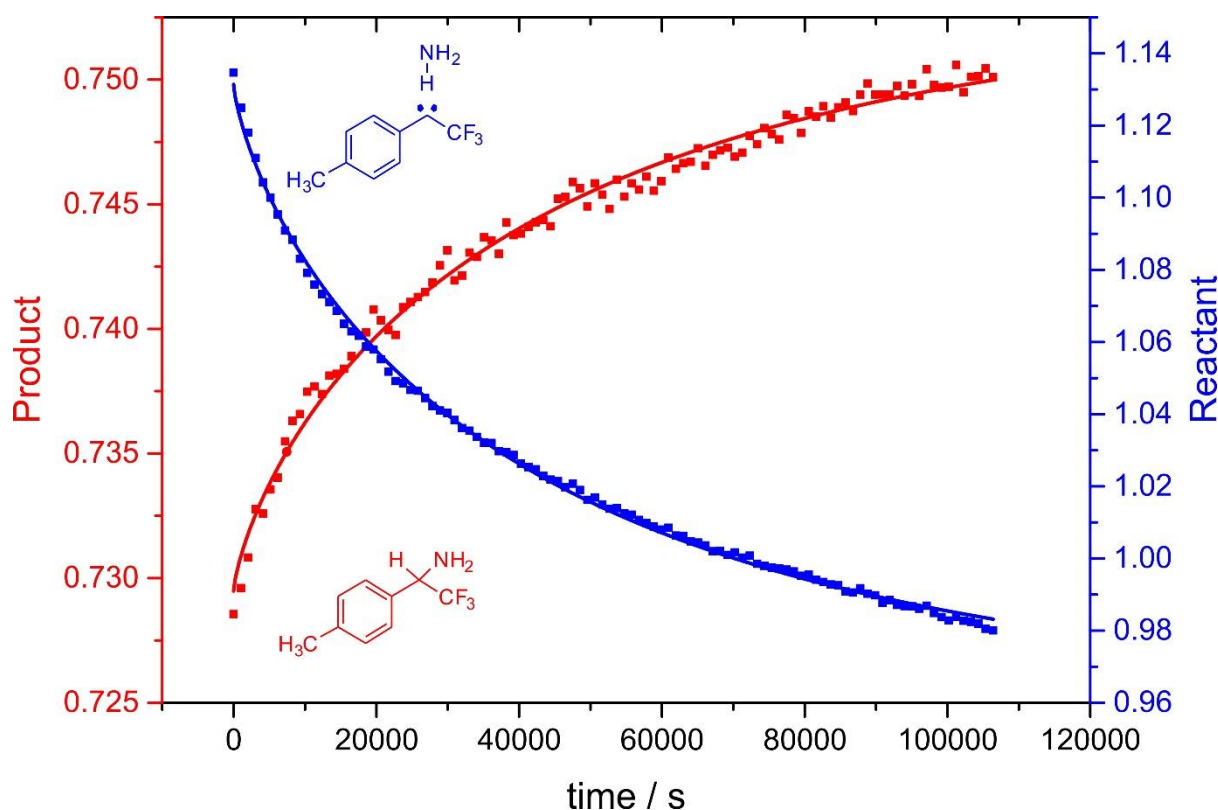


**Figure 43.** Simultaneous fit of the increasing intensities of the IR peaks of *p*-tolyl(trifluoromethyl)ethanamine **36b** at  $1160\text{ cm}^{-1}$  as well as the decreasing intensity of the IR peaks of *S*-**7b** $\cdots\text{H-NH}_2$  at  $1172\text{ cm}^{-1}$  to a pseudo first order reaction (E1) as recorded in argon doped 1% ammonia matrix at 3 K.

### Reaction of *p*-fluorophenyl(trifluoromethyl)carbene in argon matrices doped with 1% of ammonia

In an effort to explain the reaction of carbene **7b** with ammonia, similar experiments with carbene **7c** in argon doped with ammonia were carried out. The principal results are identical for both carbenes and thus only the main results of **7c** are given here. Photolysis of the diazo compound **19c** matrix-isolated in argon doped with 1% of  $\text{NH}_3$  at 3 K produced carbenes T-**7c** and S-**7c** in high yields. Warming of such matrices from 3 K to 25 K for several minutes allows ammonia to interact with the carbene, resulting in the formation of the complex S-**7c** $\cdots\text{H-NH}_2$ . The complex rapidly leads to the  $\text{NH}_2$ -insertion product **36c** via QMT (Figure 44). With  $\text{ND}_3$ , the rearrangement does not proceed, indicating a very large kinetic isotope effect (KIE), as expected for a tunneling reaction.

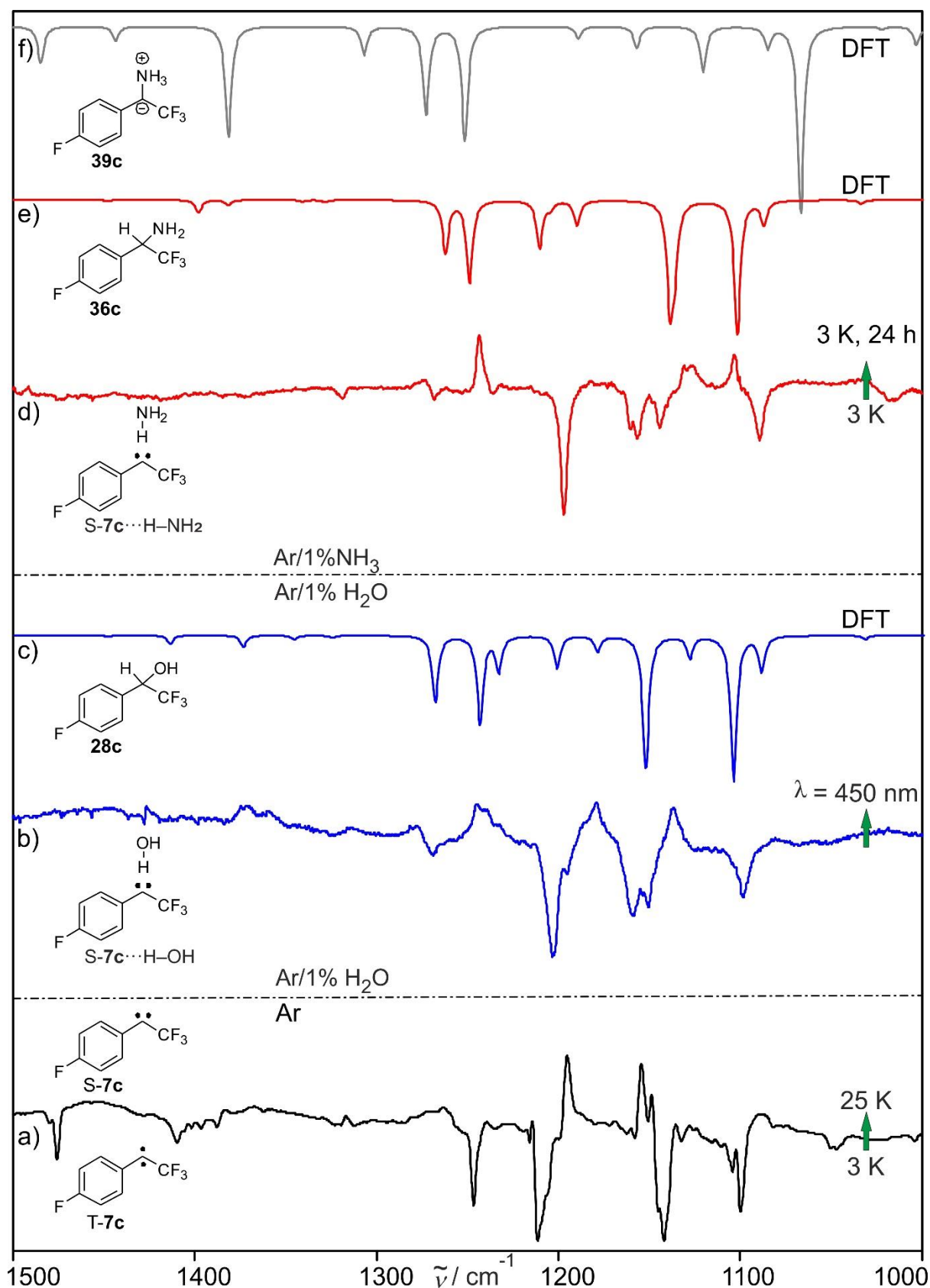


**Figure 44.** IR spectra of the water complex  $S-7c \cdots H-OH$  and ammonia complex  $S-7c \cdots H-NH_2$  matrix-isolated in argon. (a) Difference IR spectrum showing changes of an argon matrix (without water and ammonia) containing  $S-7c$  and  $T-7c$  at 3 K after annealing for 10 min at 25 K (black line). Bands pointing downward, assigned to  $T-7c$ , are disappearing, and bands pointing upward, assigned to  $S-7c$ , are appearing. (b) Difference IR spectrum in argon

doped with 1% of water showing changes after 1 hr irradiation ( $\lambda = 450$  nm) of **S-7c**···H–OH (blue line). Bands pointing downward are assigned to **S-7c**···H–OH, and bands pointing upward are assigned to **28c**. (d) Difference IR spectrum of a similar experiment in argon doped with 1% of ammonia showing changes after keeping **S-7c**···H–NH<sub>2</sub> in dark at 3 K for 24 hrs (red line). Bands pointing downward are assigned to **S-7c**···H–NH<sub>2</sub>, and bands pointing upward are assigned to **36c**. Calculated IR spectrum of (c) **28c**, (e) **36c** and (f) **39c** at the B3LYP-D3/Def2-TZVP level of theory.

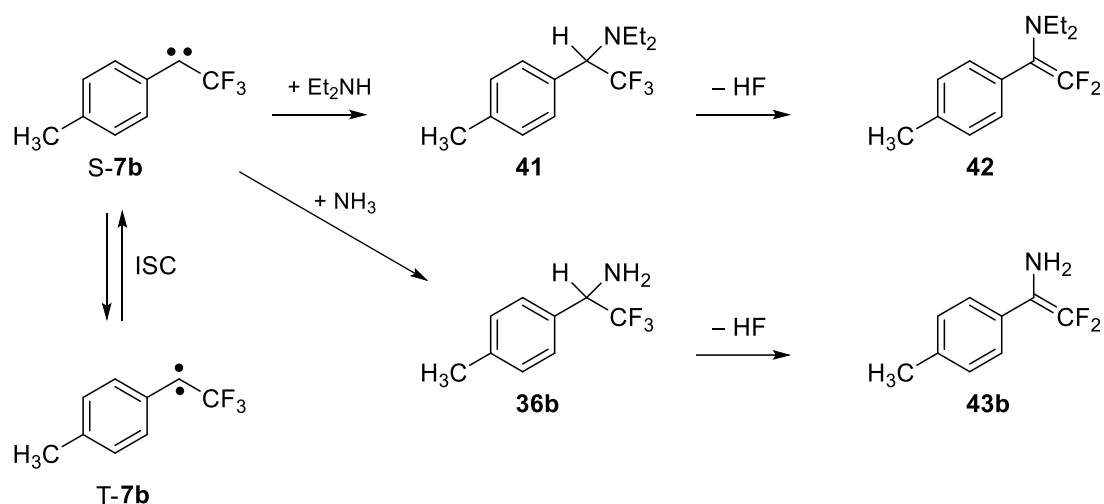
## Reaction of aryl(trifluoromethyl)carbenes in LDA ammonia ice

### UV–vis spectroscopy

The UV–vis spectrum of **19b** in LDA ammonia ice is shown in Figure 45 and found similar to that obtained in LDA water ice (Chapter 3, Figure 25). Photolysis of the matrix with visible light ( $\lambda = 450$  nm) for a few minutes produces a new broad band at 325 nm, assigned to the complex **S-7b**···H–NH<sub>2</sub> and/or traces of **S-7b**, while **T-7b** is not detected under these conditions. The assignment of this species is based on the UV–vis spectra obtained for LDA water and rare gas matrices described before. Prolonged irradiation of the ammonia matrices produces new bands at 243 and 253 nm that have not been detected in other matrices previously. In 1991, Platz *et al.* studied the reaction of carbene **7b** in solution with diethylamine, and observed the formal insertion product **41** followed by a rapid base-catalyzed elimination of hydrogen fluoride to afford styrene **42** (Scheme 16).<sup>[147]</sup> Thus, we speculate that the new bands at 243 and 253 nm detected in ammonia ice are due to formation of styrene **43b**.

**43b** can be formed in a three step process from **19b** in LDA ammonia ice. In the first step, photolysis of the diazo precursor produced carbene **7b**, which immediately forms a strongly hydrogen-bonded complex with ammonia, which subsequently rearranges to give the insertion adduct **36b**. This adduct might then reacts with the surrounding excess ammonia, which act as a base, to afford the enamine by elimination of hydrogen fluoride.

In an effort to explain the reactivity of carbene **7b** in LDA ammonia ice, similar experiments for carbenes **7c** were carried out. After complete photolysis of **19c**, new bands in the UV–vis spectra obtained at 238 and 246 nm are assigned to the corresponding styrene **43c**. These values are comparable to the absorption maxima of the analogues styrene **44b** at  $\lambda = 243$  nm and **44c** at  $\lambda = 237.7$  nm, respectively, reported in literature.<sup>[148]</sup> In LDA ammonia, carbenes **T-7b** and **T-7c** are not detected at any time with short/long irradiation of the corresponding precursors, suggesting the carbenes are readily reacting with the surrounding ammonia molecules.



Scheme 16. Reaction of **7b** with diethylamine<sup>[147]</sup> and LDA ammonia ice.

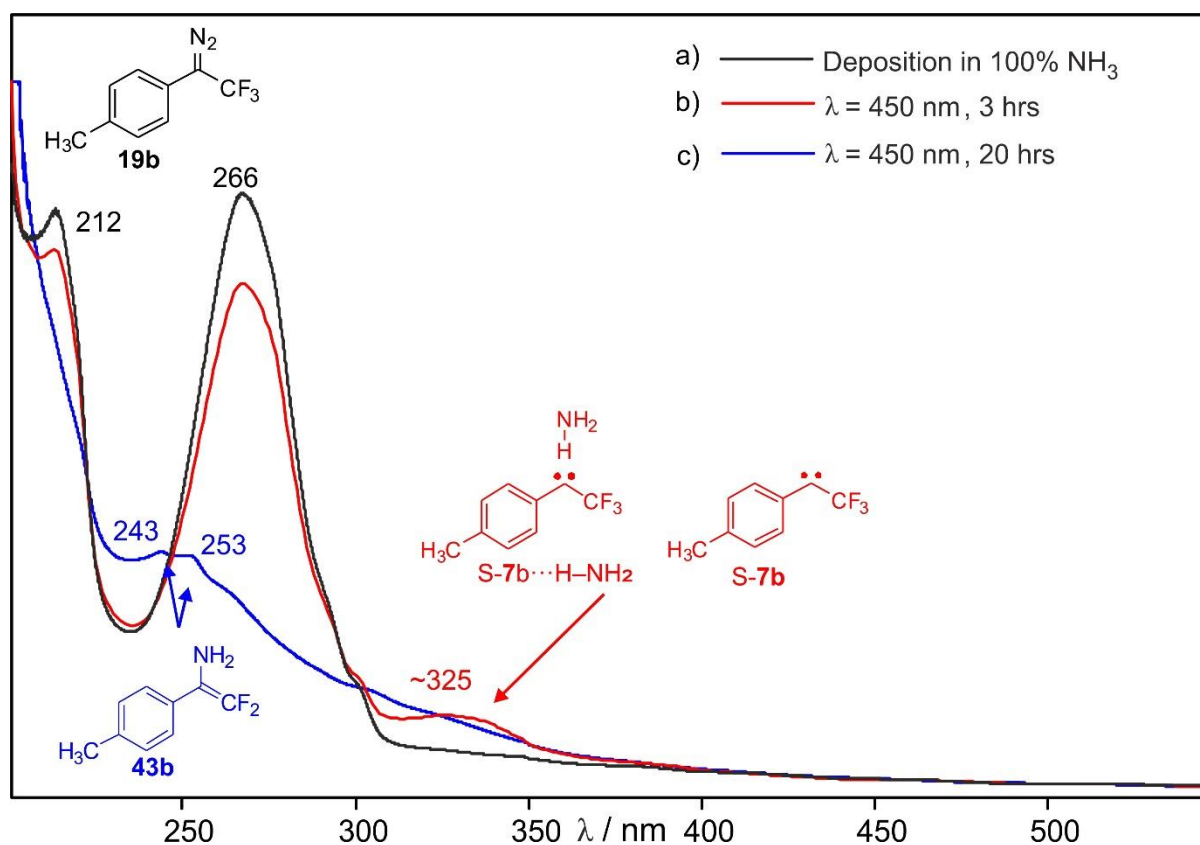
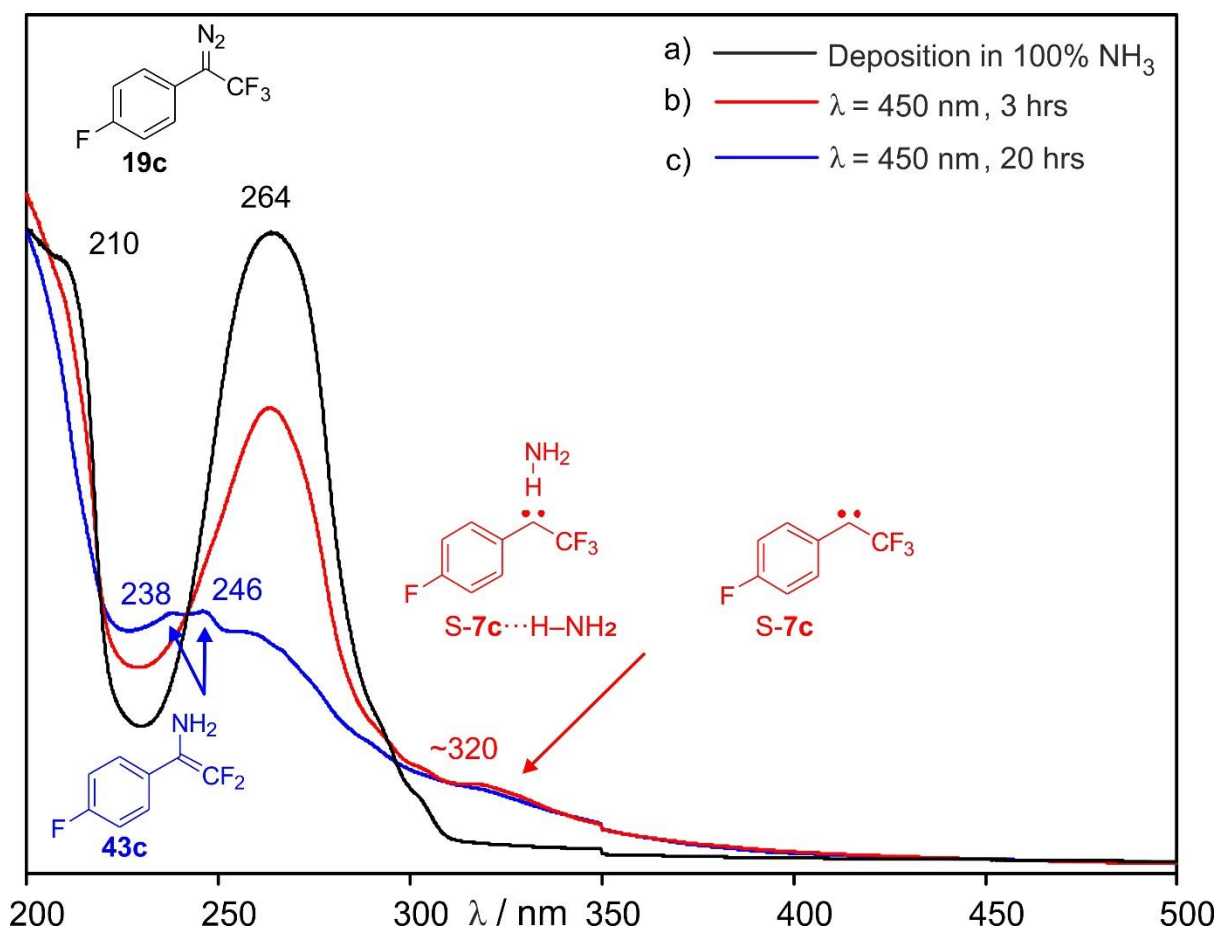


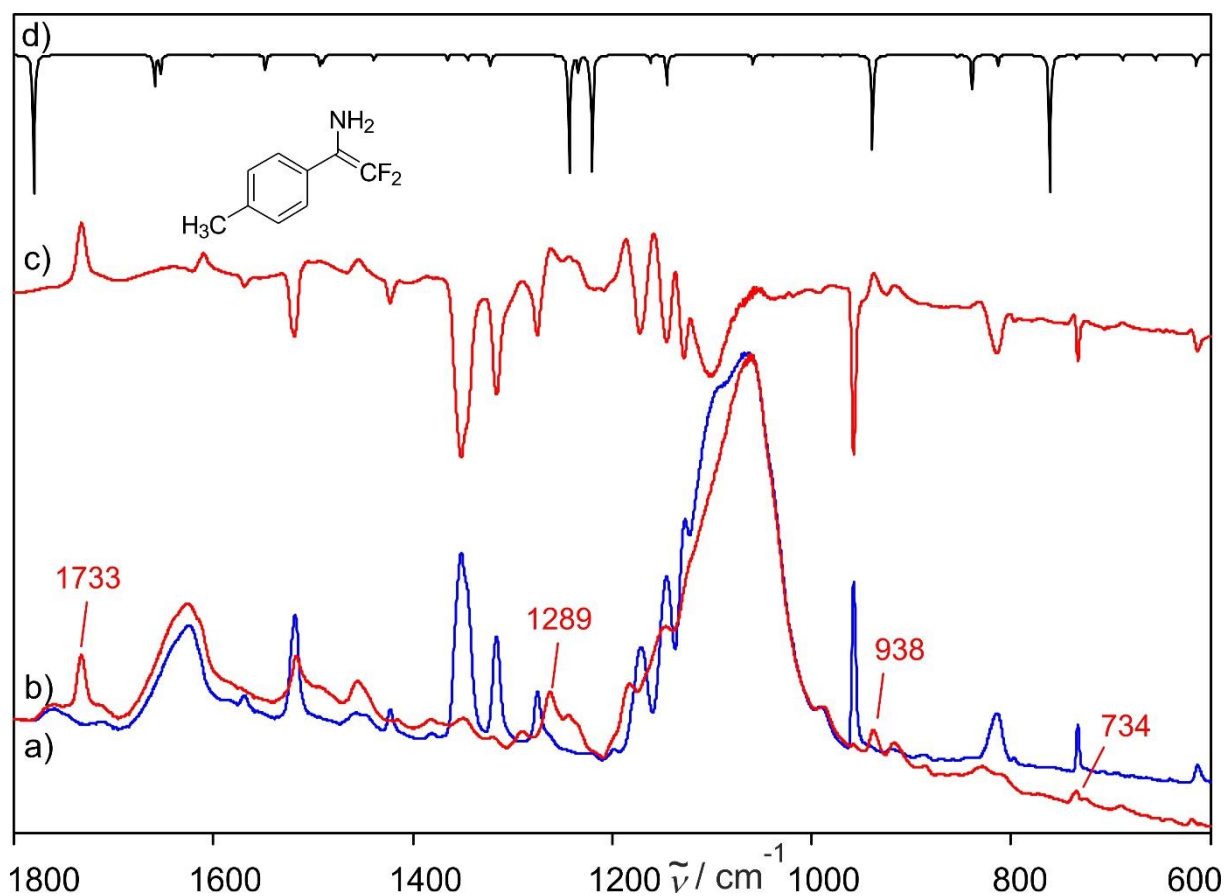
Figure 45. Photochemistry of *p*-tolyl(trifluoromethyl)diazomethane **19b** in LDA ammonia ice at 8 K. a) **19b** in LDA ice. b) UV-vis spectrum of the same matrix after 30 minutes of 450 nm irradiation showing the formation of **S-7b**· $\text{H-OH}$  and/or traces of **S-7b**. c) UV-vis spectrum of the same matrix after several hours of 450 nm irradiation showing the formation of new bands at 243 and 253, tentatively assigned to styrene **43b**.



**Figure 46.** Photochemistry of *p*-fluorophenyl(trifluoromethyl)diazomethane **19c** in LDA ammonia ice. a) **19c** in LDA ice at 8 K. b) UV-vis spectrum of the same matrix after 30 minutes of 450 nm irradiation showing the formation of *S*-**7c**·H-NH<sub>2</sub> and/or traces of *S*-**7c**. c) UV-vis spectrum of the same matrix after several hours of 450 nm irradiation showing the formation of new bands at 243 and 253, tentatively assigned to styrene **43c**.

### IR spectroscopy

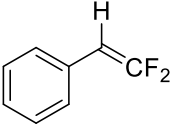
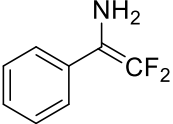
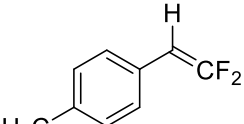
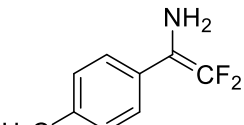
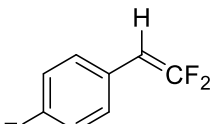
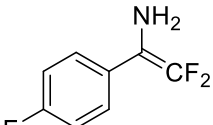
In order to clarify the reactivity of carbenes **7b** and **7c** in LDA ammonia ice, the experiments were also monitored by IR spectroscopy. After several hours of visible light irradiation of **19b** at 3 K, a new species appears with a characteristic IR band at  $1733\text{ cm}^{-1}$ , which has not been detected in other experiment previously. In the light of the UV-vis experiments, this band is assigned to the olefinic C–F stretching of styrene **43b**. This also agrees with a calculated spectrum (Figure 47). Under similar conditions, the C–F stretching band could also be observed for styrene **43a** at  $1731\text{ cm}^{-1}$  and for styrene **43c** at  $1734\text{ cm}^{-1}$ . These bands are furthermore comparable to the reported C–F stretching mode of the analogues styrene **44a** obtained at  $1748\text{ cm}^{-1}$ .<sup>[106]</sup>



**Figure 47.** Photochemistry of *p*-tolyl(trifluoromethyl)diazomethane **19b** in LDA ammonia ice. a) **19b** in LDA ice at 8 K (blue line). b) IR spectrum of the same matrix after several hours of 450 nm irradiation showing the formation of new bands at 734, 938, 1280 and 1733, tentatively assigned to styrene **43b**.

In summary, visible light photolysis of aryl(trifluoromethyl)diazomethane **19** in LDA water and ammonia ices produces the formal insertion product. In contrast to the experiments in water ice, this insertion product is not stable in a more basic medium ammonia, and yields styrene **43** by elimination of HF (Table 15).

**Table 15.** Summary of absorption maxima and olefinic C–F Stretching of styrene **43a-c** and **44a-c**.

Styrene	$\lambda_{\text{max}}$	IR (Olefinic C–F str.) ( $\text{cm}^{-1}$ )	
		Experimental <sup>[c]</sup>	Calculated <sup>[d]</sup>
 <b>44a</b>	239.7 <sup>[a]</sup>	1748 <sup>[b]</sup>	1790
 <b>43a</b>	-	1731	1779
 <b>44b</b>	243 <sup>[a]</sup>	-	1790
 <b>43b</b>	243, 253 <sup>[c]</sup>	1733	1780
 <b>44c</b>	237.7 <sup>[a]</sup>	-	-
 <b>43c</b>	238, 246 <sup>[c]</sup>	1734	1781

[a] Reference.<sup>[148]</sup> [b] Obtained by pyrolysis of **18a**.<sup>[106]</sup> [c] In LDA ammonia ice at 8 K. [d] Calculated at the B3LYP-D3/6-311++ G(d,p) level of theory.

## Conclusion

In Chapter 3, we showed that aryl(trifluoromethyl)carbenes **7b** and **7c** can be generated in both their triplet and singlet states, and both states coexist under the conditions of matrix isolation. In addition, the singlet carbenes was prepared upon the reaction of the triplet carbenes with water molecules by annealing water-doped matrices at 25 K. This results in the irreversible formation of a hydrogen-bonded complex between the singlet carbenes and water,

**S-7b**···H–OH and **S-7c**···H–OH, respectively. In this chapter we extended the study and the reaction between carbenes **7b** and **7c** with ammonia was investigated. Hydrogen-bonded singlet ground state complexes **S-7b**···H–NH<sub>2</sub> and **S-7c**···H–NH<sub>2</sub>, respectively, was obtained. Compared to the free singlet species (**S-7b** and **S-7c**), the maximum shift observed in ammonia complexes 2 cm<sup>-1</sup> is much weaker than the shift observed in water complexes (9 cm<sup>-1</sup>), rationalized in terms of the strength of the Lewis acidity of the solvents.

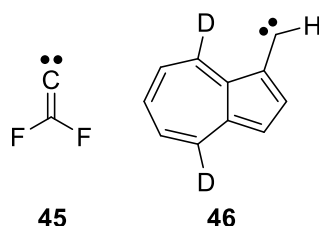
Once formed, these complexes was metastable and rearranged slowly to form the formal N–H insertion products **36b** and **36c**, respectively, even at low temperatures as 3 K. The reaction rate ( $2.5 \pm 0.5 \times 10^{-5} \text{ s}^{-1}$ ) was found independent of temperatures between 3 and 20 K, strongly indicating a tunneling reaction. Similarly, **S-7b**···D–ND<sub>2</sub> and **S-7c**···D–ND<sub>2</sub>, was prepared in argon doped with 1% ND<sub>3</sub>. However, **S-7b**···D–ND<sub>2</sub> and **S-7c**···D–ND<sub>2</sub> was found stable under our experimental conditions at 3 K, indicating a very large kinetic isotope effect (KIE) as expected for a tunneling reactions.

Finally, compared to the water complexes, the tunneling rate in the ammonia complex is at least 3 orders of magnitude faster (Table 14). This is presumably due to the higher barrier for the OH insertion product of **S-7b**···H–OH (9.2 kcal at the B3LYP-D3/6-311++g(d,p) level of theory) compared to that of **S-7b**···H–NH<sub>2</sub> (not known at the same level of theory). Therefore, high-level calculations are required for the theoretical predictions of the tunneling paths and reaction rates of **S-7b**···H–NH<sub>2</sub> → **36b**.

## 5. Spin-selective hydrogenation of aryl(trifluoromethyl)carbenes

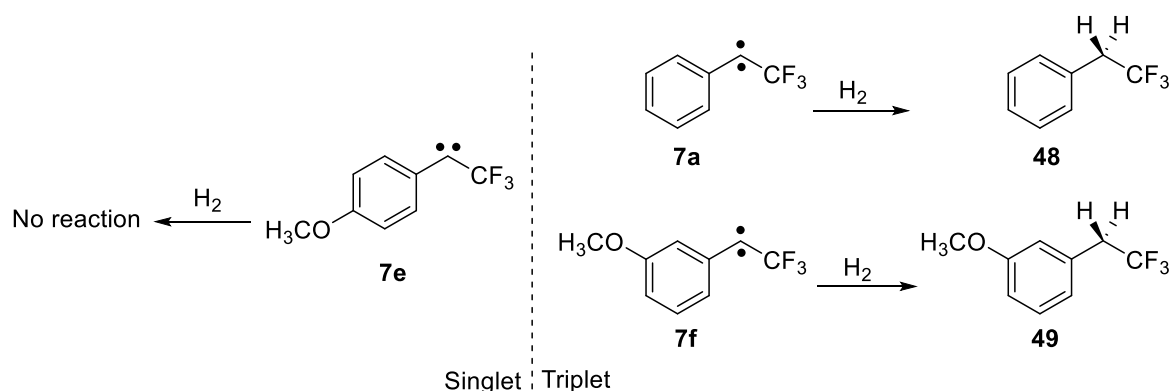
### Introduction

During the last decades the activation and subsequent utilization of dihydrogen has received great interest from the scientific community due to its importance from organic synthesis to energy storage.<sup>[128, 149]</sup> However, the key role in these processes almost exclusively involves the use of metal-based catalysis.<sup>[129]</sup> Carbenes,<sup>[133]</sup> along with nitrenes,<sup>[150]</sup> germynes and stannylenes,<sup>[151-153]</sup> fullerenes<sup>[154]</sup> and frustrated Lewis pairs<sup>[155-156]</sup> are among the few metal-free molecules that have recently been used to break the strong H–H bond (~104 kcal/mol). Stable singlet carbenes such as (alkyl)(amino) carbenes **32** and **33**,<sup>[133]</sup> as well as highly electrophilic singlet **45**,<sup>[157]</sup> have been shown to split the H<sub>2</sub> molecule. Whereas triplet carbenes are generally known to undergo hydrogenation reaction,<sup>[158]</sup> carbene **46** is the only known singlet carbene besides **45** that readily react with H<sub>2</sub> at cryogenic temperatures.<sup>[159]</sup>



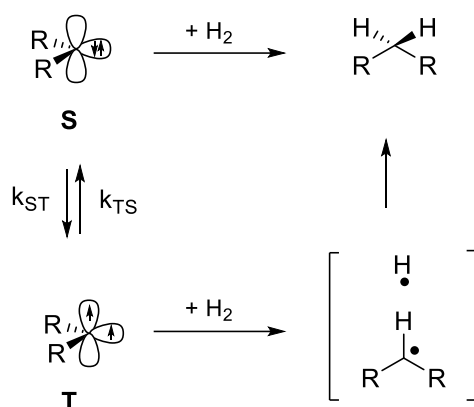
**Scheme 17.** The only singlet carbenes reported to be activating H<sub>2</sub> at cryogenic temperatures.

A similar observation was reported by Sheridan and co-workers for aryl(trifluoromethyl)carbenes: triplet ground state carbenes **7a**<sup>[158]</sup> and **7f**<sup>[111]</sup> readily insert into H<sub>2</sub> whereas singlet carbene **7e**<sup>[111]</sup> is unreactive under the same conditions at cryogenic temperatures (Scheme 18).



**Scheme 18.** Spin-selective reaction of aryl(trifluoromethyl)carbenes with H<sub>2</sub> at 30 K.

Generally, singlet and triplet carbenes exhibit different reactivity towards small molecules which can be explained by their electronic structure. Thus, the mechanisms of the activation of hydrogen by singlet and triplet carbenes are different (Scheme 19).<sup>[160]</sup> Triplet carbenes undergo tunneling-assisted hydrogen abstraction that leads to a radical pair followed by recombination process to eventually form the insertion product, whereas singlet carbenes react in a single concerted approach.<sup>[161]</sup>



**Scheme 19.** Mechanism of the reaction of singlet and triplet carbenes with H<sub>2</sub>.

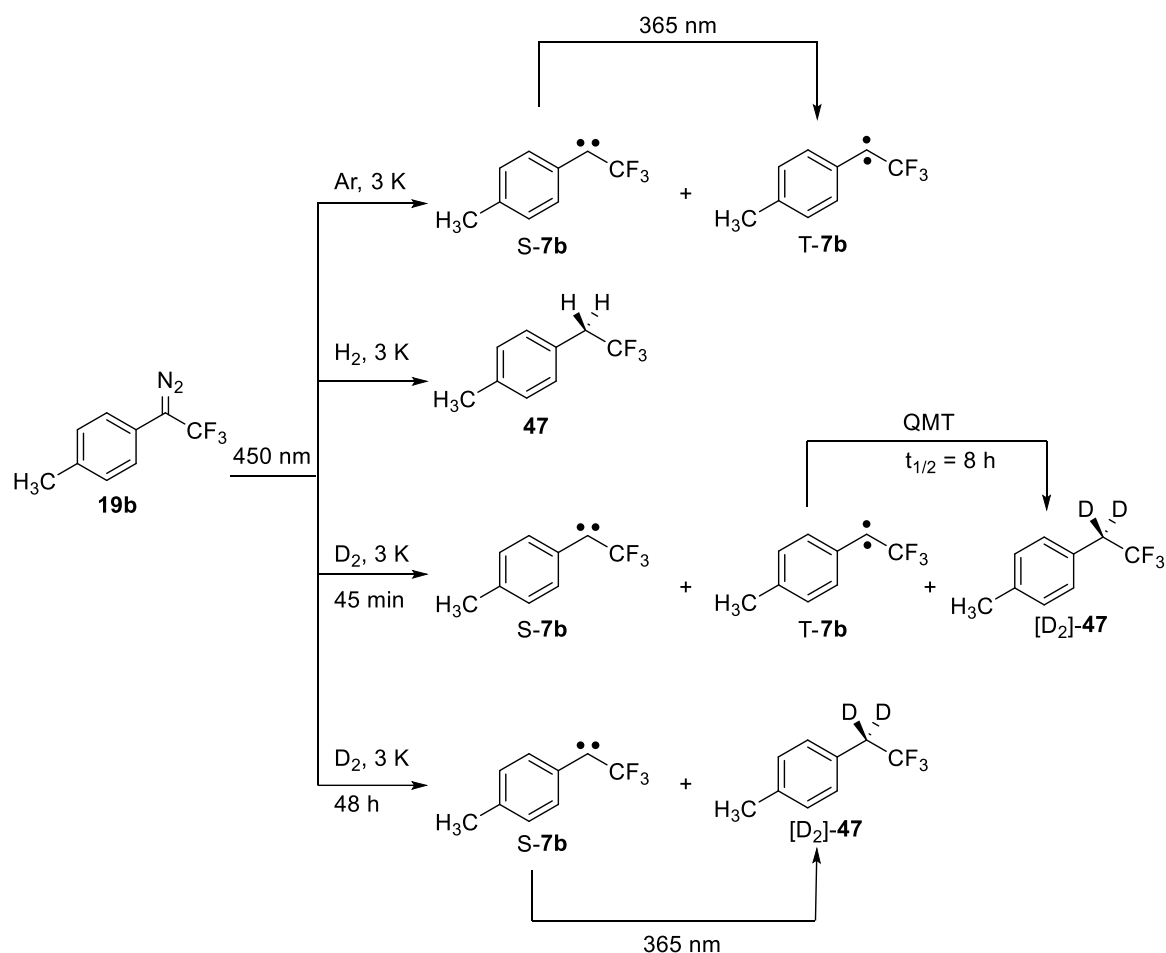
In previous chapters, we described that carbene **7b** could be isolated in rare gas matrices both in its lowest singlet and triplet states. At temperatures below 10 K, both spin states coexist indefinitely and can be interconverted by irradiation into the absorption maxima of S-**7b** in the UV or T-**7b** in the visible range, respectively. Since the activation of hydrogen is a fundamental reaction for carbenes, we investigated the spin-specific reactivity of carbene **7b** using matrix-isolation UV-vis, IR and EPR spectroscopy and by kinetics studies in solid H<sub>2</sub> and D<sub>2</sub> at temperatures as low as 3 K. The reaction of the related phenyl(trifluoromethyl)carbene **7a** in argon doped with 2% H<sub>2</sub> has been reported previously.<sup>[158]</sup> Here, we also performed the reaction of **7a** with solid H<sub>2</sub> and D<sub>2</sub> to avoid complications that might arise from the diffusion of H<sub>2</sub> in solid argon as well as to compare **7a** and **7b** under the same conditions.

## Results and discussion

### IR spectroscopy

Several hours irradiation ( $\lambda = 450$  nm) of matrix-isolated **19b** in solid H<sub>2</sub> rapidly results in the complete photolysis of the diazo precursor and exclusive formation of the H<sub>2</sub>-insertion product **47** (Scheme 20, Figure 48). The IR spectrum obtained after complete photolysis is in good

agreement with the calculated spectrum of **47** at the B3LYP-D3/def2TZVP level of theory (Figure 48, bottom). Under these conditions, neither T-**7b** nor S-**7b** is detected at any time with short/long irradiation. This indicates that carbene **7b** rapidly reacts with the surrounding H<sub>2</sub> molecule even at such low temperatures at 3 K without noticeable activation barrier. Similarly, irradiation ( $\lambda = 254$  nm) of **19a** in H<sub>2</sub> matrix at 3 K resulted in exclusive formation of the corresponding insertion product **48**, whereas carbene **7a** is not formed under these conditions (Figure 48, top). The IR spectrum of **48** is in good agreement with the authenticated matrix-isolated spectrum of **48** in solid H<sub>2</sub> (Scheme 21, Figure 48).

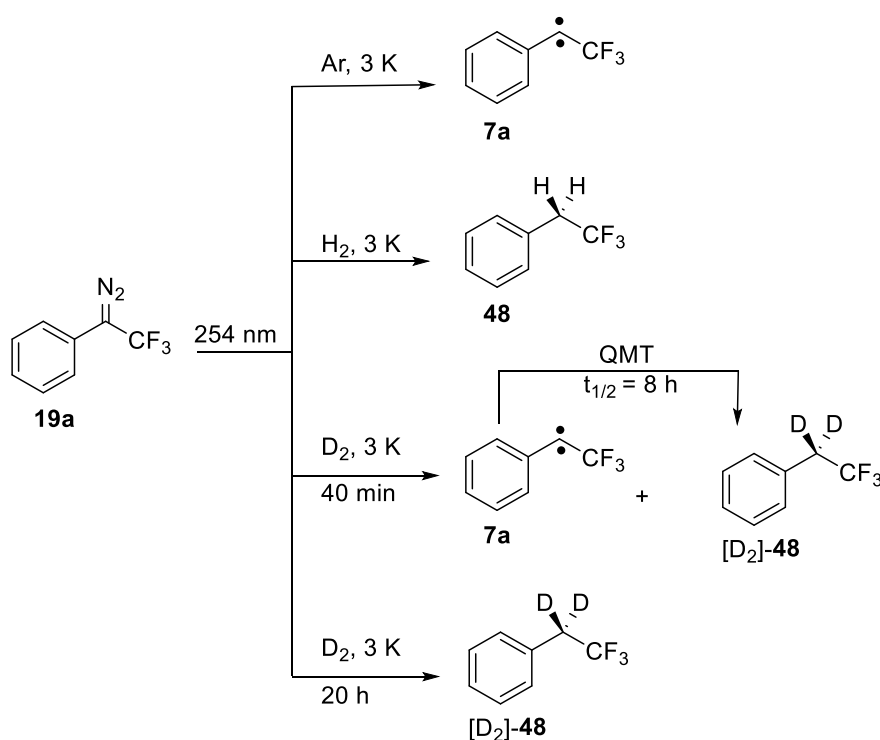


**Scheme 20.** Photochemistry of **19b** in solid argon, H<sub>2</sub> and D<sub>2</sub> matrices.

In contrast to the experiments in solid H<sub>2</sub>, carbene **7b** is detected upon short time irradiation of **19b** in D<sub>2</sub> matrices both in its lowest singlet (S-**7b**) and triplet (T-**7b**) states (Figure 49). However, in contrast to that of the experiments in rare gas matrices, T-**7b** is only metastable and slowly rearranges in darkness at 3 K to give the corresponding insertion product [D<sub>2</sub>-**47**] with a half-life time of approximately 8 h. Assuming a pseudo first order reaction (Equation 1), the rate constant for the insertion of T-**7b** into D<sub>2</sub> was determined to be  $1.7 \pm 0.1 \times 10^{-5} \text{ cm}^{-1}$ .

Similar rates were determined for carbene–D<sub>2</sub> reactions reported in literatures.<sup>[160]</sup> On the other hand, **S-7b** is unreactive towards D<sub>2</sub> in darkness at 3 K (up to 48 hrs in our experimental conditions), which was only activated upon further photolysis into the absorption maxima of **S-7b** in the UV region ( $\lambda = 365$  nm) (Figure 50). As we discussed before, **S-7b** can be converted completely into **T-7b** upon UV photolysis in rare gas matrices. Thus, in the presence of the surrounding D<sub>2</sub> molecule, UV irradiation of **S-7b** resulted in the formation of [D<sub>2</sub>]-**47** via **T-7b** (Figure 50). Considering that the reaction of carbene **7b** with H<sub>2</sub> is too fast to be observable with our experimental conditions and that of a slow reaction with D<sub>2</sub> suggested that the H/D kinetic isotope effect is highly pronounced.

Likewise, short time irradiation of **19a** in solid D<sub>2</sub> produces carbene **7a** as the main product accompanied by small amounts of [D<sub>2</sub>]-**48**. However, similar to carbene **T-7b**, carbene **7a** is only metastable in solid D<sub>2</sub> even at temperatures as low as 3 K, and slowly reacts to give [D<sub>2</sub>]-**48** with a half-life time of approximately 8 h. The reaction rate was determined to be  $1.1 \pm 0.1 \times 10^{-5} \text{ cm}^{-1}$ . It is noteworthy to mention that the insertion of carbenes **7a** and **T-7b** into H<sub>2</sub> is too fast to be measured in our experimental conditions whereas the  $10^{-5}$  rates measured for the insertion of these carbenes into D<sub>2</sub> suggested that the reaction proceeds through Quantum Mechanical Tunneling (QMT).



**Scheme 21.** Photochemistry of **19a** in solid argon, H<sub>2</sub> and D<sub>2</sub> matrices.

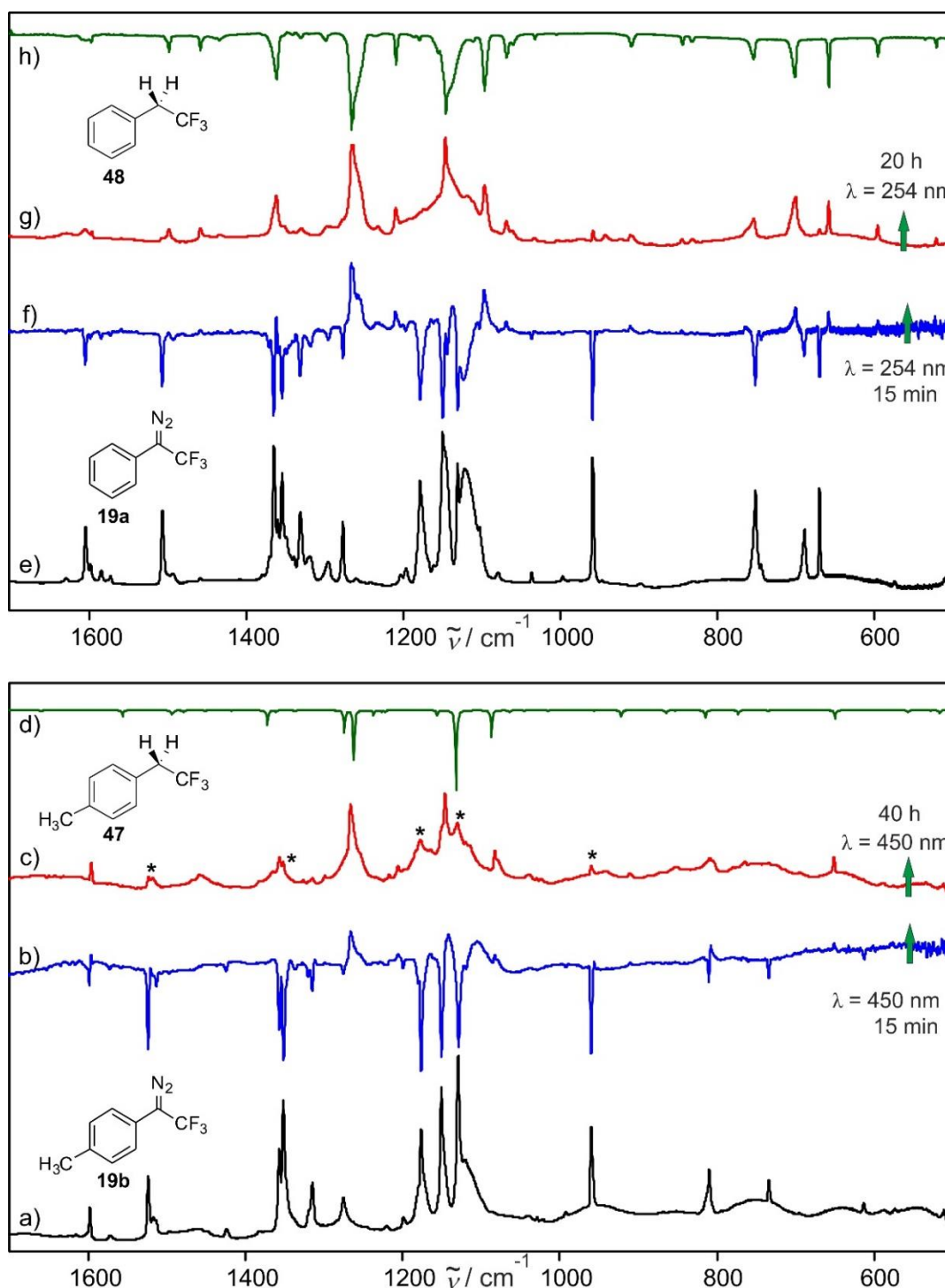


**Figure 48.** IR spectra showing the reaction between aryl(trifluoromethyl)carbenes and  $\text{H}_2$ . (a) Matrix-isolated IR spectrum of **19b** in solid  $\text{H}_2$  at 3 K. (b) Difference IR spectrum showing changes after 15 min irradiation ( $\lambda = 450$  nm) of the same matrix. Bands pointing downward, assigned to **19b**, are disappearing, and bands pointing upward, assigned to **47**, are appearing (blue line). (c) IR spectrum showing after prolonged irradiation ( $\lambda = 450$  nm) of the same matrix. The bands marked with an asterisk are due to unreacted **19b**. (d) IR spectrum of **47** calculated at the B3LYP-D3/def2TZVP level of theory. (e) Matrix-isolated IR spectrum of **19a** in solid  $\text{H}_2$  at 3 K. (f) Difference IR spectrum showing changes after 15 min irradiation ( $\lambda = 254$  nm) of the same matrix. Bands pointing downward, assigned to **19a**, are disappearing, and bands pointing upward, assigned to **48**, are appearing (blue line). (g) IR spectrum showing after prolonged irradiation ( $\lambda = 254$  nm) of the same matrix. (h) Reference spectrum of **48** matrix-isolated in  $\text{H}_2$  at 3 K.

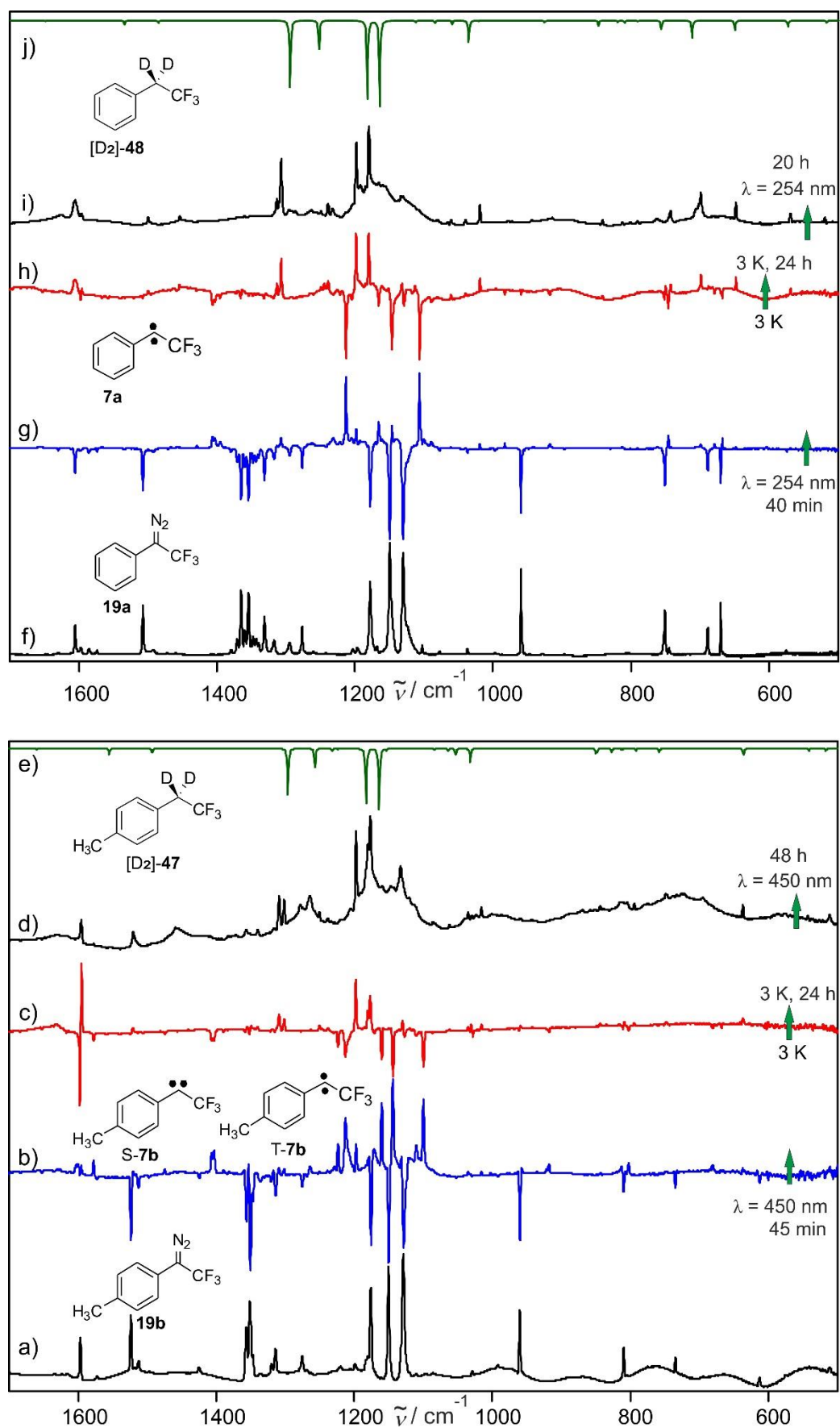


**Figure 49.** IR spectra showing the reaction between aryl(trifluoromethyl)carbenes and  $D_2$ . (a) Matrix-isolated IR spectrum of **19b** in solid deuterium at 3 K. (b) Difference IR spectrum showing changes after 45 min irradiation

( $\lambda = 450$  nm) of the same matrix. Bands pointing downward, assigned to **19b**, are disappearing, and bands pointing upward, assigned to **S-7b**, **T-7b** and traces of **[D<sub>2</sub>]-47** are appearing (blue line). (c) Difference IR spectrum showing changes after keeping the same matrix in darkness at 3 K for 24 hrs. Bands pointing downward, assigned to **T-7b**, are decreasing, and bands pointing upward, assigned to **[D<sub>2</sub>]-47**, are increasing (red line). (d) IR spectrum showing changes after prolonged irradiation ( $\lambda = 450$  nm) of the same matrix. (e) IR spectrum of **[D<sub>2</sub>]-47** calculated at the B3LYP-D3/def2TZVP level of theory. (f) Matrix-isolated IR spectrum of **19a** in solid deuterium at 3 K. (g) Difference IR spectrum showing changes after 40 min irradiation ( $\lambda = 254$  nm) of the same matrix. Bands pointing downward, assigned to **19a** are decreasing, and bands pointing upward, **7a** and traces of **[D<sub>2</sub>]-48** are appearing (blue line). (h) Difference IR spectrum showing changes after keeping the same matrix in darkness at 3 K for 24 hrs. Bands pointing downward, assigned to **7a**, are decreasing, and bands pointing upward, assigned to **[D<sub>2</sub>]-48** are increasing (red line). (i) IR spectrum showing changes after prolonged irradiation ( $\lambda = 254$  nm) of the same matrix. (j) IR spectrum of **[D<sub>2</sub>]-48** calculated at the B3LYP-D3/def2TZVP level of theory.

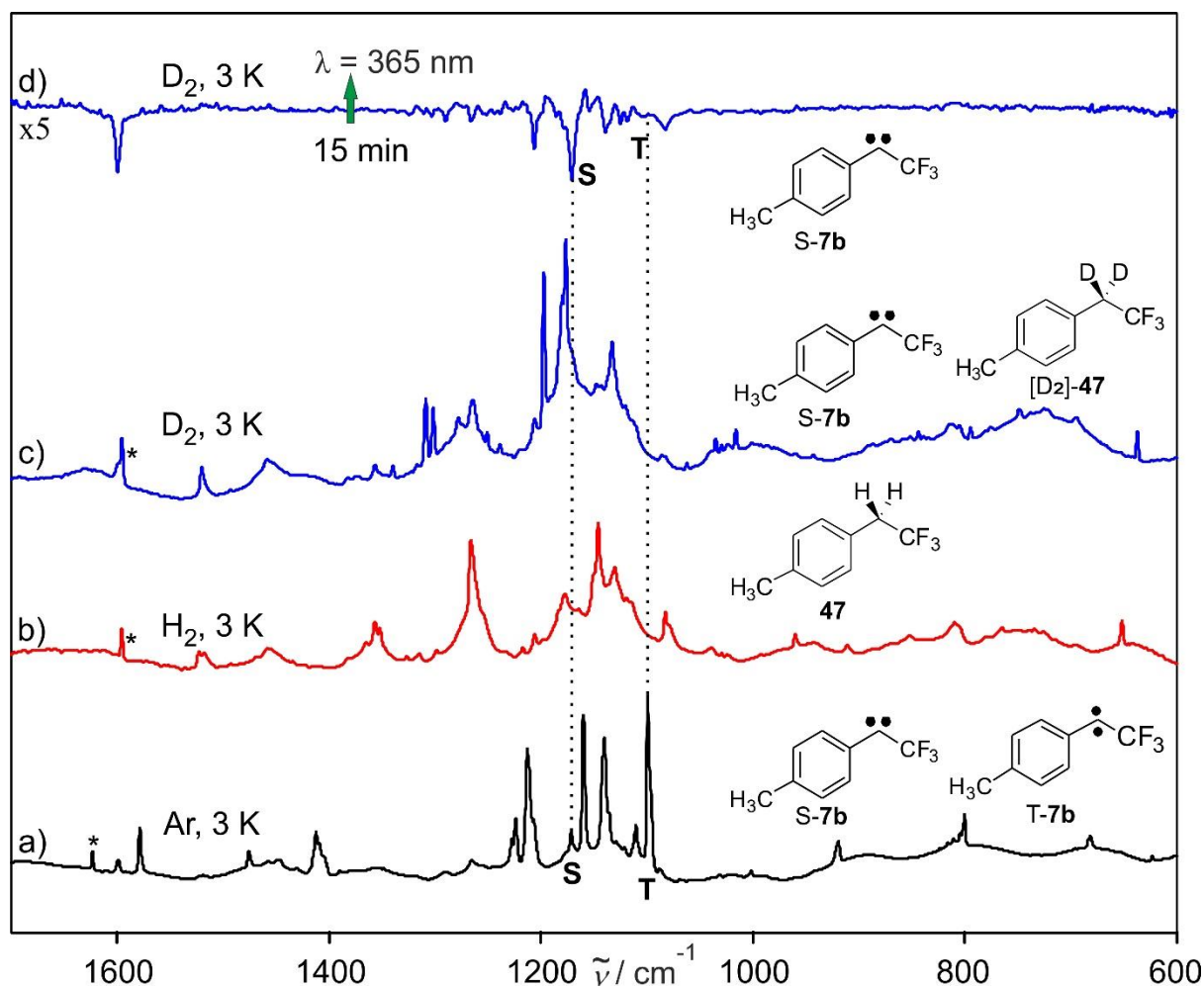


**Figure 50.** IR spectra showing the photochemistry of **19b** matrix-isolated in argon, H<sub>2</sub> and D<sub>2</sub> at 3 K. (a) Matrix-isolated IR spectrum after several hours of 450 nm irradiation of **19b** in argon at 3 K. (b) Matrix-isolated IR spectrum after several hours of 450 nm irradiation of **19b** in H<sub>2</sub> at 3 K. (c) Matrix-isolated IR spectrum after 48 hours of 450 nm irradiation of **19b** in deuterium at 3 K. (d) Difference IR spectrum showing changes after 15 min irradiation ( $\lambda = 365$  nm) of the same deuterium matrix. Bands pointing downward, assigned to **S-7b**, are disappearing, and bands pointing upward, assigned to **[D<sub>2</sub>]-47** are increasing (blue line). Asterisks show bands of water, H<sub>2</sub>, and D<sub>2</sub> respectively.

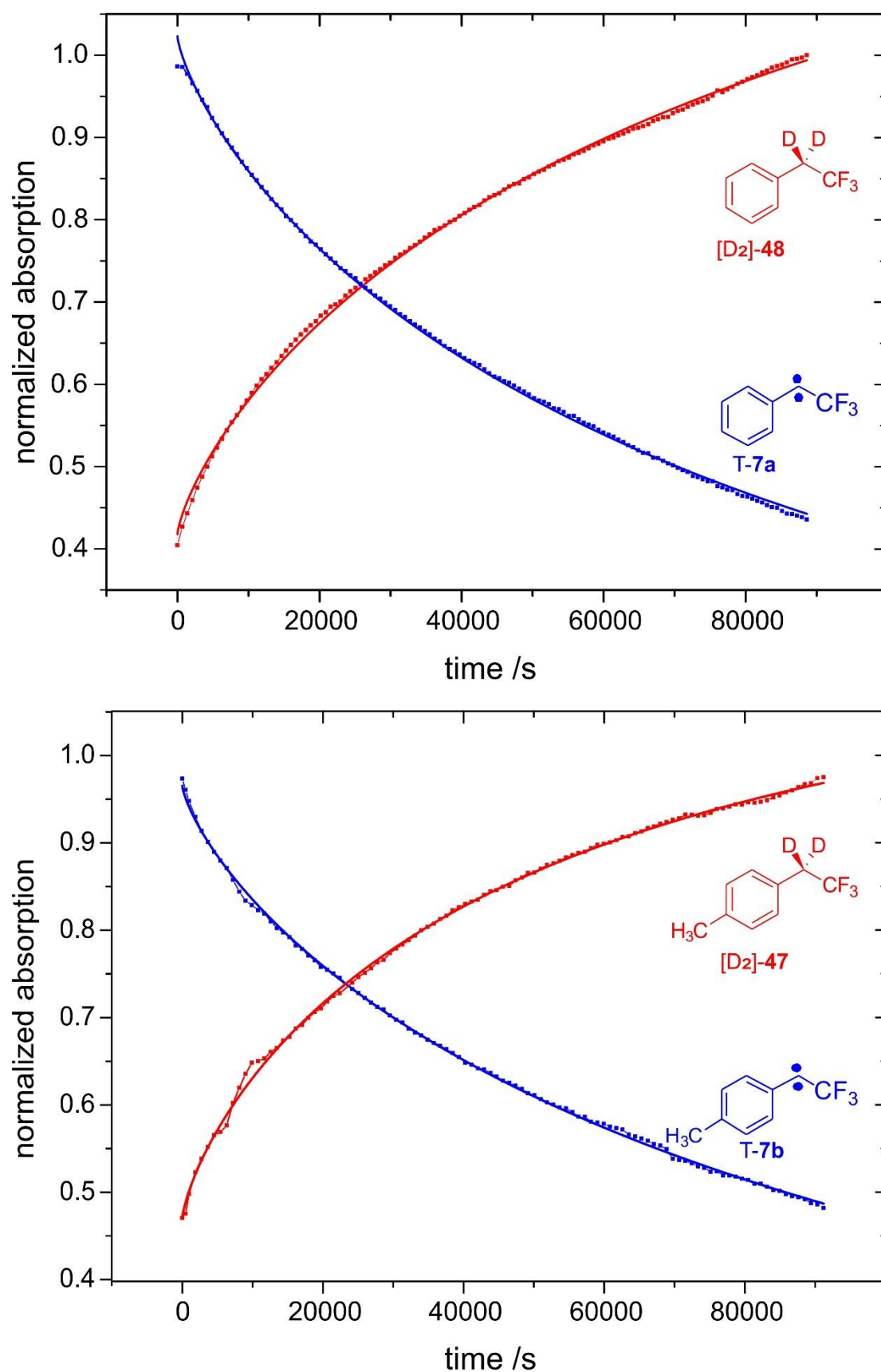


**Figure 51.** (Bottom) Simultaneous fit of the increasing intensities of the IR peaks of [D<sub>2</sub>]-47 at 1198 cm<sup>-1</sup> as well as the decreasing intensity of the IR peaks of T-7b at 1144 cm<sup>-1</sup> and (Top) increasing intensities of the IR peaks of [D<sub>2</sub>]-48 at 1198 cm<sup>-1</sup> as well as the decreasing intensity of the IR peaks of 7a at 1106 cm<sup>-1</sup> to E1 as recorded in D<sub>2</sub> matrix at 3 K.

## UV–vis spectroscopy

In analogy to the IR experiments, UV–vis experiments were carried out to monitor the reaction between particularly carbene **S-7b** with deuterium. Photolysis ( $\lambda = 450$ ) of **19b** in a deuterium matrix at 3 K produces the UV–vis spectrum shown in Figure 52. As discussed before, **S-7b** features a broad band with  $\lambda_{\text{max}} = 326$  nm in argon matrix at 3 K whereas **T-7b** shows absorption at 304, 422 and 436 nm. In a solid deuterium matrix, the band at 326 nm is produced in the same intensity as in argon matrix in contrast to the bands at 304, 422 and 434 nm, which are only obtained in trace amount. In addition, after keeping the matrix in darkness at 3 K for 24 hours, we observe that the UV signals of **T-7b** are disappearing whereas the **S-7b** band is unchanged. These experiments described that  $\text{D}_2$  selectively react with the triplet state of carbene **7b**, which nicely confirms the conclusion from the IR experiments. However, it is not possible to identify the UV absorption of the  $\text{D}_2$  insertion product  $[\text{D}_2]\text{-47}$  since it would come below 300 nm, and thus overlaid by signals of precursor **19b** and/or unreacted **T-7b**.

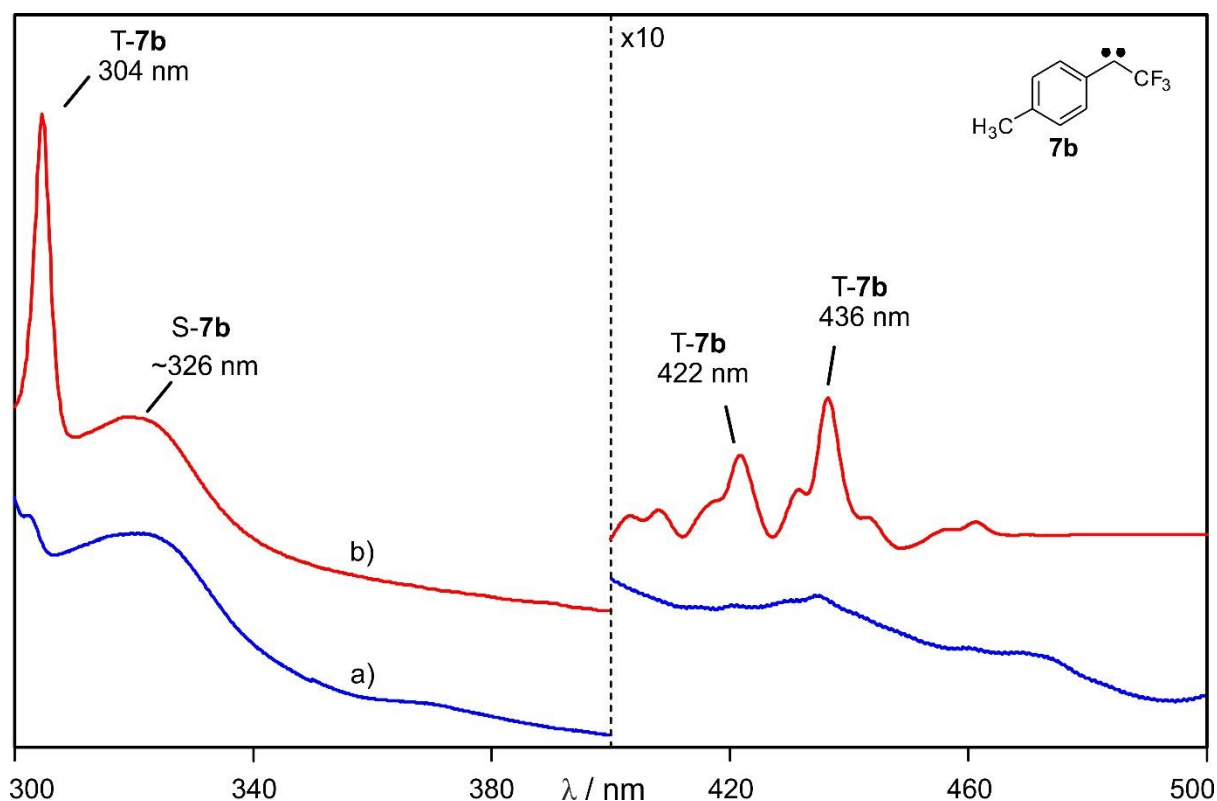


**Figure 52.** UV–vis spectra showing the reactivity of **7b** in  $\text{D}_2$  matrix at 3 K. a) Matrix-isolated UV–vis spectrum of **7b** obtained after 2 hours of 450 nm irradiation of **19b** in solid deuterium followed by keeping the matrix for 24 h in the dark at 3 K (blue line). Only bands of **S-7b** ( $\sim 326$  nm) and traces of **T-7b** (304, 422 and 436 nm) could be detected under these conditions – proving the high reactivity of **T-7b** against the surrounding deuterium molecules. (b) Matrix-isolated UV–vis spectrum of carbenes **S-7b** and **T-7b** obtained after 10 hours of 450 nm irradiation of **19b** in solid argon at 3 K (red line).

## EPR spectroscopy

These findings were further proved by following the reactivity behavior of T-7b using a complementary EPR spectroscopy. Photolysis ( $\lambda = 450$  nm) of 19b in D<sub>2</sub> at 4 K resulted in the formation of T-7b with an EPR spectrum typical of a triplet carbene ( $|D/hc| = 0.5229$  and  $|E/hc| = 0.0308$  cm<sup>-1</sup>, Figure 53). In a similar experiment in argon matrices, ZFS parameters  $|D/hc| = 0.5219$  and  $|E/hc| = 0.0305$  cm<sup>-1</sup> were obtained for carbene T-7b. In an attempt to check the proposed abstraction/recombination mechanism of the reaction between carbenes and D<sub>2</sub>, we kept the matrix at 4 K for 24 hours resulted in up to 60% signal loss of T-7b and concurrently in an increase of the absorptions of D atoms (Figure 53, inset). These experiments indicating that the irreversible reaction of T-7b to an EPR-silent singlet species D<sub>2</sub>-47 via deuterium tunneling which nicely confirms the conclusion from the IR and UV-vis experiments.

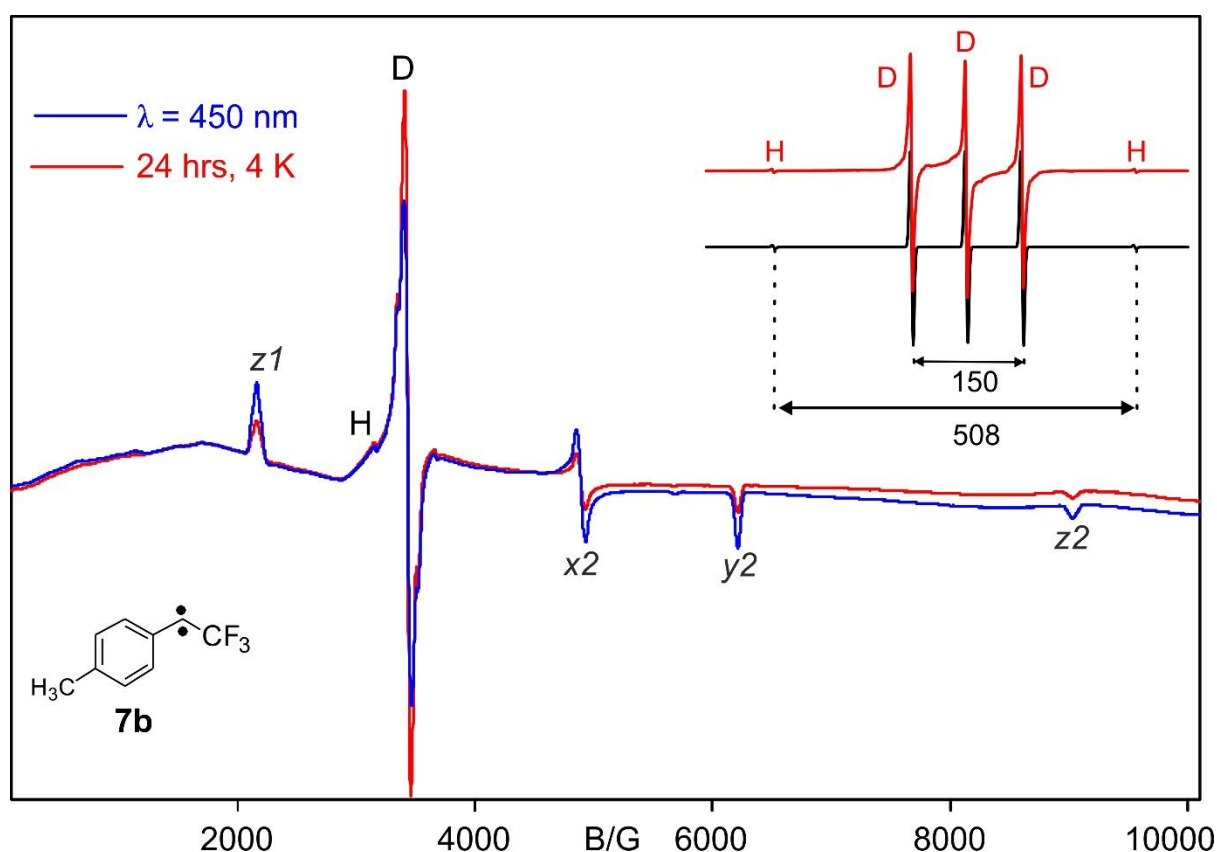


**Figure 53.** X-band CW EPR spectra showing the reaction of carbene T-7b with D<sub>2</sub> at 4 K. (a) D<sub>2</sub> matrix at 4 K showing the spectrum of T-7b (blue line; ZFS parameters  $|D/hc| = 0.5259$  cm<sup>-1</sup> and  $|E/hc| = 0.0308$  cm<sup>-1</sup>). (b) EPR spectrum showing changes after keeping the same matrix for 24 h in the dark at 4 K (red line). Inset show the radical region of the spectra together with simulated spectra of H and D atoms.

## DFT calculations

The experimental findings were verified by DFT calculations at the B3LYP-D3/def2-TZVP level of theory which shows geometrical similarity for activation of H<sub>2</sub> by carbenes **7a** and **7b** (Figures 54 and 55). For the reaction of T-**7a**, S-**7a**, T-**7b** and S-**7b** with H<sub>2</sub>, an activation barrier of 4.7 (4.1), 2.8 (3.5), 4.6 (4.0) and 3.6 (4.2) kcal/mol, respectively, was calculated (values in parenthesis are including ZPVE). Zuev and Sheridan reported activation barrier between 3–6 kcal mol<sup>-1</sup> for a series of triplet carbenes, which showed reactivity towards H<sub>2</sub>.<sup>[158]</sup> These barriers are clearly too high to account for fast thermal reaction occurring at cryogenic temperatures ( $E_{a(3K)} = kT = 0.006$  kcal/mol). Furthermore, comparing to the H–H bond length in H<sub>2</sub> gas (0.74 Å), the H–H bond in the carbene-H<sub>2</sub> transition state and radical pair for T-**7b** are elongated by 0.85 and 2.40 Å, respectively – suggesting that the primary interaction between H<sub>2</sub> and carbene is happening via the lone pair of the carbene and antibonding of the H<sub>2</sub> molecule.

Although DFT calculations at the B3LYP-D3/def2-TZVP level of theory predicted to have a very similar activation barrier for T-**7b** (4.0 kcal/mol) and S-**7b** (4.2 kcal/mol), it is not well understood the reactivity difference between them against hydrogen. At the same level of theory, we calculated a relatively similar activation barrier for the analogues T-**7e** and S-**7f** to be 5.7 and 4.0 kcal/mol, respectively, which showed contrary reactivity against hydrogen (Scheme 18).<sup>[111]</sup> Thus, the barrier height doesn't appear to be the reason why these singlet carbenes doesn't react (or less reactive) against hydrogen. As Sheridan and co-workers pointed out earlier, the less reactivity of the singlet carbene can instead be explained by the lower QMT involving two hydrogens simultaneously.<sup>[158]</sup> This is shown structurally in Figures 54 and 55, both of the hydrogen are moving towards the  $\pi$  and  $\sigma$  orbitals of the singlet carbene center (TS(S-**7a**···H<sub>2</sub>), TS(S-**7b**···H<sub>2</sub>)). Finally, the IRC calculation predicts a broader barrier for singlet carbene S-**7b** comparing to the triplet T-**7b** energy curves, which might add explanation on the lack of reactivity of S-**7b** with D<sub>2</sub>. However, it should be mention as well that a high-level calculations might be necessary for an accurate predictions of the tunneling paths and reaction rates.

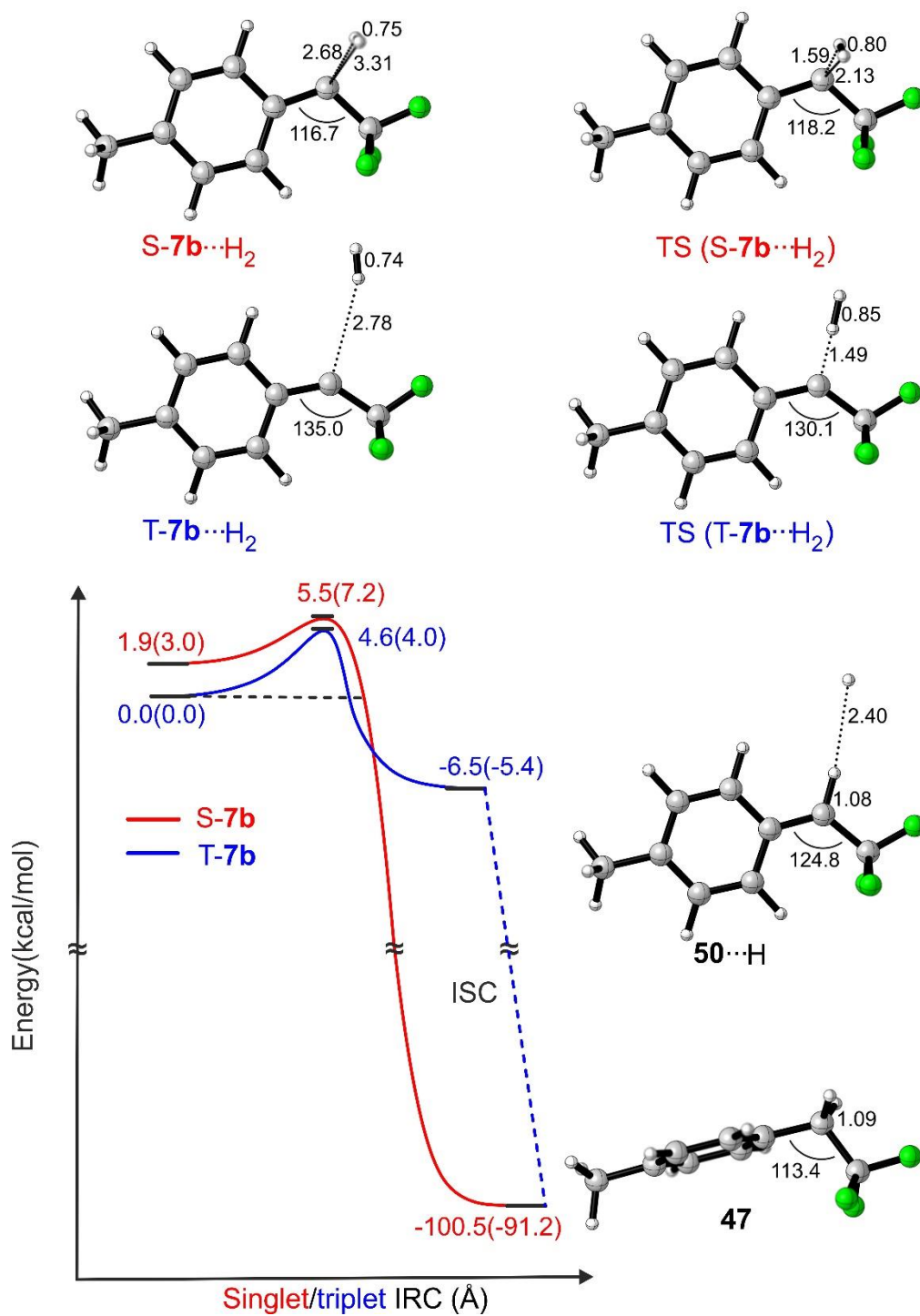


**Figure 54.** Optimized geometries of the hydrogenation reaction of *p*-tolyl(trifluoromethyl)carbene **7b** in the singlet (blue) and triplet (red) state calculated at the (U)B3LYP-D3/def2-TZVP level of theory. Energies are given in kcal/mol relative to triplet carbene hydrogen complex **S-7b**···H<sub>2</sub> (values in parentheses include ZPVE).

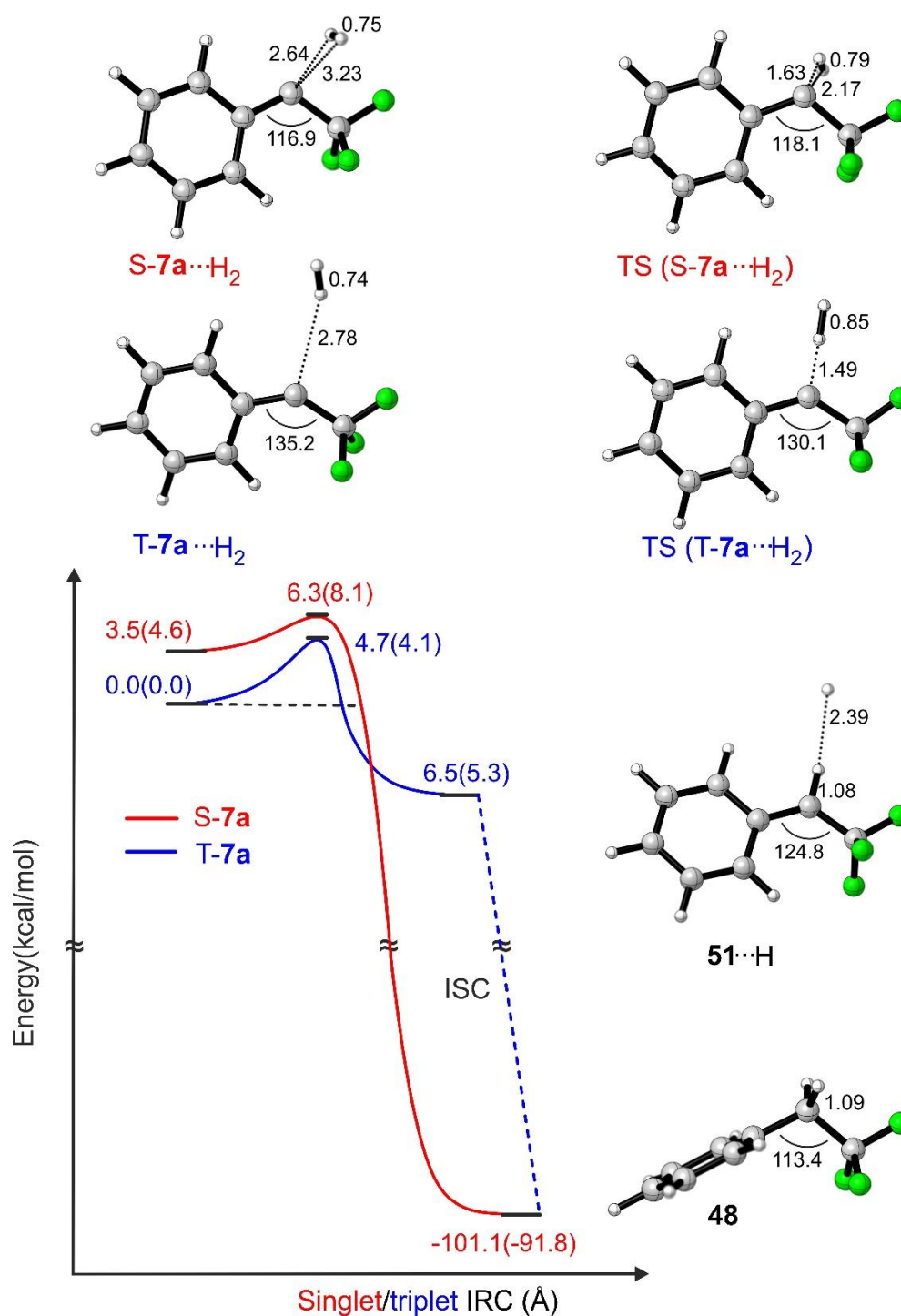


**Figure 55.** Optimized geometries of the hydrogenation reaction of phenyl(trifluoromethyl)carbene **7a** in the singlet (blue) and triplet (red) state calculated at the (U)B3LYP-D3/def2-TZVP level of theory. Energies are given in kcal/mol relative to triplet carbene hydrogen complex S-7a···H<sub>2</sub> (values in parentheses include ZPVE).

## Conclusion

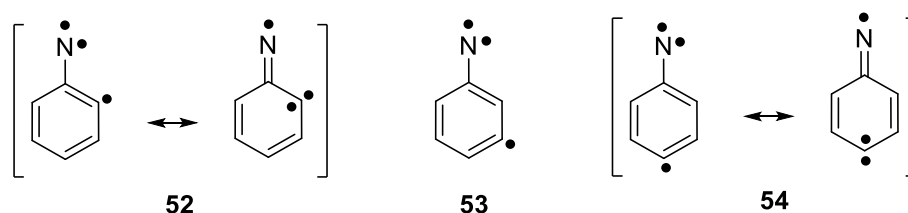
The reactivity of aryl(trifluoromethyl)carbenes **7a** and **7b** were carried out in solid H<sub>2</sub> and D<sub>2</sub> matrices and characterized by IR, UV–vis and EPR spectroscopy as well as by DFT calculations. Both carbenes, despite their spin-states, were not observed in H<sub>2</sub>-matrix but they

were detected in solid D<sub>2</sub> at 3 K. Whereas, carbenes **7a** and T-**7b** were only metastable and slowly rearranges even at 3 K to give the corresponding insertion products [D<sub>2</sub>-**48**] and [D<sub>2</sub>-**47**], respectively, with reaction rate in the order of 10<sup>-5</sup>, S-**7b** was found unreactive against D<sub>2</sub> under our experimental conditions. The high activation barriers (3–6 kcal/mol), the remarkable KIE and the reaction itself happening at 3 K suggest that the hydrogenation of aryl(trifluoromethyl)carbenes to form H<sub>2</sub>-insertion product is assisted by QMT. However, the calculation at the (U)B3LYP-D3/def2-TZVP level of theory does not plainly explain why S-**7b** is less reactive than T-**7b** against hydrogen.

## 6. Dehydroarylnitrenes

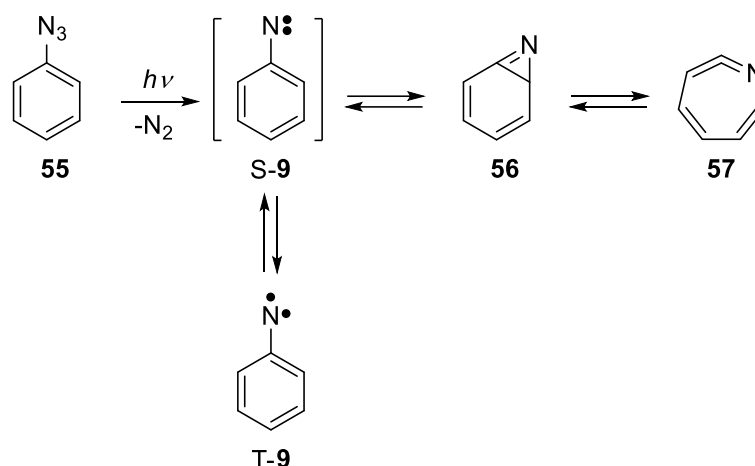
### Introduction

The chemistry of arylnitrenes have been investigated in detail both experimentally and theoretically for the last 50 decades.<sup>[50, 162]</sup> More recently, researchers in our group investigated a new class of intermediate by introducing additional radical center at the aromatic ring.<sup>[163-165]</sup> The resulting species is called dehydroarylnitrenes also known as arylnitreno radicals. Briefly, dehydroarylnitrenes are  $\sigma$ ,  $\sigma$ ,  $\pi$  - triradicals which bear one  $\sigma$ - and one  $\pi$ - electron at a nitrene center and one additional  $\sigma$  - radical center at the aromatic ring. These class of intermediates show relatively large zero field splitting (ZFS) parameter E values compared to arylnitrenes. The origin of these E values is the carbene character of the systems (Scheme 22).<sup>[166]</sup> The ground state of dehydroarylnitrenes can be either a low spin doublet such as **53** or a high spin quartet (**52**, **54**) depending on the electron structure of the system,<sup>[165]</sup> which has been described in detail in a preceding work elsewhere.<sup>[167]</sup>



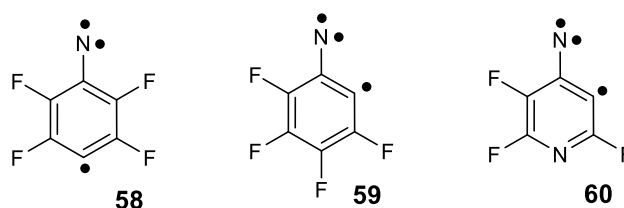
**Scheme 22.** Dehydrophenylnitrenes.

A common synthetic route to dehydrophenylnitrenes starts from iodophenylazide precursors. Upon UV irradiation (254 nm), the iodophenylazides release a nitrogen molecule to form triplet phenylnitrenes as the primary photoproduct. After subsequent irradiation with the same wavelength the C–I bond is cleaved and the triradicals are formed. However, phenylnitrenes are photolabile and easily rearranges to azirine **56** and ketenimine **57** (Scheme 23).<sup>[168]</sup> Therefore, the yield of dehydrophenylnitrenes is generally quite low due to competing with these kind of rearrangements. So far, triradicals **52-54** have not been detected even with the highly sensitive EPR spectroscopy.

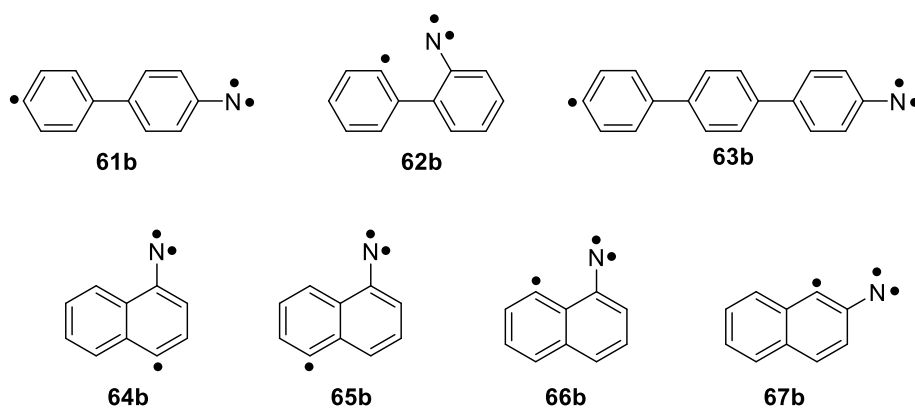


**Scheme 23.** Photochemistry of phenylazide.

In order to use dehydrophenylnitrenes in practical applications, their thermal and photochemical rearrangement must be inhibited. One approach is through *ortho* substitution of the nitrene moiety by fluorine atoms as to extend the life time of the nitrenes.<sup>[169]</sup> Using this strategy several quarter nitrenes such as **58-60** could be characterized under matrix isolation EPR and IR spectroscopy.<sup>[170-172]</sup>



Here we extend these works and investigate if triradicals can be generated by introducing spin centers into the biphenyl, terphenyl and naphthyl rings even if there are no fluorine substituents in *ortho* position to the nitrene centers. It is also interesting to see whether the same spin polarization considerations that can predict the spin state of dehydrophenylnitrenes also be applied to biphenyl, terphenyl and naphthyl systems that have more possible positions for spin centers at the aromatic ring and how the carbene character in these systems influence the ZFS parameters of the quartet systems. For this reason, triradicals compiled in Scheme 24 are investigated. Topology rules predicted quartet ground states for **61b-65b** and **67b** in contrast to a doublet ground state for triradical **66b**. This can be rationalized in terms of resonance structure similar to the description in Scheme 22.

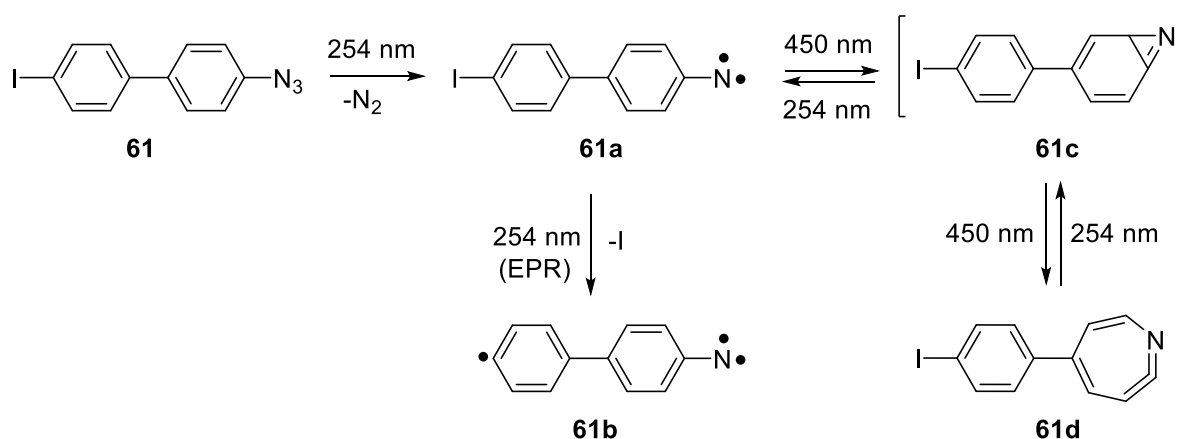


**Scheme 24.** Dehydroarylnitrenes investigated in this work.

## Results and discussion

### Photochemistry of iodobiphenylazides and terphenylazide

The main findings from these experiments are summarized in Scheme 25 for the case of **61**. As for phenylazides (Scheme 22),<sup>[168]</sup> the primary photoproduct of iodobiphenylazides **61**, **62** and terphenylazide **63** are the corresponding nitrenes **61a**, **62a** and **63a** respectively, which can undergo ring rearrangement reactions on the singlet surface quite similar to those observed for phenylnitrenes. Likewise, under prolonged irradiation these nitrenes are converted to the corresponding quartet systems **61b-63b** (Scheme 25).



**Scheme 25.** Photochemistry of iodobiphenylazide **61**.

### IR spectroscopy

Upon irradiation of 4,4'-iodobiphenylazide **61** in argon matrix at 3 K with UV light (254 nm) new IR absorptions are formed, the most intense bands appear at 806.8, while the IR bands of

the azide decrease. By comparing with DFT calculations at the UB3LYP/6-311G(d,p) level of theory, the newly formed species is assigned to 4,4'-iodobiphenylnitrene **61a**. Further irradiation of the same matrix with 450 nm results in the formation of a new set of IR bands which can be assigned to ketenimine **61d** (Figure 56). The characteristic cumulene bond is obtained at  $1890.9\text{ cm}^{-1}$ . The formation of the ketenimine is reversible, irradiation ( $\lambda = 254\text{ nm}$ ) of the matrix containing **61d** yields again nitrene **61a**. The analogues 2,2'-iodobiphenylazide **62** showed similar photochemistry with the characteristic IR bands of ketenimine **62d** observed at  $1867.1\text{ cm}^{-1}$ . As expected, the yield of nitrene **62a** is quite low due to rapid rearrangement to ketenimine **62d** and other species.<sup>[173]</sup>

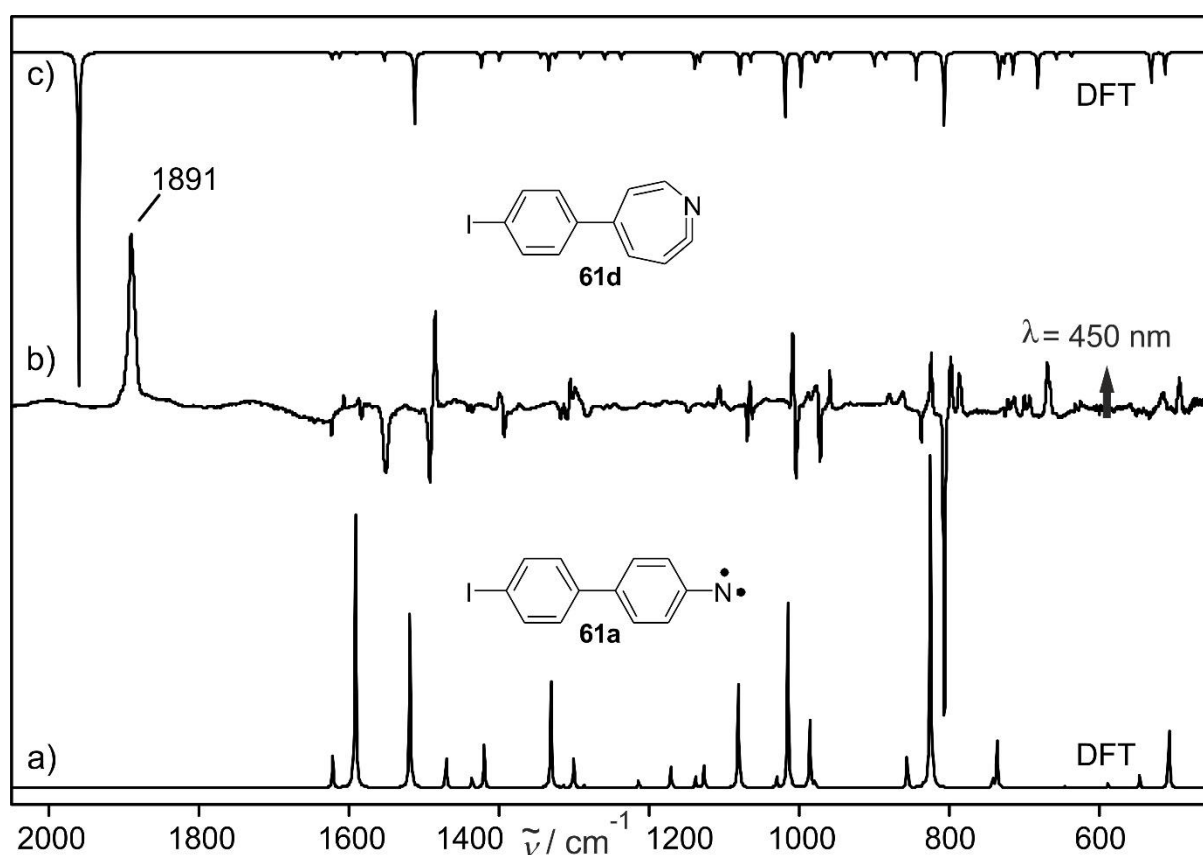


**Figure 56.** IR spectra showing the rearrangement of **61a** to ketenimine **61d** in argon matrix at 3 K. a) IR spectrum of **61a** calculated at the B3LYP/6-311G(d,p) level of theory. b) Difference IR spectrum showing the **61a** to **61d** rearrangement with 10 min of 450 nm irradiation. c) IR spectrum of **61d** calculated at the B3LYP/6-311G(d,p) level of theory.

### UV–vis spectroscopy

Similar experiments were carried out using UV–vis spectroscopy. UV light photolysis ( $\lambda = 254\text{ nm}$ ) of **61** produces the UV–vis spectrum shown in Figure 57 with strong absorptions stretching from 280 to 350 nm. These absorptions can be assigned to 4,4'-iodobiphenylnitrene

**61a** in accordance to previous studies on *para*-biphenylnitrene.<sup>[173]</sup> Next, a broad band with  $\lambda_{\text{max}} = 250$  nm appears after 450 nm irradiation and completely disappears after 254 nm irradiation, and thus is assigned to ketenimine **61d**. This process was reproducible in repeated 254 nm / 450 nm irradiation cycles. Likewise iodoterphenylazide **63** has maximum absorption at 294 nm. Irradiation in to this band (254 nm) produces nitrene **63a** with a series of absorptions stretching from 245 to 460 nm.

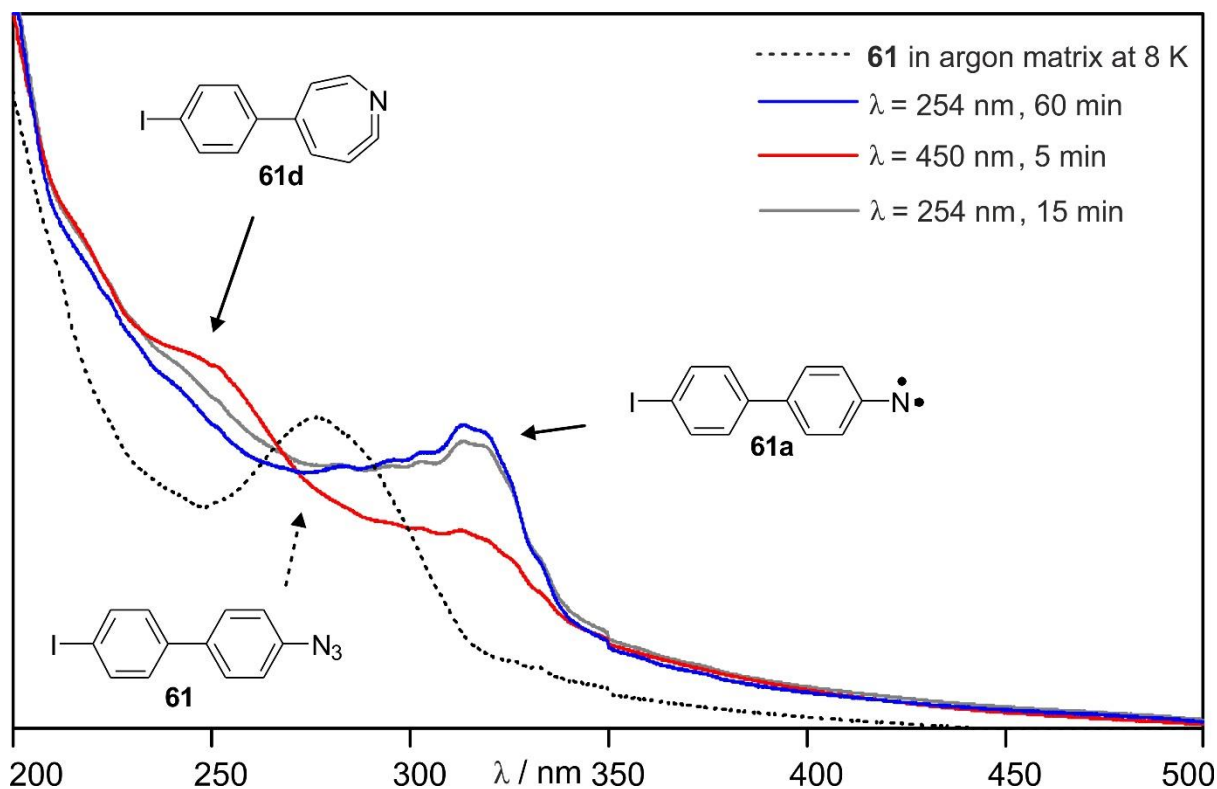


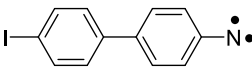
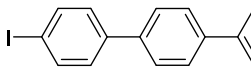
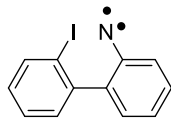
**Figure 57.** UV-vis spectra showing the rearrangement of **61a** to ketenimine **61d** in argon matrix at 8 K. (a) 4,4'-iodobiphenylazide **61** (dotted black line). (b) Spectrum of **61a** obtained after 30 min irradiation of **61** with  $\lambda = 254$  nm (blue line). (c) Spectrum of **61d** obtained after 5 min irradiation of **61a** with  $\lambda = 450$  nm (red line). (d) Spectrum of **61a** obtained after 15 min irradiation of **61d** with  $\lambda = 254$  nm (gray line).

### EPR spectroscopy

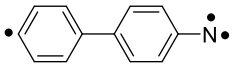
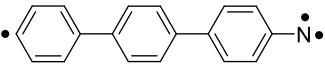
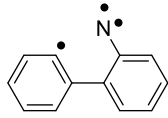
We did not observe the formation of quartets **61b**, **62b** and **63b** in the IR and UV-vis detection, similar to previous studies on dehydrophenylnitrenes.<sup>[172]</sup> This can be characterized with the more sensitive EPR spectroscopy under the conditions of matrix isolation. Figure 58 shows the X-band EPR spectra after irradiation (254 nm) of arylazides **61-63** in argon matrix at 4 K. Intense  $x^2N$  and  $y^2N$  signals of the triplet nitrenes **61a**, **62a**, **63a** can be observed around 6700 G. Simulation of the EPR signals yields  $|D/hc|$  and  $|E/hc|$  ( $\text{cm}^{-1}$ ) values for **61a** (0.930 and 0.001), **62a** (1.021 and 0.001) and **63a** (0.937 and 0.001), respectively. Additional weak signals,

obtained after prolonged irradiation, can be assigned to a quartet system  $S = 3/2$  by simulation, resulting the ZFS parameters of  $|D/hc|$  and  $|E/hc|$  ( $\text{cm}^{-1}$ ) for **61b** (0.276 and 0.009), **62b** (0.289 and 0.005) and **63b** (0.276 and 0.004), respectively. An intense signal around  $g = 2$  is formed showing radical decomposition products.

This values can be interpreted similar to our discussion in preceding chapters. The D value is related to the spin density ( $\rho$ ) at the nitrogen atom. The  $\rho$  of **61a** and **63a** at the B3LYP/6-31G(d,p) level of theory is the same ( $\rho = 1.55$ ). Hence, the D values of **61a** (0.930) and **63a** (0.937) are very close (Scheme 26). However, due to the heavy iodine atom present at a proximity distance, nitrene **62a** is experiencing a very huge spin-orbit coupling which influenced the D value significantly.<sup>[166]</sup> For the same reasons, the D value of quartet **63b** is close to a value obtained for **61b** (Scheme 27). On the other hand the E values of quartet nitrenes are measuring the carbene character of the systems, and thus related to the spin density at their radical center. Compared to quartet **61b** (0.009), **63b** has smaller E value (0.004).

			
	<b>61a</b>	<b>63a</b>	<b>62a</b>
$ D  / \text{cm}^{-1} =$	0.930	0.937	1.021
$ E  / \text{cm}^{-1} =$	0.001	0.001	0.001
$\rho_N =$	1.55	1.55	1.57

**Scheme 26.** ZFS parameters and Mulliken spin density (B3LYP/6-31G(d, p)) at the nitrene centers of **61a-63a**.

			
	<b>61b</b>	<b>63b</b>	<b>62b</b>
$ D  / \text{cm}^{-1} =$	0.2756	0.2764	0.2891
$ E  / \text{cm}^{-1} =$	0.009	0.004	0.005
$\rho_N =$	1.55	1.54	1.56
$\rho_C =$	1.04	0.99	1.02

**Scheme 27.** ZFS parameters and Mulliken spin density (B3LYP/6-31G (d, p)) at the nitrene ( $\rho_N$ ) and radical centers ( $\rho_C$ ) of **61b-63b**.

Calculation of the ZFS parameters at the B3LYP/6-31G(d,p) level of theory are compiled in Table 16. The agreement between experimental findings and calculations are reasonable. As expected, the largest contribution to the ZFS tensor is the spin-spin interaction, which amounts

89.5 % in **61b**, 90.1 % in **62b** and 89.7 % in **63b** of the total D value. The other contribution to D is coming from the spin-orbit coupling, 10.5 % in **61b**, 9.9 % in **62b** and 10.3 % in **63b**.

**Table 16.** Analysis of the calculated D-tensor (in  $\text{cm}^{-1}$ ) of **61b**, **62b** and **63b** at the B3LYP/6-31G (d, p) level of theory.

		<b>61b</b>		<b>63b</b>		<b>62b</b>	
		D	E	D	E	D	E
Experiment		0.2756	0.0090	0.2764	0.0040	0.2891	0.0050
Calculations	Total	0.2754	0.0030	0.2816	0.0009	0.3219	0.0272
	Spin-spin	0.2466	0.0029	0.2528	0.0001	0.2900	0.0269
	Spin-orbit	0.0288	0.0001	0.0288	0.0008	0.0319	0.0003

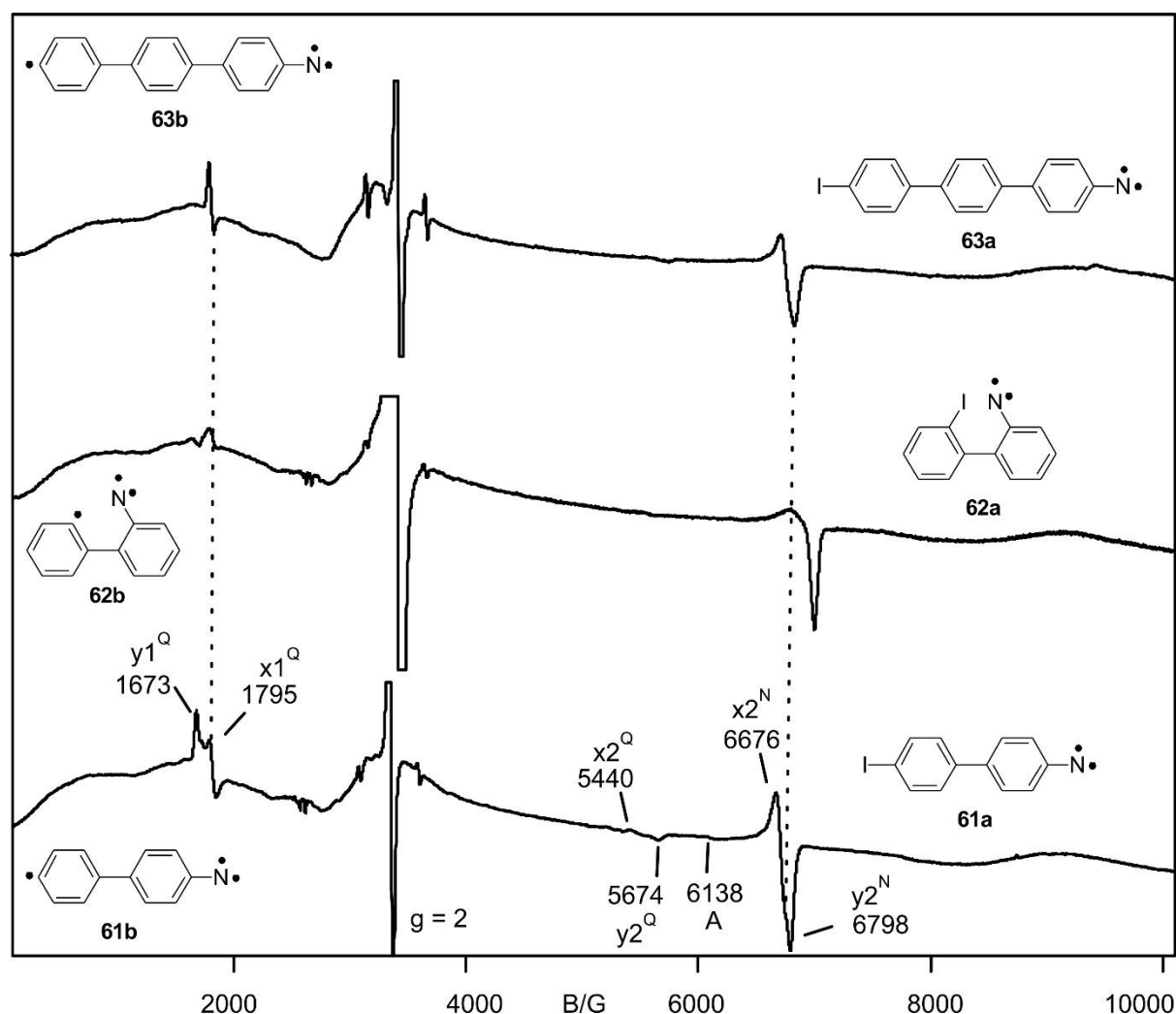
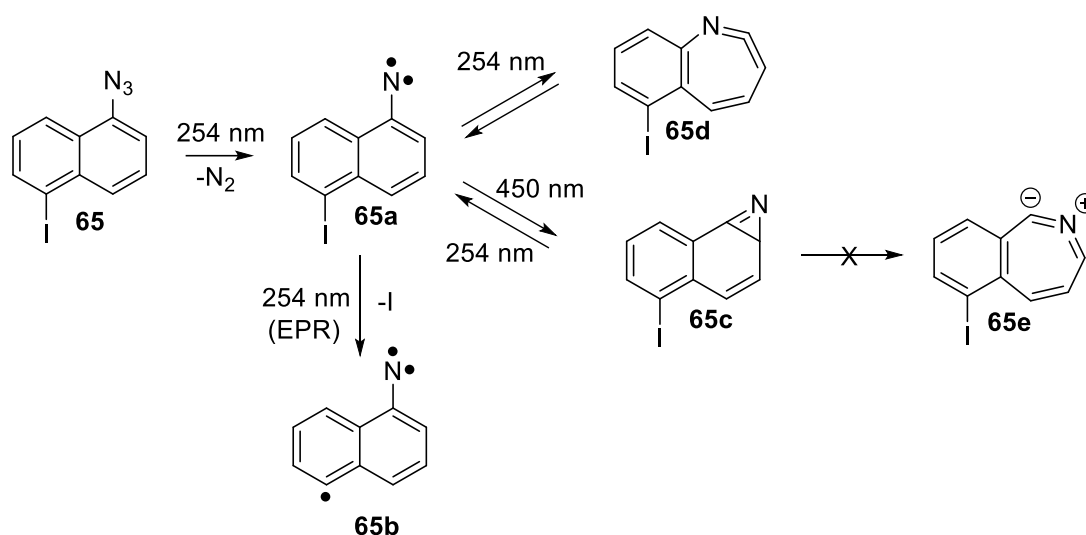


**Figure 58.** X-band CW EPR spectra of triplet iodobiphenylnitrenes and terphenylnitrene (signals marked with N) together with quartet dehydrobiphenylnitrenes and dehydroterphenylnitrene (signals marked with Q) matrix-isolated in argon at 4 K. The ZFS parameters of these species are compiled in Schemes 26 and 27, and Table 16. All nitrenes were generated by prolonged 254 nm irradiation of the corresponding diazo precursors.

## Photochemistry of iodonaphthylazides

We reported the photochemistry of iodonaphthylazides in detail in a preceding work.<sup>[167]</sup> Here we focus on results which are not included in the previous report. The main findings are summarized in Scheme 28 for the case of **65**. We found the photochemistry of iodonaphthylazides are quite similar to iodophenylazides. The only exception is that it has been suggested the kinetic and thermodynamics balances of the intermediates could be affected due to aromaticity of the second ring in naphthalene systems.<sup>[174]</sup> Accordingly, ketenimine is the major photoproduct from phenyl-, biphenyl-, and terphenylnitrenes in contrast to azirine for naphthylnitrenes.



**Scheme 28.** Photochemistry of 1,5-iodonaphthylazide **65**.

### IR spectroscopy

The photochemistry of 1,4-iodonaphthylazide **64** was investigated in argon matrix at 3 K. The primary photoproduct of **64** upon irradiation with UV light ( $\lambda = 254$ ) leads to the formation of a new set of bands assigned to nitrene **64a**. Irradiation of the argon matrix containing nitrene **64a** with 450 nm give rise to newly formed bands. Comparing with DFT calculations at the B3LYP/6-311G(d,p) level of theory, the newly formed species is assigned to azirine **64c** with characteristic band at  $1727.3\text{ cm}^{-1}$  (Figure 59).

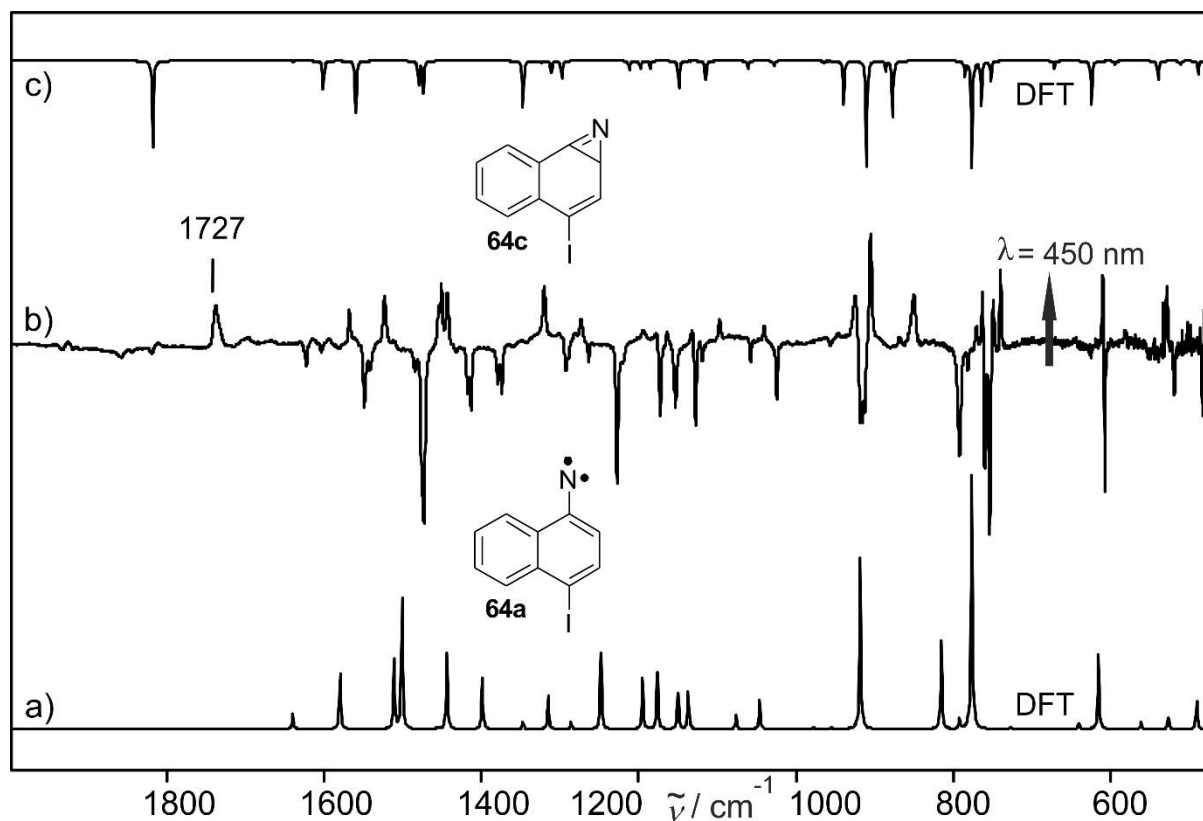


**Figure 59.** IR spectra showing the rearrangement of **64a** to azirine **64c** in argon matrix at 3 K. a) IR spectrum of **64a** calculated at the B3LYP/6-311G(d,p) level of theory. b) Difference IR spectrum showing the **64a** to **64c** rearrangement with 10 min of 450 nm irradiation. c) IR spectrum of **64c** calculated at the B3LYP/6-311G(d,p) level of theory.

Likewise, irradiation ( $\lambda = 254$  nm) of 1,8-iodonaphthylazide **66** isolated in argon matrix at 3 K leads to the formation of a set of new bands assigned to triplet 1,8-iodonaphthylnitrene **66a** (Figure 60). Upon prolonged irradiation ( $\lambda = 254$  nm), no further products could be generated. Ketenimine **66d** and ylide **66e** is not formed under these conditions. Irradiation of an argon matrix at 3 K containing nitrene **66a** with visible light ( $\lambda = 450$  nm) leads to the formation of azirine **66c**.

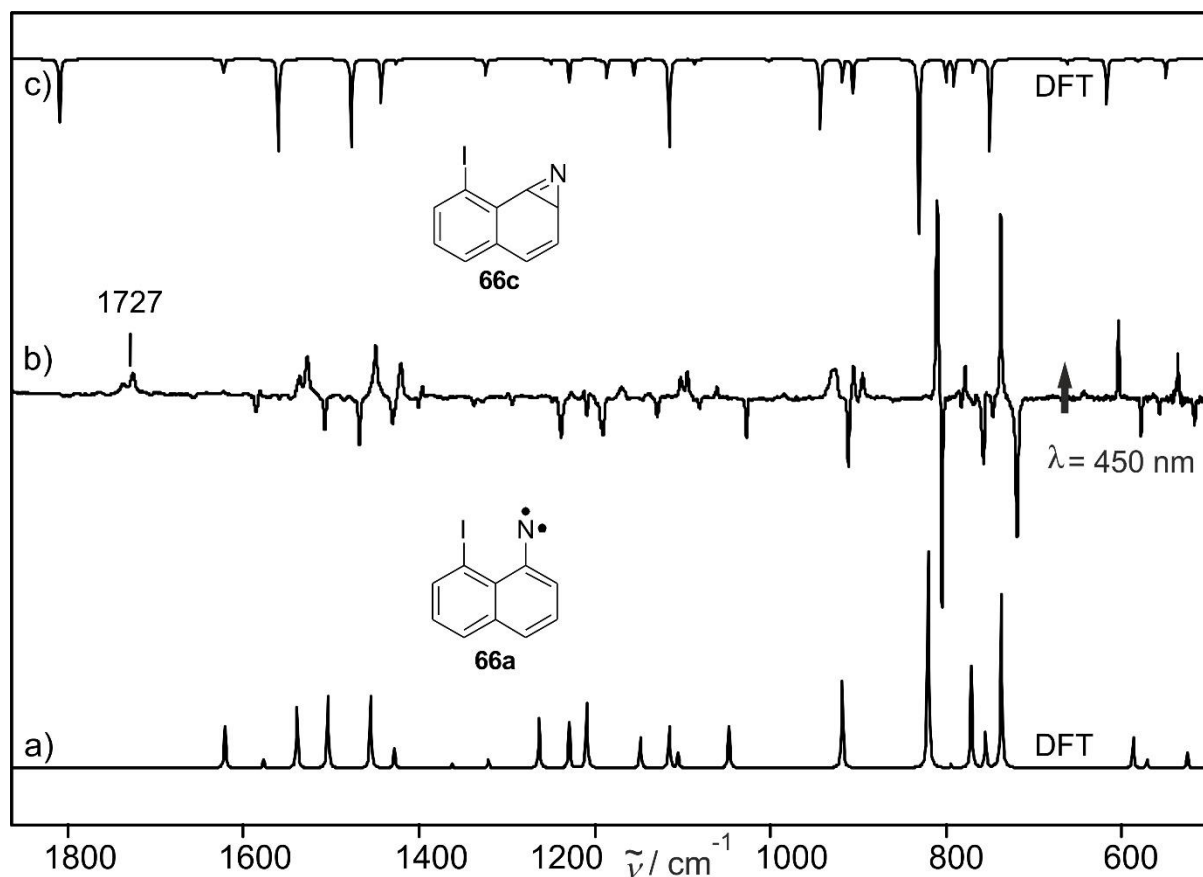


**Figure 60.** IR spectra showing the 450 nm photochemistry of **66a** after 5 min irradiation in argon matrix at 3 K. a) IR spectrum of **66a** calculated at UB3LYP/6-311 G (d,p) level of theory. b) Difference IR spectrum: Bands pointing downwards disappear during irradiation and belong to **66a**, bands pointing upward appear and are assigned to azirine **66c**. c) IR spectrum of **66c** calculated at the B3LYP/6-311 G (d,p) level of theory.

### UV-vis spectroscopy

Similar experiments were performed with a complementary UV-vis spectroscopy. Figure 61 shows the UV-vis spectra of nitrenes **64a-68a** after about 30 minutes of UV light ( $\lambda = 254$  nm) irradiation of the corresponding azides matrix-isolated in argon at 8 K. UV-vis spectra of these nitrenes show a series of absorption stretching from 200 to 620 nm. Noteworthy irradiation with 450 nm results in the rearrangement of nitrenes to the corresponding azirines.

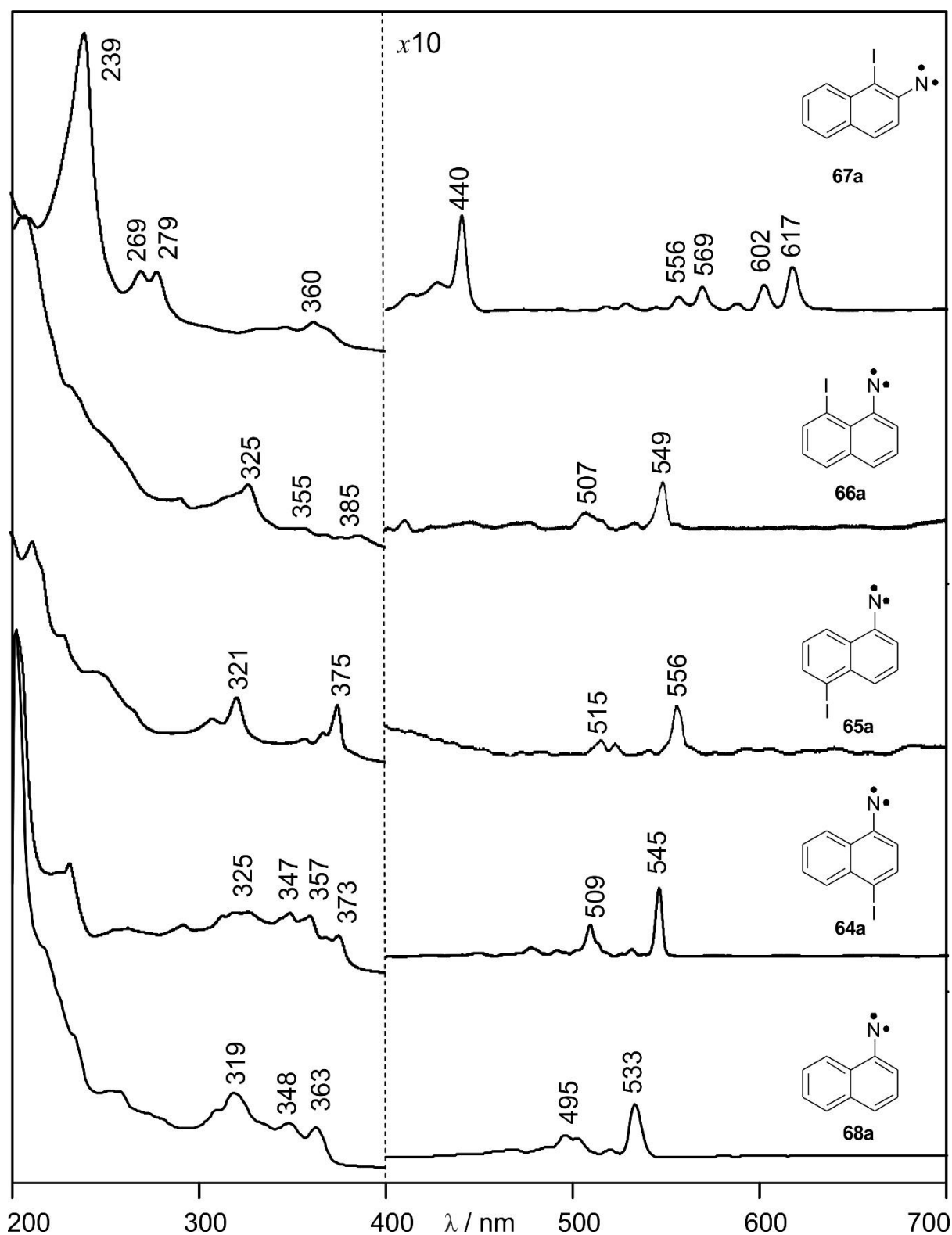


**Figure 61.** UV-vis spectra of naphthylnitrene **68a** and iodonaphthylnitrenes **64a-67a** obtained after about 30 minutes irradiation ( $\lambda = 254$  nm) of the corresponding azides matrix-isolated in argon at 8 K.

Furthermore, the rearrangement between nitrenes and azirines are found reversible. As an example, here we describe the photochemistry of 1,5-iodonaphthylazide **65** in detail. The

UV-vis experiments in argon matrix at 8 K shows a rapid decrease of the azide bands upon short time irradiation ( $\lambda = 254$  nm) and a rapid increase of newly formed stretching from 200 to 560 nm assigned to 1,5-iodonaphthyl nitrene **65a**. In accordance with the EPR and IR experiments, after short irradiation times, **65a** is the only detectable photoproduct. However, with prolonged irradiation with the same wavelength, all bands assigned to **65a** decrease, but no new bands appear (Figure 62c). This could be due to the transformation of the triplet to the quartet as well as to the ketenimine, even if the yield of these products might be too low to be detected or the new species are bad chromophores in the UV-vis region. These observations are comparable with the UV-vis data of **68** reported in literature.<sup>[174]</sup>

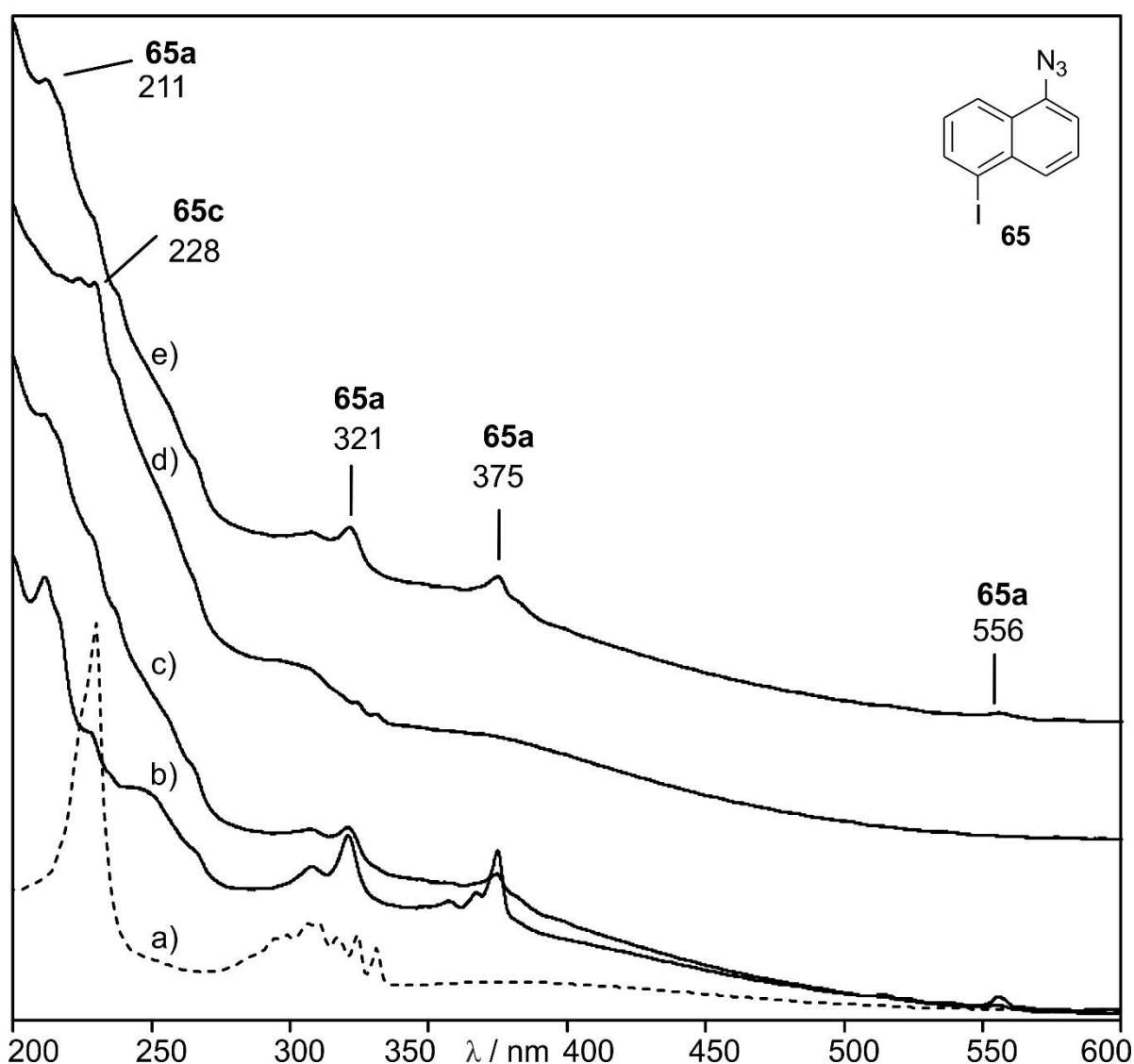


**Figure 62.** UV-vis spectra showing the photochemistry of 1,5-iodonaphthylazide **65** in argon matrix at 8 K. a) UV-vis spectrum of **65**. b) UV-vis spectrum of **65a** obtained after 30 minutes irradiation ( $\lambda = 254$  nm) of **65**. c) Prolonged irradiation of the same matrix (254 nm): bands of **65a** are decreasing but no new band is appearing. d) UV-vis spectrum of **65c** obtained after 10 minutes irradiation ( $\lambda = 450$  nm) of the same matrix. e) UV-vis spectrum of **65a** obtained after 10 minutes irradiation ( $\lambda = 254$  nm) of **65c**.

## EPR spectroscopy

Since we could not detect quartet dehydronaphthylnitrenes using IR and UV–vis spectroscopy, we employ a complementary highly sensitive EPR detection technique. Triplet nitrenes **64a–67a** are observed after short time irradiation (254 nm) of the corresponding naphthylazides **64–67**. The D value of the 2-naphthylnitrene **67a** is higher than the D values of the 1-naphthylnitrenes **64a–66a**, which is an accord with the ZFS parameters of the parent systems (1-naphthylnitrene:  $D/\text{cm}^{-1} = 0.793$ ; 2-naphthylnitrene:  $D/\text{cm}^{-1} = 0.925$ ).<sup>[175]</sup> There is also a correlation between the D value and the spin density ( $\rho$ ): **67a** bears the highest spin density at the nitrogen center and shows the highest D value whereas **66a** has both the lowest spin density and the lowest D value (Scheme 29). Note that, due to the heavy iodine atom present at the 8 position which has strong steric effect on the nitrene center, **66a** has extreme ZFS parameter D and E values comparing to the isomeric nitrenes.<sup>[166]</sup>

	<b>64a</b>	<b>65a</b>	<b>66a</b>	<b>67a</b>
$ D  / \text{cm}^{-1} =$	0.726	0.793	0.426	0.993
$ E  / \text{cm}^{-1} =$	0.009	0.009	0.046	0.001
$\rho =$	1.46	1.47	1.40	1.51

**Scheme 29.** ZFS parameters and Mullikan spin density (B3LYP/6-31G(d, p)) at the nitrene centers of **64a–67a**.

With prolonged irradiation (254 nm), we obtained quartet species for dehydronaphthylnitrenes **65b** ( $D = 0.2515$  and  $E = 0.0037 \text{ cm}^{-1}$ ) and **67b** ( $D = 0.3420$  and  $E = 0.0058 \text{ cm}^{-1}$ ), but for **66b** we could not observe signals because it is a doublet species and thus EPR inactive. On the other hand, triradical radical **64b** is expected to bear a quartet ground state, but is not observed in the EPR spectra as well.

Calculation of the ZFS parameters at the B3LYP level of theory are compiled in Table 17. The agreement between theory and experiment is reasonable. As expected, the largest contribution to the ZFS tensor is the spin-spin interaction, which amounts 88 % in **65b** and 89 % in **67b** of the total D value. The other contribution to D is coming from the spin-orbit coupling, 12 % in

**65b** and 11 % in **67b**. This is consistent with the analysis of ZFS contributions of dehydrobiphenylnitrenes and dehydroterphenylnitrene discussed before.

**Table 17.** Analysis of the calculated D-tensor (in  $\text{cm}^{-1}$ ) of **65b** and **67b** at the B3LYP/6-31G (d, p) level of theory.

		<b>65b</b>		<b>67b</b>	
		D	E	D	E
Experimental		0.2515	0.0037	0.3420	0.0058
Calculations	Total	0.2148	0.0040	0.2852	0.0132
	Spin-spin	0.1895	0.0029	0.2546	0.0112
	Spin-orbit	0.0250	0.0011	0.0310	0.0020

DFT calculations also shows that the nitrene radicals simultaneously have both nitrene and carbene character that contribute to the overall D tensor. As discussed in Chapter 1, the D-value correlates with the distance between the electrons along a z-axis. This interaction depends on the spin density at the nitrogen atom and the delocalization of the  $\pi$  electron into the aromatic ring, whereas the E value correlates with the difference of the spin density perpendicular to this axis in an xy plane in a cylindrical symmetry naphthalene molecule. The spin population at the radical center is a measure for the carbene character of the spin system, resulting in magnetically inequivalent xy-directions and reflect the E value of the system.

The direction of the x,y,z – axes of quartet **65b** and **67b** are shown in Figure 63. The z axes of the nitrene radical is parallel or anti-parallel to the C-N bond, while the xy plane is perpendicular to the molecular plane and the z axis. The D value of nitreno radical **65b** is relatively lower than **67b** which explains in terms of spin population on the nitrogen center, i.e., 1.42 in **65b** and 1.54 in **67b**. Likewise the spin population at the radical center in **65b** (1.08) is relatively lower than in **67b** (1.42) which explains the low E value in **65b** due to less carbene contribution to the dipolar interaction.

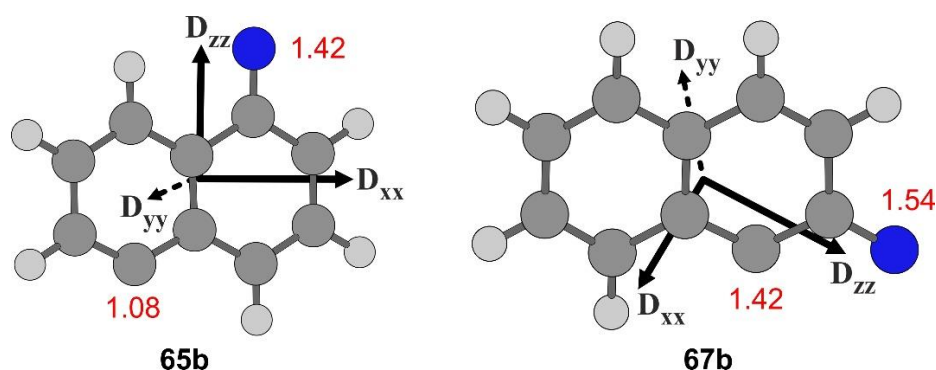


**Figure 63.** Orientation of the magnetic axes of **65b** and **67b** and Mulliken spin density (B3LYP/6-31G(d, p)) at the nitrene- and radical centers.

## Conclusion

The photochemistry of iodinated biphenyl-, terphenyl- and naphthyl- azides (**61-67**) were investigated in argon matrices at 3–8 K and characterized by EPR, IR and UV-vis spectroscopy as well as quantum chemical calculations. The primary photoproducts, as expected, are the corresponding nitrenes (**61a-67a**). These nitrenes are highly photolabile and rearranges to the corresponding ketenimine and azirine, in accordance to the photochemistry of the parent arylnitrene molecules (without the iodine group). Despite these competing rearrangements, however, prolonged irradiation of nitrenes **61a-67a** produced the analogues quartet dehydroarylnitrenes, which was detected by EPR spectroscopy. The obtained ZFS parameters  $D$  and  $E$  are related to the spin density at their nitrene and radical centers, respectively. Among all the quartet species investigated, the  $E$  value of terphenylnitrene **63b** is lower, suggesting that the interaction between the nitrene and the radical center of **63b** is very weak.

## 7. Formation of hydroxylamine in interstellar model ices

### Introduction

As discussed in the introduction section, ISM is host to a rich chemistry. With the number of molecules detected in space increasing in number and growing in complexity, one of the main goals of astrochemistry today is therefore to link astrochemistry to astrobiology. In this context, the hydroxylamine molecule ( $\text{NH}_2\text{OH}$ ) has received considerable attention due to its potential role as a precursor to biorelevant molecules like amino acids.<sup>[176-178]</sup>

Theoretical and laboratory studies suggest that protonated glycine ( $\text{NH}_3\text{CH}_2\text{COOH}^+$ ) and  $\alpha$ - ( $\text{NH}_3\text{CH}_2\text{CH}_2\text{COOH}^+$ ) or  $\beta$ -alanine ( $\text{CH}_3\text{CH}(\text{NH}_3)\text{COOH}^+$ ) might be formed in the gas phase via the reaction of protonated hydroxylamine ( $\text{NH}_3\text{OH}^+$ ) with acetic acid ( $\text{CH}_3\text{COOH}$ ) and propanoic acid ( $\text{CH}_3\text{CH}_2\text{COOH}$ ), respectively (Reactions 1–3).<sup>[176-177]</sup> Dissociative recombination with an electron was proposed to yield amino acids (Reactions 4–6). While acetic acid is a well-known interstellar molecule<sup>[179-181]</sup> and propanoic acid is a plausible species in the regions where acetic acid is found,<sup>[182]</sup> hydroxylamine has not been observed so far in the ISM although the stability of ionized and protonated hydroxylamine<sup>[183-184]</sup> (Reactions 7 and 8) was revealed computationally<sup>[177-178]</sup> as well as experimentally.<sup>[176, 185]</sup>



Therefore, recent laboratory studies focused on the formation of hydroxylamine in the condensed phase on ice-coated interstellar grains at temperatures as low as 10 K. Upon irradiation of a mixture of ammonia ( $\text{NH}_3$ ) and water ( $\text{H}_2\text{O}$ ) ices with UV photons,<sup>[186]</sup> electrons,<sup>[187]</sup> and heavy ions of nickel and zinc,<sup>[188]</sup> hydroxylamine was efficiently formed through radical-radical recombination involving amidogen ( $\text{NH}_2$ ) and hydroxyl radicals ( $\text{OH}$ )(Reaction 9). Via modeling, Charnley et al proposed that hydroxylamine might also be

formed through successive hydrogenation reaction of nitric oxide (NO) ice under dark cloud conditions (Reaction 10).<sup>[189]</sup> This was confirmed experimentally.<sup>[190-195]</sup> Recently, He et al reported the formation of hydroxylamine on amorphous silicate surfaces via oxidation of ammonia at 70 K (Reaction 11), but mechanistical details are absent.<sup>[196]</sup>



Astrochemical models propose that the formation of hydroxylamine involves radical-radical reactions *within* the ice-coated interstellar grains. The chemical models developed by Garrod et al<sup>[197-198]</sup> considered NH, NH<sub>2</sub>, and OH radicals along with hydrogen atoms; these are produced by GCR-induced dissociation of ammonia and water molecules in the ice. The model speculated that the radicals are not mobile at 10 K, and only become mobile on the grain surface and eventually take part in successive radical reactions upon heating. Moreover, a model by He et al suggested that the oxidation of ammonia represents an efficient pathway for the formation of hydroxylamine in the condensed phase on ice-coated interstellar grains. These studies were expanded computationally revealing that hydroxylamine might be formed by radical-radical recombination such as reactions between the amidogen (NH<sub>2</sub>) and the hydroxyl radical (OH) (Reaction 9)<sup>[199]</sup> or via oxidation of ammonia (Reaction 11).<sup>[200]</sup>

Although laboratory work and theoretical studies demonstrated the possibility of the formation of NH<sub>2</sub>OH in the ISM, it has not been detected in space. Several unsuccessful attempts were reported that struggled to detect the emission of NH<sub>2</sub>OH toward a selection of bright sources including the Galactic center hot-core source Sgr B2(N) using the NRAO<sup>[201]</sup> as well as toward the L1157-B1 and B2 shocked regions using CSO and CARMA.<sup>[202]</sup>

Considering the fact that ammonia is present in icy mantles of interstellar grains at levels of up to 30% of water,<sup>[64-66, 203-205]</sup> we probe the hypothesis to what extent hydroxylamine can be formed *inside* interstellar ices via reactions of ammonia (NH<sub>3</sub>) with oxygen atoms (O). Suprathermal oxygen atoms, which are not in equilibrium with the surrounding ice, can be generated from oxygen bearing molecules like water,<sup>[76, 206-208]</sup> carbon dioxide (CO<sub>2</sub>),<sup>[209]</sup> and methanol (CH<sub>3</sub>OH)<sup>[210]</sup> at temperatures as low as 5 K. The newly formed hydroxylamine (NH<sub>2</sub>OH) molecules along with their fully deuterated counterparts (ND<sub>2</sub>OD) molecule were

probed via infrared spectroscopy *online* and *in situ* during the processing of astrophysically relevant ices by energetic electrons as a proxy for secondary electrons generated in the track of GCRs penetrating ices on interstellar grains.<sup>[211-212]</sup> Quantitatively, rate constants are calculated and the formation mechanisms are discussed based on the kinetic profiles fit by solving the set of coupled differential equations.<sup>[213-214]</sup> After irradiation, the newly formed molecules were allowed to sublime during the controlled heating of the irradiated samples to 300 K (temperature programmed desorption; TPD). During this phase, the solid state (ices) was monitored spectroscopically in the infrared, while the gas phase was probed via single photon reflectron time-of-flight mass spectroscopy (PI-ReTOF-MS).

## Results and discussion

### IR spectroscopy

Experimental details on how we prepared the ices and a step-by-step procedures on our experiments are compiled in the experimental section.

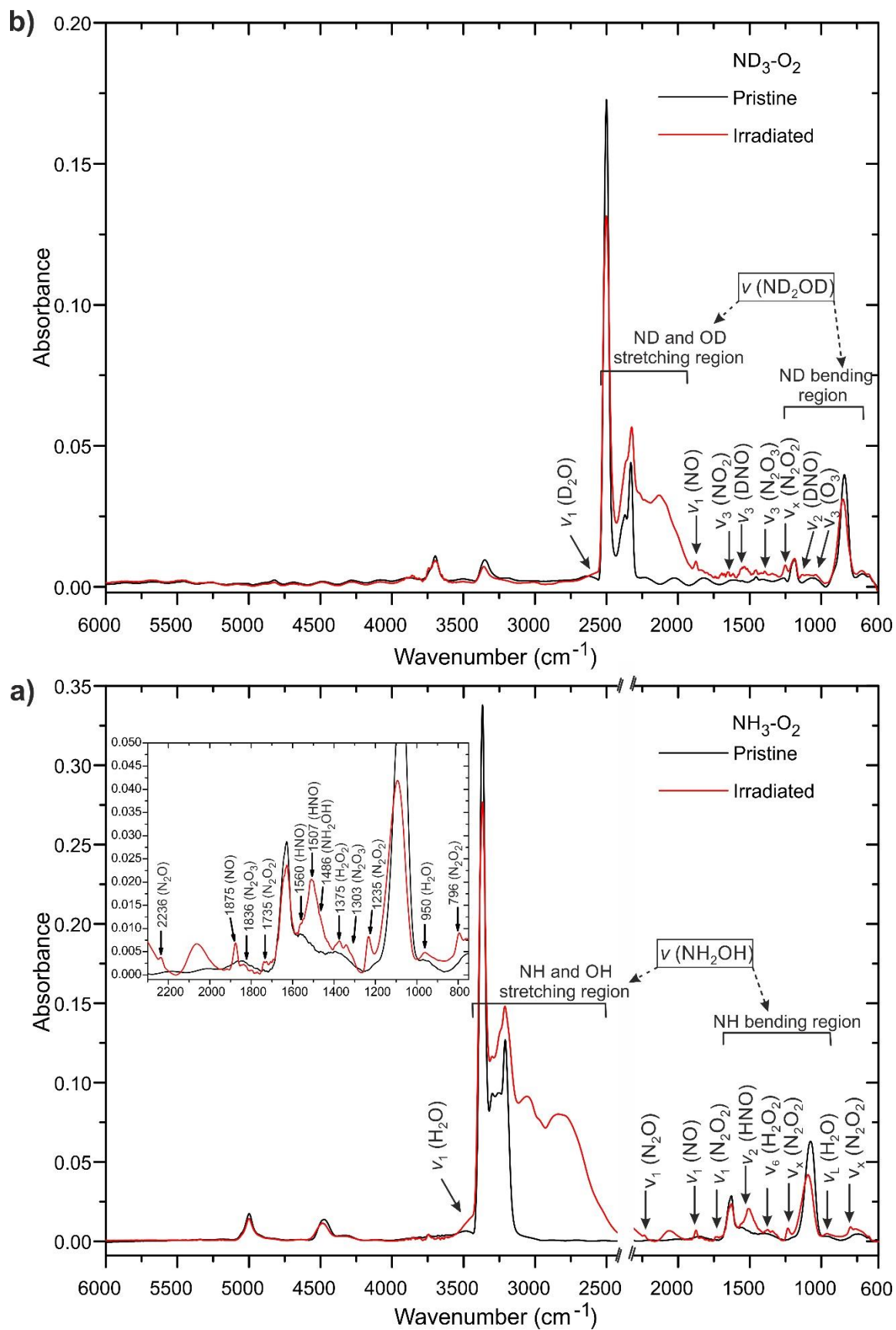
### Qualitative analysis

Figure 64 reveals the IR spectra of the electron-irradiated ammonia–oxygen ( $\text{NH}_3\text{-O}_2$ ) and D3-ammonia–oxygen ( $\text{ND}_3\text{-O}_2$ ) ices before and after the irradiation. The newly formed species after the radiolysis are identified and compiled along with their vibrational assignments in Tables 18 and A1, respectively. Before irradiating the sample, the absorption peaks of the reactant molecule  $\text{NH}_3/\text{ND}_3$  are observed, which nicely match the IR spectra of solid ammonia ices reported previously.<sup>[75, 215-218]</sup> After the irradiation, the  $\text{NH}_3$  fundamentals at 3369 and 1077  $\text{cm}^{-1}$  and the  $\text{ND}_3$  absorptions at 2500 and 840  $\text{cm}^{-1}$  decrease significantly in intensity. Nitrogen monoxide (NO) with its absorption band appears at 1875  $\text{cm}^{-1}$  and dinitrogen dioxide ( $\text{N}_2\text{O}_2$ ) at 1735  $\text{cm}^{-1}$  were evident in the electron-irradiated (D3-) ammonia–oxygen ices.<sup>[191, 194, 219-220]</sup> The IR absorptions bands at 1235 and 796  $\text{cm}^{-1}$  in the irradiated ammonia–oxygen ices and at 1252 and 796  $\text{cm}^{-1}$  in the irradiated (D3-) ammonia–oxygen ices are assigned to dinitrogen dioxide ( $\text{N}_2\text{O}_2$ ) based on its IR TPD profile, which was growing during the warm-up phase of the ice simultaneously with the decay of the NO band.<sup>[221]</sup> Further, a new band at 2236  $\text{cm}^{-1}$  from ammonia–oxygen ices was assigned to nitrous oxide ( $\text{N}_2\text{O}$ ) in accordance with literatures value.<sup>[191, 194, 222]</sup> A weak band at 1616  $\text{cm}^{-1}$  in the irradiated  $\text{ND}_3\text{-O}_2$  sample is attributed to the antisymmetric stretch  $\nu(\text{N-O})$  of nitrogen dioxide ( $\text{NO}_2$ ) in agreement with the

literature value at  $1614\text{ cm}^{-1}$ .<sup>[222]</sup> However, this band is hidden in the irradiated ammonia–oxygen ( $\text{NH}_3\text{--O}_2$ ) ice by the intense  $\text{NH}_3$  fundamental. Small, but distinct levels of dinitrogen trioxide ( $\text{N}_2\text{O}_3$ ) were observed in both irradiated ices at  $1836$  and  $1303\text{ cm}^{-1}$ .<sup>[191, 194, 219, 223]</sup>

The next species observed in the irradiated  $\text{NH}_3\text{--O}_2$  ices at  $5.5\text{ K}$  is  $\text{HNO}$  with its stretching and bending fundamental absorption bands appearing at  $1560$  and  $1507\text{ cm}^{-1}$ , respectively, in agreement with literature values.<sup>[191, 224–225]</sup> Similarly, the fundamental absorption bands of  $\text{DNO}$  at  $1543$  and  $1135\text{ cm}^{-1}$  were found in the irradiated  $\text{ND}_3\text{--O}_2$  ices at  $5.5\text{ K}$ .<sup>[191, 224]</sup> Furthermore,  $\text{H}_2\text{O}$  could be identified with its out-of-phase symmetric stretch appearing at  $3452\text{ cm}^{-1}$  and the libration band at  $950\text{ cm}^{-1}$  in the electron-irradiated  $\text{NH}_3\text{--O}_2$  ices.<sup>[76]</sup> Note that assignments of other bands of water such as the in-phase symmetric stretch were difficult at  $5.5\text{ K}$  due to overlying absorption of  $\text{NH}_3$ . Similarly, the two bands in the energetic electron-irradiated  $\text{ND}_3\text{--O}_2$  ices at  $2567$  and  $708\text{ cm}^{-1}$  were assigned to  $\text{D}_2\text{O}$ , in agreements with the literature data at  $2572$  and  $701\text{ cm}^{-1}$ .<sup>[206]</sup> Next, a weak band appearing at  $1038\text{ cm}^{-1}$  in the irradiated  $\text{ND}_3\text{--O}_2$  sample was assigned to the fundamental absorption band ( $\nu_3$ ) of ozone ( $\text{O}_3$ ), in accordance with literature value at  $1037\text{ cm}^{-1}$ .<sup>[226]</sup> This band could not be detected in the irradiated  $\text{NH}_3\text{--O}_2$  ices due to overlapping absorption of  $\text{NH}_3$  and  $\text{NH}_2\text{OH}$ . Further, a new band at  $1375\text{ cm}^{-1}$  in the irradiated  $\text{NH}_3\text{--O}_2$  ices was tentatively assigned to antisymmetric bending ( $\nu_6$ ) vibration of  $\text{H}_2\text{O}_2$ , in agreement with the literature data at  $1389\text{ cm}^{-1}$ .<sup>[76]</sup> However, the analogues  $\text{D}_2\text{O}_2$  could not be detected in the irradiated  $\text{ND}_3\text{--O}_2$  ices due to overlying absorption of  $\text{O}_3$ .

Finally, a set of new bulk absorptions appeared at about  $3213$ ,  $3024$ ,  $2748$  and  $1145\text{ cm}^{-1}$  that raised during radiation exposure of  $\text{NH}_3\text{--O}_2$  ice at  $5.5\text{ K}$ . These bands were persistent on the substrate up to about  $200\text{ K}$  and were assigned to  $\text{NH}_2\text{OH}$  in accordance with literature values.<sup>[187, 191]</sup> Although  $\text{NH}_2\text{OH}$  was produced in irradiated ice at  $5.5\text{ K}$  (Figure 64a), it was difficult to assign all absorptions at  $5.5\text{ K}$  due to broadening and overlapping of peaks. In the  $\text{NH}$  bending region  $\text{NH}_2\text{OH}$  peaks were overlapping mainly with the aforementioned species, whereas in the  $\text{NH}$  and  $\text{OH}$  stretching region they were masked by the host molecule  $\text{NH}_3$  as well as by  $\text{H}_2\text{O}$  peaks making the assignments difficult. Similarly, broad bands centered at about  $2346$ ,  $2267$ ,  $2075$  and  $881\text{ cm}^{-1}$  in the irradiated  $\text{ND}_3\text{--O}_2$  ices are assigned to  $\text{ND}_2\text{OD}$ .<sup>[191]</sup>



**Figure 64.** IR spectra of (a)  $\text{NH}_3\text{-O}_2$  and (b)  $\text{ND}_3\text{-O}_2$  ices at 5.5 K before (black line) and after (red line) the electron irradiation. The IR assignments are compiled in Tables 18 and A1.

**Table 18.** IR absorption features recorded before and after the electron irradiation of NH<sub>3</sub>-O<sub>2</sub> ices at 5.5 K.

Band position (cm <sup>-1</sup> )		ref.	Assignment <sup>a</sup>		
This work	Literature value		Species	Vibration	Characterization
Before irradiation					
5000	4994	[75]	NH <sub>3</sub>	$\nu_3 + \nu_4$	combination
4477	4478	[75]	NH <sub>3</sub>	$\nu_3 + \nu_2$	combination
4345	4345	[75]	NH <sub>3</sub>	$\nu_1 + \nu_2$	combination
3488	3472	[75]	NH <sub>3</sub>	$\nu_1 + \nu_L$	combination
3369	3372	[75]	NH <sub>3</sub>	$\nu_3$	antisymmetric stretch
3300	3290	[75]	NH <sub>3</sub>	2 $\nu_4$	overtone
3211	3212	[75]	NH <sub>3</sub>	$\nu_1$	symmetric stretch
1624, 1646	1628	[75]	NH <sub>3</sub>	$\nu_4$	degenerated deformation
1077	1097	[75]	NH <sub>3</sub>	$\nu_2$	symmetric deformation
After irradiation					
3452	3452	[76]	H <sub>2</sub> O	$\nu_1$	symmetric stretch(out-of-phase)
3248	3261	[187, 191]	NH <sub>2</sub> OH	$\nu_7$	N-H stretch (antisymmetric)
3213	3209	[187, 191]	NH <sub>2</sub> OH	$\nu_2$	N-H stretch (symmetric)
3109	3107	[76]	H <sub>2</sub> O	$\nu_1$	symmetric stretch (in-phase)
3024	3074	[187, 191]	NH <sub>2</sub> OH	$\nu_2$	N-H stretch (symmetric)
2963	2943–2507	[187, 191]	NH <sub>2</sub> OH	$\nu_3 + \nu_4$	combination
2916		[187, 191]	NH <sub>2</sub> OH	2 $\nu_4$	overtone
2748		[187, 191]	NH <sub>2</sub> OH	$\nu_3 + \nu_5$	combination
2525		[187, 191]	NH <sub>2</sub> OH	$\nu_4 + \nu_8$	combination
2236	2235	[191, 194, 222]	N <sub>2</sub> O	$\nu_1$	N-N stretch
1875	1875	[191, 194, 219-220]	NO	$\nu_1$	fundamental
1836	1833–1851	[191, 194, 219, 223]	N <sub>2</sub> O <sub>3</sub>	$\nu_1$	N=O stretch
1735	1737	[191, 194, 219]	N <sub>2</sub> O <sub>2</sub>	$\nu_1$	N=O stretch
1560	1561	[191, 224-225]	HNO	$\nu_3$	N=O stretch
1507	1507	[191, 224-225]	HNO	$\nu_2$	HNO bend
1486	1486	[187, 191]	NH <sub>2</sub> OH	$\nu_4$	NOH bend
1375	1389	[76]	H <sub>2</sub> O <sub>2</sub>	$\nu_6$	antisymmetric bend
1342	1359	[187, 191]	NH <sub>2</sub> OH	$\nu_4$	NOH bend
1303	1303	[191, 194, 219, 223]	N <sub>2</sub> O <sub>3</sub>	$\nu_3$	NO <sub>2</sub> stretch
1235	1240	[221]	N <sub>2</sub> O <sub>2</sub>	$\nu_?$	NO <sub>2</sub> stretch (antisymmetric)
1145	1144	[187, 191]	NH <sub>2</sub> OH	$\nu_5$	NH <sub>2</sub> wag
950	941	[76]	H <sub>2</sub> O	$\nu_L$	libration
796	880	[221]	N <sub>2</sub> O <sub>2</sub>	$\nu_?$	N-N stretch

<sup>a</sup> Assignment based on references.

## Deconvolution

Since the main topic of this work is probing the formation of hydroxylamine under conditions relevant to astrochemical environments, hereafter we focus on its formation during the oxidation of the  $\text{NH}_3$  ( $\text{ND}_3$ ) sample. First, IR spectra of the present work revealed the formation of  $\text{NH}_2\text{OH}$  ( $\text{ND}_2\text{OD}$ ) in electron-irradiated ( $\text{D}_3$ -) $\text{NH}_3$ - $\text{O}_2$  ices at 5.5 K. However, as mentioned earlier, the absorptions of ( $\text{D}_3$ -) $\text{NH}_3$  and ( $\text{D}_2$ -) $\text{H}_2\text{O}$  made the ( $\text{D}_3$ -) $\text{NH}_2\text{OH}$  assignments difficult at lower temperatures. In addition, absorptions were broad and not well defined. Thus, it was necessary to perform their deconvolution to discriminate the peaks and probe which species were truly represented by these absorptions. The spectra for selected temperatures at 5.5, 30, 150, 175 and 200 K, corresponding to the sublimation temperatures of oxygen, ( $\text{D}_3$ -) $\text{NH}_3$  and ( $\text{D}_2$ -) $\text{H}_2\text{O}$  as observed via PI-ReTOF-MS and EI-QMS, were deconvoluted. Figures 65 (a)–(e) exhibit the deconvoluted spectra of the NH and OH stretching region of  $\text{NH}_2\text{OH}$  in the region of 2420–3550  $\text{cm}^{-1}$ , and their associated assignments are compiled in Table A2. Likewise, Figures 65 (f)–(j) exhibit the deconvoluted spectra of the ND and OD stretching region of  $\text{ND}_2\text{OD}$  in the region of 1930–2600  $\text{cm}^{-1}$ , and their associated assignments are compiled in Table A3.

The deconvolution identified three absorptions of  $\text{NH}_3$  centered at 3366, 3307 and 3204  $\text{cm}^{-1}$  and similarly  $\text{ND}_3$  at 2500, 2350 and 2323  $\text{cm}^{-1}$  in irradiated  $\text{NH}_3/\text{ND}_3$ - $\text{O}_2$  ices at 5.5 K, which are matching the absorption of  $\text{NH}_3$  and  $\text{ND}_3$  before irradiation, respectively. Next, three bands centered at 3452, 3336 and 3109  $\text{cm}^{-1}$  in the irradiated  $\text{NH}_3$ - $\text{O}_2$  ice at 5.5 K can be correlated to the out-of-phase symmetric stretch ( $\nu_1$ ), the antisymmetric stretch (longitudinal mode) ( $\nu_3$ ) and the in-phase symmetric stretch ( $\nu_1$ ) of  $\text{H}_2\text{O}$ , respectively, which are in agreement with the literature data at 3452, 3332 and 3107  $\text{cm}^{-1}$ , respectively.<sup>[76]</sup> Similarly, three bands at 2567, 2474 and 2297  $\text{cm}^{-1}$  in the irradiated  $\text{ND}_3$ - $\text{O}_2$  ice at 5.5 K are assigned to  $\text{D}_2\text{O}$ , in agreement with the literature data at 2572, 2470 and 2305  $\text{cm}^{-1}$ , respectively.<sup>[206]</sup> Further, the band at 3163  $\text{cm}^{-1}$  in the irradiated  $\text{NH}_3$ - $\text{O}_2$  ice at 150 K, that is after most of the host molecule ammonia sublimed, are linked to the antisymmetric stretch (transversal mode) ( $\nu_3$ ) of  $\text{H}_2\text{O}$ . Note that, this band is observed only after most of the  $\text{NH}_3$  molecule sublimed. Likewise, the band centered at 2364  $\text{cm}^{-1}$  in the irradiated  $\text{ND}_3$ - $\text{O}_2$  ice at 150 K are assigned to the antisymmetric stretch (transversal mode) ( $\nu_3$ ) of  $\text{D}_2\text{O}$ , in agreement with the literature value at 2370  $\text{cm}^{-1}$ .<sup>[206]</sup>

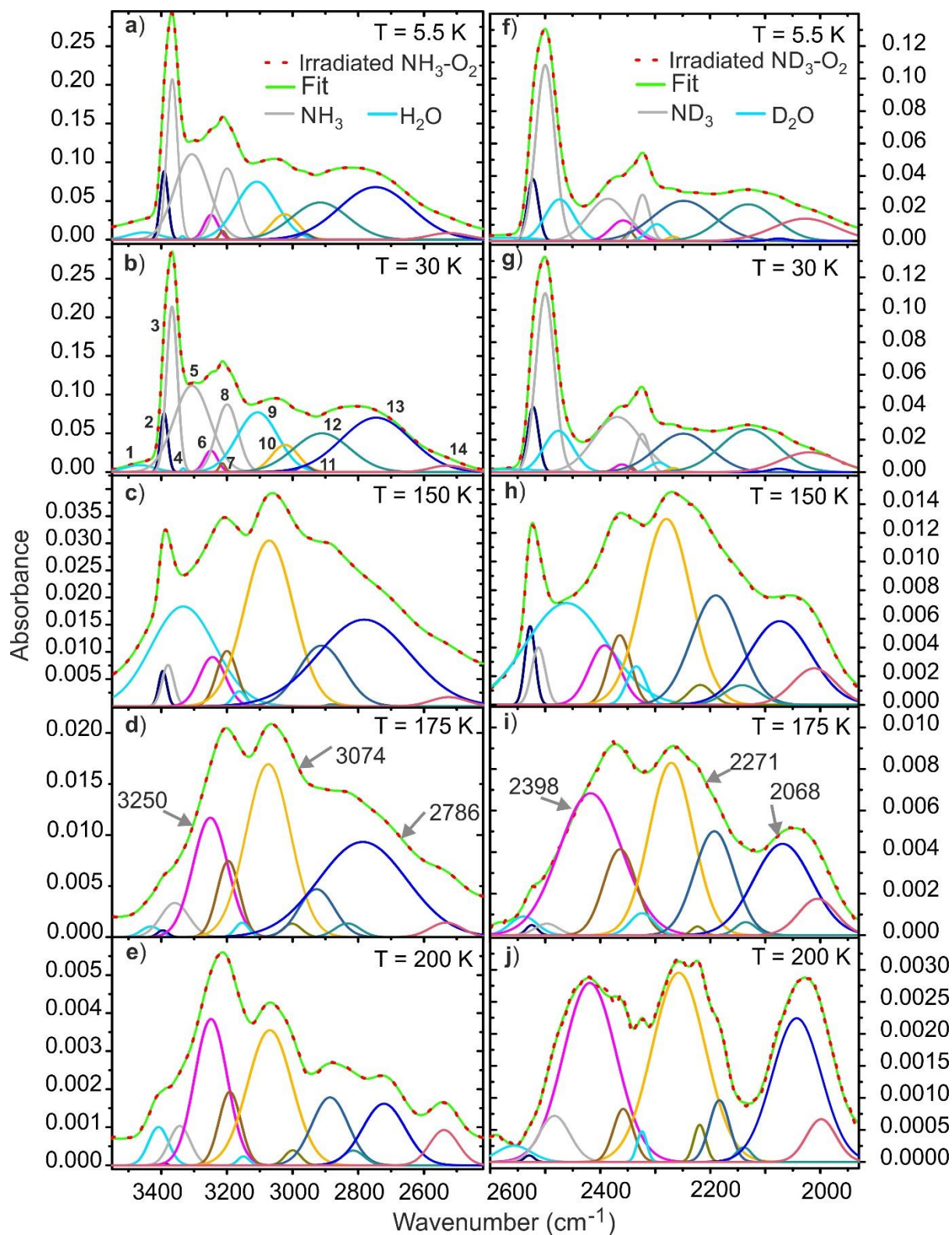


**Figure 65.** Deconvoluted infrared spectra of water, ammonia, hydroxylamine from 2420–3550  $\text{cm}^{-1}$  (left panel) and D2-water, D3-ammonia, D3-hydroxylamine from 1930–2600  $\text{cm}^{-1}$  (right panel) for selected temperatures corresponding to the sublimation temperatures of oxygen, (D3-)ammonia and (D2-)water as observed via PI-ReTOF-MS and QMS. The individual band with particular color as marked 1–14 in (b) and their assignments are compiled in Tables A2 and A3. The IR features of (D3-)hydroxylamine are increasing in intensity after most of the host molecule (D3-)ammonia (gray lines) and (D2-)water (sky blue lines) sublimed.

Concerning the hydroxylamine, the deconvolution revealed eight absorptions centered at 3391, 3248, 3213, 3024, 2963, 2916, 2748 and 2525  $\text{cm}^{-1}$  in the irradiated  $\text{NH}_3\text{-O}_2$  ice, and similarly at 2522, 2358, 2346, 2267, 2248, 2131, 2075 and 2027  $\text{cm}^{-1}$  in the irradiated  $\text{ND}_3\text{-O}_2$  ice at 5.5 K, which are close to the literatures values of (D3-)  $\text{NH}_2\text{OH}$ .<sup>[187, 191, 227-228]</sup> These IR bands are affected by the absorptions of the ammonia and water molecules at lower temperatures and are increasing in intensity once these molecules sublimed at higher temperatures as monitored via TPD IR study.

In summary, deconvolution of the TPD IR spectra revealed three molecules in the region of 2420–3550  $\text{cm}^{-1}$  in the irradiated  $\text{NH}_3\text{-O}_2$  ices at 5.5 K:  $\text{NH}_3$ ,  $\text{H}_2\text{O}$  and  $\text{NH}_2\text{OH}$ ; with  $\text{NH}_3$  dominating the IR spectra below 145 K, and then water sit on top of  $\text{NH}_2\text{OH}$  up to 174 K. These findings were confirmed by the radiolysis of isotope-labeled  $\text{ND}_3\text{-O}_2$  experiments as well. Finally, Figure 66 show the decay of absorption features of  $\text{NH}_2\text{OH}$  at temperatures of above 175 K, with its vibrational mode frequencies compiled and compared with literature values in Table A2.<sup>[187, 191]</sup> Similarly, the data of  $\text{ND}_2\text{OD}$  is compiled in the Appendix (Figure A3 and Table A3).

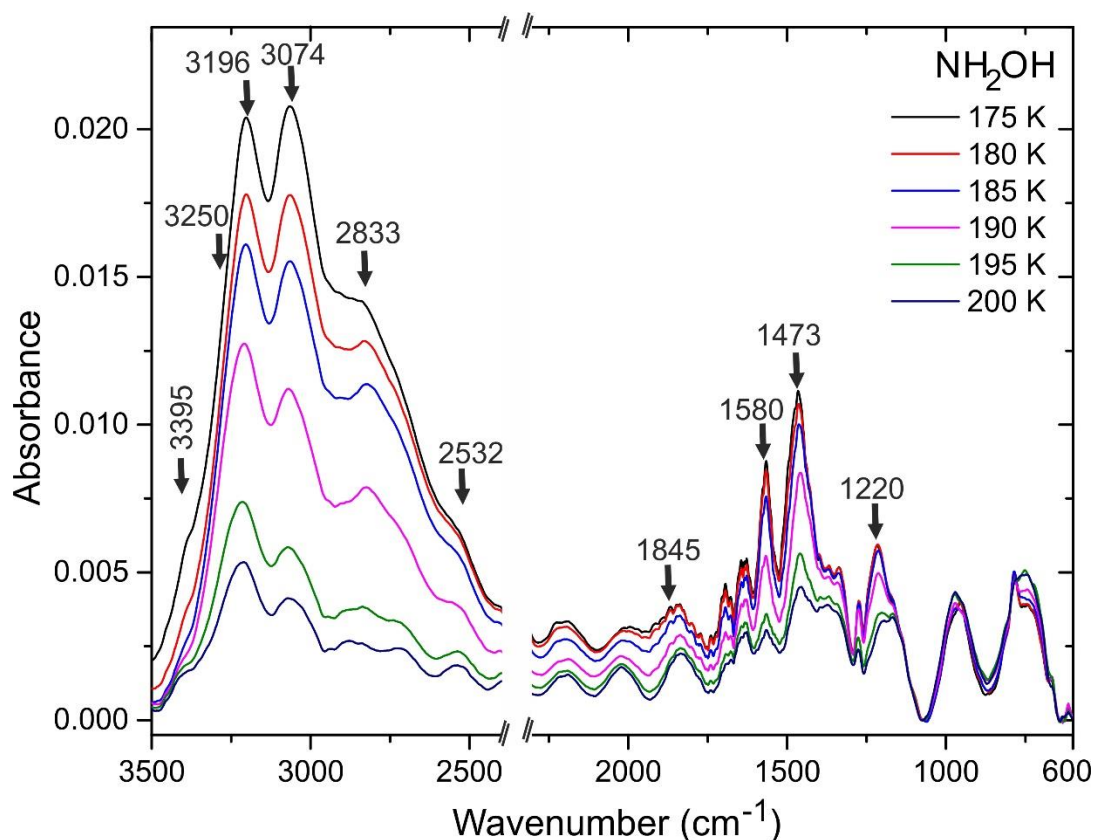


**Figure 66.** IR absorption features of the  $\text{NH}_2\text{OH}$  species at 175, 180, 185, 190, 195 and 200 K after most of the host molecules  $\text{NH}_3$  and oxygen  $\text{O}_2$  as well as computing by-products such as  $\text{H}_2\text{O}$  sublimed.

**Table 19.** Assignment of the NH<sub>2</sub>OH absorption bands (cm<sup>-1</sup>) at 175 K compared to reference values.

This work (NH <sub>3</sub> -O <sub>2</sub> ice)	Ref.1 <sup>a,b,[187]</sup> (NH <sub>3</sub> -H <sub>2</sub> O ice)	Ref.2 <sup>a,c,[191]</sup> (NO + H ice)	Assignment <sup>a</sup>
3395	...	3317	$\nu_1(a')$ O-H stretch
3250	3332	3261	$\nu_7(a'')$ N-H stretch (antisymmetric)
3196, 3074	3209-3074	3194	$\nu_2(a')$ N-H stretch (symmetric)
2912	2943-2507	2899	$\nu_3 + \nu_4$ combination
2833	...	...	$2\nu_4$ overtone
2786	...	2716	$\nu_3 + \nu_5$ combination
2532	...	...	$\nu_4 + \nu_8$ combination
1845	1886	...	$2\nu_6(a')$ overtone
1695	...	1608	$\nu_3(a')$ NH <sub>2</sub> bend
1580	1616	1592	$\nu_3(a')$ NH <sub>2</sub> bend
...	...	1514	$\nu_4(a')$ NOH bend
1473	1486	1359	$\nu_4(a')$ NOH bend
1220	1201	1203	$\nu_8(a'')$ NH <sub>2</sub> rock
1145	1107	1144	$\nu_5(a')$ NH <sub>2</sub> wag
928	921	919	$\nu_6(a')$ N-O stretch
...	...	889	$\nu_6(a')$ N-O stretch

<sup>a</sup> Assignment based on references. <sup>b</sup> at 175 K. <sup>c</sup> at 15 K.

### Quantitative analysis, mass balances (Provided by Dr. Sándor Góbi and Prof. Dr. Ralf I. Kaiser)

The number of reactant molecules decomposed during the radiolysis in the NH<sub>3</sub>-O<sub>2</sub> ices can be calculated if the decrease in their integrated infrared areas and their absorption coefficients are known; these are summarized in Table 20. When comparing the number of destroyed ammonia molecules ( $(4.8 \pm 0.7) \times 10^{17} \text{ cm}^{-2}$ ) to the exposed reactants ( $(5.0 \pm 0.7) \times 10^{17} \text{ cm}^{-2}$ ), it can be concluded that  $95 \pm 5\%$  of them are destroyed within the penetration depth of the electrons. The same values for molecular oxygen (O<sub>2</sub>) are  $(1.6 \pm 0.3) \times 10^{17} \text{ cm}^{-2}$  and  $(2.5 \pm 0.3) \times 10^{17} \text{ cm}^{-2}$  meaning that  $66 \pm 13\%$  of the irradiated molecules decomposed. In order to calculate the number of molecules degraded, the integrated absorption coefficients of  $3.11 \times 10^{-17} \text{ cm molecule}^{-1}$  of the  $\nu_3$  NH<sub>3</sub> band between 3700-3000 cm<sup>-1</sup> based on the results of Sill et al.<sup>[229]</sup> and  $5.00 \times 10^{-21} \text{ cm molecule}^{-1}$  ( $\nu_1$  O<sub>2</sub> band at 1550 cm<sup>-1</sup>)<sup>[230]</sup> were used, respectively.

**Table 20.** Mass balance of the NH<sub>3</sub>-O<sub>2</sub> ice as well as that of the irradiation products determined from their experimental IR decay/growth curves.

Process	Decay Product	Number of Molecules Produced/Decomposed During Irradiation
NH <sub>3</sub> → X		$(4.8 \pm 0.7) \times 10^{17}$
Fraction of NH <sub>3</sub> degraded		$95 \pm 5\%$
O <sub>2</sub> → O	O	$(1.6 \pm 0.3) \times 10^{17}$
Fraction of O <sub>2</sub> degraded		$66 \pm 13\%$
	NH <sub>2</sub> OH	$(1.6 \pm 0.2) \times 10^{17}$
	NO <sup>c</sup>	$(1.6 \pm 0.3) \times 10^{16}$
	N <sub>2</sub> O <sub>2</sub>	$(3.2 \pm 0.1) \times 10^{15}$
	(NO) <sub>2</sub> <sup>c</sup>	$(2.15 \pm 0.03) \times 10^{15}$
	H <sub>2</sub> O	$(2.1 \pm 0.2) \times 10^{15}$
Number of molecules in sample after irradiation	O <sub>3</sub> <sup>d</sup>	$(7.9 \pm 1.4) \times 10^{14}$
	H <sub>2</sub> O <sub>2</sub>	$(5.5 \pm 0.2) \times 10^{14}$
	N <sub>2</sub> O	$(3.7 \pm 0.1) \times 10^{14}$
	NO <sub>2</sub> <sup>d</sup>	$(3.5 \pm 0.2) \times 10^{14}$
	HNO	$(6.0 \pm 4.1) \times 10^{13}$
	N <sub>2</sub> O <sub>3</sub>	$(5.7 \pm 1.3) \times 10^{13}$
Nitrogen balance <sup>a</sup>		$39 \pm 8\%$
Oxygen balance <sup>b</sup>		$29 \pm 4\%$

<sup>a</sup> Fraction of nitrogen atoms originating from ammonia destruction that are needed for the formation of the irradiation products. <sup>b</sup> Fraction of oxygen atoms originating from molecular oxygen destruction that are needed for the formation of the irradiation products. <sup>c</sup> The NO monomer and dimer were treated together during the simulations. <sup>d</sup> Determined by using the integrated band areas of the ND<sub>3</sub>-O<sub>2</sub> ice sample.

The integrated band areas can also be determined for the radiolysis products if their absorption coefficients are known, it allows for the calculation of their concentration in the sample. Based on the absorption coefficient of  $4.16 \times 10^{-18}$  cm molecule<sup>-1</sup> for the vibrational band of the hydroxylamine ( $\nu_4$  NH<sub>2</sub>OH) at 1486 cm<sup>-1</sup> (utilizing the findings of Saldyka & Mielke),<sup>[231]</sup> its column density is found to be  $(1.6 \pm 0.2) \times 10^{17}$  cm<sup>-2</sup>. The same value for nitrogen monoxide ( $\nu_1$  NO at 1875 cm<sup>-1</sup>) equals to  $(1.6 \pm 0.3) \times 10^{16}$  cm<sup>-2</sup> when the absorption coefficient of  $6.80 \times 10^{-18}$  cm molecule<sup>-1</sup> is used.<sup>[220]</sup> An absorption coefficient of  $1.66 \times 10^{-17}$  cm molecule<sup>-1</sup> can be used for the vibrational band of the nitrosyl hydride ( $\nu_3$  HNO) at 1560 cm<sup>-1</sup> corresponding to  $(6.0 \pm 4.1) \times 10^{13}$  cm<sup>-2</sup>; the estimation is based on the absorption coefficients obtained for its isomer isonitrosyl hydride (HON).<sup>[232]</sup> The column density of dinitrogen dioxide (N<sub>2</sub>O<sub>2</sub>) was calculated to be  $(3.2 \pm 0.1) \times 10^{15}$  cm<sup>-2</sup> based on the integrated area of its vibrational band at

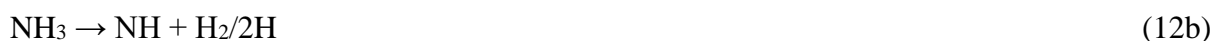
1235  $\text{cm}^{-1}$  (O–N–O antisymmetric stretching) for this the absorption coefficient ( $5.00 \times 10^{-17}$   $\text{cm molecule}^{-1}$ ) had to be estimated as well. This was conducted by using the absorption coefficients of the same vibrational mode of similar dinitrogen oxides ( $\text{N}_2\text{O}_x$ ,  $x = 3-5$ ).<sup>[220]</sup> The number of nitrogen monoxide dimer ( $(\text{NO})_2$ ) molecules are determined to be  $(2.15 \pm 0.03) \times 10^{15}$   $\text{cm}^{-2}$  if its absorption coefficient of  $2.72 \times 10^{-17}$   $\text{cm molecule}^{-1}$  for its  $\nu_1$  vibrational band (at 1735  $\text{cm}^{-1}$ ) is utilized.<sup>[233]</sup> The column density of water molecules formed upon irradiation can also be determined ( $(2.1 \pm 0.2) \times 10^{15}$   $\text{cm}^{-2}$ ) through the integrated area of its vibrational band at 950  $\text{cm}^{-1}$  ( $\nu_L$   $\text{H}_2\text{O}$ ,  $3.10 \times 10^{-17}$   $\text{cm molecule}^{-1}$ ).<sup>[234]</sup> The vibrational bands of ozone are completely hidden by the more intense ammonia ( $\text{NH}_3$ ) and hydroxylamine ( $\text{NH}_2\text{OH}$ ) signals at 1038  $\text{cm}^{-1}$  ( $\nu_3$   $\text{O}_3$ ,  $1.53 \times 10^{-17}$   $\text{cm molecule}^{-1}$ ) in the irradiated  $\text{NH}_3\text{-O}_2$  ices.<sup>[235]</sup> However, it can be observed in the deuterated sample ( $\text{ND}_3\text{-O}_2$ ) and its column density can then be estimated ( $(7.9 \pm 1.4) \times 10^{14}$   $\text{cm}^{-2}$ ). Tentatively, hydrogen peroxide is also produced upon irradiation; the integrated area of its band at 1375  $\text{cm}^{-1}$  ( $\nu_6$   $\text{H}_2\text{O}_2$ ) with an estimated absorption coefficient of  $6.00 \times 10^{-17}$   $\text{cm molecule}^{-1}$  can be used to obtain its column density ( $(5.5 \pm 0.2) \times 10^{14}$   $\text{cm}^{-2}$ ). It is worth noting that the absorption coefficient was obtained based on the known one of the combinational band close to 2900  $\text{cm}^{-1}$  ( $\nu_2 + \nu_6$   $\text{H}_2\text{O}_2$ ).<sup>[236]</sup> The number of nitrous oxide ( $\nu_1$   $\text{N}_2\text{O}$  at 2236  $\text{cm}^{-1}$  with an absorption coefficient of  $5.20 \times 10^{-17}$   $\text{cm molecule}^{-1}$ ),<sup>[237]</sup> and nitrogen dioxide ( $\nu_2$   $\text{NO}_2$  at 1616  $\text{cm}^{-1}$ ,  $6.36 \times 10^{-17}$   $\text{cm molecule}^{-1}$ )<sup>[220]</sup> could also be determined; these values are  $(3.7 \pm 0.1) \times 10^{14}$   $\text{cm}^{-2}$  and  $(3.5 \pm 0.2) \times 10^{14}$   $\text{cm}^{-2}$ , respectively. It should be noted that the signal of nitrogen dioxide – similarly to that of the ozone ( $\text{O}_3$ ) molecule – is hidden in the normal ice, it can be determined by using the results of the deuterated  $\text{ND}_3\text{-O}_2$  ice mixture. The last species that could be detected in the radiolyzed ice is dinitrogen trioxide ( $\text{N}_2\text{O}_3$ ) having an absorption coefficient of  $6.43 \times 10^{-17}$   $\text{cm molecule}^{-1}$  for the vibrational band at 1836  $\text{cm}^{-1}$  ( $\nu_1$   $\text{N}_2\text{O}_3$ )<sup>[220]</sup> meaning its column density corresponds to  $(5.7 \pm 1.3) \times 10^{13}$   $\text{cm}^{-2}$ .

If the number of nitrogen and oxygen atoms that can be found in the irradiation products is added up, the values obtained can be compared to the number of these elements originated from the destruction of ammonia ( $\text{NH}_3$ ) and oxygen ( $\text{O}_2$ ). Their total number required for the formation of the aforementioned species are found to be  $(1.9 \pm 0.2) \times 10^{17}$   $\text{cm}^{-2}$  and  $(9.6 \pm 1.2) \times 10^{16}$   $\text{cm}^{-2}$ , whereas  $(4.8 \pm 0.7) \times 10^{17}$   $\text{cm}^{-2}$  and  $(3.3 \pm 0.5) \times 10^{17}$   $\text{cm}^{-2}$  nitrogen and oxygen atoms were formed when the two parent molecules were destroyed. This means that they account for the  $39 \pm 8\%$  and  $29 \pm 4\%$  of the total number of nitrogen and oxygen atoms formed

upon the irradiation. Some of the oxygen that cannot be accounted for combines with another one recycling molecular oxygen (O<sub>2</sub>),<sup>[238]</sup> which sublimates from the irradiated sample upon TPD at around 35 K and its signal at  $m/z = 32$  can be detected via the EI-QMS instrument.<sup>[239-240]</sup> The missing nitrogen is likely present as molecular nitrogen (N<sub>2</sub>) formed via the radiolysis of ammonia.<sup>[78]</sup>

**Quantitative analysis, reaction pathways** (*Provided by Dr. Sándor Góbi and Prof. Dr. Ralf I. Kaiser*)

Having already assigned the NH<sub>2</sub>OH/ND<sub>2</sub>OD formed after energetic electron irradiation of NH<sub>3</sub>/ND<sub>3</sub>-O<sub>2</sub> ices, we are now proposing the possible formation pathway. For the IR data, we fit the temporal profiles of the reactants and of the newly formed molecules with a system of coupled differential equations (Figures 67 and 68) and reported the inherent rate constants (Table 21). First, upon exposure to energetic electrons, the ammonia (NH<sub>3</sub>) molecule is known to undergo decomposition to form atomic hydrogen (H) and amidogen (NH<sub>2</sub>) via reaction (12a) as well as a spin-forbidden molecular decomposition to molecular hydrogen (H<sub>2</sub>) and the triplet amino hydride (NH) via reaction 12b.<sup>[78, 241]</sup> The amidogen radical can undergo barrierless recombination with a second amidogen radical forming hydrazine (N<sub>2</sub>H<sub>4</sub>) followed by stepwise radiolysis via diimide (N<sub>2</sub>H<sub>2</sub>) to form eventually molecular nitrogen (N<sub>2</sub>) (Reactions 13 – 15).<sup>[78]</sup> In the present system, this scheme is expressed with the overall rate constant  $k_3$  (Rice-Herzfeld chain). Likewise, molecular oxygen was shown to decompose to two oxygen atoms<sup>[226]</sup> ( $k_1$ ) thus supplying a highly oxidizing environment and a reactant to form ozone (O<sub>3</sub>) ( $k_{12}$ ).



Ammonia was found to be oxidized via two pathways eventually leading to nitrosyl hydride (HNO): the oxidation via reaction with two oxygen atoms and water (H<sub>2</sub>O) elimination ( $k_4$ ) and in one step to hydroxylamine (NH<sub>2</sub>OH) ( $k_2$ ), which itself can be oxidized to nitrosyl hydride (HNO) ( $k_5$ ). Note that the oxidation of ammonia to hydroxylamine is a factor of about

5 faster than the oxidation to nitrosyl hydride (HNO). As evident from Figure 68, nitrosyl hydride (HNO) builds up very rapidly within the first few minutes of the experiments reaching then a steady concentration. This can only be accounted for by introducing a destruction pathway of nitrosyl hydride (HNO) ( $k_6$ ) to nitrogen monoxide (NO). The latter can either dimerize to dinitrogen dioxide ( $N_2O_2$ ) ( $k_7$ ) or is oxidized to nitrogen dioxide ( $NO_2$ ) ( $k_8$ ). Both processes are barrier-less since they involve a recombination of radicals/atoms. A second production pathway of dinitrogen dioxide ( $N_2O_2$ ) proceed through oxidation of nitrogen to dinitrogen monoxide ( $N_2O$ ) ( $k_{10}$ ),<sup>[222]</sup> which itself can be oxidized to form dinitrogen dioxide ( $N_2O_2$ ) ( $k_{11}$ ). To avoid overproduction, an additional oxidation route to dinitrogen trioxide ( $N_2O_3$ ) ( $k_9$ ) was incorporated.

Considering the formation of hydroxylamine ( $NH_2OH$ ), recall that three possible formation routes were proposed in the interstellar medium. These are the synthesis of hydroxylamine ( $NH_2OH$ ) via an exoergic reaction ( $\Delta H_{r,298}^0 = -278 \text{ kJ mol}^{-1}$ )<sup>[242]</sup> involving radical recombination between amidogen ( $NH_2$ ) and hydroxyl radical (OH) (Reaction 9)<sup>[187, 197, 199]</sup> and/or through a barrierless successive hydrogenation of nitrogen monoxide (NO) (Reaction 10)<sup>[189-190]</sup> at low temperatures. However, our kinetics scheme reveals that these two reaction pathways are insignificant to the synthesis of hydroxylamine ( $NH_2OH$ ) in our experiments. The third and the most likely reaction route for the formation of hydroxylamine ( $NH_2OH$ ) in our experiment is via the insertion of triplet atomic oxygen (O) into the N–H bond of ammonia ( $NH_3$ ) followed by intersystem crossing (ISC) to the singlet surface. Recall that both are among the most abundant species in our system of interest. These reaction pathways are further verified by kinetically fitting the temporal evolution of the column densities of all species formed during irradiation (Figures 67 and 68, Table 21).

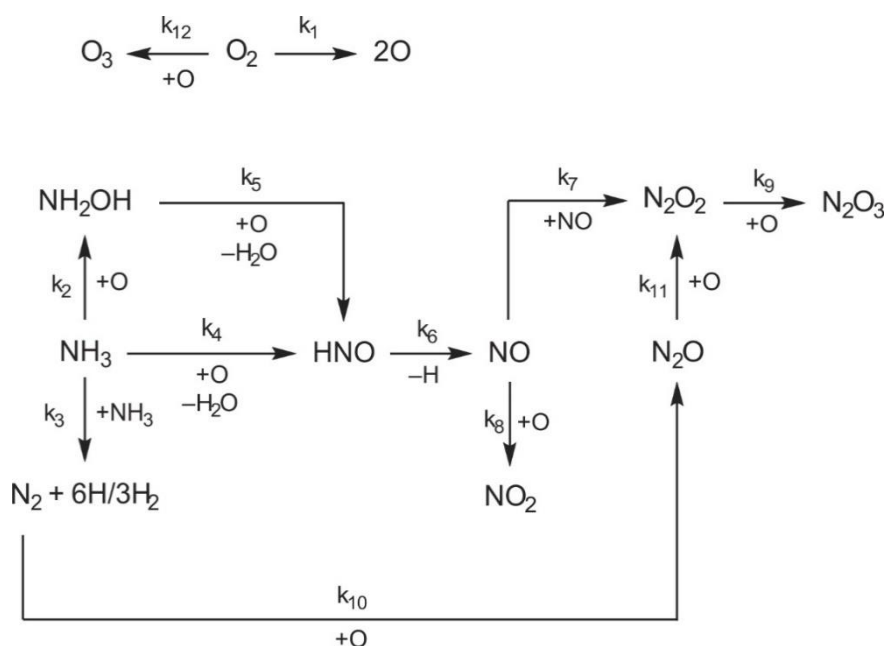


**Figure 67.** Reaction scheme exploited for the kinetics fits of the temporal profiles of the newly formed molecules during photolysis of ammonia–oxygen ices as compiled in Table 21.

**Table 21.** Decay rate constants of the  $NH_3$ – $O_2$  ice as well as the formation rates of the irradiation products based on their experimental IR decay/growth curves.

Reaction Number	Equation	Rate Constant	(Pseudo) First-order value
R1	$O_2 \rightarrow 2O$	$k_1$	$(3.4 \pm 0.5) \times 10^{-4}$
R2	$NH_3 + O \rightarrow NH_2OH$	$k_2^a$	$(2.5 \pm 0.7) \times 10^{-4}$
R3	$NH_3 + NH_3 \rightarrow N_2 + 6H/3H_2$	$k_3^a$	$(8.6 \pm 1.4) \times 10^{-5}$
R4	$NH_3 + 2O \rightarrow HNO + H_2O$	$k_4^a$	$(4.6 \pm 1.7) \times 10^{-5}$
R5	$NH_2OH + O \rightarrow HNO + H_2O$	$k_5^a$	$(6.0 \pm 1.7) \times 10^{-6}$
R6	$HNO \rightarrow NO + H$	$k_6$	$(2.0 \pm 0.2) \times 10^{-1}$
R7	$NO + NO \rightarrow N_2O_2$	$k_7^a$	$(1.5 \pm 0.2) \times 10^{-4}$
R8	$NO + O \rightarrow NO_2$	$k_8^a$	$(7.8 \pm 0.6) \times 10^{-6}$
R9	$N_2O_2 + O \rightarrow N_2O_3$	$k_9^a$	$(4.9 \pm 0.2) \times 10^{-6}$
R10	$N_2 + O \rightarrow N_2O$	$k_{10}^a$	$(2.1 \pm 0.2) \times 10^{-6}$
R11	$N_2O + O \rightarrow N_2O_2$	$k_{11}^a$	$(2.7 \pm 0.2) \times 10^{-4}$
R12	$O_2 + O_2 \rightarrow O_3 + O$	$k_{12}^a$	$(1.0 \pm 0.3) \times 10^{-6}$

<sup>a</sup> Higher-order reaction rate, its corresponding pseudo first-order rate can be obtained by multiplying it by the average number of the reactant(s) during the irradiation. These are the following species depending on the reaction equation:  $NH_3$  ( $[NH_3]_{av} = ((2.1 \pm 1.3) \times 10^{17})$ ),  $O_2$  ( $[O_2]_{av} = ((1.5 \pm 0.5) \times 10^{17})$ ),  $NO$  ( $[NO]_{av} = (1.4 \pm 0.6) \times 10^{16}$ ), and  $O$  ( $[O]_{av} = ((6.6 \pm 1.7) \times 10^{13})$ ).

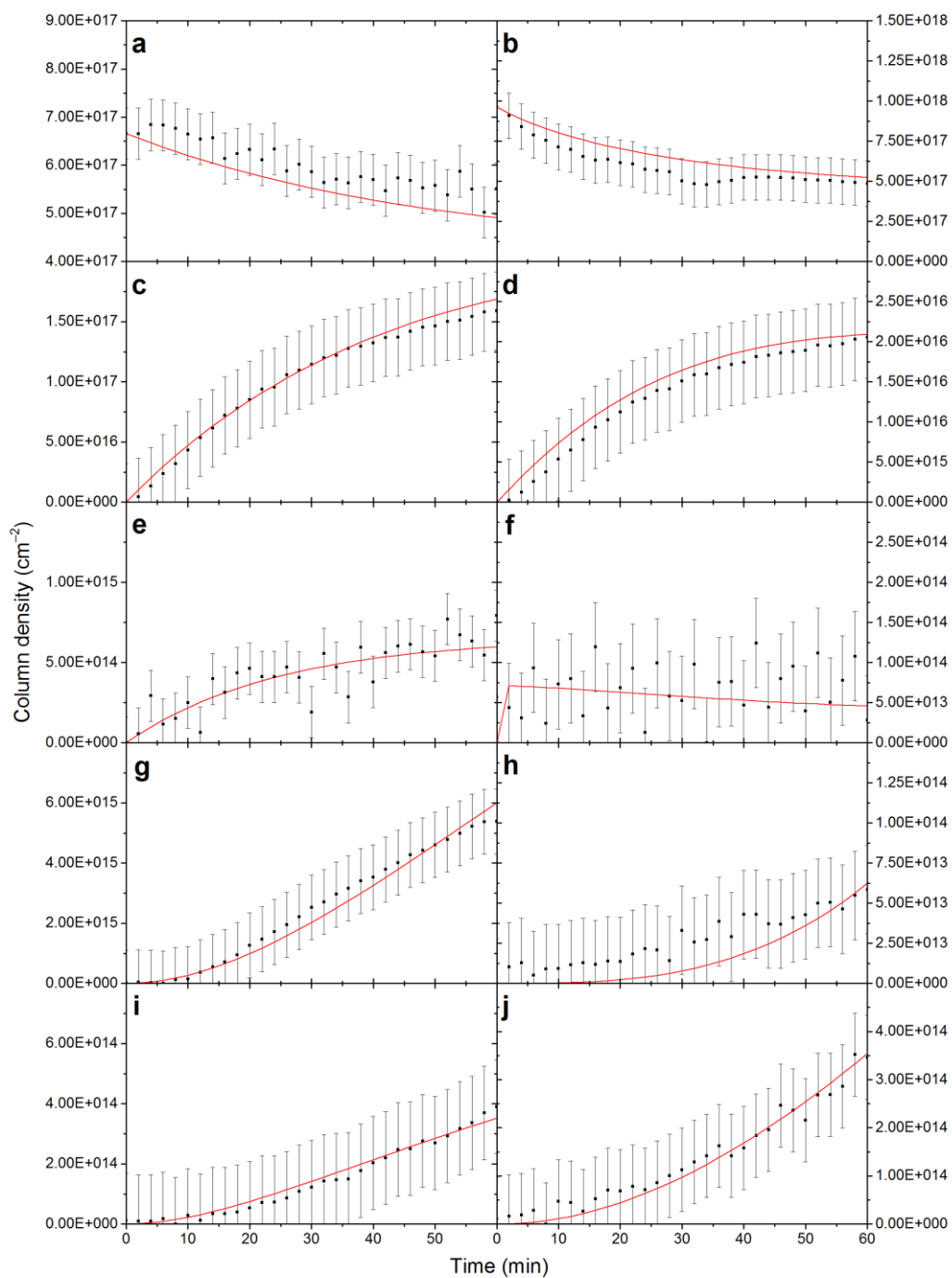


**Figure 68.** Decay curves of the IR bands of the  $\text{NH}_3 - \text{O}_2$  ice upon energetic electron irradiation (a) at  $1550 \text{ cm}^{-1}$  ( $\nu_1 \text{ O}_2$ ) and (b) at  $3369 \text{ cm}^{-1}$  ( $\nu_3 \text{ NH}_3$ ), respectively. Growth curves of the IR bands of the same sample (c) at  $1486 \text{ cm}^{-1}$  ( $\nu_4 \text{ NH}_2\text{OH}$ ), (d)  $1875 \text{ cm}^{-1}$  ( $\nu_1 \text{ NO}$ ), (e)  $1038 \text{ cm}^{-1}$  ( $\nu_3 \text{ O}_3$ ), (f)  $1560 \text{ cm}^{-1}$  ( $\nu_3 \text{ HNO}$ ), (g)  $1235 \text{ cm}^{-1}$  ( $\nu \text{ N}_2\text{O}_2$ ), (h)  $1836 \text{ cm}^{-1}$  ( $\nu_1 \text{ N}_2\text{O}_3$ ), (i)  $2236 \text{ cm}^{-1}$  ( $\nu_1 \text{ N}_2\text{O}$ ), and (j)  $1616 \text{ cm}^{-1}$  ( $\nu_2 \text{ NO}_2$ ), respectively.

## PI-ReTOF mass spectroscopy

It is of interest to correlate the IR observation with a highly sensitive mass spectroscopic analysis of the molecules subliming into the gas phase. The PI-ReTOF-MS data of the subliming molecules taken at the photoionization energy of 10.49 eV are compiled in Figure 69. The TPD profiles are dominated by the signal of the host matrix molecule ammonia ( $\text{NH}_3$ ) at mass-to-charge ratio ( $m/z$ ) = 17 ( $IE = 10.07 \pm 0.01$  eV)<sup>[243]</sup> and, respectively at  $m/z = 20$  from D3-ammonia ( $\text{ND}_3$ ) ( $IE = 10.08 \pm 0.01$  eV).<sup>[243]</sup> The TPD profile suggests two sublimation events for this species from about 75 and 145 K with a maximum peak at around 125 K and from about 170 and 220 K with maximum peak at 190 K.<sup>[241]</sup> The next highest contribution found in the 10.49 eV probed (D3)- ammonia-oxygen samples is that of the nitrogen monoxide (NO) ( $IE = 9.2643 \pm 0.0002$  eV)<sup>[244]</sup> with its mass-to-charge-ratio at 30 peaking at  $165 \pm 2$  K and second sublimation event maximum at about  $191 \pm 2$  K. Further, nitrosyl hydride (HNO) ( $m/z = 31$  and  $IE = 10.18 \pm 0.01$ )<sup>[245]</sup> with its counterpart deuterated nitrosyl hydride (DNO) ( $m/z = 32$  and  $IE = 10.29 \pm 0.14$ )<sup>[246]</sup> were observed in the 10.49 eV probed (D3-) ammonia-oxygen sample peaking at  $187 \pm 5$  K. Finally  $\text{NH}_2\text{OH}$  ( $IE = 10.00$  eV)<sup>[183]</sup> at  $m/z = 33$  and  $\text{ND}_2\text{OD}$  at  $m/z = 36$  were detected with 10.49 eV photolyzed  $\text{NH}_3\text{-O}_2$  and  $\text{ND}_3\text{-O}_2$  samples, respectively. The TPD profiles found for  $\text{NH}_2\text{OH}$  and  $\text{ND}_2\text{OD}$  molecules are essentially identical peaking at  $191 \pm 2$  and  $196 \pm 1$  K, respectively. Note that the formation of a series of nitrogen oxides evident in the FTIR experiment such as nitrous oxide ( $\text{N}_2\text{O}$ ) ( $IE = 12.880 \pm 0.005$  eV)<sup>[247]</sup> were unable to be detected using the PI-ReTOF-MS as their ionization energy is higher than the energy of the photons applied in our experiments (10.49 eV). For the same reason, water ( $\text{H}_2\text{O}$ ) ( $IE = 12.6188 \pm 0.0009$  eV)<sup>[248]</sup>, D2-water ( $\text{D}_2\text{O}$ ) ( $IE = 12.6398 \pm 0.0009$  eV)<sup>[248]</sup>, hydrogen peroxide ( $\text{H}_2\text{O}_2$ ) ( $IE = 10.92 \pm 0.05$  eV)<sup>[249]</sup> and ozone ( $\text{O}_3$ ) ( $IE = 12.519 \pm 0.004$  eV)<sup>[250]</sup> were not detected in our PI-ReTOF-MS experiments.

Special attention is paid to the detection of hydroxylamine utilizing the highly sensitive PI-ReTOF-MS technique based on its mass-to-charge ratio, the sublimation temperature, and how the mass-to-charge ratios shift upon isotope labeling. Here, due to the simplicity of the host ice, made up of only three elements (H, N, and O), the identification of the observed mass-to-charge ratios are straightforward (Figure 70). Thus, the signal at  $m/z = 33$  must stem from molecule(s) with a chemical formula  $\text{N}_2\text{H}_5$ ,  $\text{HO}_2$ ,  $\text{NH}_3\text{O}$  and/or  $\text{NH}_2\text{OH}$ . First we ruled out the formation of the hydroperoxyl radical ( $\text{HO}_2$ ) as its ionization energy ( $IE = 11.35 \pm 0.01$  eV)<sup>[251]</sup> resides well above the energy of our photons (10.49 eV). Next, although  $\text{N}_2\text{H}_5$  is claimed to

exist as intermediate,<sup>[252]</sup> it has never been isolated in pure form and the ionization energy is not known as a result. Also, no signal was observed for  $\text{N}_2\text{D}_5$  in the deuterated ammonia – oxygen samples. This suggests that the signal at  $m/z = 33$  can only arise from  $\text{NH}_2\text{OH}$  and/or its zwitterionic form  $\text{NH}_3\text{O}$ . However, a recent study at the CCSD(T)/BSIII//MP2/BSIII level of theory suggests that the normal hydroxylamine isomer  $\text{NH}_2\text{OH}$  is more stable than the zwitterionic form  $\text{NH}_3\text{O}$  by about 1 eV.<sup>[253]</sup>

Hydroxylamine was detected in temperatures range of 160–220 K peaking at  $191 \pm 2$  K, in agreement with literature values.<sup>[187, 190, 194, 196, 254]</sup> Moreover, the TPD profile reveals that  $\text{NH}_2\text{OH}$  peaks at the same temperature ( $191 \pm 2$  K) as the signals of  $m/z = 31$  ( $\text{HNO}$ ) and  $m/z = 30$  ( $\text{NO}$ ) (Figure 70). This is consistent with the findings of Congiu et al.<sup>[190]</sup> who carried out the hydrogenation of  $\text{NO}$  and observed  $\text{NH}_2\text{OH}$  in the TPD along with its thermal degradation in the region of 160–200 K peaking at 190 K. These findings are also consistent with the isotope-labeled experiment, namely the electron irradiation of  $\text{ND}_3\text{--O}_2$  ices. As can be seen in the right-panel of Figure 70, signals are recorded at  $m/z = 36$  ( $\text{ND}_2\text{OD}$ ),  $m/z = 32$  ( $\text{DNO}$ ) and  $m/z = 30$  ( $\text{NO}$ ) after exposing the  $\text{ND}_3\text{--O}_2$  ices to 10.49 eV photons.

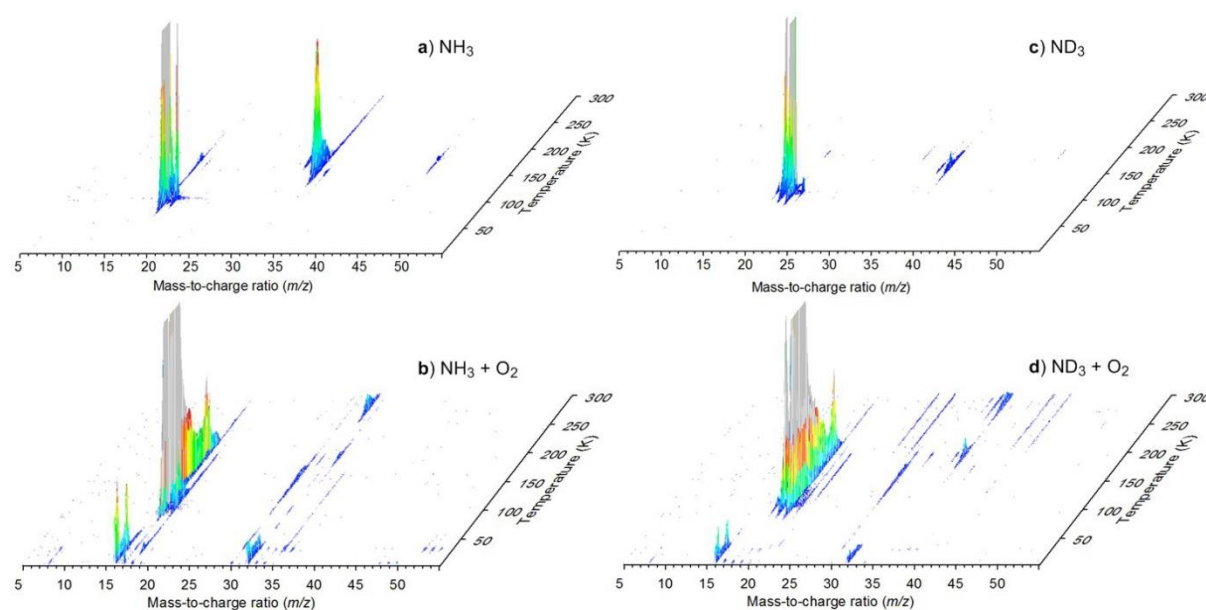


**Figure 69.** 3D visualization of the PI-ReTOF-MS data of the irradiated (a) ammonia, (b) ammonia–oxygen, (c) D3-ammonia and (d) D3-ammonia–oxygen ices at a photon energy of 10.49 eV collected during the temperature programmed desorption (TPD) of the reactants and products subliming into the gas phase.

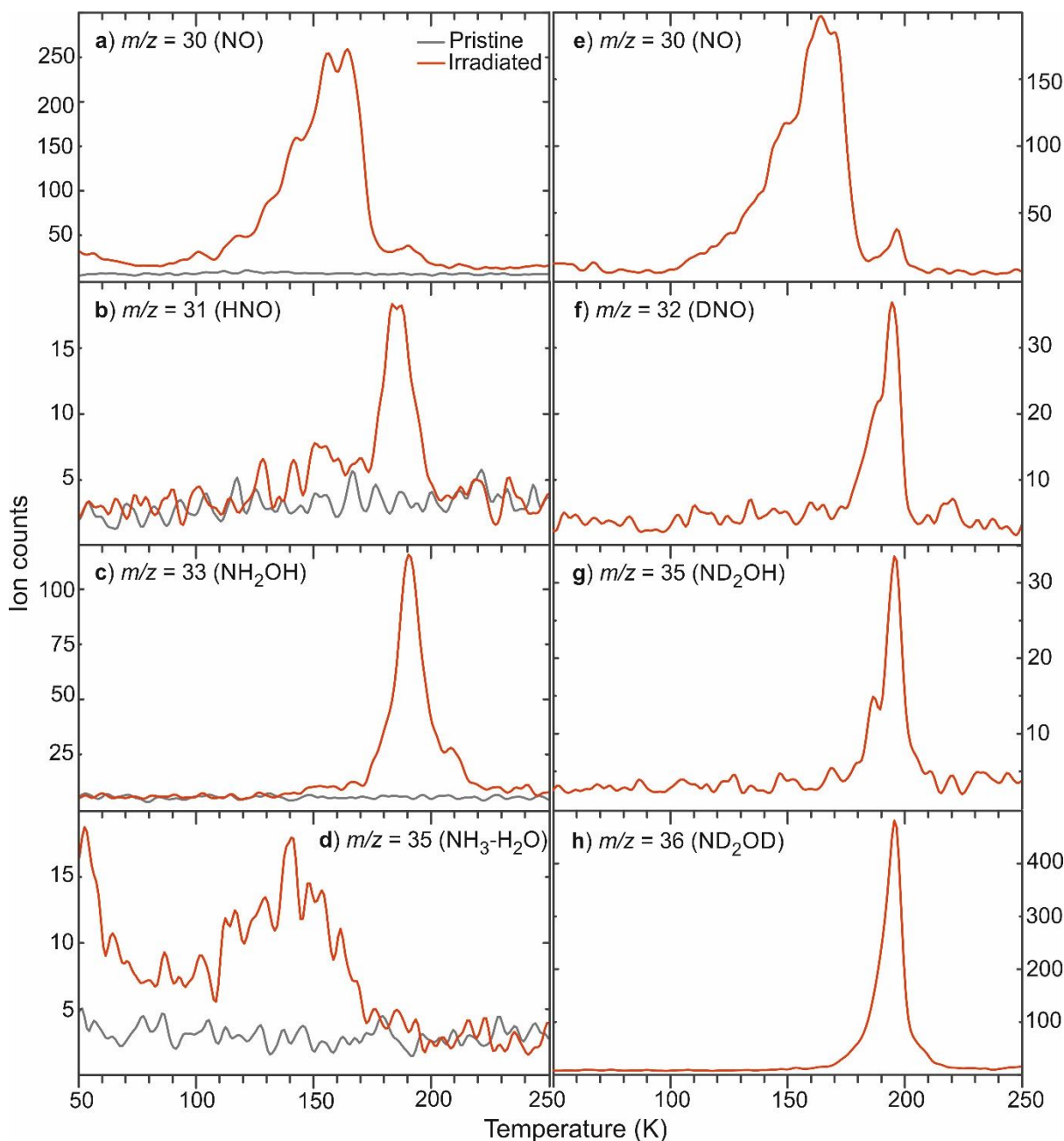


**Figure 70.** Selected TPD profiles extracted from the PI-ReTOF-MS spectra shown in Figure 69. TPD profiles of (a)  $m/z = 30$  ( $\text{NO}^+$ ), (b)  $m/z = 31$  ( $\text{HNO}^+$ ), (c)  $m/z = 33$  ( $\text{NH}_2\text{OH}^+$ ) and (d)  $m/z = 35$  ( $\text{NH}_3\text{-H}_2\text{O}^+$ ) subliming from the irradiated ammonia–oxygen ( $\text{NH}_3\text{-O}_2$ ) ices shown on the left panel and TPD profiles of (e)  $m/z = 30$  ( $\text{NO}^+$ ), (f)  $m/z = 32$  ( $\text{DNO}^+$ ), (g)  $m/z = 35$  ( $\text{ND}_2\text{OH}^+$ ) and (h)  $m/z = 36$  ( $\text{ND}_2\text{OD}^+$ ) subliming from the irradiated D3-ammonia–oxygen ( $\text{ND}_3\text{-O}_2$ ) ices shown on the right panel recorded at photoionization energies of 10.49 eV.

### Astrochemical implications

Since its first detection in 1968 in the center of our galaxy,<sup>[54]</sup> ammonia has been known to be one of the most common species adsorbed onto the colder interstellar dust icy-grain surface, with an abundance of around 20–30% relative to water ice.<sup>[204-205]</sup> Oxygen is also the third most abundant element in the universe<sup>[255-256]</sup> and has been detected in recent comets with local

abundances ranging from 1–10% with respect to water.<sup>[257-258]</sup> Thus, significant experimental and theoretical work dedicated to understand the energetic radiation effect on oxygen and ammonia ices is crucial to accurately model the chemistry of the ISM. In cold dense molecular clouds where the temperatures are lower than the desorption temperature of oxygen, i.e., below 20–25 K in our experimental conditions, ammonia and oxygen ices could be exposed to different forms of energetic irradiation and thus be responsible for the formation of various nitrogen and oxygen bearing building blocks of prebiotic species such as hydroxylamine (NH<sub>2</sub>OH) through insertion or radical-radical combination mechanisms. On the other hand, at temperatures around or higher than 25 K, oxygen could start to diffuse and would be able to collide with ammonia ices to form the same species. In the present study, we have shown the formation of hydroxylamine from energetic electron-irradiated ammonia–oxygen interstellar model ices under UHV conditions and cryogenic temperatures at 5.5 K, using infrared spectroscopic analysis complemented by temperature programmed desorption (TPD) studies utilizing highly sensitive reflectron time-of-flight mass spectrometry coupled with pulsed photoionization (PI-ReTOF-MS) at photoionization energies of 10.49 eV. According to our kinetic studies, the major reaction pathway for the formation of hydroxylamine is found to occur via insertion of suprathreshold singlet oxygen into ammonia or by insertion of triplet oxygen followed by intersystem crossing (ISC).

To date, and to the best of our knowledge, hydroxylamine has not been detected in the ISM either in solid state in dark molecular clouds or in gas phase in the star-forming regions. Our experimental results show that hydroxylamine may be present both in condensed phase on ice-coated interstellar grains as well as in gas phase in the so called “hot-core” protostar regions. Our study also suggests that hydroxylamine can be easily oxidized to nitrosyl hydride (HNO) with the latter detected in the ISM as early as 1977.<sup>[259]</sup> Accordingly, it might be difficult to detect hydroxylamine, if it is formed in strongly oxidizing environments. However, we expect hydroxylamine to be detected in the near future by ALMA at a temperature at which hydroxylamine might be sublimed into the gas phase prior to excessive oxidation (around 160 K according to our experiments).

Parts of chapter 7 were "Reprinted (adapted) with permission from *J. Phys. Chem. A*, **2017**, 121 (40), pp 7477–7493. Copyright 2018 American Chemical Society."

## 8. Formation of triazene in ammonia bearing ices

### Introduction

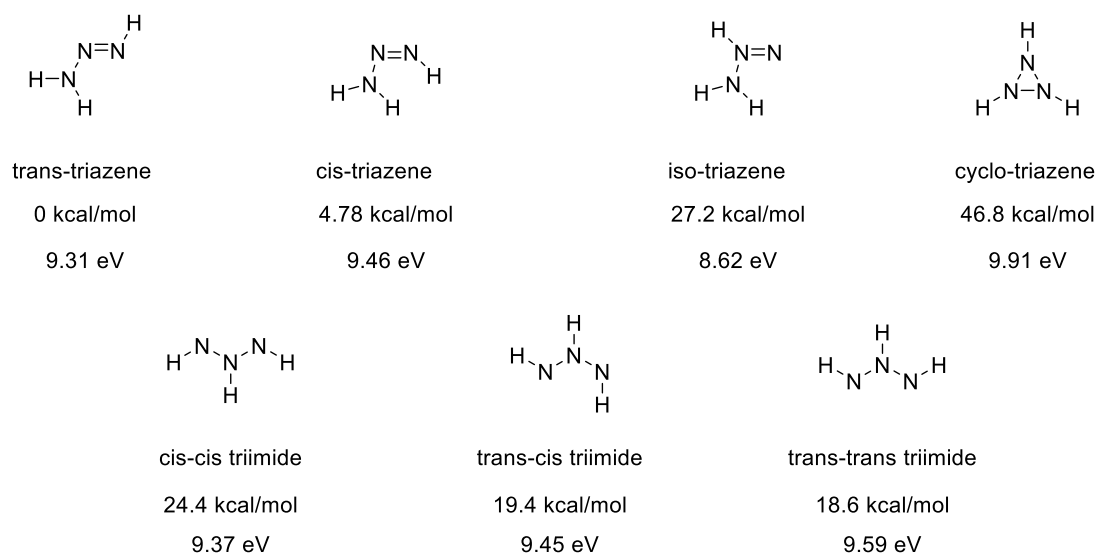
*This project was carried out in collaboration with Dr. Marko Förstel, Dr. Pavlo Maksyutenko, Prof. Dr. Ralf I. Kaiser (University of Hawaii) and Prof. Dr. Alexander M. Mebel (Florida International University), and the results were published in ChemPhysChem. Here we describe the main findings of the experimental results only.*

The carbon–carbon single bond is about two times stronger than the nitrogen–nitrogen single bond ( $C-C = \sim 83$  and  $N-N = \sim 38$  kcal/mol). This could be rationalized in terms of the influence of the non-bonding electrons located at the nitrogen atoms which will significantly destabilize the  $N-N$  bond. Thus, unlike the rich chemistry of carbon, there are only two acyclic hydronitrogen molecules isolated to date, ammonia ( $NH_3$ ) and hydrazine ( $N_2H_4$ ).

Triazenes, a class of compounds with  $R_1R_2N-N=N-$  moiety, is a potential key intermediate in hydrogen–nitrogen chemistry ranging from polymer synthesis to anticancer drugs such as dacarbazine and temozolomide.<sup>[260-266]</sup> Thus, considerable interest have been devoted both from theoretical and experimental communities over the last 70 years. However, their stem compound triazene ( $N_3H_3$ ) has not been isolated so far.<sup>[267]</sup>

Computational studies by several groups identified seven stable isomers of  $N_3H_3$  (Scheme 30). The main conclusion from these studies show that the stabilities of triazenes decrease in the order trans-triazene, cis-triazene, triimide, iso-triazene and cyclo-triazene.<sup>[268-272]</sup>

Here, we report the experimental detection of  $N_3H_3$  along with its isotopologues counter parts in the gas phase upon electron irradiation of  $NH_3$ ,  $ND_3$ ,  $NH_3:N_2$  ( $1:1.0 \pm 0.2$ ) and  $NH_3:^{15}N_2$  ( $1:1 \pm 0.2$ ) ices at 5.5 K. The thickness of the ices were  $600 \pm 50$  nm. Upon sublimation of the newly formed molecules, triazene is identified for the first time via single photon reflectron time-of-flight mass spectroscopy (PI-ReTOF-MS).<sup>[273-275]</sup> Furthermore, isomers of triazene are identified by tuning the photoionization energy above and below the computed ionization energy of triazene ( $IE = 8.62 - 9.91$  eV) using the PI-ReTOF-MS technique. Results obtained from isotope labelled ices help us further to propose the actual mechanism(s) of triazene formation.



**Scheme 30.** Ionization energies (eV) and energies (kcal/mol) relative to the most stable isomer of the triazene isomers under discussion, calculated at the CCSD(T)-F12/cc-pVTZ-f12//B3LYP/6-311G\*\* level of theory.<sup>[241]</sup>

## Results and discussion

The PI-ReTOF-MS data of the subliming regular and isotopologue molecules taken at the photoionization energy of 10.49 eV, 9.67 eV and 9.1 eV are compiled in Figure 71. Similar to the discussion in Chapter 7, the TPD profiles are dominated by the signal of the host matrix molecules NH<sub>3</sub> and ND<sub>3</sub> measured at the 10.49 eV ionization energy. On the other hand, only a few molecules are ionized while using 9.67 eV and 9.1 eV photons.

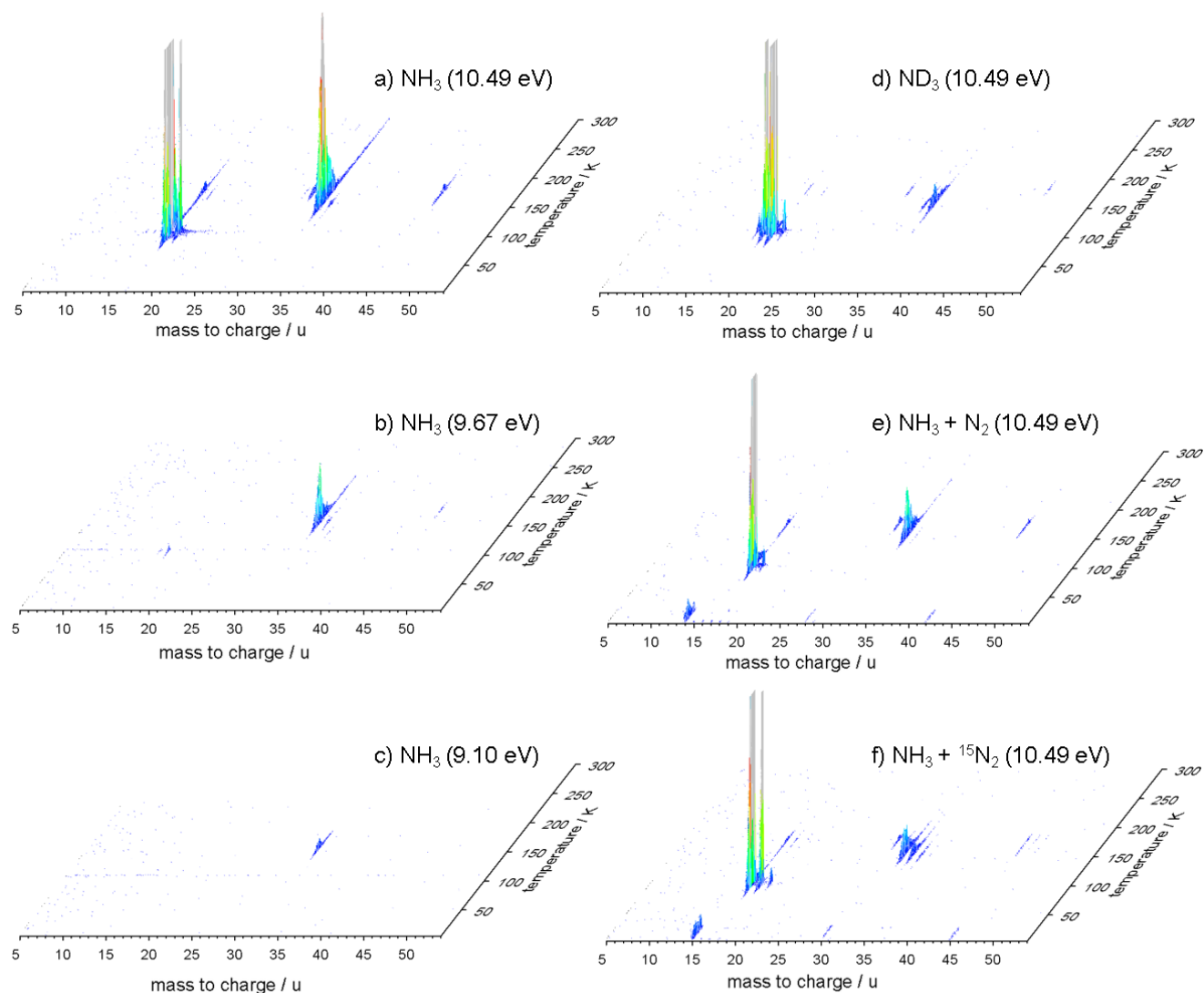


**Figure 71.** PI-ReTOF-MS spectra with the initial ice composition and the ionization energy given in each panel. (Left panel measured at three different ionization energies (10.49 eV, 9.67 eV and 9.1 eV), and right panel measured all at 10.49 eV).

Since the main goal of this work is related to  $\text{N}_3\text{H}_3$ , we pursue the following strategy to discuss our results. First, we aim to detect the  $\text{N}_3\text{H}_3$  molecule, then identify the stable isomers and finally figure out the formation mechanism(s).

## Detection

The TPD profiles of key species subliming from the irradiated ammonia and deuterated ammonia ices measured at 10.49 eV are compiled in Figure 72. At temperatures below 130 K, only  $\text{NH}_3/\text{ND}_3$  are sublimed. However, when the temperature rises, additional species start to sublime. The diimide ( $\text{N}_2\text{H}_2$ ) together with its deuterated counterpart ( $\text{N}_2\text{D}_2$ ) are observable

through their parent ions at  $m/z = 30$  and  $32$  ( $IE = 9.58$  eV)<sup>[276]</sup>, respectively. The TPD profile suggests that the sublimation of this species occurs in the range from 157 to 180 K, peaking at 172 K. Next, hydrazine ( $N_2H_4$ ), ( $m/z = 32$  and  $IE = 8.10 \pm 0.15$ )<sup>[88]</sup> together with its deuterated counterpart ( $N_2D_4$ ), ( $m/z = 34$ ) are detected with 10.49 eV photoionized  $NH_3$  and  $ND_3$  samples, respectively, peaking at 160 K. Finally, triazene ( $N_3H_3$ ), ( $IE = 10.00$  eV) at  $m/z = 45$  and  $N_3D_3$  at  $m/z = 48$  are observed with 10.49 eV photoionized  $NH_3$  and  $ND_3$  samples, respectively. This signal has an onset of 150 K, peaks at around 180 K and reaches zero intensity above 200 K. The assignment of the observed  $m/z = 30$  to  $N_2H_2^+$ ,  $m/z = 32$  to  $N_2H_4^+$  and  $m/z = 45$  to  $N_3H_3^+$  are straightforward since the host ice is comprising only of two different atoms.

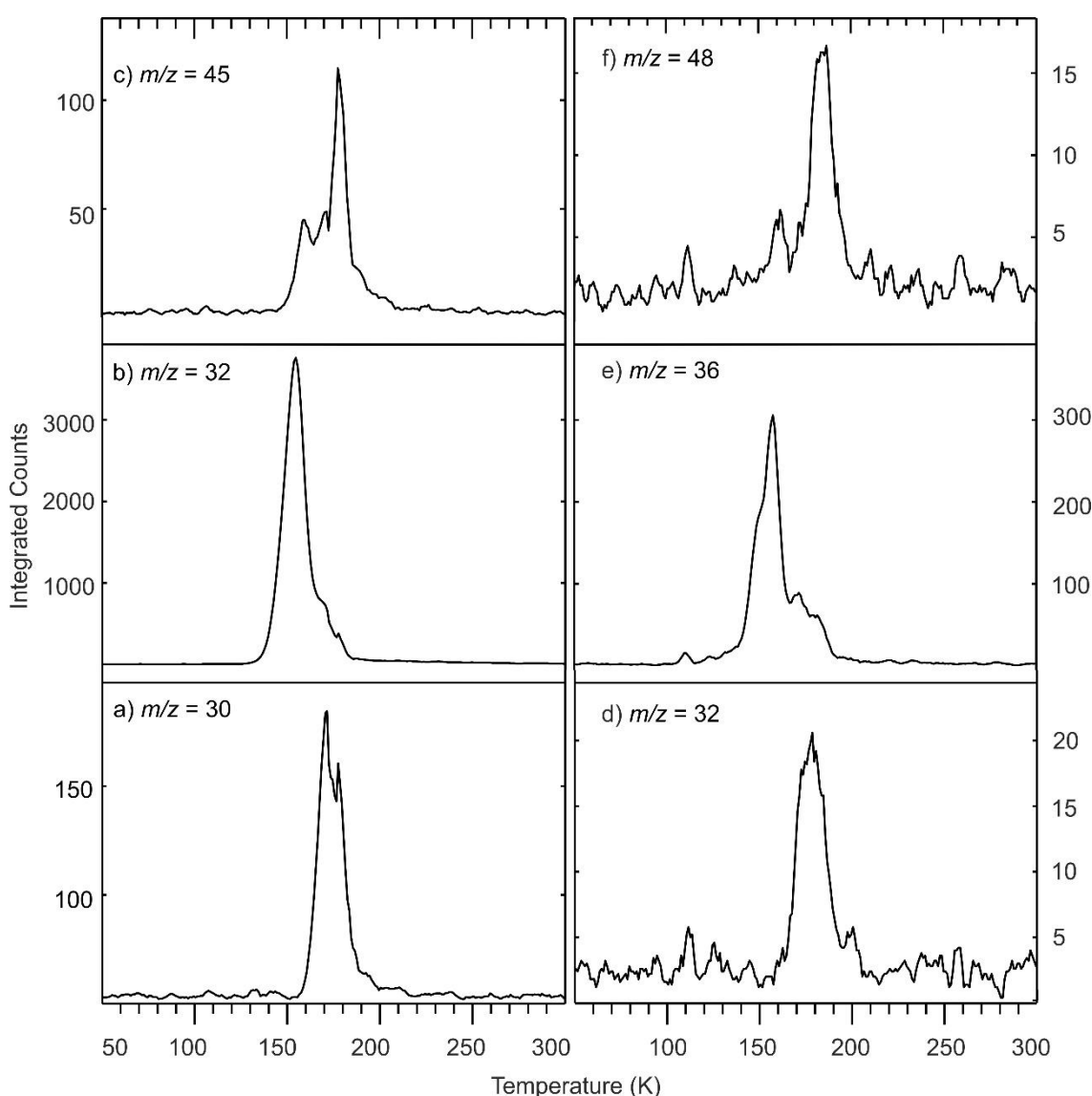


**Figure 72.** Selected TPD profiles extracted from the PI-ReTOF-MS spectra shown in Figure 71. TPD profiles of (a)  $m/z = 30$  ( $N_2H_2^+$ ), (b)  $m/z = 32$  ( $N_2H_4^+$ ) and (c)  $m/z = 45$  ( $N_3H_3^+$ ) subliming from the irradiated  $NH_3$  ice shown on the left panel and TPD profiles of (d)  $m/z = 32$  ( $N_2D_2^+$ ), (e)  $m/z = 34$  ( $N_2D_4^+$ ) and (f)  $m/z = 48$  ( $N_3D_3^+$ ) subliming from the irradiated  $ND_3$  ice shown on the right panel recorded at photoionization energies of 10.49 eV.

## Isomer identification

Having already assigned the  $\text{N}_3\text{H}_3/\text{N}_3\text{D}_3$  formed after energetic electron irradiation of  $\text{NH}_3/\text{ND}_3$  ices, we are now identifying the possible isomers. For this, we probed the  $\text{NH}_3$  ice at additional ionization energies (9.67 eV and 9.1 eV) and compiled in Figure 73 for the species at  $m/z$  of 45 ( $\text{N}_3\text{H}_3$ ). As can be seen in the figure, the total observed intensity in 9.67 eV is a factor of six lower than that measured in the 10.49 eV experiments. However, the TPD profile shows the same shape as that measured at 10.49 eV (see normalized TPD profile, Figure 73 top), strongly indicating that cyclo-triazene is not observed in our experiment (the calculated  $IE = 9.91$  eV is above the applied photon of  $IE = 9.67$  eV (Scheme 30)). Further, at 9.1 eV photoionization energy, we observe no signal of  $m/z$  of 45 at all. This lead us to exclude iso-triazene, since the ionization energy in the 9.1 eV experiment is well above the ionization energy of this isomer ( $IE = 8.62$  eV). A discrimination between the remaining isomers of  $\text{N}_3\text{H}_3$  based solely on their ionization energies is difficult due to the uncertainty of the calculated ionization energies in the order of up to  $\pm 0.2$  eV.<sup>[277-278]</sup> However, we argue that the observed isomers are cis- and/or trans-triazene but not triimide (see details in our original publication).<sup>[241]</sup>

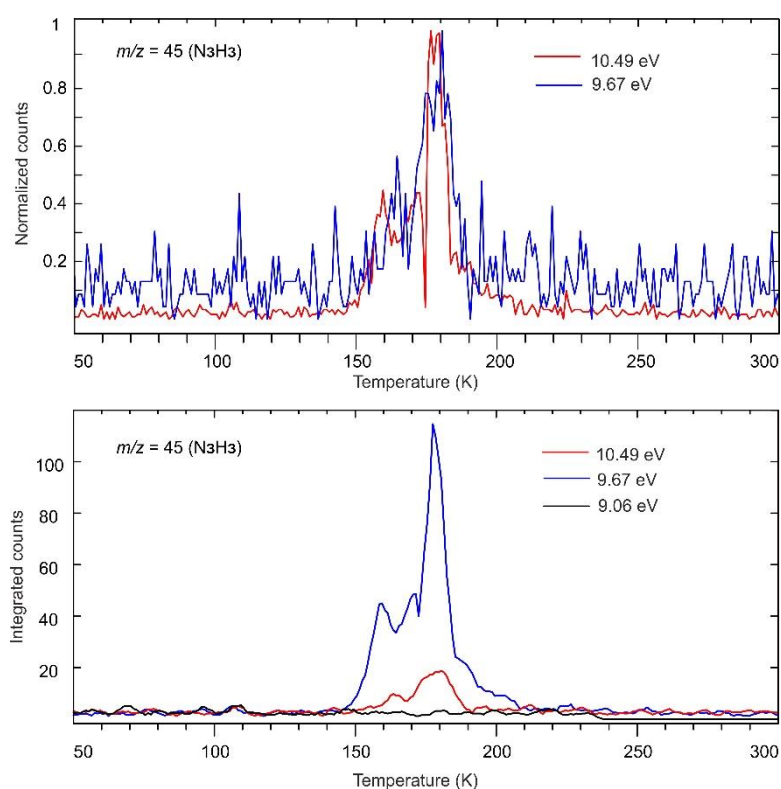
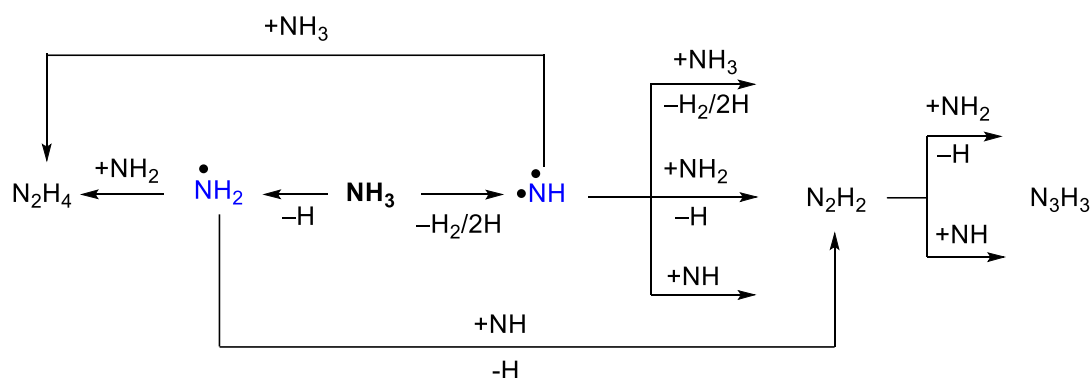


**Figure 73.** Selected TPD profiles extracted from the PI-ReTOF-MS spectra shown in Figure 71. (Bottom) TPD profiles of  $m/z = 45$  ( $\text{N}_3\text{H}_3^+$ ) subliming from the irradiated  $\text{NH}_3$  ice recorded at photoionization energies of 10.49 eV (red), 9.67 eV (blue) and 9.06 eV (black). (Top) For intensity and shape comparison, the normalized spectrum is also shown in the figure.

## Reaction pathways

Having already established that cis/trans-triazenes and/or triimide isomers are forming in the ice, we are now proposing the possible formation pathway(s). For this, we carried out additional experiments on  $\text{NH}_3:\text{N}_2$  ( $1:1.0 \pm 0.2$ ) and  $\text{NH}_3:^{15}\text{N}_2$  ( $1:1 \pm 0.2$ ) ices at 10.49 eV ionization energy compiled in Figure 74. The principal results are identical to  $\text{NH}_3$  ices ionized at 10.49 eV discussed above. However, compared to the pure  $\text{NH}_3$  ices, the yield of  $\text{N}_2\text{H}_2$ ,  $\text{N}_2\text{H}_4$  and  $\text{N}_3\text{H}_3$  decreases by a factor of 1.6, 4.3 and 2.5, respectively, in the  $\text{NH}_3:\text{N}_2$  ice, indicating  $\text{N}_3\text{H}_3$  might be synthesized via diimide ( $\text{N}_2\text{H}_2 + \bullet\text{NH} \rightarrow \text{N}_3\text{H}_3$ ) but not from hydrazine ( $\text{N}_2\text{H}_4 + \bullet\text{NH}_2 \rightarrow \text{N}_3\text{H}_3 + \text{H}_2$ ), as  $\text{N}_3\text{H}_3$  did not decrease as much as  $\text{N}_2\text{H}_4$ . A further proof to  $\text{N}_2\text{H}_2$  as the reaction intermediate in the  $\text{N}_3\text{H}_3$  formation is that, the experiment with  $\text{NH}_3:^{15}\text{N}_2$  ice gives the ratio of  $\text{N}_2\text{H}_2$  to  $^{15}\text{NN}_2\text{H}_2$  ( $0.53 \pm 0.05$ ) the same as that of  $\text{N}_3\text{H}_3$  to  $^{15}\text{NN}_2\text{H}_3$  ( $0.52 \pm 0.05$ ). The experiment with  $\text{NH}_3:^{15}\text{N}_2$  ice also ruled out the formation of  $\text{N}_3\text{H}_3$  involving  $\text{N}_2$  since we obtained only trace amount of  $^{15}\text{NN}_2\text{H}_3$  and  $^{15}\text{N}_2\text{NH}_3$  (Figure 74). Additional possible reaction pathways leading to  $\text{N}_3\text{H}_3$  are compiled in Scheme 31.



**Scheme 31.** Principal reaction pathways towards the formation of  $\text{N}_3\text{H}_3$  starting with  $\text{NH}_3$  and  $\text{N}_2\text{H}_2$  as an intermediate. The primary reaction products are shown in blue. Also included are two principal reaction towards  $\text{N}_2\text{H}_4$ .

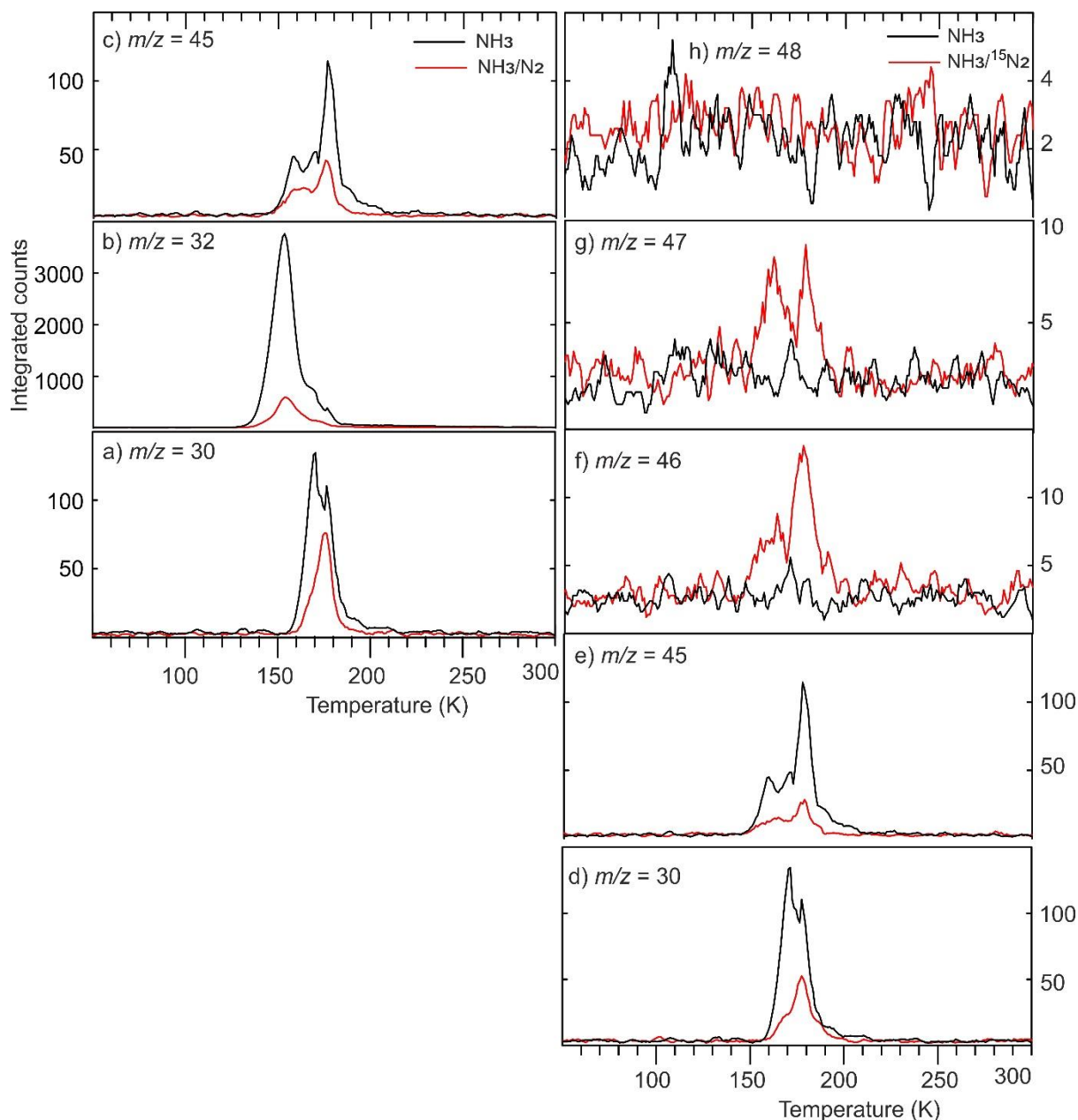


**Figure 74.** Selected TPD profiles extracted from the PI-ReTOF-MS spectra shown in Figure 71. TPD profiles of (a)  $m/z = 30$  ( $\text{N}_2\text{H}_2^+$ ), (b)  $m/z = 32$  ( $\text{N}_2\text{H}_4^+$ ) and (c)  $m/z = 45$  ( $\text{N}_3\text{H}_3^+$ ) subliming from the irradiated  $\text{NH}_3$  (black) and  $\text{NH}_3/\text{N}_2$  (red) ices shown on the left panel and TPD profiles of (d)  $m/z = 32$  ( $\text{N}_2\text{H}_2^+$ ), (e)  $m/z = 45$  ( $\text{N}_3\text{H}_3^+$ ), (f)  $m/z = 46$  ( $^{15}\text{NN}_2\text{H}_3^+$ ), (g)  $m/z = 47$  ( $^{15}\text{N}_2\text{NH}_3^+$ ) and (h)  $m/z = 48$  ( $^{15}\text{N}_3\text{H}_3^+$ ) subliming from the irradiated  $\text{NH}_3$  (black) and  $\text{NH}_3/^{15}\text{N}_2$  (red) ices shown on the right panel recorded at photoionization energies of 10.49 eV.

## Conclusion

Upon energetic electron irradiation of  $\text{NH}_3$ ,  $\text{ND}_3$ ,  $\text{NH}_3:\text{N}_2$  and  $\text{NH}_3:^{15}\text{N}_2$  ices at 5.5 K, the highly elusive  $\text{N}_3\text{H}_3$ ,  $\text{N}_3\text{D}_3$ ,  $^{15}\text{N}_2\text{NH}_3$  and  $^{15}\text{NN}_2\text{H}_3$  were detected for the first time using PI-ReTOF-MS technique. We did not detect cyclo-triazenes or iso-triazenes, suggesting that

cis/trans triazene is the most stable  $N_3H_3$  isomer. This study also suggests that the most likely formation pathway of  $N_3H_3$  is via the diimide ( $N_2H_2$ ).

Parts of chapter 8 were "Reprinted (adapted) with permission from *ChemPhysChem*, 17 (2016), pp. 2726–2735. Copyright 2016, John Wiley and Sons."



attributed to nitrogen monoxide (NO) and methoxy (CH<sub>3</sub>O) radicals. Hereafter, Chachaty *et al.* (1965) carried out  $\alpha$ -particle irradiation of nitromethane at 77 K and revealed the presence of methyl (CH<sub>3</sub>), nitrogen dioxide (NO<sub>2</sub>), and nitromethyl (CH<sub>2</sub>NO<sub>2</sub>) radicals.<sup>[301]</sup> The same group (1969) suggested that the photolysis of nitromethane in a perfluoromethylcyclohexane at 77 K produced mainly the methoxy (CH<sub>3</sub>O) radical.<sup>[302]</sup> Finally, Symons (1988) exposed nitromethane and D3-nitromethane to <sup>60</sup>Co  $\gamma$ -rays at 77 K and observed mainly methyl (CH<sub>3</sub>) and nitrogen dioxide (NO<sub>2</sub>) radicals.<sup>[304]</sup> We would like to point out that none of the previous experiments was able to detect more than three radicals simultaneously. Here, using EPR spectroscopy, we investigate the photochemistry of nitromethane (CH<sub>3</sub>NO<sub>2</sub>) along with its isotopically labeled counterpart D3-nitromethane (CD<sub>3</sub>NO<sub>2</sub>) in detail, at discrete wavelength between 266 nm and 121 nm in argon and neon matrices as well as in the pure solid at 5 K.

## Results and discussion

The photolysis of nitromethane (CH<sub>3</sub>NO<sub>2</sub>) and D3-nitromethane (CD<sub>3</sub>NO<sub>2</sub>) in both argon and neon matrices as well as in the pure solid at 5 K resulted in the appearance of multiple new features in the EPR spectrum (Figure 75). In order to assign these features, we pursue the following strategy. First, we simulate the EPR spectrum of each of the *individual* carbon-, nitrogen-, and oxygen-centered radicals predicted to be formed during the photolysis.<sup>[295, 297]</sup> Second, we exploit a linear combination of these individual spectra as base functions to simulate the experimentally obtained EPR spectra after the photolysis. Figure 75 demonstrates that distinct matrices in the experiments have little effects on the newly identified species; as expected, the peaks were found to be sharper in the matrix-isolated samples (Figure 75a). Also as can be seen in Figure 75a, no additional peaks are emerging after about 20 min irradiation; only the yield is enhanced. Finally, an annealing of the irradiated samples to 30 K decreases the intensity of the (radical) peaks as the result of radical diffusion and hence recombination (Figure 75b).

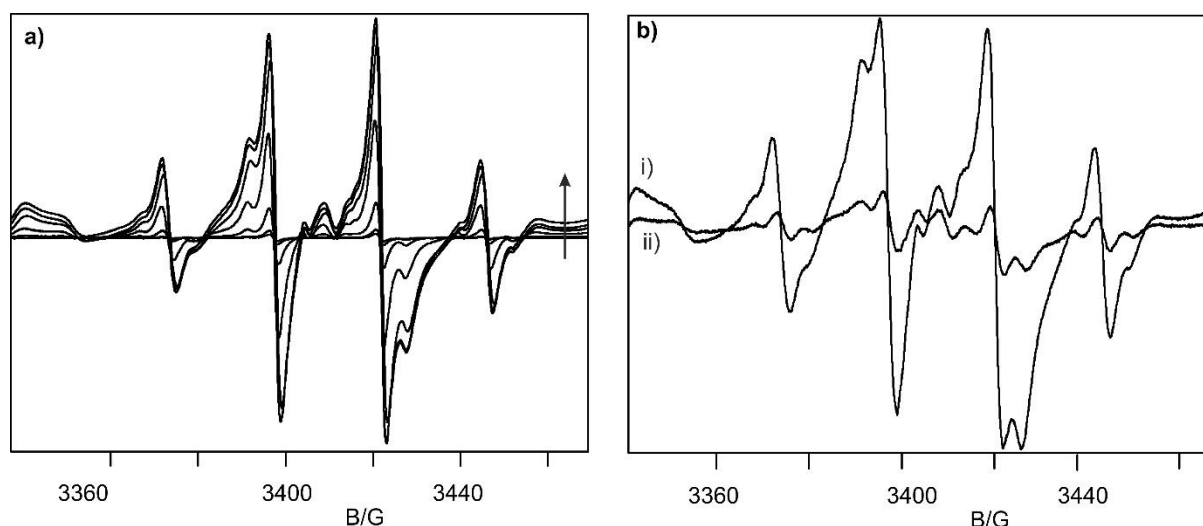


**Figure 75.** EPR spectra obtained after  $\lambda = 254$  nm photolysis of matrix-isolated and neat nitromethane, respectively, at 5 K. a) 0.2 % nitromethane ( $\text{CH}_3\text{NO}_2$ ) in solid argon after irradiation times of 1, 2, 10, 15, 25, 55, and 85 min. b) Neat nitromethane ( $\text{CH}_3\text{NO}_2$ ) after 180 min irradiation (i) and subsequent annealing at 30 K for 5 minutes (ii).

### Individual EPR spectra

#### Atomic hydrogen (H) and deuterium (D)

The theoretical predictions of atomic hydrogen and deuterium spectra have been discussed in detail in Chapter 1. The EPR parameters of atomic hydrogen trapped in low-temperature matrices are also frequently reported in the literature.<sup>[305-307]</sup> It was shown that atomic hydrogen has two spectral lines separated by about 510 G, centered at approximately  $g = 2$  and hfcc  $A = 504.9$  G. The hfcc and  $g$ -factor of free hydrogen atom are also theoretically known to be 506.8 G and 2.00228384 respectively.<sup>[307-310]</sup> These reports agreed well with our finding of two lines for atomic hydrogen produced by photolysis of nitromethane, which are separated by about 508 G, centered at  $g = 2.002$  and described by hfcc of ( $A \text{ } ^1\text{H}$ ) = 505.62 G (Figure 76). Similarly, upon decomposition of D<sub>3</sub>-nitromethane, we observe three lines assigned to deuterium atoms which are separated by about 150 G with a  $g$ -factor of 2.007 and hfcc of 77.43 G. These values agree well with the reported values of 150 G, 2.0023 and 77.88 G, respectively (Figure 76).  
[306, 310]

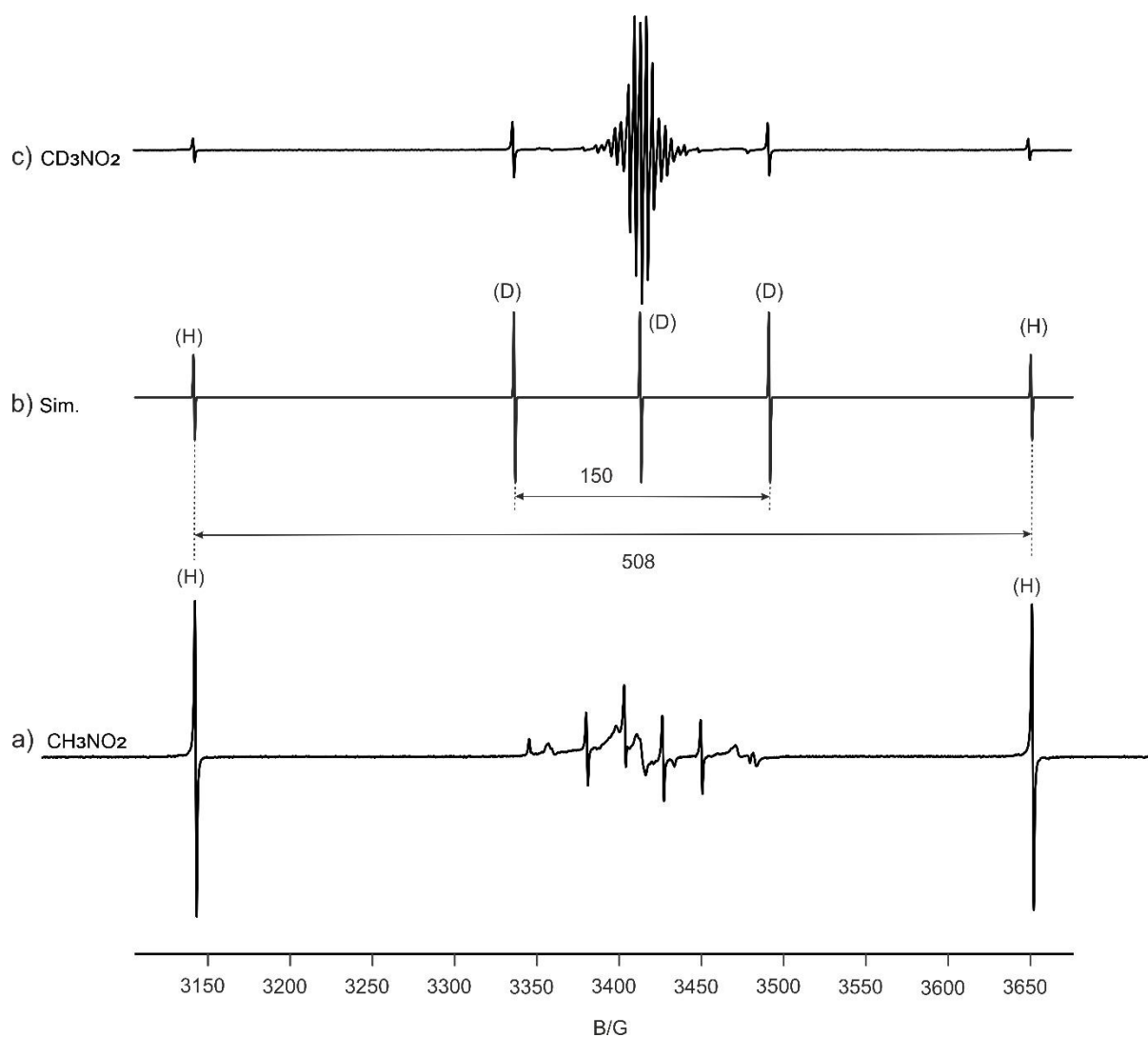


**Figure 76.** EPR spectrum of atomic hydrogen and deuterium. (a) EPR spectrum produced by  $\lambda = 266$  nm irradiation of nitromethane ( $\text{CH}_3\text{NO}_2$ ) for 30 min matrix-isolated in argon (0.05 %) at 5 K. (b) Simulated spectrum of atomic hydrogen and deuterium. (c) The individual EPR spectrum of atomic hydrogen and deuterium produced by  $\lambda = 266$  nm laser irradiation of the mixture of excess D3-nitromethane ( $\text{CD}_3\text{NO}_2$ ) and nitromethane ( $\text{CH}_3\text{NO}_2$ ) for 30 minutes matrix isolated in argon (0.05 %) at 5 K.

### Methyl ( $\text{CH}_3$ ) and D3-methyl ( $\text{CD}_3$ ) radicals

The EPR spectrum of the methyl radical ( $\text{CH}_3$ ) consists of four lines (Figure 77), which are observed after short irradiation times of about 10 min of nitromethane ( $\text{CH}_3\text{NO}_2$ ) at 5 K. Since the unpaired electron is localized at the carbon atom, which is surrounded by three chemically equivalent hydrogen atoms, we expect a quartet of lines for the methyl ( $\text{CH}_3$ ) radical as a result of the hyperfine interactions between the spin of the electron and the nuclear spin of three protons  $^1\text{H}$  ( $I = 1/2$ ). Similarly, we predict septet lines for the D3-methyl radical ( $\text{CD}_3$ ) due to interaction of the unpaired electron with the three adjacent deuterium atoms  $^2\text{H}$  ( $I = 1$ ). The methyl radical trapped in low-temperature matrices have been studied by EPR spectroscopy

previously and thus the EPR parameters are already known.<sup>[92, 311-317]</sup> It was shown that at 4.2 K, the methyl radical has four EPR lines with a hyperfine coupling constant (hfcc) of an average of about 23.1 G. In agreement with these studies, our experiment at 5 K yields well resolved and separated quartet lines attributed to the methyl radical with hfccs of 23.06, 23.12 and 23.27 G (Figure 77). Bielski *et al.* reported that the total separation of the four lines of the methyl radical formed after photolysis of nitromethane in a water matrix or a tetrachloride matrix at 77 K was found to be 65 G, in a close agreement to our experimental findings of 69.45 G.<sup>[293]</sup> The EPR parameters of the D3-methyl radical trapped in low-temperature matrices were also reported.<sup>[92, 311-312]</sup> It shows a septet of lines with hfcc of an average of about 3.59 G. In our experiments we measured an average of 3.8 G hfcc of septet lines for the D3-methyl radical ( $\text{CD}_3$ ).<sup>[92]</sup>

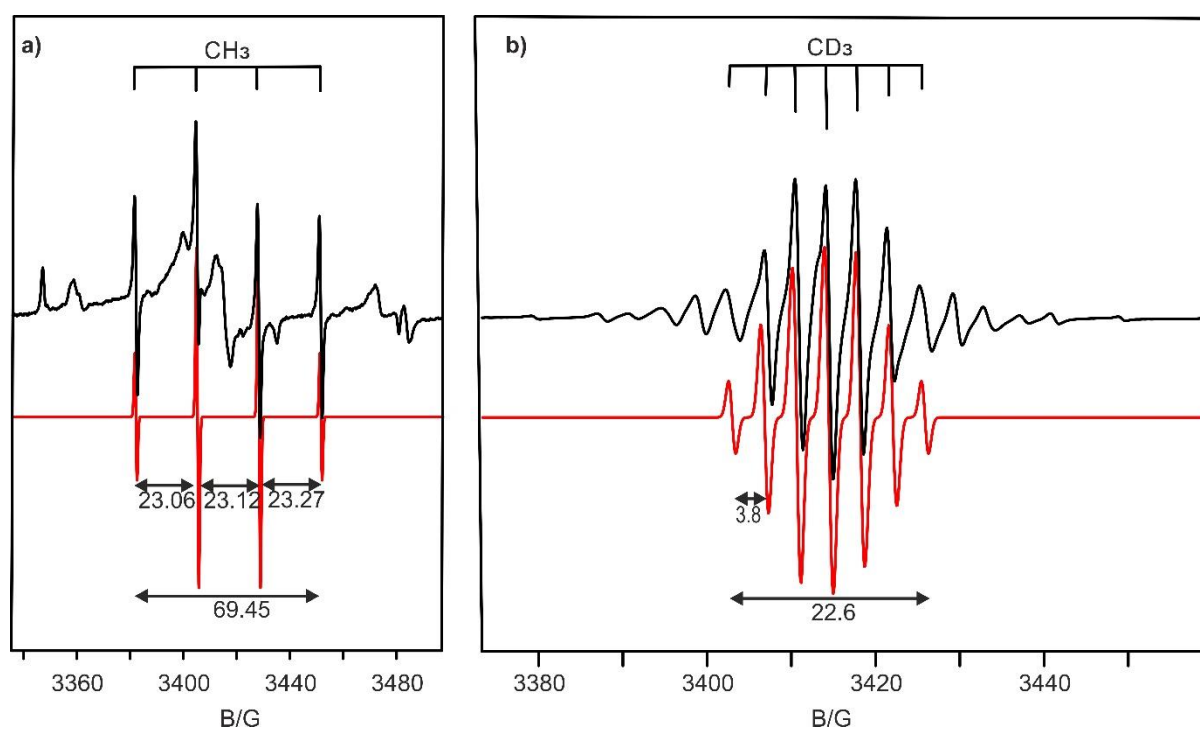


**Figure 77.** The EPR spectra of methyl (a) and D3-methyl (b) radicals produced by  $\lambda = 254$  nm irradiation of nitromethane ( $\text{CH}_3\text{NO}_2$ ) and D3-nitromethane ( $\text{CD}_3\text{NO}_2$ ), respectively, matrix isolated in argon (0.05 %) at 5 K followed by annealing to 30 K for 5 minutes (black). The simulated spectra of the  $\text{CH}_3$  and  $\text{CD}_3$  radical are shown in red with the simulation parameters compiled in Table 22.

**Table 22.** EPR parameters of methyl (CH<sub>3</sub>) and D3-methyl (CD<sub>3</sub>) radicals at 5 K.

Sample	Temp/(K)	g-values			Hyperfine coupling constant (hfcc) /(G)				Reference
		g1	g2	g3	A1	A2	A3	Aiso	
H <sub>2</sub> +CO	4.2	2.0026	2.0026	2.0022	23.50	23.50	22.20	23.07	[316]
D <sub>2</sub> +CO	4.2	2.0026	2.0026	2.0022	3.62	3.62	3.42	3.55	[316]
CH <sub>4</sub>	4.1	-	-	-	23.00	23.15	23.33	23.15	[92]
CH <sub>3</sub> NO <sub>2</sub>	5.0	2.0005	2.0005	2.0005	23.06	23.12	23.27	23.15	This work
CD <sub>3</sub> NO <sub>2</sub>	5.0	2.0007	2.0008	2.0009	3.73	3.84	3.84	3.80	This work

### Nitromethyl (CH<sub>2</sub>NO<sub>2</sub>) and D2-nitromethyl (CD<sub>2</sub>NO<sub>2</sub>) radicals

In the case of the nitromethyl radical (CH<sub>2</sub>NO<sub>2</sub>), the unpaired electron is localized at the carbon atom. Due to coupling between the spin of the electron and the nuclear spin of the two adjacent protons <sup>1</sup>H ( $I = 1/2$ ) as well as the nitrogen atom <sup>14</sup>N ( $I = 1$ ), we expect to see a triplet of triplets EPR lines for the CH<sub>2</sub>NO<sub>2</sub> radical (Figure 78a). The simulation enables us to extract the spin Hamiltonian parameters of CH<sub>2</sub>NO<sub>2</sub>: the hfccs of the hydrogen atoms ( $A_H = 23.19$  G) and the nitrogen atom ( $A_N = 4.3$  G) and the g-value  $g_{iso} = 2.0020$ . This was found to be in close agreement to the reported values of  $A1$  (<sup>1</sup>H) = 22 G,  $A2$  (<sup>1</sup>H) = 22 G,  $A3$  (<sup>14</sup>N) = 6 G.<sup>[301, 303-304]</sup>

Similarly, we expect a quintet of triplets for D2-nitromethyl (CD<sub>2</sub>NO<sub>2</sub>) radical. The two chemically equivalent deuterium atoms <sup>2</sup>H ( $I = 1$ ) result in 5 lines, of which each component will then further split into three lines due to coupling with <sup>14</sup>N of the nitrogen dioxide nitrogen atom ( $I = 1$ ) to give a total of  $5 \times 3 = 15$  lines. The simulation of the experimental spectrum of CD<sub>2</sub>NO<sub>2</sub> fits best with the following parameters:  $A1$  (<sup>2</sup>H) = 11.4 G,  $A2$  (<sup>2</sup>H) = 11.4 G,  $A3$  (<sup>14</sup>N) = 3.85 G,  $g_{iso} = 2.0010$  (Figure 78b).

**Table 23.** EPR parameters of nitromethyl (CH<sub>2</sub>NO<sub>2</sub>) and D2-nitromethyl (CD<sub>2</sub>NO<sub>2</sub>) radicals.

Sample	Temp/(K)	g-values			Hyperfine coupling constant (hfcc) /(G)			Reference
		g1	g2	g3	A1	A2	A3	
CH <sub>3</sub> NO <sub>2</sub>	5	2.0020	2.0020	2.0020	23.19	23.19	4.30	This work
CH <sub>3</sub> NO <sub>2</sub>	77	-	-	-	22	22	5	[303]
CD <sub>3</sub> NO <sub>2</sub>	5	2.0010	2.0010	2.0010	11.4	11.4	3.85	This work

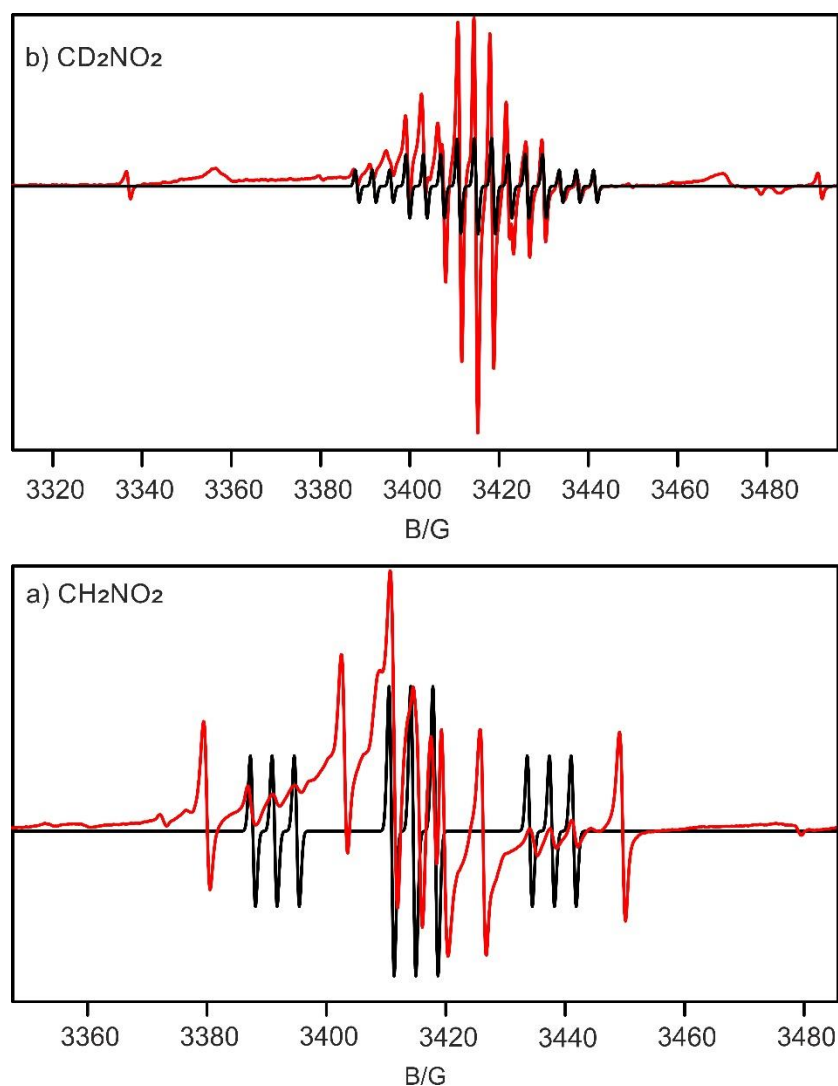


**Figure 78.** EPR spectra of nitromethyl ( $\text{CH}_2\text{NO}_2$ ) (a) and D2-nitromethyl ( $\text{CD}_2\text{NO}_2$ ) radicals (b) produced by  $\lambda = 266$  nm (4.7 eV) irradiation of nitromethane ( $\text{CH}_3\text{NO}_2$ ) (doped with  $\text{CD}_3\text{NO}_2$ ) and D3-nitromethane ( $\text{CD}_3\text{NO}_2$ ) (doped with  $\text{CH}_3\text{NO}_2$ ), respectively, matrix isolated in argon (0.05 %) at 5 K: simulated spectra of the  $\text{CH}_2\text{NO}_2$  and  $\text{CD}_2\text{NO}_2$  radical are shown in black; experimental spectra of the individual radicals are depicted in red. The simulation parameters are given in Table 23.

### Methoxy ( $\text{CH}_3\text{O}$ ) and D3-methoxy ( $\text{CD}_3\text{O}$ ) radicals

The EPR spectrum of the methoxy radical ( $\text{CH}_3\text{O}$ ) formed upon photolysis of nitromethane in a perfluoromethylcyclohexane matrix at 77 K is documented.<sup>[302]</sup> The reported parameters are as follows: hyperfine coupling constant ( $A^1\text{H}$ ) = 9 G and g-factors = 2.0135 (perpendicular) and 1.9932 (parallel). These data are in agreement to our simulations proposing a best fit to the experimental spectrum ( $A^1\text{H}$ ) = 9 G and g-factors  $g_1 = 2.0122$ ,  $g_2 = 1.9934$ ,  $g_3 = 2.0315$  (Figure 79). However, we failed to detect the D3-methoxy radical ( $\text{CD}_3\text{O}$ ) upon photolysis of D3-nitromethane; this is likely due to the overlap with the spectral lines of the  $\text{CD}_2\text{NO}_2$  and  $\text{CD}_3$  photoproducts.

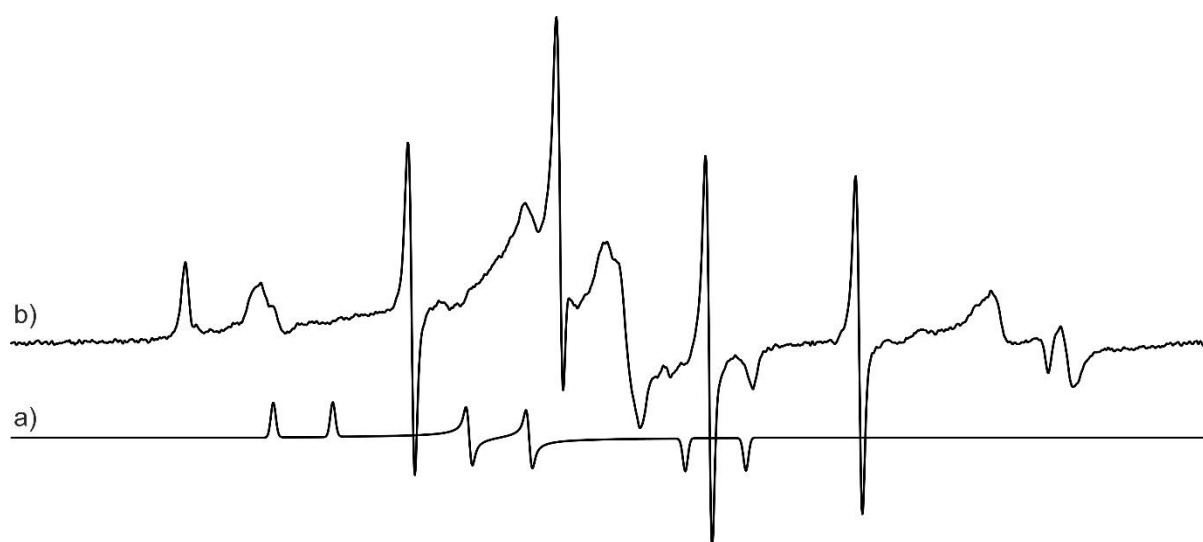


**Figure 79.** Comparison of (a) simulated spectrum of the methoxy ( $\text{CH}_3\text{O}$ ) radical with (b) the EPR spectrum of the methoxy radical produced by  $\lambda = 254$  nm irradiation of nitromethane ( $\text{CH}_3\text{NO}_2$ ) for 18 hours, matrix isolated in argon (0.05 %) at 5 K followed by annealing at 30 K for 5 minutes .

### Nitrogen dioxide ( $\text{NO}_2$ )

We expect three EPR lines ( $M_I = +1, 0, -1$ ) for nitrogen dioxide ( $\text{NO}_2$ ), which result from the interaction of the unpaired electron with the nuclear spin of the nitrogen atom  $^{14}\text{N}$  ( $I = 1$ ). In addition, in a randomly oriented nitrogen dioxide ( $\text{NO}_2$ ) molecule, each  $M_I$  values will split further into three  $x$ ,  $y$ , and  $z$  components to give a total of  $3 \times 3 = 9$  lines.<sup>[318-319]</sup> Experimentally, the EPR spectrum of nitrogen dioxide ( $\text{NO}_2$ ) in low-temperature matrices has been extensively investigated.<sup>[318, 320-325]</sup> It was shown that the spectral line shapes as well as line positions of the nitrogen dioxide ( $\text{NO}_2$ ) are temperature dependent. Thus, the value of the hfcc due to the interaction of the magnetic moment of the unpaired electron with the nitrogen atom varies from about 55 G at 4 K to 12 G at 173 K, of average splitting of the triplet spectrum observed for nitrogen dioxide ( $\text{NO}_2$ ).<sup>[321]</sup> It was also reported that the rotational motion of the nitrogen dioxide ( $\text{NO}_2$ ) radical is axially symmetric about the  $y$  axis over the temperature range from 12 to 87 K.<sup>[320, 322, 324]</sup> Therefore, even at the low temperature of 4 K, the  $x$  and  $z$  components of the  $g$  and  $A$  tensors of nitrogen dioxide are less resolved, whereas the  $y$  components are observable up to 102 K.<sup>[320]</sup> In accordance to these studies, we observed in the present experiments well resolved a  $y$ -components of the nitrogen dioxide ( $\text{NO}_2$ ) radical at 5 K (Figure 80).

The spin Hamiltonian parameters (the  $g$  and  $A$  tensor components) for nitrogen dioxide ( $\text{NO}_2$ ) in various selected matrices over a wide range of temperature are summarized in Table 24. The

values reported in literature were found to be in good agreement with our experimental results. Our simulation best fit to the experimental spectrum of nitrogen dioxide ( $\text{NO}_2$ ) produced by irradiation of nitromethane using the parameters  $g_x = 2.0026$ ,  $g_y = 1.9907$ ,  $g_z = 2.0025$ ,  $A_x = 51.0$  G,  $A_y = 43.7$  G,  $A_z = 67.9$  G and  $A_{\text{iso}} = 54.4$  at 5 K; the parameters were slightly changed when the matrix was annealed between 20 and 30 K  $g_x = 2.0009$ ,  $g_y = 1.9892$ ,  $g_z = 2.0010$ ,  $A_x = 56.5$  G,  $A_y = 44.6$  G,  $A_z = 68.5$  G and  $A_{\text{iso}} = 56$ .

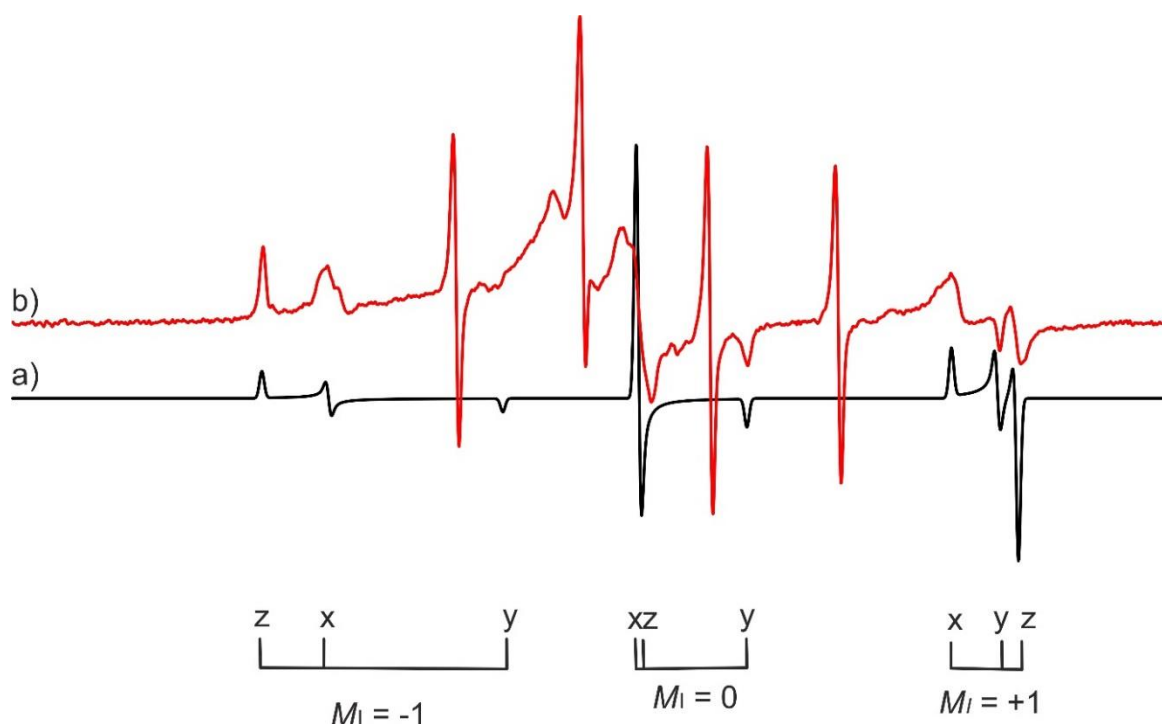


**Figure 80.** (a) Simulated spectrum of nitrogen dioxide ( $\text{NO}_2$ ) and (b) the EPR spectrum produced by  $\lambda = 254$  nm (4.9 eV) irradiation of nitromethane ( $\text{CH}_3\text{NO}_2$ ) for 18 hours matrix isolated in argon (0.05 %) at 5 K followed by annealing to 30 K for 5 min. The simulation parameters are compiled in Table 24.

**Table 24.** EPR parameters of nitrogen dioxide ( $\text{NO}_2$ ) in various media.

Sample	Temp (K)	g-values			Hyperfine coupling constant (hfcc) (G)				Reference
		g1	g2	g3	A1	A2	A3	Aiso	
$\text{CH}_3\text{NO}_2$	5	2.0026	1.9907	2.0025	51.5	43.7	67.9	54.4	This work
$\text{CH}_3\text{NO}_2$	30	2.0009	1.9892	2.0010	56.5	44.6	68.5	56.5	This work
$\text{CD}_3\text{NO}_2$	5	2.0026	1.9907	2.0025	51.5	43.7	67.9	54.4	This work
$\text{CD}_3\text{NO}_2$	30	2.0026	1.9900	2.0008	56.5	45.5	68.6	56.8	This work
$\text{CH}_3\text{NO}_2$	77	2.0060	1.9910	2.0020	47	46	66	53.0	[304]
Vycor <sup>a</sup>	4.8	2.0051	1.9913	2.0017	50	46	65.5	53.8	[322]
Zeolite <sup>a</sup>	4.8	2.0051	1.9913	2.0017	50	46	65.5	53.8	[322]
$\text{SiO}_2$ <sup>a</sup>	4.2	2.0057	1.9920	2.0020	50.1	45.8	65.5	53.8	[320]
$\text{MgO}$ <sup>a</sup>	77	2.005	2.002	1.9910	52	65	49	55.3	[326]

<sup>a</sup>  $\text{NO}_2$  adsorbed on surface studies

Bielski *et al.* reported two triplet lines for the NO<sub>2</sub> radical: one major triplet with an average separation of 58 G and one minor triplet with a 46 G separation, giving a total of 3 + 3 = 6 lines in the EPR spectrum which were observed upon photolysis of nitromethane at 77 K.<sup>[293]</sup> This is in agreement with our experimental results at 5 K:  $A_y = 46$  G and an average of  $A_x$  and  $A_z = 57.5$  G. The fact that we have got a well resolved and separated triplet of triplets in the spectrum of nitrogen dioxide (NO<sub>2</sub>) upon photolysis of nitromethane could be explained with the difference in temperature and the use of argon matrices in our experiments. While we used inert gas matrices at 5 K in the present experiments, previous experiments exploited water and carbon tetrachloride matrices at 77 K.<sup>[293]</sup>

### Nitrogen monoxide (NO)

The EPR spectrum of nitrogen monoxide (NO) has been reported previously.<sup>[327-332]</sup> The coupling between the unpaired electron and the nitrogen atom results in spin Hamiltonian parameters of  $g_1 = 2.008$ ,  $g_2 = 2.0061$ ,  $g_3 = 2.0027$ ,  $A_1 = 5.7$  G,  $A_2 = 5.7$  G,  $A_3 = 30.7$  G and  $A_{iso} = 14.1$  G.<sup>[327]</sup> These are in a close agreement with our best fit simulations of the nitrogen monoxide (NO) radical with the parameters  $g_1 = 2.0027$ ,  $g_2 = 2.0064$ ,  $g_3 = 2.0002$ ,  $A_1 = 6.4$  G,  $A_2 = 3.6$  G,  $A_3 = 30.7$  G and  $A_{iso} = 13.6$  (Figure 81).

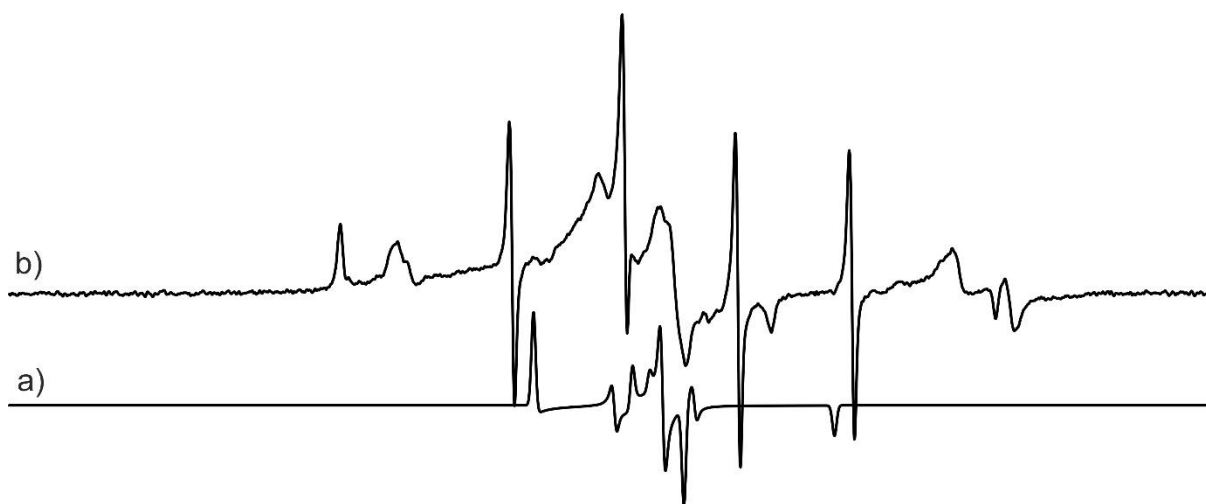


**Figure 81.** Comparison of (a) simulated spectrum of nitrogen monoxide radical (NO) (b) with the EPR spectrum of the nitrogen monoxide (NO) radical produced by  $\lambda = 254$  nm (4.9 eV) irradiation of nitromethane (CH<sub>3</sub>NO<sub>2</sub>) for 18 hours, matrix isolated in argon (0.05 %) at 5 K followed by annealing to 30 K for 5 minutes.

Finally, we would like to stress that despite the extensive searches, we were unable to identify atomic oxygen (O), methylene nitrite (CH<sub>2</sub>ONO), or nitrosomethyl (CH<sub>2</sub>NO) radicals in the

irradiated ices, that was predicted to be formed upon decomposition of nitromethane ( $\text{CH}_3\text{NO}_2$ ; Scheme 32).

### Simulation of the experimental EPR spectra

We use a linear combination of the individual EPR spectra showed above to simulate the complex experimental EPR spectra of the photolysis products (Figures 82 and 83). The results are compiled in Table 25. The photolysis of (D3)-nitromethane ices at 266 nm, 254 nm, and 121 nm at 5 K excites the  $\pi^* \leftarrow n$ ,  $\pi^* \leftarrow \pi$ , and  $\pi^* \leftarrow \sigma$  transitions.<sup>[333-336]</sup> Generally spoken, the radicals observed are not found to be wavelength dependent with the exception that the (D2)-nitromethyl ( $\text{CH}_2\text{NO}_2/\text{CD}_2\text{NO}_2$ ) radicals are obtained in higher yield while using 266 nm and 121.5 nm photons.

The (D3)-methyl radical ( $\text{CH}_3/\text{CD}_3$ ) was detected at all three photolysis wavelengths in neat and also isotopically mixed ices. Similarly, hydrogen (H) and deuterium (D) could be monitored in all samples as well. The absorptions of these four species are prominent in the EPR spectra already after the first minute of photolysis at all wavelengths and contribute to the dominating EPR signal and account for up to  $55 \pm 10\%$  ( $\text{CH}_3/\text{CD}_3$ ) and  $30 \pm 10\%$  (H/D) of all open shell products. Also, the nitrogen-centered radicals, nitrogen dioxide ( $\text{NO}_2$ ) and nitrogen monoxide (NO) were identified upon photolysis of the low-temperature ices at all wavelengths. These species account for up to  $15 \pm 5\%$  and  $10 \pm 5\%$  of the open shell reaction products, respectively. Further, the oxygen-centered methoxy radical ( $\text{CH}_3\text{O}$ ) could be verified to be formed upon photolysis of the nitromethane samples at all wavelengths at levels of up to  $10 \pm 5\%$ . Finally, the EPR studies provided compelling evidence of the formation of the (D2)-nitromethyl radical ( $\text{CH}_2\text{NO}_2/\text{CD}_2\text{NO}_2$ ) at levels of up to  $25 \pm 5\%$ .

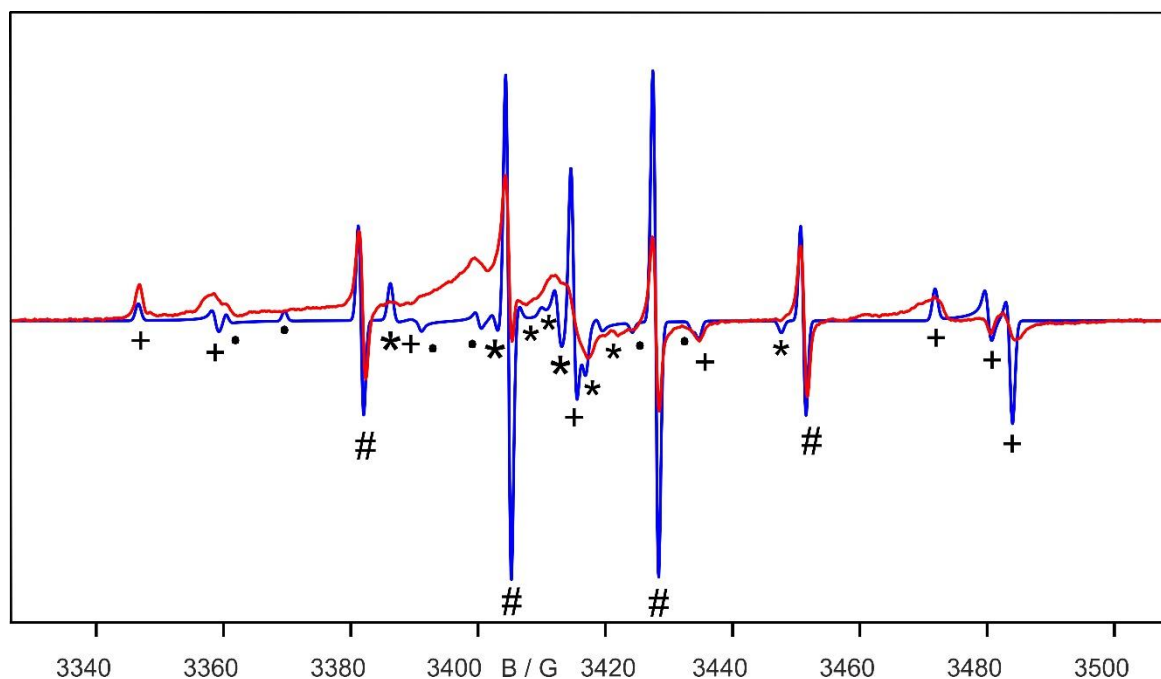


**Figure 82.** EPR spectra produced by  $\lambda = 254$  nm irradiation of nitromethane ( $\text{CH}_3\text{NO}_2$ ) over 18 hours matrix-isolated in argon (0.05 %) at 5 K followed by annealing to 30 K for 5 minutes. The simulated spectra of the methyl ( $\text{CH}_3$ , #), nitrogen dioxide ( $\text{NO}_2$ , +), methoxy ( $\text{CH}_3\text{O}$ , dot), and nitrogen monoxide ( $\text{NO}$ , \*) radicals are shown in blue with the experimental spectrum overlaid in red.

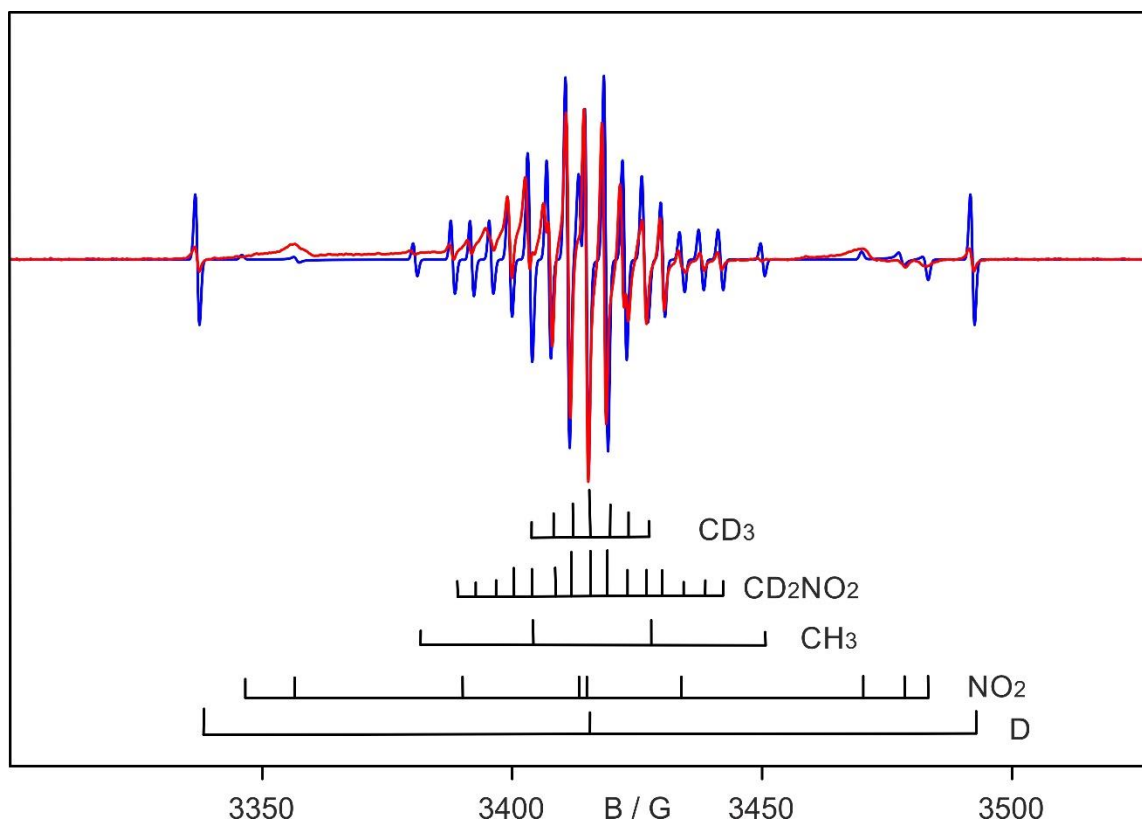


**Figure 83.** EPR spectra produced by  $\lambda = 254$  nm irradiation of a mixture of D3-nitromethane ( $\text{CD}_3\text{NO}_2$ ) and nitromethane ( $\text{CH}_3\text{NO}_2$ ) for 18 hours followed by annealing to 30 K for 5 minutes matrix-isolated in argon (0.05 %) at 5 K. The simulated spectra of D3-methyl ( $\text{CD}_3$ ), D2-nitromethyl ( $\text{CD}_2\text{NO}_2$ ), deuterium atoms (D), nitrogen dioxide ( $\text{NO}_2$ ), and methyl ( $\text{CH}_3$ ) radicals are shown in blue; the experimental spectrum is overlaid in red.

**Table 25.** Summary of photolysis experiments of nitromethane and D3-nitromethane in various media.

Sample	Wavelength/ (nm)	Irradiation Time (min)	Matrix	Temp (K)	Observed products
CH <sub>3</sub> NO <sub>2</sub>	254	1	Ar, Ne	5	CH <sub>3</sub> , H
		5	Ar, Ne	5	CH <sub>3</sub> , H, NO <sub>2</sub>
		20	Ar, Ne	5	CH <sub>3</sub> , NO <sub>2</sub> , H, NO, CH <sub>3</sub> O
		5	Ar, Ne	20-30 <sup>(a)</sup>	CH <sub>3</sub> , NO <sub>2</sub> , H, NO, CH <sub>3</sub> O
	254	30	Neat	5	CH <sub>3</sub> , NO <sub>2</sub> , H, NO, CH <sub>3</sub> O
	266	20	Ar, Ne	5	CH <sub>3</sub> , NO <sub>2</sub> , H, NO, CH <sub>3</sub> O, CH <sub>2</sub> NO <sub>2</sub>
	121.5	20	Ar	5	CH <sub>3</sub> , NO <sub>2</sub> , H, NO, CH <sub>3</sub> O, CH <sub>2</sub> NO <sub>2</sub>
	121.5	50	Neat	5	CH <sub>3</sub> , NO <sub>2</sub> , H, NO, CH <sub>3</sub> O, CH <sub>2</sub> NO <sub>2</sub>
CH <sub>3</sub> NO <sub>2</sub> + CD <sub>3</sub> NO <sub>2</sub>	254	20	Ar	5	CH <sub>3</sub> , CD <sub>3</sub> , NO <sub>2</sub> , H, D, CH <sub>2</sub> NO <sub>2</sub> , CD <sub>2</sub> NO <sub>2</sub>
		5	Ar	20-30 <sup>(a)</sup>	CH <sub>3</sub> , CD <sub>3</sub> , NO <sub>2</sub> , CH <sub>2</sub> NO <sub>2</sub> , CD <sub>2</sub> NO <sub>2</sub> , H, D
	266	20	Ar	5	CH <sub>3</sub> , CD <sub>3</sub> , NO <sub>2</sub> , CH <sub>2</sub> NO <sub>2</sub> , CD <sub>2</sub> NO <sub>2</sub> , H, D
	121.5	20	Ar	5	CH <sub>3</sub> , CD <sub>3</sub> , NO <sub>2</sub> , CH <sub>2</sub> NO <sub>2</sub> , CD <sub>2</sub> NO <sub>2</sub> , H, D
CD <sub>3</sub> NO <sub>2</sub>	254	25	Ar, Ne	5	CD <sub>3</sub> , D, NO <sub>2</sub> , CD <sub>2</sub> NO <sub>2</sub>
		5	Ar	20-30 <sup>(a)</sup>	CD <sub>3</sub> , D, NO <sub>2</sub> , CD <sub>2</sub> NO <sub>2</sub>
	266	20	Ar	5	CD <sub>3</sub> , D, NO <sub>2</sub> , CD <sub>2</sub> NO <sub>2</sub>
	121.5	20	Ar	5	CD <sub>3</sub> , D, NO <sub>2</sub> , CD <sub>2</sub> NO <sub>2</sub>

After 18 hours irradiation at 5 K, the matrix was annealed to 20-30 K for 5 minutes.

## Conclusion

The photolysis of nitromethane (CH<sub>3</sub>NO<sub>2</sub>) and D3-nitromethane (CD<sub>3</sub>NO<sub>2</sub>) both in argon and neon matrices as well as in the pure solid at 5 K at discrete wavelength between 266 and 121 nm were studied using EPR spectroscopy. These studies revealed the formation of two carbon-centered radicals [methyl (CH<sub>3</sub>), nitromethyl (CH<sub>2</sub>NO<sub>2</sub>)], one oxygen-centered radical [methoxy (CH<sub>3</sub>O)], two nitrogen-centered radicals [nitrogen monoxide (NO), nitrogen dioxide (NO<sub>2</sub>)], as well as atomic hydrogen (H). The decomposition products of these channels and the carbon-centered nitromethyl (CH<sub>2</sub>NO<sub>2</sub>) radical in particular represent crucial reaction intermediates leading via sequential molecular mass growth processes in the exposed nitromethane samples to complex organic molecules as predicted previously by dynamics calculations.

Parts of chapter 9 were "Reprinted (adapted) with permission from *J. Phys. Chem. A*, 120 (2016), pp. 1577–1587. Copyright 2018 American Chemical Society."

## Experimental section

### Synthesis

All starting materials and solvents were purchased from commercial suppliers and used as received without further purification. All solvents were of reagent grade and distilled by using the appropriate methods. Thin layer chromatography (TLC) analyses were carried out using Polygram G/UV<sub>254</sub> silica gel pre-coated plates and the spots were analyzed using a CAMAG UV lamp. ICN silica 32-63 (60 Å) was used for column chromatography. The NMR spectra were recorded (0-16 ppm region) with DPX 200, 250 and 400 Bruker instruments. NMR shifts are reported in parts per million (ppm) downfield from tetramethylsilane and referenced with respect to the solvent signal. Signal multiplicities are reported according to standard assignments. Mass spectra were recorded on a Varian MAT-CH5 spectrometer at 70 eV with electron impact as ion source. HR-MS-EI spectra were recorded on a Joel AccuTOF GCv JMS-T100GCV apparatus.

***p*-Tolyl(trifluoromethyl)diazirine (18b)** was synthesized according to a literature procedure.<sup>[337]</sup> IR (Ar, 3 K): 1616 (m), 1615 (m), 1593 (m), 1527 (m), 1459 (m), 1353 (s), 1328 (m), 1244 (s), 1233 (m), 1228 (m), 1220 (s), 1216 (m), 1200 (s), 1190 (vs), 1166 (vs), 1136 (m), 1058 (s), 940 (s), 808 (s), 732 (s), 588 (m), 574 (m), 537 (m) cm<sup>-1</sup>. <sup>1</sup>H NMR (200 MHz, CDCl<sub>3</sub>): δ/ppm = 7.21 (d, J = 8.2 Hz, 2H), 7.09 (d, J = 8.2 Hz, 2H), 2.37 (s, 3H) ppm. <sup>13</sup>C NMR (200 MHz, CDCl<sub>3</sub>): δ/ppm = 139.8, 129.5, 127.1, 126.5, 126.1, 124.9, 119.5, 28.1, 21.3 ppm.

**Phenyl(trifluoromethyl)diazomethane (19a)** was synthesized according to a literature procedure.<sup>[338]</sup> A mixture of 1 eq. of 2,2,2-trifluoroacetophenone and 1.5 eq. of *p*-toluenesulfonyl hydrazide was refluxed for 40 hrs. in absolute methanol. The crude product was purified by recrystallization in methanol. The tosylhydrazone obtained after recrystallization was treated with 1.1 eq. of NaH (previously washed three times with dry pentane to remove the mineral oil) dissolved in dry dichloromethane to generate the corresponding tan color sodium salt. Sublimation of the salt directly on a cold substrate at 40 °C under reduced pressure yields **19a**. IR (Ar, 3 K): 2092 (vs), 1606 (m), 1507 (m), 1369 (m), 1364 (m), 1354 (m), 1340 (m), 1329 (m), 1292 (m), 1275 (w), 1177 (m), 1151 (s), 1132 (s), 1129 (s), 959 (s), 748 (m), 688 (m), 670 (m) cm<sup>-1</sup>.

***p*-Tolyl(trifluoromethyl)diazomethane (19b)** was synthesized in analogy to **19a**. IR (Ar, 3 K): 2094 (vs), 2086 (vs), 1523 (s), 1425 (s), 1353 (s), 1349 (s), 1318 (m), 1276 (m), 1200 (m), 1175 (s), 1151 (s), 1129 (s), 991 (m), 959 (s), 810 (m), 736 (m), 614 (m), 575 (m), 512 (m), 490 (m)  $\text{cm}^{-1}$ .  $^1\text{H}$  NMR (200 MHz,  $\text{CDCl}_3$ ):  $\delta/\text{ppm}$  = 7.94 (s, 1H), 7.81 (d,  $J$  = 8.4 Hz, 1H), 7.42 – 7.25 (m, 4H), 7.12 (d,  $J$  = 8.1 Hz, 2H), 2.46 (s, 3H), 2.41 (s, 3H).  $^{13}\text{C}$  NMR (200 MHz,  $\text{CDCl}_3$ ):  $\delta/\text{ppm}$  = 144.9, 142.1, 141.8, 134.6, 130.7, 129.9, 128.0, 122.1, 119.0, 21.7, 21.5.

***p*-Fluorophenyl(trifluoromethyl)diazomethane (19c)** was synthesized in analogy to **19a**. IR (Ar, 3 K): 2991 (s), 1754 (m), 1484 (s), 1375 (s), 1360 (s), 1248 (m), 1119 (s), 1057 (s), 941 (s), 855 (s), 603 (s)  $\text{cm}^{-1}$ .  $^1\text{H}$  NMR (200 MHz,  $\text{CDCl}_3$ ):  $\delta/\text{ppm}$  = 7.48 – 7.28 (m, 2H) 7.13 – 6.84 (m, 2H).

**Pentafluorophenyl(trifluoromethyl)diazomethane (19d)** was synthesized in analogy to **19a**. IR (Ar, 3 K): 2096 (vs), 2088 (vs), 1597 (m), 1524 (m), 1356 (m), 1351 (m), 1314 (m), 1275 (m), 1176 (s), 1150 (s), 1129 (s), 960 (s), 810 (m), 835 (m)  $\text{cm}^{-1}$ .

**2-(1-diazo-2,2,2-trifluoroethyl)naphthalene (19h)** was synthesized in analogy to **19a**.  $^1\text{H}$  NMR (200 MHz,  $\text{CDCl}_3$ ):  $\delta/\text{ppm}$  = 7.88 (d,  $J$  = 8.7 Hz, 1H), 7.79 (dd,  $J$  = 8.4, 6.3 Hz, 2H), 7.54 (s, 1H), 7.52 – 7.44 (m, 2H), 7.19 (dd,  $J$  = 8.7, 2.0 Hz, 1H).  $^{13}\text{C}$  NMR (50 MHz,  $\text{D}_2\text{O}$ ):  $\delta/\text{ppm}$  = 204.98, 127.43, 127.16, 127.01, 125.73, 90.16, 79.80, 75.15, 74.52, 73.88, 48.18, 19.07.

**2-(1-diazo-2,2,2-trifluoroethyl)-9H-fluorene (19i)** was synthesized in analogy to **19a** after the ketone was prepared according to a literature procedure.<sup>[113]</sup> IR (Ar, 3 K): 2089 (vs), 1499 (m), 1461 (m), 1407 (m), 1361 (m), 1334 (m), 1304 (m), 1278 (m), 1206 (m), 1179 (m), 1165 (m), 1159 (m), 1153 (m), 1209 (s), 997 (m), 984 (m), 767 (m), 731 (m)  $\text{cm}^{-1}$ .

**2,2,2-Trifluoro-1-(4-methylphenyl)ethanol (28b)** was synthesized according to a literature procedure.<sup>[339]</sup> IR (Ar, 3 K): 3633 (s), 1600 (m), 1520 (m), 1459 (m), 1394 (m), 1355 (s), 1322 (m), 1301 (m), 1276 (vs), 1222 (m), 1176 (vs), 1132 (vs), 1088 (s), 868 (m), 851 (m), 804 (s), 774 (m), 722 (m), 694 (m), 576 (m), 507 (m)  $\text{cm}^{-1}$ .  $^1\text{H}$  NMR (200 MHz,  $\text{CDCl}_3$ ):  $\delta/\text{ppm}$  = 7.28 (d, 2H), 7.13 (m, 2H), 4.89 (m, 1H), 2.53 (m, 1H), 2.29 (s, 3H).

***p*-Tolyl(trifluoromethyl)ethanamine (36b)** was synthesized according to a literature procedure with a slight modification.<sup>[340]</sup> IR (Ar, 3 K): 1275 (m), 1214 (m), 1159 (s), 1130 (m), 819 (m) cm<sup>-1</sup>. <sup>1</sup>H NMR (200 MHz, CDCl<sub>3</sub>): δ = 7.32 (d, J = 8.0 Hz, 2H), 7.26-7.13 (m, 2H), 4.36 (q, J = 7.5 Hz, 2H), 2.36 (s, 3H) ppm. <sup>13</sup>C NMR (200 MHz, CDCl<sub>3</sub>): 138.97, 132.57, 129.49, 127.80, 127.78, 58.10, 57.51, 56.92, 21.28 ppm.

**(2,2,2-Trifluoroethyl)benzene (48)** was purchased and deposited in matrix as received. IR (H<sub>2</sub>, 3 K): 1598 (m), 1499 (m), 1459 (m), 1362 (s), 1299 (m), 1266 (vs), 1264 (vs), 1210 (m), 1146 (vs), 1097 (s), 1069 (m), 1033 (m), 910 (m), 845 (m), 754 (m), 701 (s), 658 (s), 598 (m), 522 (m) cm<sup>-1</sup>.

**4-Azido-4'-iodobiphenyl (61)** was synthesized according to a literature procedure.<sup>[341]</sup> IR (Ar, 3 K): 2137 (s), 2100 (vs), 1514 (m), 1485 (m), 1478 (m), 1299 (s), 1276 (m), 1002 (m), 846 (m), 810 (m), 668 (m) cm<sup>-1</sup>.

**2-Azido-2'-iodobiphenyl (62)** was synthesized according to a literature procedure.<sup>[341]</sup> IR (Ar, 3 K): 2137 (vs), 2099 (vs), 1581 (m), 1498 (s), 1466 (s), 1442 (s), 1433 (m), 1421 (m), 1331 (m), 1315 (s), 1295 (s), 1269 (m), 1150 (m), 1021 (m), 1004 (s), 819 (m), 750 (s), 739 (m), 724 (m), 665 (s), 648 (m), 617 (m), 565 (m), 565 (m), 536 (m) cm<sup>-1</sup>.

**1-Azido-4-iodonaphthalene (64)** was synthesized according to a literature procedure.<sup>[342]</sup> IR(Ar, 3 K):  $\tilde{\nu}/\text{cm}^{-1}$  (%) = 2124.64 (100), 2108.63 (14), 2076.61 (6), 1587.04 (5), 1506.09 (4), 1454.96 (5), 1421.55(8), 1379.96 (15), 1364.28 (4), 1314.51 (21), 1284.51 (46), 1196.44 (4), 1009.75 (7), 895.69 (3), 813.48 (8), 760.05 (13), 660.37 (4). <sup>1</sup>H NMR(CDCl<sub>3</sub>, 200MHz): δ/ppm = 8.07 (m, 3H), 7.58 (m, 2H), 7.01 (d, 1H). <sup>13</sup>C NMR(CDCl<sub>3</sub>, 200MHz): δ/ppm = 136.80, 132.14, 131.49, 128.74, 127.94, 127.83, 126.92, 125.61, 123.03, 115.03. *m/z* (EI)<sup>+</sup> = 294.90.

**1-Azido-5-iodonaphthalene (65)** was synthesized according to a literature procedure starting from 1,5-diaminonaphthalene.<sup>[341]</sup> IR(Ar, 3 K):  $\tilde{\nu}/\text{cm}^{-1}$  (%) = 2153.76 (13), 2120.50 (100), 2065.45 (3), 1500.02 (9), 1461.24 (3), 1410.54 (7), 1393.67 (18), 1382.17 (3), 1367.04 (3), 1300.64 (2), 1294.48 (32), 1220.04 (2), 1089.11 (2), 860.88 (2), 783.04 (20), 698.75 (13). <sup>1</sup>H NMR(CDCl<sub>3</sub>, 250MHz): δ/ppm = 7.93(dd, 2H), 7.70(d, 1H), 7.36(t, 1H), 7.10(t, 1H), 6.98(d, 1H). <sup>13</sup>C NMR(CDCl<sub>3</sub>, 250 MHz): δ/ppm = 138.6, 136.9, 135.1, 129.0, 127.2, 127.0, 126.9, 123.5, 114.6. *m/z* (EI)<sup>+</sup> = 294.96. Elemental analysis: calculated C = 40.7, N = 14.24, H = 2.05; found C = 40.68, N = 14.18, H = 2.17.

**1-Azido-8-iodonaphthalene (66)** was synthesized in analogy to **65**. IR(Ar, 3 K):  $\tilde{\nu}/\text{cm}^{-1}$  (%) = 2126.16 (100), 2093.61 (27), 2072.97 (24), 1558.41 (27), 1452.05 (8), 1369.68 (19), 1327.53 (24), 1302.95 (49), 1217.31 (3), 1161.11 (3), 1004.08 (3), 890.70 (7), 814.50 (17), 759.60 (10), 747.51 (9), 681.45 (10).  $^1\text{H}$  NMR( $\text{CDCl}_3$ , 250MHz):  $\delta/\text{ppm}$  = 8.16 (dd, 1H), 7.71(d, 1H), 7.55(t, 1H), 7.40(t, 1H), 7.30(d, 1H), 7.01(d, 1H).  $^{13}\text{C}$  NMR( $\text{CDCl}_3$ , 250 MHz):  $\delta/\text{ppm}$  = 142.45, 136.05, 135.52, 129.30, 127.46, 126.29, 125.99, 125.49, 117.33.  $m/z$  (EI+) = 294.9. Elemental analysis: calculated N = 14.24, C = 40.70, H = 2.05; found N = 14.3, C = 40.78 and H = 2.44.

**2-Azido-1-iodonaphthalene (67)** was synthesized according to a combined literature procedures.<sup>[343-344]</sup> IR(Ar, 3 K):  $\tilde{\nu}/\text{cm}^{-1}$  (%) = 2201.74 (4), 2117.23 (100), 2108.25 (9), 2054.70 (5), 1625.26 (6), 1597.97 (4), 1560.04 (4), 1505.43 (5), 1464.46 (5), 1372.78 (3), 1354.86 (9), 1327.25 (6), 1306.25 (29), 1287.85 (8), 960.67 (4), 803.18 (10), 766.40 (4), 743.67 (4).  $^1\text{H}$  NMR(400MHz,  $\text{CDCl}_3$ ):  $\delta/\text{ppm}$  = 8.06(d, 1H), 7.80(d,1H), 7.69(d, 1H), 7.51(t, 1H), 7.39(t, 1H), 7.23(d, 1H).  $^{13}\text{C}$  NMR( $\text{CDCl}_3$ , 400 MHz):  $\delta/\text{ppm}$  = 143.98, 136.78, 134.66, 131.84, 131.25, 129.75, 128.58, 126.04, 124.90, 116.30.  $m/z$  (EI)<sup>+</sup> = 294.90.

## Matrix isolation

Matrix isolation measurements were performed by standard techniques as was described in literatures.<sup>[86, 118]</sup> To reach cryogenic temperatures, Sumitomo Heavy Industries two-staged closed-cycle helium refrigerator systems (3 K) or Air Products Diplex close-cycle helium refrigerator systems (8 K) are used. High vacuum ( $10^{-5}$  –  $10^{-7}$  mbar) is reached by using an oil diffusion pump for IR and UV–vis experiments, while a turbo pump is used for X-band EPR experiments. Cesium iodide, sapphire and an oxygen-free high-conductivity copper were used as materials for the IR, UV–vis and EPR spectroscopic windows, respectively. For the matrix isolation experiments, argon, neon, xenon and nitrogen (Messer-Griesheim; 99.9999%), ammonia, hydrogen (Air Liquide, 99.999%), deuterium (Merck Schuchardt, 99.5%) and D3-ammonia (Sigma Aldrich, 99%) were exploited. The required precursor was sublimed (**18b** at  $-30$  °C; **19a** at  $40$  °C; **19b** at  $35$  °C; **19c** at  $35$  °C; **19d** at  $45$  °C; **19h** at  $60$  °C; **19i** at  $55$  °C; **28b** at  $-20$  °C; **36b** at  $-40$  °C; **48** at  $-40$  °C; **61** at  $55$  °C; **62** at  $60$  °C; **63** at  $120$  °C; **64** at  $55$  °C; **65** at  $55$  °C; **66** at  $45$  °C; **67** at  $60$  °C) and codeposited on the cold spectroscopic window (3–8 K for IR and UV–vis, and 4 K for EPR) with a large excess of inert gases with a flow rate of approximately 1.90 sccm. Typically, the deposition time takes approximately 60 minutes. The

experiments in argon matrices doped with 1% of water were carried out as described in literatures.<sup>[124, 345]</sup> Similar procedures were applied for other argon doped experiments. Ultrapure water used in these experiments was degassed by several freeze-thaw cycles and deposited onto the cold window held at 50 K, by controlling the deposition rate with a fine metering valve.

Matrix isolation IR spectra were recorded with Bruker IFS66 and IFS66s FTIR spectrometers in the range between 400 and 4000  $\text{cm}^{-1}$  with a resolution of 0.5  $\text{cm}^{-1}$ . The IR spectrometers were purged by dry air for avoiding  $\text{CO}_2$  and water from atmosphere. Matrix isolation UV–vis spectra were recorded with a Varian Cary 5000 UV-Vis-NIR spectrophotometer in the range between 200 and 800 nm with a resolution of 0.1 nm. Matrix isolation EPR spectra were recorded with a Bruker ELEXSYS 500 X-band spectrometer.

Broadband photolysis of the matrices was performed using a high-pressure mercury lamp (Ushio 500 W) equipped with dichroic mirrors (Oriel) and long pass cut-off filters (Schott, 50% transmission), and custom-made LEDs with  $\lambda = 530, 450, \text{ or } 365 \text{ nm}$  (max. 5 W). A low-pressure mercury lamp with  $\lambda = 254 \text{ nm}$  (Grüntzel) was used for narrowband irradiation. Monochromatic irradiation was conducted with a 308 and 266 nm XeCl excimer laser (Lambda Physik). For visible irradiation in the range between  $\lambda = 420 - 450 \text{ nm}$ , a lamp-pumped OPO laser (InnoLas Laser model SpitLight 600 midband) was used.

### **Ammonia bearing ices**

The description below corresponds to the experiments conducted at University of Hawaii (Chapters 7 and 8). The experiments were conducted in a contamination-free ultrahigh vacuum (UHV) chamber evacuated to a base pressure of  $(5 \pm 2) \times 10^{-11} \text{ Torr}$ .<sup>[346-347]</sup> A rhodium-coated silver wafer located in the center of the chamber served as a substrate and was interfaced to a cold finger designed from oxygen-free high-conductivity copper with a 0.2 mm sheet of indium foil to ensure thermal conductivity. The entire assembly is cooled down to  $5.5 \pm 0.2 \text{ K}$  by a closed-cycle helium refrigerator (Sumitomo Heavy Industries, RDK-415E). The ices were prepared by depositing the individual gas or gas mixtures of  $\text{NH}_3$  (Matheson; 99.999%),  $\text{ND}_3$  (Isotopes Inc; 99+ % D),  $\text{N}_2$  (Matheson; 99.9999%),  $^{15}\text{N}_2$  (Cambridge Isotope Inc. 98+%  $^{15}\text{N}$ ) and  $\text{O}_2$  (BOC Gases, 99.999%) via a glass capillary array positioned 30 mm in front of the silver target. Deposition times range between 5 and 10 min. During the deposition, the main

chamber pressure was increased to  $(3 \pm 2) \times 10^{-8}$  torr; the thickness of the ices were measured online via *in situ* He-Ne laser interferometry (CVI Melles-Griot, 25-LHP-213) at  $\lambda = 632.8$  nm striking the surface at an angle of incidence of  $\theta = 4^\circ$ .<sup>[277, 348-349]</sup>

Each sample was then irradiated for 60 min with 5 keV electrons at a current of 0 nA (blank experiment) and at  $15 \pm 2$  nA generated by a SPECS EQ 22/35 electron gun measured by a Faraday cup mounted between the electron gun and the sample. Before, during, and after irradiation, chemical modifications of the ices were recorded *online* and *in situ* using Fourier Transform Infrared Spectroscopy (FTIR; Thermo Nicolet 6700), in the range of 6000 to 600  $\text{cm}^{-1}$  with a resolution of 4  $\text{cm}^{-1}$ , and an EI-QMS device (Extrel 5221) to monitor molecules released into the gas phase (70 eV, 2 mA). One hour after the irradiation, TPD studies were conducted by heating the irradiated ices to 300 K at a constant rate of 0.5 K  $\text{minute}^{-1}$ . The spectra for selected temperatures were deconvoluted exploiting Gaussian fits utilizing the peak fitting using the least number of peaks resulting in a residual within the signal-to-noise ratio of the original spectra as described elsewhere.<sup>[346, 350]</sup> After irradiating the ices, molecules subliming into the gas phase were photoionized with 10.49 eV photons using soft vacuum ultraviolet (VUV) photoionization coupled with a reflectron time-of-flight mass spectrometer (ReTOF; Jordan TOF Products, Inc.), which has been described in detail previously.<sup>[346-347, 349]</sup> The 10.49 eV photons were generated by frequency tripling of the third harmonic of an Nd:YAG (354.7 nm) (Spectra Physics, PRO-250, 30 Hz) laser in a jet of pulsed xenon (Xe) gas, as was reported earlier.<sup>[346]</sup> The 9.67 eV and 9.1 eV photons were produced using resonant four wave mixing of two frequencies ( $\omega_1$ ;  $\omega_2$ ), as was described in literatures.<sup>[275, 351-353]</sup>

## Calculations

Geometry optimizations, vibrational frequencies, and IRC profiles were calculated using the B3LYP<sup>[354]</sup> or B2PLYP<sup>[355]</sup> density functional with D3 or GD3BJ<sup>[356-357]</sup> dispersion corrections as implemented in *Gaussian 09*.<sup>[358]</sup> Several basis sets such as def2-TZVP,<sup>[359]</sup> cc-pV(D/T)Z,<sup>[360]</sup> and aug-cc-pVTZ<sup>[361]</sup> were employed. Tight convergence criteria were used throughout. Relaxed scans were carried out by fixing the carbene angle in  $3^\circ$  intervals. CCSD(T) single-point calculations were performed using the MOLPRO program.<sup>[362]</sup> EPR parameters were calculated with ORCA using pre-optimized structures and the EPR III and 6-31G(d,p) basis sets.<sup>[363]</sup> Experimental EPR spectra were analyzed using the Easyspin program package<sup>[364]</sup> and Xsophe computer simulations software.<sup>[365]</sup>

## References

- [1] M. E. Jacox, *Chem. Soc. Rev.* **2002**, *31*, 108.
- [2] W. E. Klotzbücher, in *The Status of Soviet Civil Science* (Ed.: C. Sinclair), Springer Netherlands, Dordrecht, **1987**, pp. 211.
- [3] M. J. Almond, N. Goldberg, *Annu. Rep. Prog. Chem., Sect. C: Phys. Chem.* **2007**, *103*, 79.
- [4] V. I. Goldanskii, *Annu. Rev. Phys. Chem.* **1976**, *27*, 85.
- [5] W. Kirmse, *Carbene chemistry*, Academic Press: New York, London, **1971**.
- [6] N. P. Bowling, R. J. Halter, J. A. Hodges, R. A. Seburg, P. S. Thomas, C. S. Simmons, J. F. Stanton, R. J. McMahon, *J. Am. Chem. Soc.* **2006**, *128*, 3291.
- [7] P. S. Thomas, N. P. Bowling, R. J. McMahon, *J. Am. Chem. Soc.* **2009**, *131*, 8649.
- [8] S. A. Fleming, *Tetrahedron* **1995**, *51*, 12479.
- [9] E. Smith, I. Collins, *Future Med. Chem.* **2015**, *7*, 159.
- [10] L. Dubinsky, B. P. Krom, M. M. Meijler, *Bioorg. Med. Chem.* **2012**, *20*, 554.
- [11] J. Brunner, H. Senn, F. M. Richards, *J. Biol. Chem.* **1980**, *255*, 3313.
- [12] R. Hoffmann, G. D. Zeiss, G. W. Van Dine, *J. Am. Chem. Soc.* **1968**, *90*, 1485.
- [13] K. B. Eisenthal, R. A. Moss, N. J. Turro, *Science* **1984**, *225*, 1439.
- [14] D. Bourissou, O. Guerret, F. P. Gabbaï, G. Bertrand, *Chem. Rev.* **2000**, *100*, 39.
- [15] S. Gronert, J. R. Keeffe, R. A. More O'Ferrall, *J. Am. Chem. Soc.* **2011**, *133*, 3381.
- [16] H. F. Schaefer, *Science* **1986**, *231*, 1100.
- [17] S. Matzinger, M. P. Fuelscher, *J. Phys. Chem.* **1995**, *99*, 10747.
- [18] S. H. Kable, S. A. Reid, T. J. Sears, *Int. Rev. Phys. Chem.* **2009**, *28*, 435.
- [19] E. Wasserman, W. A. Yager, V. J. Kuck, *Chem. Phys. Lett.* **1970**, *7*, 409.
- [20] A. R. W. McKellar, P. R. Bunker, T. J. Sears, K. M. Evenson, R. J. Saykally, S. R. Langhoff, *J. Chem. Phys.* **1983**, *79*, 5251.
- [21] D. G. Leopold, K. K. Murray, A. E. S. Miller, W. C. Lineberger, *J. Chem. Phys.* **1985**, *83*, 4849.
- [22] R. L. Schwartz, G. E. Davico, T. M. Ramond, W. C. Lineberger, *J. Phys. Chem. A* **1999**, *103*, 8213.
- [23] I. Alkorta, J. Elguero, *Chem. Phys. Lett.* **2018**, *691*, 33.
- [24] M. N. Hopkinson, C. Richter, M. Schedler, F. Glorius, *Nature* **2014**, *510*, 485.
- [25] A. J. Arduengo, R. L. Harlow, M. Kline, *J. Am. Chem. Soc.* **1991**, *113*, 361.
- [26] D. A. Dixon, *J. Phys. Chem.* **1986**, *90*, 54.
- [27] J. E. O'Gara, W. P. Dailey, *J. Am. Chem. Soc.* **1994**, *116*, 12016.
- [28] A. Nemirowski, P. R. Schreiner, *J. Org. Chem.* **2007**, *72*, 9533.
- [29] M.-G. Song, R. S. Sheridan, *J. Phys. Org. Chem.* **2011**, *24*, 889.
- [30] J. Wang, R. S. Sheridan, *Org. Lett.* **2007**, *9*, 3177.
- [31] D. L. S. Brahms, W. P. Dailey, *Chem. Rev.* **1996**, *96*, 1585.
- [32] R. A. Moss, *Acc. Chem. Res.* **1989**, *22*, 15.
- [33] H. Tomioka, *Res. Chem. Intermed.* **1994**, *20*, 605.
- [34] P. S. Skell, R. C. Woodworth, *J. Am. Chem. Soc.* **1956**, *78*, 4496.
- [35] L. M. Hadel, M. S. Platz, J. C. Scaiano, *J. Am. Chem. Soc.* **1984**, *106*, 283.
- [36] W. Kirmse, J. Kilian, S. Steenken, *J. Am. Chem. Soc.* **1990**, *112*, 6399.
- [37] H. L., C. A., *Angew. Chem. Int. Ed.* **1963**, *2*, 599.
- [38] M. S. Platz, in *In Reactive Intermediate Chemistry* (Eds.: R. A. Moss, M. S. Platz, M. S. Jones), John Wiley & Sons, Inc.: Hoboken, NJ, **2004**, p. 501.
- [39] A. Rajca, J. Wongsriratanakul, S. Rajca, *Science* **2001**, *294*, 1503.
- [40] S. Murata, H. Iwamura, *J. Am. Chem. Soc.* **1991**, *113*, 5547.

- [41] B. Stefan, G. Carmen, K. Kerstin, Z. Viktor, *Angew. Chem. Int. Ed.* **2005**, *44*, 5188.
- [42] E. W. Meijer, S. Nijhuis, F. C. B. M. Van Vroonhoven, *J. Am. Chem. Soc.* **1988**, *110*, 7209.
- [43] S. Vyas, A. H. Winter, C. M. Hadad, in *Nitrenes and Nitrenium Ions* (Eds.: D. E. Falvey, A. D. Gudmundsdottir), John Wiley & Sons, Inc.: Hoboken, NJ, **2013**.
- [44] E. Wasserman, in *Progress in Physical Organic Chemistry* (Eds.: A. Streitwieser, R. W. Taft), John Wiley & Sons, Inc., **1968**.
- [45] P. C. Engelking, W. C. Lineberger, *J. Chem. Phys.* **1976**, *65*, 4323.
- [46] N. R. Wijeratne, M. D. Fonte, A. Ronemus, P. J. Wyss, D. Tahmassebi, P. G. Wenthold, *J. Phys. Chem. A* **2009**, *113*, 9467.
- [47] A. Admasu, A. D. Gudmundsdóttir, M. S. Platz, *J. Phys. Chem. A* **1997**, *101*, 3832.
- [48] N. Gritsan, M. Platz, in *Organic Azides: Syntheses and Applications* (Eds.: S. Bräse, K. Banert), John Wiley & Sons, Ltd: Chichester, U.K., **2010**, p. 311.
- [49] G. B. Schuster, M. S. Platz, *Adv. Photochem.* **2007**, 69.
- [50] A. K. Schrock, G. B. Schuster, *J. Am. Chem. Soc.* **1984**, *106*, 5228.
- [51] W. A. Brown, *Phys. Chem. Chem. Phys.* **2014**, *16*, 3343.
- [52] E. Herbst, *Phys. Chem. Chem. Phys.* **2014**, *16*, 3344.
- [53] E. Herbst, J. T. Yates, *Chem. Rev.* **2013**, *113*, 8707.
- [54] A. C. Cheung, D. M. Rank, C. H. Townes, D. D. Thornton, W. J. Welch, *Phys. Rev. Lett.* **1968**, *21*, 1701.
- [55] E. F. van Dishoeck, *Faraday Discuss.* **2014**, *168*, 9.
- [56] A. Tielens, *Rev. Mod. Phys.* **2013**, *85*, 1021.
- [57] E. Herbst, E. F. v. Dishoeck, *Annu. Rev. Astron. Astrophys.* **2009**, *47*, 427.
- [58] H. S. P. Müller, F. Schlöder, J. Stutzki, G. Winnewisser, *J. Mol. Struct.* **2005**, *742*, 215.
- [59] J. M. Hollis, F. J. Lovas, P. R. Jewell, *Astrophys. J. Lett.* **2000**, *540*, L107.
- [60] J. M. Hollis, F. J. Lovas, J. R. Anthony, P. R. Jewell, V. V. Ilyushin, I. Kleiner, *Astrophys. J. Lett.* **2006**, *643*, L25.
- [61] A. G. G. M. Tielens, *Annu. Rev. Astron. Astrophys.* **2008**, *46*, 289.
- [62] J. Cami, J. Bernard-Salas, E. Peeters, S. E. Malek, *Science* **2010**, *329*, 1180.
- [63] A. C. A. Boogert, P. A. Gerakines, D. C. B. Whittet, *Annu. Rev. Astron. Astrophys.* **2015**, *53*, 541.
- [64] E. L. Gibb, D. C. B. Whittet, A. C. A. Boogert, A. G. G. M. Tielens, *Astrophys. J. Suppl.* **2004**, *151*, 35.
- [65] S. Bottinelli, A. C. A. Boogert, J. Bouwman, M. Beckwith, E. F. van Dishoeck, K. I. Öberg, K. M. Pontoppidan, H. Linnartz, G. A. Blake, N. J. Evans II, F. Lahuis, *Astrophys. J.* **2010**, *718*, 1100.
- [66] K. Öberg, I. , A. C. A. Boogert, K. M. Pontoppidan, S. v. d. Broek, E. F. van Dishoeck, S. Bottinelli, G. A. Blake, N. J. Evans II, *Astrophys. J.* **2011**, *740*, 109.
- [67] N. Biver, J. Crovisier, D. Bockelée-Morvan, S. Szutowicz, D. C. Lis, P. Hartogh, M. de Val-Borro, R. Moreno, J. Boissier, M. Kidger, M. Küppers, G. Paubert, N. Dello Russo, R. Vervack, H. Weaver, H. Team, *A&A* **2012**, *539*, A68.
- [68] E. F. van Dishoeck, E. Herbst, D. A. Neufeld, *Chem. Rev.* **2013**, *113*, 9043.
- [69] A. G. G. M. Tielens, S. B. Charnley, *Origins Life Evol. Biosphere* **1997**, *27*, 23.
- [70] M. P. Callahan, K. E. Smith, H. J. Cleaves, J. Ruzicka, J. C. Stern, D. P. Glavin, C. H. House, J. P. Dworkin, *Proc. Natl. Acad. Sci.* **2011**, *108*, 13995.
- [71] K. Hiraoka, A. Yamashita, Y. Yachi, K. Aruga, T. Sato, H. Muto, *Astrophys. J.* **1995**, *443*, 363.
- [72] G. B. I. Scott, D. A. Fairley, C. G. Freeman, M. J. McEwan, *Chem. Phys. Lett.* **1997**, *269*, 88.

- [73] F. Datchi, S. Ninet, M. Gauthier, A. M. Saitta, B. Canny, F. Decremps, *Phys. Rev. B* **2006**, *73*, 174111.
- [74] E. L. Zins, L. Krim, *RSC Advances* **2013**, *3*, 10285.
- [75] W. Zheng, R. I. Kaiser, *Chem. Phys. Lett.* **2007**, *440*, 229.
- [76] W. Zheng, D. Jewitt, R. I. Kaiser, *Astrophys. J.* **2006**, *639*, 534.
- [77] G. A. Jeffrey, *An introduction to hydrogen bonding*, Vol. 32, Oxford university press New York, **1997**.
- [78] W. Zheng, D. Jewitt, Y. Osamura, R. I. Kaiser, *Astrophys. J.* **2008**, *674*, 1242.
- [79] H. Zewail Ahmed, in *Pure Appl. Chem.*, Vol. 72, **2000**, p. 2219.
- [80] T. Bally, in *Reactive Intermediate Chemistry* (Eds.: R. A. Moss, M. S. Platz, M. Jones), John Wiley & Sons, Inc.: Hoboken, NJ, **2005**, p. 797.
- [81] E. Whittle, D. A. Dows, G. C. Pimentel, *J. Chem. Phys.* **1954**, *22*, 1943.
- [82] I. Norman, G. Porter, *Nature* **1954**, *174*, 508.
- [83] M. S. Gudipati, *J. Phys. Chem. A* **2004**, *108*, 4412.
- [84] T. Momose, H. Hoshina, M. Fushitani, H. Katsuki, *Vib. Spectrosc* **2004**, *34*, 95.
- [85] W. Sander, *Angew. Chem. Int. Ed.* **1985**, *24*, 988.
- [86] P. Costa, W. Sander, *Angew. Chem. Int. Ed.* **2014**, *53*, 5122.
- [87] R. J. H. Clark, J. R. Dann, *J. Phys. Chem.* **1996**, *100*, 532.
- [88] P. J. Linstrom, W. G. Mallard, National Institute of Standards and Technology, Gaithersburg MD, 20899.
- [89] J. A. Weil, J. R. Bolton, *Electron paramagnetic resonance: elementary theory and practical applications*, John Wiley & Sons, Inc.: Hoboken, NJ, **2007**.
- [90] M. M. Roessler, E. Salvadori, *Chem. Soc. Rev.* **2018**, *47*, 2534.
- [91] B. A. G., B. P. G., *Phys. Status Solidi B* **1980**, *97*, 95.
- [92] T. Yamada, K. Komaguchi, M. Shiotani, N. P. Benetis, A. R. Sørnes, *J. Phys. Chem. A* **1999**, *103*, 4823.
- [93] E. Wasserman, L. C. Snyder, W. A. Yager, *J. Chem. Phys.* **1964**, *41*, 1763.
- [94] C. Thomson, *Chem. Soc. Rev.* **1968**, *22*, 45.
- [95] M. A. El-Sayed, *Pure Appl. Chem.* **1970**, *24*, 475.
- [96] H. Tomioka, in *Reactive Intermediate Chemistry* (Eds.: R. A. Moss, M. S. Platz, M. Jones), John Wiley & Sons, Inc.: Hoboken, NJ, **2005**.
- [97] S. Henkel, PhD Thesis, Ruhr-Universität Bochum **2014**.
- [98] W. M. Jones, R. C. Joines, J. A. Myers, T. Mitsuhashi, K. E. Krajca, E. E. Waali, T. L. Davis, A. B. Turner, *J. Am. Chem. Soc.* **1973**, *95*, 826.
- [99] G. Rolf, R. Wolfgang, W. Curt, *Helv. Chim. Acta* **1974**, *57*, 2111.
- [100] C. Wentrup, C. Mayor, J. Becker, H. J. Lindner, *Tetrahedron* **1985**, *41*, 1601.
- [101] W. M. Jones, *Acc. Chem. Res.* **1977**, *10*, 353.
- [102] S. Matzinger, T. Bally, E. V. Patterson, R. J. McMahon, *J. Am. Chem. Soc.* **1996**, *118*, 1535.
- [103] P. Costa, W. Sander, *J. Phys. Org. Chem.* **2015**, *28*, 71.
- [104] R. J. Blanch, C. Wentrup, *Aust. J. Chem.* **2015**, *68*, 36.
- [105] W. W. Sander, *J. Org. Chem.* **1988**, *53*, 121.
- [106] K. H. Fischer, P. Hemberger, I. Fischer, A. M. Rijs, *ChemPhysChem* **2010**, *11*, 3228.
- [107] B. Noller, L. Poisson, R. Maksimenka, I. Fischer, J.-M. Mestdagh, *J. Am. Chem. Soc.* **2008**, *130*, 14908.
- [108] A. Admasu, A. D. Gudmundsdottir, M. S. Platz, D. S. Watt, S. Kwiatkowski, P. J. Crocker, *J. Chem. Soc., Perkin Trans. 2* **1998**, 1093.
- [109] A. M. Trozzolo, E. Wasserman, W. A. Yager, *J. Am. Chem. Soc.* **1965**, *87*, 129.
- [110] E. Wasserman, L. Barash, W. A. Yager, *J. Am. Chem. Soc.* **1965**, *87*, 4974.
- [111] M.-G. Song, R. S. Sheridan, *J. Am. Chem. Soc.* **2011**, *133*, 19688.

- [112] J. Wang, J. Kubicki, H. Peng, M. S. Platz, *J. Am. Chem. Soc.* **2008**, *130*, 6604.
- [113] J. Wang, J. Kubicki, T. L. Gustafson, M. S. Platz, *J. Am. Chem. Soc.* **2008**, *130*, 2304.
- [114] Z. Zhu, T. Bally, L. L. Stracener, R. J. McMahon, *J. Am. Chem. Soc.* **1999**, *121*, 2863.
- [115] Y. Wang, C. M. Hadad, J. P. Toscano, *J. Am. Chem. Soc.* **2002**, *124*, 1761.
- [116] Y. Wang, T. Yuzawa, H.-o. Hamaguchi, J. P. Toscano, *J. Am. Chem. Soc.* **1999**, *121*, 2875.
- [117] Y. Zhang, J. Kubicki, J. Wang, M. S. Platz, *J. Phys. Chem. A* **2008**, *112*, 11093.
- [118] P. Costa, T. Lohmiller, I. Trosien, A. Savitsky, W. Lubitz, M. Fernandez-Oliva, E. Sanchez-Garcia, W. Sander, *J. Am. Chem. Soc.* **2016**, *138*, 1622.
- [119] W. Siebrand, T. A. Wildman, *Acc. Chem. Res.* **1986**, *19*, 238.
- [120] R. K. Lengel, R. N. Zare, *J. Am. Chem. Soc.* **1978**, *100*, 7495.
- [121] J. C. Poutsma, J. J. Nash, J. A. Paulino, R. R. Squires, *J. Am. Chem. Soc.* **1997**, *119*, 4686.
- [122] C.-H. Hu, *Chem. Phys. Lett.* **1999**, *309*, 81.
- [123] Y. A. Tsegaw, P. E. Kadam, N. Tötsch, E. Sanchez-Garcia, W. Sander, *J. Am. Chem. Soc.* **2017**, *139*, 12310.
- [124] P. Costa, I. Trosien, M. Fernandez-Oliva, E. Sanchez-Garcia, W. Sander, *Angew. Chem. Int. Ed.* **2015**, *54*, 2656.
- [125] P. Costa, W. Sander, *Angew. Chem. Int. Ed.* **2014**, *53*, 5122.
- [126] J. I. van der Vlugt, *Chem. Soc. Rev.* **2010**, *39*, 2302.
- [127] P. Sabatier, *Ind. Eng. Chem.* **1926**, *18*, 1005.
- [128] G. J. Kubas, *J. Organomet. Chem.* **2014**, *751*, 33.
- [129] G. S. McGrady, G. Guilera, *Chem. Soc. Rev.* **2003**, *32*, 383.
- [130] A. Werner, *Z. Anorg. Chem.* **1893**, *3*, 267.
- [131] a. D F McMillen, D. M. Golden, *Annu. Rev. Phys. Chem.* **1982**, *33*, 493.
- [132] D. Martin, M. Soleilhavoup, G. Bertrand, *Chem. Sci.* **2011**, *2*, 389.
- [133] G. D. Frey, V. Lavallo, B. Donnadiou, W. W. Schoeller, G. Bertrand, *Science* **2007**, *316*, 439.
- [134] T. W. Hudnall, J. P. Moerdyk, C. W. Bielawski, *Chem. Commun.* **2010**, *46*, 4288.
- [135] J. P. Moerdyk, G. A. Blake, D. T. Chase, C. W. Bielawski, *J. Am. Chem. Soc.* **2013**, *135*, 18798.
- [136] S. M. McCarthy, Y.-C. Lin, D. Devarajan, J. W. Chang, H. P. Yennawar, R. M. Rioux, D. H. Ess, A. T. Radosevich, *J. Am. Chem. Soc.* **2014**, *136*, 4640.
- [137] A. Jana, C. Schulzke, H. W. Roesky, *J. Am. Chem. Soc.* **2009**, *131*, 4600.
- [138] A. Jana, I. Objartel, H. W. Roesky, D. Stalke, *Inorg. Chem.* **2009**, *48*, 798.
- [139] Y. Peng, B. D. Ellis, X. Wang, P. P. Power, *J. Am. Chem. Soc.* **2008**, *130*, 12268.
- [140] D. Bethell, J. Hayes, A. R. Newall, *J. Chem. Soc., Perkin Trans. 2* **1974**, 1307.
- [141] J. J. Zupancic, P. B. Grasse, S. C. Lapin, G. B. Schuster, *Tetrahedron* **1985**, *41*, 1471.
- [142] J. A. Pople, K. Raghavachari, M. J. Frisch, J. S. Binkley, P. V. R. Schleyer, *J. Am. Chem. Soc.* **1983**, *105*, 6389.
- [143] J. Knorr, P. Sokkar, S. Schott, P. Costa, W. Thiel, W. Sander, E. Sanchez-Garcia, P. Nuernberger, *Nat. Commun.* **2016**, *7*, 12968.
- [144] G. Richter, E. Mendez-Vega, W. Sander, *J. Phys. Chem. A* **2016**, *120*, 3524.
- [145] E. F. Vansant, J. H. Lunsford, *J. Phys. Chem. A* **1972**, *76*, 2716.
- [146] S. Süzer, L. Andrews, *J. Chem. Phys.* **1987**, *87*, 5131.
- [147] M. Platz, A. S. Admasu, S. Kwiatkowski, P. J. Crocker, N. Imai, D. S. Watt, *Bioconjugate Chem.* **1991**, *2*, 337.
- [148] X. K. Jiang, G. Z. Ji, D. Z. R. Wang, *J. Phys. Org. Chem.* **1995**, *8*, 143.
- [149] D. W. Stephan, *Chem. Commun.* **2010**, *46*, 8526.
- [150] H. F. Bettinger, M. Filthaus, P. Neuhaus, *Chem. Commun.* **2009**, 2186.

- [151] Y. Peng, M. Brynda, B. D. Ellis, J. C. Fettinger, E. Rivard, P. P. Power, *Chem. Commun.* **2008**, 6042.
- [152] G. H. Spikes, J. C. Fettinger, P. P. Power, *J. Am. Chem. Soc.* **2005**, *127*, 12232.
- [153] Y. Wang, J. Ma, *J. Organomet. Chem.* **2009**, *694*, 2567.
- [154] B. Li, Z. Xu, *J. Am. Chem. Soc.* **2009**, *131*, 16380.
- [155] G. C. Welch, R. R. S. Juan, J. D. Masuda, D. W. Stephan, *Science* **2006**, *314*, 1124.
- [156] D. W. Stephan, *Dalton Trans.* **2009**, 3129.
- [157] C. Kötting, W. Sander, *J. Am. Chem. Soc.* **1999**, *121*, 8891.
- [158] P. S. Zuev, R. S. Sheridan, *J. Am. Chem. Soc.* **2001**, *123*, 12434.
- [159] S. Henkel, W. Sander, *Angew. Chem. Int. Ed.* **2015**, *54*, 4603.
- [160] S. Henkel, M. Ertelt, W. Sander, *Chem. Eur. J.* **2014**, *20*, 7585.
- [161] C. W. Bauschlicher, K. Haber, H. F. Schaefer, C. F. Bender, *J. Am. Chem. Soc.* **1977**, *99*, 3610.
- [162] G. T. Burdzinski, T. L. Gustafson, J. C. Hackett, C. M. Hadad, M. S. Platz, *J. Am. Chem. Soc.* **2005**, *127*, 13764.
- [163] M. Winkler, W. Sander, *Acc. Chem. Res.* **2014**, *47*, 31.
- [164] W. Sander, M. Winkler, B. Cakir, D. Grote, H. F. Bettinger, *J. Org. Chem.* **2007**, *72*, 715.
- [165] H. F. Bettinger, W. Sander, *J. Am. Chem. Soc.* **2003**, *125*, 9726.
- [166] W. Sander, D. Grote, S. Kossmann, F. Neese, *J. Am. Chem. Soc.* **2008**, *130*, 4396.
- [167] Y. A. Tsegaw, Master thesis, Ruhr-Universität Bochum **2014**.
- [168] W. T. Borden, N. P. Gritsan, C. M. Hadad, W. L. Karney, C. R. Kemnitz, M. S. Platz, *Acc. Chem. Res.* **2000**, *33*, 765.
- [169] W. L. Karney, W. T. Borden, *J. Am. Chem. Soc.* **1997**, *119*, 3347.
- [170] D. Grote, W. Sander, *J. Org. Chem.* **2009**, *74*, 7370.
- [171] D. Grote, C. Finke, P. Neuhaus, W. Sander, *Eur. J. Org. Chem.* **2012**, *2012*, 3229.
- [172] D. Grote, C. Finke, S. Kossmann, F. Neese, W. Sander, *Chem. Eur. J.* **2010**, *16*, 4496.
- [173] M.-L. Tsao, N. Gritsan, T. R. James, M. S. Platz, D. A. Hrovat, W. T. Borden, *J. Am. Chem. Soc.* **2003**, *125*, 9343.
- [174] A. Maltsev, T. Bally, M.-L. Tsao, M. S. Platz, A. Kuhn, M. Vosswinkel, C. Wentrup, *J. Am. Chem. Soc.* **2004**, *126*, 237.
- [175] C. Wentrup, C. Thétaz, H. Lüerssen, N. Aylward, D. Kvaskoff, *J. Org. Chem.* **2016**, *81*, 4601.
- [176] V. Blagojevic, S. Petrie, D. K. Bohme, *Mon. Not. R. Astron. Soc.* **2003**, *339*, L7.
- [177] J. L. Snow, G. Orlova, V. Blagojevic, D. K. Bohme, *J. Am. Chem. Soc.* **2007**, *129*, 9910.
- [178] L. Largo, V. M. Rayón, C. Barrientos, A. Largo, P. Redondo, *Chem. Phys. Lett.* **2009**, *476*, 174.
- [179] D. M. Mehringer, L. E. Snyder, Y. Miao, F. J. Lovas, *Astrophys. J. Lett.* **1997**, *480*, L71.
- [180] A. Remijan, L. E. Snyder, D. N. Friedel, S. Y. Liu, R. Y. Shah, *Astrophys. J.* **2003**, *590*, 314.
- [181] Y. S. J. Shiao, W. L. Leslie, J. R. Anthony, E. S. Lewis, N. F. Douglas, *Astrophys. J.* **2010**, *716*, 286.
- [182] A. Karton, D. Talbi, *Chem. Phys.* **2014**, *436–437*, 22.
- [183] S. G. Lias, J. E. Bartmess, J. F. Liebman, J. L. Holmes, R. D. Levin, W. G. Mallard, *J. Phys. Chem. Ref. Data.* **1988**, *17*, 861.
- [184] P. Boulet, F. Gilardoni, J. Weber, H. Chermette, Y. Ellinger, *Chem. Phys.* **1999**, *244*, 163.
- [185] E. L. Øiestad, E. Uggerud, *Int. J. Mass Spectrom. Suppl.* **1999**, *185–187*, 231.
- [186] N. Nishi, H. Shinohara, T. Okuyama, *J. Chem. Phys.* **1984**, *80*, 3898.
- [187] W. Zheng, R. I. Kaiser, *J. Phys. Chem. A* **2010**, *114*, 5251.

- [188] V. Bordalo, E. F. d. Silveira, X. Y. Lv, A. Domaracka, H. Rothard, E. S. Duarte, P. Boduch, *Astrophys. J.* **2013**, 774, 105.
- [189] S. B. Charnley, S. D. Rodgers, P. Ehrenfreund, *Astron. Astrophys.* **2001**, 378, 1024.
- [190] E. Congiu, G. Fedoseev, S. Ioppolo, F. Dulieu, H. Chaabouni, S. Baouche, Jean L. Lemaire, C. Laffon, P. Parent, T. Lamberts, H. M. Cuppen, H. Linnartz, *Astrophys. J. Lett.* **2012**, 750, L12.
- [191] G. Fedoseev, S. Ioppolo, T. Lamberts, J. F. Zhen, H. M. Cuppen, H. Linnartz, *J. Chem. Phys.* **2012**, 137, 054714.
- [192] G. Fedoseev, K.-J. Chuang, E. F. van Dishoeck, S. Ioppolo, H. Linnartz, *Mon. Not. R. Astron. Soc.* **2016**, 460, 4297.
- [193] E. Congiu, H. Chaabouni, C. Laffon, P. Parent, S. Baouche, F. Dulieu, *J. Chem. Phys.* **2012**, 137, 054713.
- [194] S. Ioppolo, G. Fedoseev, M. Minissale, E. Congiu, F. Dulieu, H. Linnartz, *Phys. Chem. Chem. Phys.* **2014**, 16, 8270.
- [195] M. Minissale, G. Fedoseev, E. Congiu, S. Ioppolo, F. Dulieu, H. Linnartz, *Phys. Chem. Chem. Phys.* **2014**, 16, 8257.
- [196] J. He, G. Vidali, J.-L. Lemaire, R. T. Garrod, *Astrophys. J.* **2015**, 799, 49.
- [197] R. T. Garrod, *Astrophys. J.* **2013**, 765, 60.
- [198] R. T. Garrod, S. L. Widicus Weaver, E. Herbst, *Astrophys. J.* **2008**, 682, 283.
- [199] S. H. Mousavipour, F. Pirhadi, A. Habibagahi, *J. Phys. Chem. A* **2009**, 113, 12961.
- [200] L. Wang, A. M. Mebel, X. Yang, X. Wang, *J. Phys. Chem. A* **2004**, 108, 11644.
- [201] R. L. Pulliam, B. A. McGuire, A. J. Remijan, *Astrophys. J.* **2012**, 751, 1.
- [202] A. M. Brett, P. B. Carroll, M. D. Niklaus, R. C. Nathan, F. C. Joanna, A. L. Ryan, M. B. Andrew, S. Christopher, A. B. Geoffrey, J. R. Anthony, *Astrophys. J.* **2015**, 812, 76.
- [203] J. Di Francesco, M. R. Hogerheijde, W. J. Welch, E. A. Bergin, *Astron. J.* **2002**, 124, 2749.
- [204] J. E. Chiar, A. Tielens, D. C. B. Whittet, W. A. Schutte, A. C. A. Boogert, D. Lutz, E. F. van Dishoeck, M. P. Bernstein, *Astrophys. J.* **2000**, 537, 749.
- [205] J. H. Lacy, H. Faraji, S. A. Sandford, L. J. Allamandola, *Astrophys. J. Lett.* **1998**, 501, L105.
- [206] W. Zheng, D. Jewitt, R. I. Kaiser, *Chem. Phys. Lett.* **2007**, 435, 289.
- [207] W. Zheng, Y. S. Kim, R. I. Kaiser, *Phys. Chem. Chem. Phys.* **2011**, 13, 15749.
- [208] W. Zheng, D. Jewitt, R. I. Kaiser, *Astrophys. J.* **2006**, 648, 753.
- [209] C. J. Bennett, C. Jamieson, A. M. Mebel, R. I. Kaiser, *Phys. Chem. Chem. Phys.* **2004**, 6, 735.
- [210] C. J. Bennett, S.-H. Chen, B.-J. Sun, A. H. H. Chang, R. I. Kaiser, *Astrophys. J.* **2007**, 660, 1588.
- [211] W. Zheng, R. I. Kaiser, *Chem. Phys. Lett.* **2007**, 450, 55.
- [212] R. I. Kaiser, G. Eich, A. Gabrysch, K. Roessler, *Astrophys. J.* **1997**, 484, 487.
- [213] C. S. Jamieson, A. M. Mebel, R. I. Kaiser, *ChemPhysChem* **2006**, 7, 2508.
- [214] C. J. Bennett, T. Hama, Y. S. Kim, M. Kawasaki, R. I. Kaiser, *Astrophys. J.* **2011**, 727, 27.
- [215] J. S. Holt, D. Sadoskas, C. J. Pursell, *J. Chem. Phys.* **2004**, 120, 7153.
- [216] W. Zheng, D. Jewitt, R. I. Kaiser, *Astrophys. J. Suppl.* **2009**, 181, 53.
- [217] M. H. Moore, R. F. Ferrante, R. L. Hudson, J. N. Stone, *Icarus* **2007**, 190, 260.
- [218] Y. S. Kim, R. I. Kaiser, *Astrophys. J.* **2011**, 729, 68.
- [219] W. G. Fateley, H. A. Bent, B. Crawford, *J. Chem. Phys.* **1959**, 31, 204.
- [220] A. Stirling, I. Papai, J. Mink, D. R. Salahub, *J. Chem. Phys.* **1994**, 100, 2910.
- [221] D. W. Arnold, D. M. Neumark, *J. Chem. Phys.* **1995**, 102, 7035.
- [222] C. S. Jamieson, C. J. Bennett, A. M. Mebel, R. I. Kaiser, *Astrophys. J.* **2005**, 624, 436.

- [223] E. J. Sluyts, B. J. Van der Veken, *J. Mol. Struct.* **1994**, 320, 249.
- [224] M. E. Jacox, D. E. Milligan, *J. Mol. Spectrosc.* **1973**, 48, 536.
- [225] M. Ruzi, D. T. Anderson, *J. Phys. Chem. A* **2015**, 119, 12270.
- [226] C. J. Bennett, R. I. Kaiser, *Astrophys. J.* **2005**, 635, 1362.
- [227] R. E. Nightingale, E. L. Wagner, *J. Chem. Phys.* **1954**, 22, 203.
- [228] A. T. Kowal, *Spectrochim. Acta, Part A* **2002**, 58, 1055.
- [229] G. Sill, U. Fink, J. R. Ferraro, *J. Opt. Soc. Am.* **1980**, 70, 724.
- [230] B. Vandenbussche, P. Ehrenfreund, A. C. A. Boogert, E. F. van Dishoeck, W. A. Schutte, P. A. Gerakines, J. Chiar, A. Tielens, J. Keane, D. C. B. Whittet, M. Breitfellner, M. Burgdorf, *Astron. Astrophys.* **1999**, 346, L57.
- [231] M. Saldyka, Z. Mielke, *Phys. Chem. Chem. Phys.* **2003**, 5, 4790.
- [232] G. Maier, H. P. Reisenauer, M. De Marco, *Angew. Chem. Int. Ed.* **1999**, 38, 108.
- [233] L. Krim, *J. Mol. Struct.* **1998**, 471, 267.
- [234] P. Gerakines, W. Schutte, J. Greenberg, E. F. van Dishoeck, *Astron. Astrophys.* **1995**, 296, 810.
- [235] S. M. Adler-Golden, S. R. Langhoff, C. W. Bauschlicher Jr, G. D. Carney, *J. Chem. Phys.* **1985**, 83, 255.
- [236] M. H. Moore, R. L. Hudson, *Icarus* **2000**, 145, 282.
- [237] F. Wang, F. P. Larkins, M. J. Brunger, M. T. Michalewicz, D. A. Winkler, *Spectrochim. Acta, Part A* **2001**, 57, 9.
- [238] A. M. Turner, M. J. Abplanalp, R. I. Kaiser, *Astrophys. J.* **2016**, 820, 127.
- [239] C. J. Bennett, C. P. Ennis, R. I. Kaiser, *Astrophys. J.* **2014**, 782, 63.
- [240] S. Góbi, A. Bergantini, R. I. Kaiser, *Astrophys. J.* **2016**, 832, 164.
- [241] M. Förstel, Y. A. Tsegaw, P. Maksyutenko, A. M. Mebel, W. Sander, R. I. Kaiser, *ChemPhysChem* **2016**, 17, 2726.
- [242] K. Fagerström, J. T. Jodkowski, A. Lund, E. Ratajczak, *Chem. Phys. Lett.* **1995**, 236, 103.
- [243] R. Loch, B. Leyh, W. Denzer, G. Hagenow, H. Baumgärtel, *Chem. Phys.* **1991**, 155, 407.
- [244] T. Ebata, Y. Anezaki, M. Fujii, N. Mikami, M. Ito, *J. Phys. Chem.* **1983**, 87, 4773.
- [245] S.-C. Kuo, Z. Zhang, S. K. Ross, R. B. Klemm, R. D. Johnson, P. S. Monks, R. P. Thorn, L. J. Stief, *J. Phys. Chem. A* **1997**, 101, 4035.
- [246] F. C. Kohout, F. W. Lampe, *J. Chem. Phys.* **1966**, 45, 1074.
- [247] P. Coppens, J. Smets, M. G. Fishel, J. Drowart, *Int. J. Mass Spectrom.* **1974**, 14, 57.
- [248] R. H. Page, R. J. Larkin, Y. R. Shen, Y. T. Lee, *J. Chem. Phys.* **1988**, 88, 2249.
- [249] S. N. Foner, R. L. Hudson, *J. Chem. Phys.* **1962**, 36, 2676.
- [250] M. J. Weiss, J. Berkowitz, E. H. Appelman, *J. Chem. Phys.* **1977**, 66, 2049.
- [251] J. M. Dyke, N. B. H. Jonathan, A. Morris, M. J. Winter, *Mol. Phys.* **1981**, 44, 1059.
- [252] M. Pelegrini, R. L. T. Parreira, L. F. A. Ferrão, G. F. Caramori, A. O. Ortolan, E. H. da Silva, O. Roberto-Neto, J. A. F. F. Rocco, F. B. C. Machado, *Theor. Chem. Acc.* **2016**, 135, 58.
- [253] Q. Wang, C. Wei, L. M. Perez, W. J. Rogers, M. B. Hall, M. S. Mannan, *J. Phys. Chem. A* **2010**, 114, 9262.
- [254] M. Jonusas, L. Krim, *Mon. Not. R. Astron. Soc.* **2016**, 459, 1977.
- [255] P. F. Goldsmith, R. Liseau, T. A. Bell, J. H. Black, J.-H. Chen, D. Hollenbach, M. J. Kaufman, D. Li, D. C. Lis, G. Melnick, D. Neufeld, L. Pagani, R. Snell, A. O. Benz, E. Bergin, S. Bruderer, P. Caselli, E. Caux, P. Encrenaz, E. Falgarone, M. Gerin, J. R. Goicoechea, A. Hjalmarson, B. Larsson, J. Le Bourlot, F. Le Petit, M. De Luca, Z. Nagy, E. Roueff, A. Sandqvist, F. van der Tak, E. F. van Dishoeck, C. Vastel, S. Viti, U. Yildiz, *Astrophys. J.* **2011**, 737, 96.

- [256] L. Pagani, A. O. H. O. on, P. Bergman, P. Bernath, J. H. Black, R. S. Booth, V. Buat, J. C. ier, C. L. Curry, P. J. Encrenaz, E. Falgarone, P. A. Feldman, M. Fich, H. G. Floren, U. F. k, M. Gerin, E. M. G. en, J. Harju, T. H. egawa, Å. H. on, L. E. B. J. on, S. Kwok, B. L. on, A. Lecacheux, T. L. tröm, M. L. t, R. L. eau, K. Mattila, G. F. Mitchell, L. H. Nordh, M. Olberg, G. O. on, I. R. torcelli, A. S. t, F. von Scheele, G. Serra, N. F. Tothill, K. Volk, T. Wiklind, C. D. W. on, *Astron. Astrophys.* **2003**, 402, L77.
- [257] A. Bieler, K. Altwegg, H. Balsiger, A. Bar-Nun, J. J. Berthelier, P. Bochslers, C. Briois, U. Calmonte, M. Combi, J. De Keyser, E. F. van Dishoeck, B. Fiethe, S. A. Fuselier, S. Gasc, T. I. Gombosi, K. C. Hansen, M. Hassig, A. Jackel, E. Kopp, A. Korth, L. Le Roy, U. Mall, R. Maggiolo, B. Marty, O. Mousis, T. Owen, H. Reme, M. Rubin, T. Semon, C. Y. Tzou, J. H. Waite, C. Walsh, P. Wurzel, *Nature* **2015**, 526, 678.
- [258] M. Rubin, K. Altwegg, E. F. Van Dishoeck, G. Schwehm, *Astrophys. J. Lett.* **2015**, 815.
- [259] B. L. Ulich, J. M. Hollis, L. E. Snyder, *Astrophys. J.* **1977**, 217.
- [260] D. B. Kimball, M. M. Haley, *Angew. Chem. Int. Ed.* **2002**, 41, 3338.
- [261] A. Schmiedekamp, R. H. Smith, Jr., C. J. Michejda, *J. Org. Chem.* **1988**, 53, 3433.
- [262] M. L. Gross, D. H. Blank, W. M. Welch, *J. Org. Chem.* **1993**, 58, 2104.
- [263] F. Marchesi, M. Turriziani, G. Tortorelli, G. Avvisati, F. Torino, L. De Vecchis, *Pharmacol. Res.* **2007**, 56, 275.
- [264] Y. A. Jeilani, T. M. Orlando, A. Pope, C. Pirim, M. T. Nguyen, *RSC Adv.* **2014**, 4, 32375.
- [265] D. E. V. Wilman, *The chemistry of antitumor agents*, Glasgow : Blackie ; New York : Chapman and Hall, **1990**.
- [266] R. B. Livingston, *Single agents in cancer chemotherapy*, Springer Science & Business Media, **2012**.
- [267] K. Saunders, 2nd ed. ed., Longmans, Green and Co., New York, **1949**, pp. 157.
- [268] C. C. Pye, K. Vaughan, J. F. Glister, *Can. J. Chem.* **2002**, 80, 447.
- [269] M. T. Nguyen, L. Hoesch, *Helv. Chim. Acta* **1986**, 69, 1627.
- [270] M. T. Nguyen, J. Kaneti, L. Hoesch, A. S. Dreiding, *Helv. Chim. Acta* **1984**, 67, 1918.
- [271] D. H. Magers, E. A. Salter, R. J. Bartlett, C. Salter, B. A. Hess, Jr., L. J. Schaad, *J. Am. Chem. Soc.* **1988**, 110, 3435.
- [272] E. A. Salter, R. Z. Hinrichs, C. Salter, *J. Am. Chem. Soc.* **1996**, 118, 227.
- [273] S. Maity, R. I. Kaiser, B. M. Jones, *Phys. Chem. Chem. Phys.* **2015**, 17, 3081.
- [274] R. I. Kaiser, S. Maity, B. M. Jones, *Phys. Chem. Chem. Phys.* **2014**, 16, 3399.
- [275] M. J. Abplanalp, A. Borsuk, B. M. Jones, R. I. Kaiser, *Astrophys. J.* **2015**, 814.
- [276] M. Forstel, P. Maksyutenko, B. M. Jones, B. J. Sun, A. H. H. Chang, R. I. Kaiser, *Chem. Commun.* **2016**.
- [277] L. Zhou, S. Maity, M. Abplanalp, A. Turner, R. I. Kaiser, *Astrophys. J.* **2014**, 790, 38.
- [278] O. Kostko, J. Zhou, B. J. Sun, J. S. Lie, A. H. Chang, R. I. Kaiser, M. Ahmed, *Astrophys. J.* **2010**, 717, 674.
- [279] S. Kelzenberg, N. Eisenreich, W. Eckl, V. Weiser, *Propellants Explos. Pyrotech.* **1999**, 24, 189.
- [280] E. Boyer, K. K. Kuo, *Proc. Combust. Inst.* **2007**, 31, 2045.
- [281] V. Bouyer, I. Darbord, P. Hervé, G. Baudin, C. Le Gallic, F. Clément, G. Chavent, *Combust. Flame* **2006**, 144, 139.
- [282] J. M. Winey, Y. M. Gupta, *J. Phys. Chem. A* **1997**, 101, 9333.
- [283] J. M. Winey, Y. M. Gupta, *J. Phys. Chem. B* **1997**, 101, 10733.
- [284] Y.-X. Zhang, S. H. Bauer, *J. Phys. Chem. B* **1997**, 101, 8717.
- [285] L. J. Butler, D. Krajnovich, Y. T. Lee, G. S. Ondrey, R. Bersohn, *J. Chem. Phys.* **1983**, 79, 1708.
- [286] Y. Q. Guo, A. Bhattacharya, E. R. Bernstein, *J. Phys. Chem. A* **2009**, 113, 85.

- [287] Y. Kohge, T. Hanada, M. Sumida, K. Yamasaki, H. Kohguchi, *Chem. Phys. Lett.* **2013**, *556*, 49.
- [288] K. Q. Lao, E. Jensen, P. W. Kash, L. J. Butler, *J. Chem. Phys.* **1990**, *93*, 3958.
- [289] D. B. Moss, K. A. Trentelman, P. L. Houston, *J. Chem. Phys.* **1992**, *96*, 237.
- [290] A. Dey, R. Fernando, C. Abeysekera, Z. Homayoon, J. M. Bowman, A. G. Suits, *J. Chem. Phys.* **2014**, *140*, 054305.
- [291] B. H. Rockney, E. R. Grant, *Chem. Phys. Lett.* **1981**, *79*, 15.
- [292] B. H. Rockney, E. R. Grant, *J. Chem. Phys.* **1982**, *77*, 4257.
- [293] B. H. J. Bielski, R. B. Timmons, *J. Phys. Chem.* **1964**, *68*, 347.
- [294] R. E. Rebbert, N. Slagg, *Bull. Soc. Chim. Belg.* **1962**, *71*, 709.
- [295] R. I. Kaiser, P. Maksyutenko, *Chem. Phys. Lett.* **2015**, *631–632*, 59.
- [296] R. I. Kaiser, P. Maksyutenko, *J. Phys. Chem. C* **2015**, *119*, 14653.
- [297] P. Maksyutenko, L. G. Muzangwa, B. M. Jones, R. I. Kaiser, *Phys. Chem. Chem. Phys.* **2015**, *17*, 7514.
- [298] F. Guo, X.-l. Cheng, H. Zhang, *J. Phys. Chem. A* **2012**, *116*, 3514.
- [299] S.-p. Han, A. C. T. van Duin, W. A. Goddard, A. Strachan, *J. Phys. Chem. B* **2011**, *115*, 6534.
- [300] M. Citroni, R. Bini, M. Pagliai, G. Cardini, V. Schettino, *J. Phys. Chem. B* **2010**, *114*, 9420.
- [301] C. Chachaty, *J. Chim. Phys. Phys.-Chim. Biol.* **1965**, *62*, 827.
- [302] C. Chachaty, A. Forchioni, *C. R. Acad. Sci., Paris, Ser. C* **1969**, *268*, 300.
- [303] C. Chachaty, C. Rosilio, *J. Chim. Phys.* **1967**, *64*, 777.
- [304] M. C. R. Symons, *Faraday Discuss.* **1988**, *86*, 99.
- [305] S. Stoll, A. Ozarowski, R. D. Britt, A. Angerhofer, *J. Magn. Reson.* **2010**, *207*, 158.
- [306] H. Dilger, E. Roduner, R. Scheuermann, J. Major, M. Schefzik, R. Stöber, M. Päch, D. G. Fleming, *Physica B* **2000**, *289–290*, 482.
- [307] C. K. Jen, S. N. Foner, E. L. Cochran, V. A. Bowers, *Phys. Rev.* **1958**, *112*, 1169.
- [308] S. G. Karshenboim, *Phys. Rep.* **2005**, *422*, 1.
- [309] J. S. Tiedeman, H. G. Robinson, *Phys. Rev. Lett.* **1977**, *39*, 602.
- [310] L. W. Anderson, F. M. Pipkin, J. C. Baird, *Phys. Rev. Lett.* **1960**, *4*, 69.
- [311] T. Takada, H. Tachikawa, *Int. J. Quantum Chem.* **2005**, *105*, 79.
- [312] Y. A. Dmitriev, *J. Low Temp. Phys.* **2005**, *31*, 423.
- [313] T. Shiga, A. Lund, *J. Phys. Chem.* **1973**, *77*, 453.
- [314] R. L. Morehouse, J. J. Christiansen, W. Gordy, *J. Chem. Phys.* **1966**, *45*, 1751.
- [315] Y. A. Dmitriev, R. A. Zhitnikov, *J. Low Temp. Phys.* **2001**, *122*, 163.
- [316] R. A. Zhitnikov, Y. A. Dmitriev, *Astron. Astrophys.* **2002**, *386*, 1129.
- [317] N. P. Benetis, Y. Dmitriev, F. Mocchi, A. Laaksonen, *J. Phys. Chem. A* **2015**, *119*, 9385.
- [318] T. J. Schaafsma, J. Kommandeur, *Mol. Phys.* **1968**, *14*, 517.
- [319] D. M. Murphy, in *Metal Oxide Catalysis*, Wiley-VCH, **2009**, pp. 1.
- [320] R. N. Schwartz, M. D. Clark, W. Chamulitrat, L. Kevan, *J. Appl. Phys.* **1986**, *59*, 3231.
- [321] B. H. J. Bielski, J. J. Freeman, J. M. Gebicki, *J. Phys. Chem.* **1968**, *72*, 1721.
- [322] M. Shiotani, J. H. Freed, *J. Phys. Chem.* **1981**, *85*, 3873.
- [323] P. H. Kasai, W. Weltner, E. B. Whipple, *J. Chem. Phys.* **1965**, *42*, 1120.
- [324] M. D. Pace, *J. Phys. Chem.* **1991**, *95*, 5858.
- [325] D. S. Burch, W. H. Tanttila, M. Mizushima, *J. Chem. Phys.* **1974**, *61*, 1607.
- [326] J. H. Lunsford, *J. Colloid Interface Sci.* **1968**, *26*, 355.
- [327] S. Stoll, A. Schweiger, in *ESR Spectroscopy in Membrane Biophysics* (Eds.: M. A. Hemminga, L. J. Berliner), Springer US, **2007**, pp. 299.
- [328] M. Jinguji, Y. Ohokubo, I. Tanaka, *Chem. Phys. Lett.* **1978**, *54*, 136.

- [329] H. Yahiro, A. Lund, M. Shiotani, *Spectrochim. Acta Mol. Biomol. Spectrosc.* **2004**, *60*, 1267.
- [330] H. Yahiro, K. Kurohagi, G. Okada, Y. Itagaki, M. Shiotani, A. Lund, *Phys. Chem. Chem. Phys.* **2002**, *4*, 4255.
- [331] A. A. McConnell, S. Mitchell, A. L. Porte, J. S. Roberts, C. Thomson, *J. Chem. Soc., Faraday Trans.* **1970**, 833.
- [332] K. Tsuchiya, M. Takasugi, K. Minakuchi, K. Fukuzawa, *Free Radic. Biol. Med.* **1996**, *21*, 733.
- [333] S. Nagakura, *Mol. Phys.* **1960**, *3*, 152.
- [334] N. S. Bayliss, E. G. McRae, *J. Phys. Chem.* **1954**, *58*, 1006.
- [335] J. W. Rabalais, *J. Chem. Phys.* **1972**, *57*, 960.
- [336] W. M. Flicker, O. A. Mosher, A. Kuppermann, *J. Chem. Phys.* **1980**, *72*, 2788.
- [337] L. Wang, T. Yoshida, Y. Muto, Y. Murai, Z. P. Tachrim, A. Ishida, S. Nakagawa, Y. Sakihama, Y. Hashidoko, K. Masuda, Y. Hatanaka, M. Hashimoto, *Eur. J. Org. Chem.* **2015**, *2015*, 3129.
- [338] E. Emer, J. Twilton, M. Tredwell, S. Calderwood, T. L. Collier, B. Liégault, M. Taillefer, V. Gouverneur, *Org. Lett.* **2014**, *16*, 6004.
- [339] D. Billen, S. D. W. Greenwood, T. L. Stuk, Google Patents, **2014**.
- [340] X. Zhang, X. Wang, Y. Gao, X. Xu, *Chem. Commun.* **2017**, *53*, 2427.
- [341] T. Bercovici, C. Gitler, A. Bromberg, *Biochemistry* **1978**, *17*, 1484.
- [342] C. Monnereau, E. Blart, F. Odobel, *Tetrahedron Lett.* **2005**, *46*, 5421.
- [343] T. Taldone, D. Zatorska, G. Chiosis, *Synth. Commun.* **2012**, *42*, 635.
- [344] R. Sathiyapriya, R. J. Karunakaran, *J. Chem.* **2009**, *6*, 1164.
- [345] P. Costa, M. Fernandez-Oliva, E. Sanchez-Garcia, W. Sander, *J. Am. Chem. Soc.* **2014**, *136*, 15625.
- [346] S. Maity, R. I. Kaiser, B. M. Jones, *Faraday Discuss.* **2014**, *168*, 485.
- [347] M. J. Abplanalp, S. Gozem, A. I. Krylov, C. N. Shingledecker, E. Herbst, R. I. Kaiser, *Proc. Natl. Acad. Sci. U.S.A.* **2016**, *113*, 7727.
- [348] M. S. Westley, G. A. Baratta, R. A. Baragiola, *J. Chem. Phys.* **1998**, *108*, 3321.
- [349] A. M. Turner, M. J. Abplanalp, S. Y. Chen, Y. T. Chen, A. H. Chang, R. I. Kaiser, *Phys. Chem. Chem. Phys.* **2015**, *17*, 27281.
- [350] B. M. McMurtry, A. M. Turner, S. E. J. Saito, R. I. Kaiser, *Chem. Phys.* **2016**, *472*, 173.
- [351] J. W. Hepburn, *Laser Techniques in Chemistry*, Wiley, New York, NY, **1994**.
- [352] R. Hilbig, R. Wallenstein, *Appl. Opt.* **1982**, *21*, 913.
- [353] R. Hilbig, G. Hilber, A. Lago, B. Wolff, R. Wallenstein, *Nonlinear Optics and Applications* **1986**, 613.
- [354] C. Lee, W. Yang, R. G. Parr, *Phys. Rev. B* **1988**, *37*, 785.
- [355] T. Schwabe, S. Grimme, *Phys. Chem. Chem. Phys.* **2006**, *8*, 4398.
- [356] S. Grimme, J. Antony, S. Ehrlich, H. Krieg, *J. Chem. Phys.* **2010**, *132*, 154104.
- [357] S. Grimme, S. Ehrlich, L. Goerigk, *J. Comput. Chem.* **2011**, *32*, 1456.
- [358] M. J. Frisch, G. W. Trucks, H. B. Schlegel, G. E. Scuseria, M. A. Robb, J. R. Cheeseman, G. Scalmani, V. Barone, B. Mennucci, G. A. Petersson, H. Nakatsuji, M. Caricato, X. Li, H. P. Hratchian, A. F. Izmaylov, J. Bloino, G. Zheng, J. L. Sonnenberg, M. Hada, M. Ehara, K. Toyota, R. Fukuda, J. Hasegawa, M. Ishida, T. Nakajima, Y. Honda, O. Kitao, H. Nakai, T. Vreven, J. Montgomery, J. A., J. E. Peralta, F. Ogliaro, M. Bearpark, J. J. Heyd, E. Brothers, K. N. Kudin, V. N. Staroverov, R. Kobayashi, J. Normand, K. Raghavachari, A. Rendell, J. C. Burant, S. S. Iyengar, J. Tomasi, M. Cossi, N. Rega, J. M. Millam, M. Klene, J. E. Knox, J. B. Cross, V. Bakken, C. Adamo, J. Jaramillo, R. Gomperts, R. E. Stratmann, O. Yazyev, A. J. Austin, R. Cammi, C. Pomelli, J. W. Ochterski, R. L. Martin, K. Morokuma, V. G. Zakrzewski, G. A. Voth,

- P. Salvador, J. J. Dannenberg, S. Dapprich, A. D. Daniels, Ö. Farkas, J. B. Foresman, J. V. Ortiz, J. Cioslowski, D. J. Fox, Gaussian Inc., Wallingford, **2009**.
- [359] F. Weigend, A. Köhn, C. Hättig, *J. Chem. Phys.* **2002**, *116*, 3175.
- [360] T. H. Dunning, *J. Chem. Phys.* **1989**, *90*, 1007.
- [361] R. A. Kendall, T. H. Dunning, R. J. Harrison, *J. Chem. Phys.* **1992**, *96*, 6796.
- [362] H.-J. Werner, P. J. Knowles, G. Knizia, F. R. Manby, M. Schütz, *WIREs Comput. Mol. Sci.* **2012**, *2*, 242.
- [363] F. Neese, *WIREs Comput. Mol. Sci.* **2012**, *2*, 73.
- [364] S. Stoll, A. Schweiger, *J. Magn. Reson.* **2006**, *178*, 42.
- [365] M. Griffin, A. Muys, C. Noble, D. Wang, C. Eldershaw, K. E. Gates, K. Burrage, G. R. Hanson, *Mol. Phys. Lett.* **1999**, *26*, 60.



## Acknowledgments

First of all, I would like to express my deepest gratitude to Prof. Dr. Wolfram Sander for providing me an opportunity to conduct doctoral research in his group as well as for the constant scientific support, encouragement and kind advice he has provided throughout my time as his student.

I would also like to thank our collaborators Prof. Dr. Elsa Sanchez-Garcia and Niklas Tötsch (Max-Planck-Institut für Kohlenforschung), Prof. Dr. Ralf I. Kaiser, Dr. Sándor Góbi, Dr. Marko Förstel and Dr. Pavlo Maksyutenko (Department of Chemistry, University of Hawaii at Manoa), Prof. Dr. Alexander M. Mebel (Florida International University), Prof. Dr. Peter R. Schreiner and Dr. Artur Mardyukov (Institute of Organic Chemistry, Justus-Liebig University) and Dr. Fabien Borget, Dr. Fabrice Duvernay and Dr. Teddy Butscher (Aix-Marseille Université).

Furthermore, I am very thankful to Prof. Dr. Ralf I. Kaiser for accepting me to visit his lab for two months internship. I am extremely fortunate to work with and to learn from him.

My sincere thanks also goes to Dr. Dirk Grote for introducing me to the EPR spectroscopy and for his help ever since.

I am grateful to Heidi, Torsten, Klaus, Catharina, Robin, Sabine, Jacinta and Hannah for their technical and administrative help in the laboratory.

I thank Frau Gundula Talbot, the coordination office of Graduate School of Chemistry and Biochemistry, for helping me in several ways.

I would like to thank all former and present colleagues of our group, namely, Adam, Akshay, André, Andreas, Arun, Bishnu, Corina, Enrique, Fee, Geneviève, Gizem, Iris, Joel, Liang, Linda, Melania, Melanie, Miguel, Mika, Mohamed, Nadja, Nesli, Paolo, Pritam, Sandra, Saonli, Soumya, Stefan, Tim and Tobias for all the help and for keeping a nice working atmosphere in the lab.

Many thanks to all the group members in Hawaii, particularly Marko and Sándor for helping me in several ways.

I would like to thank Pritam not only for his collaboration throughout this work but also the fun times we have shared together in lab and outdoor activities. I also thank Liang who contributed in this work with her effort in the lab during her in-depth practical, specialization and master thesis projects. I am grateful to Enrique and Joel for helping me with the calculations, and Iris for her help with the German language related staffs. I thank Stefan for his help in several ways.

My sincere thanks also goes to Akshay, Marko, Mika, Sándor and Stefan for proofreading some of the sections of this manuscript.

Finally, I would like to thank my family and friends for supporting and encouraging me throughout my life. I am grateful to Amen, Akiste, Barich, Beyu, Nati and Wube: እንግዲህ ጠጅ የጣለ እጁን ያውጣ፤ የጀበና ቡና ይጣፍጥ አባሽ፤ ባለ ገንፎ ወዲህ በል፤ ጉርሻውማ ተወዳዳሪ የለውም፤ ደግሞ ጨቅጫ ቃነታቸውን አልረሳውትም...ሁላቸውም የየድርሻቸውን ወሰዱ፤ በረካ ሁኑልኝ፡፡

## Appendix

## Figures

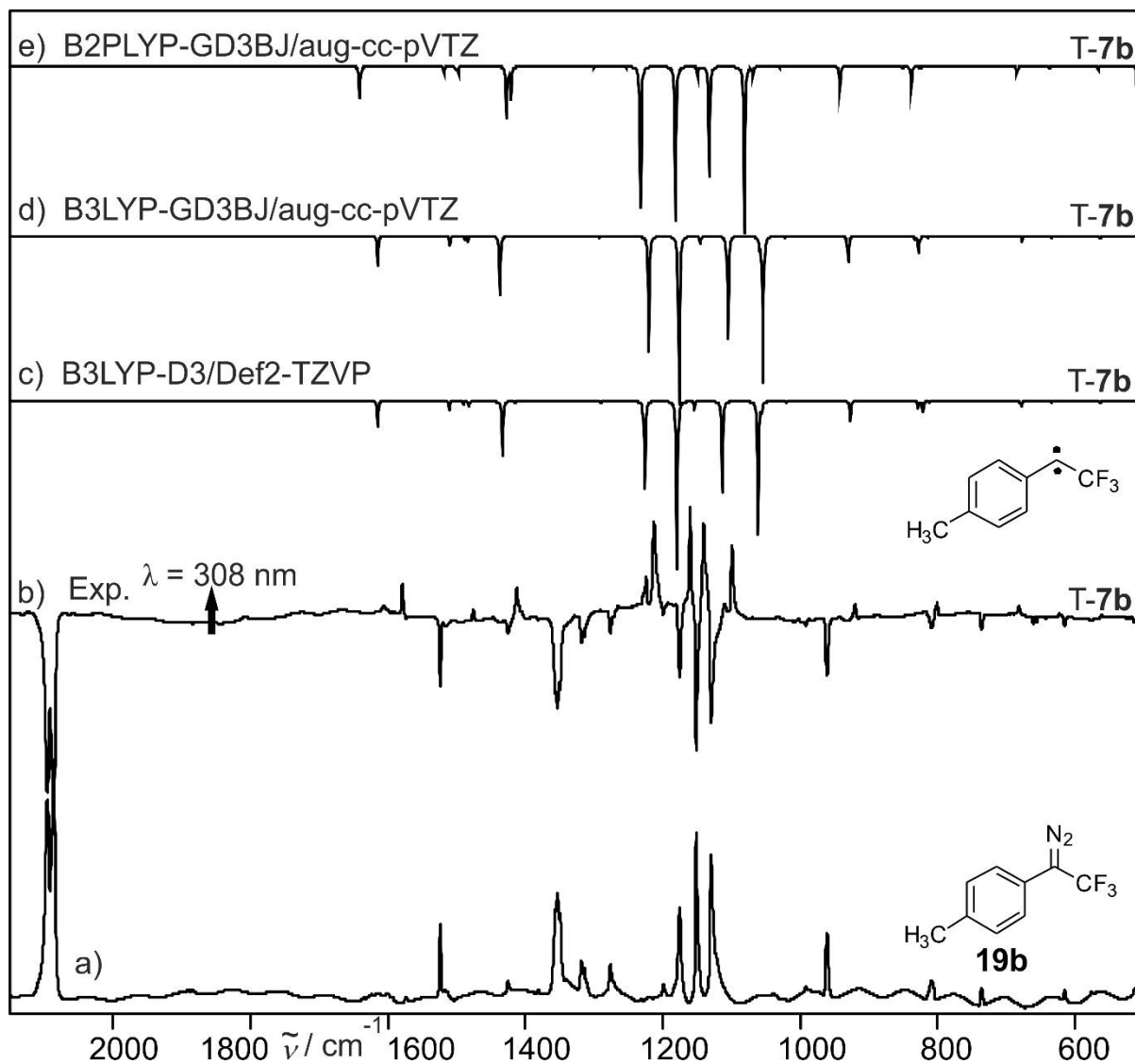


**Figure A1.** IR spectra showing the formation of T-7b after 90 minutes of 308 nm laser irradiation of 19b in argon matrix at 3K. a) IR spectrum of 19b. b) Difference IR spectrum at 3 K showing changes after 90 min of 308 nm laser irradiation of the same matrix. Bands pointing downward, assigned to 19b, are disappearing, and bands pointing upward, assigned to T-7b are appearing. Only traces of S-7b is obtained under these conditions. IR spectrum of T-7b calculated c) at the B3LYP-D3/Def2-TZVP level of theory, d) at the B3LYP-GD3BJ/aug-cc-pVTZ level of theory and e) at the B2PLYP-GD3BJ/aug-cc-pVTZ level of theory.

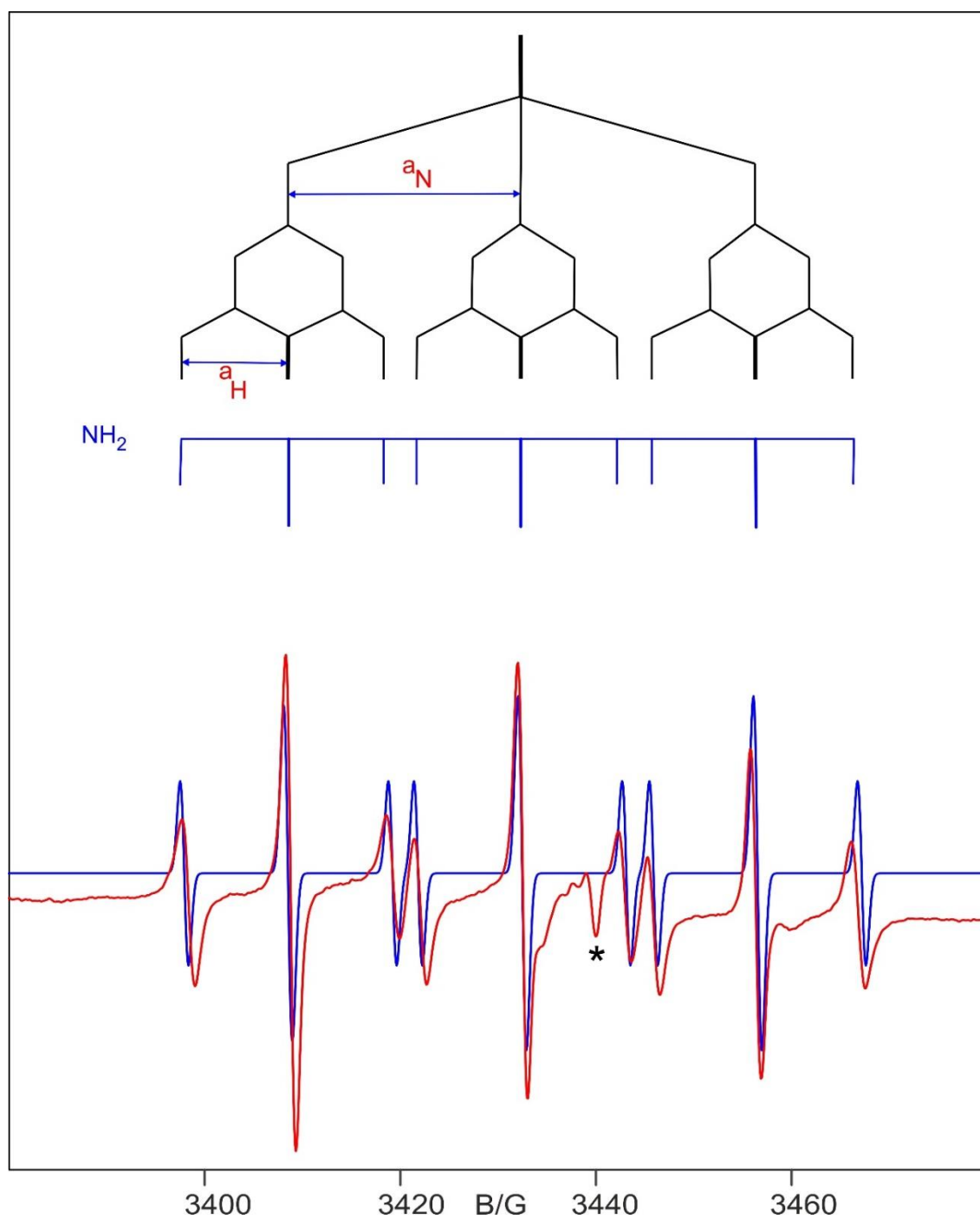


**Figure A2.** EPR spectra of  $\text{NH}_2$  radicals. a) Experimental spectrum obtained upon 450 nm irradiation of a matrix containing **7b** and 1% of ammonia at 4 K. The band assigned with asterisks is due to the signal coming from the copper rod. b) Simulated spectrum with ( $\mu = 9.6280$  GHz;  $g_{\text{iso}} = 2.004$ ;  $A_1 = 67.3$ ,  $A_2 = 29.6$  and  $A_3 = 30.2$  MHz).

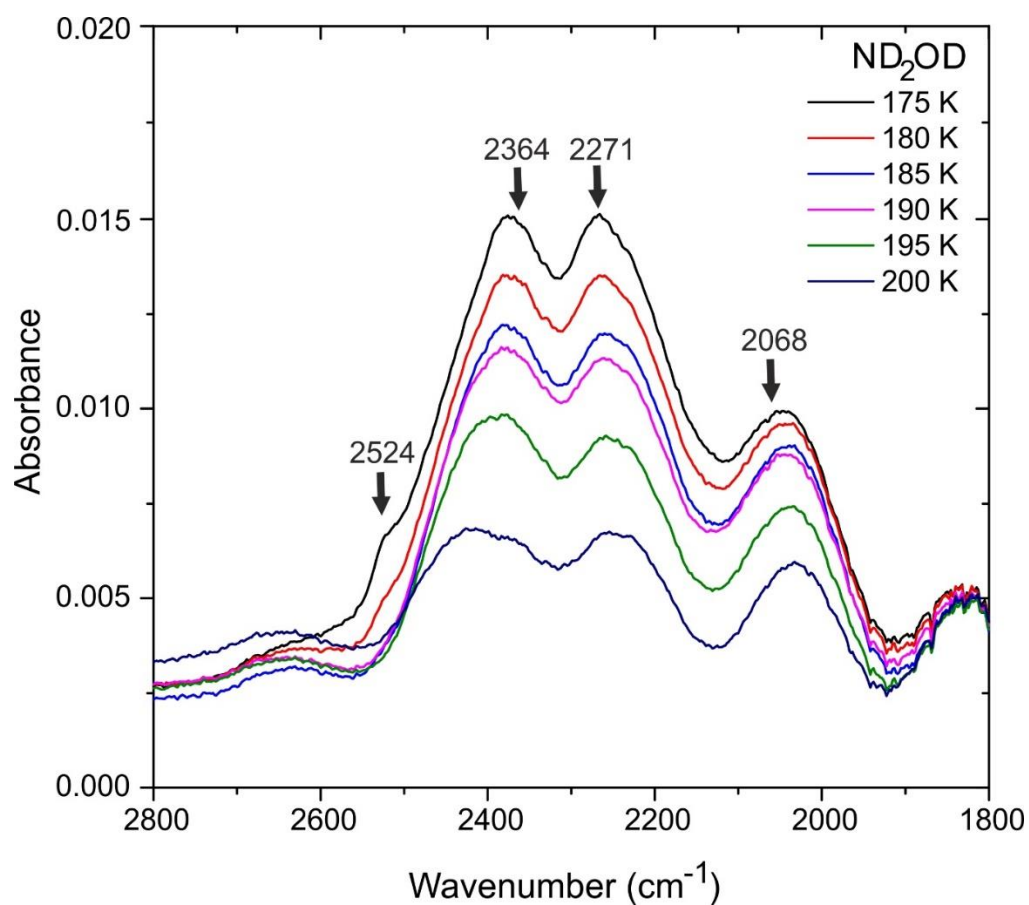


**Figure A3.** Infrared absorption features of the D3-hydroxylamine (ND<sub>2</sub>OD) species at 175, 180, 185, 190, 195 and 200 K after most of the host molecules D3-ammonia (ND<sub>3</sub>) and oxygen (O<sub>2</sub>) as well as computing by-products such as water (D<sub>2</sub>O) sublimed. The deconvoluted absorption features of the ND<sub>2</sub>OD at 5.5, 30, 150, 175 and 200 K are shown in Figure 65. The individual band assignments are compiled in Table A2. Atmospheric carbon dioxide has been traced out.

## Tables

**Table A1.** IR absorption features recorded before and after the electron irradiation of D3-ammonia–oxygen (ND<sub>3</sub>–O<sub>2</sub>) ices at 5.5 K.

Band position (cm <sup>-1</sup> )		ref.	Assignment <sup>a</sup>		
This work	Literature value		Species	Vibration	Characterization
before irradiation					
3700			ND <sub>3</sub>	$\nu_3 + \nu_4$	combination
3348			ND <sub>3</sub>	$\nu_3 + \nu_2$	combination
3178			ND <sub>3</sub>	$\nu_1 + \nu_2$	combination
2642			ND <sub>3</sub>	$\nu_1 + \nu_L$	combination
2500	2503	[215]	ND <sub>3</sub>	$\nu_3$	antisymmetric stretch
2342			ND <sub>3</sub>	2 $\nu_4$	overtone
2330	2326	[215]	ND <sub>3</sub>	$\nu_1$	symmetric stretch
1184, 1204	1185	[215]	ND <sub>3</sub>	$\nu_4$	degenerated deformation
840	833	[215]	ND <sub>3</sub>	$\nu_2$	symmetric deformation
after irradiation					
2567	2572	[206]	D <sub>2</sub> O	$\nu_1$	symmetric stretch (out-of-phase)
2522	2482	[191]	ND <sub>2</sub> OD	$\nu_1$	O–D stretch
2358	2393	[191]	ND <sub>2</sub> OD	$\nu_7$	N–D stretch (antisymmetric)
2346		[191]	ND <sub>2</sub> OD	$\nu_2$	N–D stretch (symmetric)
2297	2305	[206]	D <sub>2</sub> O	$\nu_1$	symmetric stretch (in-phase)
2267		[191]	ND <sub>2</sub> OD	$\nu_2$	N–D stretch (symmetric)
2248	2184	[191]	ND <sub>2</sub> OD	$\nu_3 + \nu_4$	combination
2075	2045	[191]	ND <sub>2</sub> OD	$\nu_3 + \nu_5$	combination
2027		[191]	ND <sub>2</sub> OD	$\nu_4 + \nu_8$	combination
1875	1875	[191, 194, 219–220]	NO	$\nu_1$	fundamental
1836	1833–1851	[191, 194, 219, 223]	N <sub>2</sub> O <sub>3</sub>	$\nu_1$	N=O stretch
1735	1737	[191, 194, 219]	N <sub>2</sub> O <sub>2</sub>	$\nu_1$	N=O stretch
1616	1614	[222]	NO <sub>2</sub>	$\nu_3$	N=O stretch (antisymmetric)
1543	1546	[191, 224]	DNO	$\nu_3$	N=O stretch
1303	1303	[191, 194, 219, 223]	N <sub>2</sub> O <sub>3</sub>	$\nu_3$	NO <sub>2</sub> stretch
1252	1240	[221]	N <sub>2</sub> O <sub>2</sub>	$\nu_?$	NO <sub>2</sub> stretch (antisymmetric)
1135	1156	[191, 224]	DNO	$\nu_2$	DNO bend
1038	1037	[226]	O <sub>3</sub>	$\nu_3$	antisymmetric stretch
881	920	[191]	ND <sub>2</sub> OD	$\nu_5$	ND <sub>2</sub> wag
796	880	[221]	N <sub>2</sub> O <sub>2</sub>	$\nu_?$	N–N stretch

<sup>a</sup> Assignment based on references.

**Table A2.** Deconvoluted peak positions of hydroxylamine (NH<sub>2</sub>OH), water (H<sub>2</sub>O) and ammonia (NH<sub>3</sub>) absorption bands observed in the processed ammonia–oxygen (NH<sub>3</sub>–O<sub>2</sub>) ices as shown in Figure 65.

Band	This work					Literature values (cm <sup>-1</sup> )				Assignment <sup>a</sup>	
	5.5 K	30 K	150 K	175 K	200 K	ref.1 <sup>[187]</sup>	ref.2 <sup>[191]</sup>	ref.3 <sup>[75]</sup>	ref.4 <sup>[76]</sup>	Species	Vibration
1	3452	3457	...	3432	3421	...	...	...	3452	H <sub>2</sub> O	$\nu_1$
2	3391	3391	3395	3395	3395	...	3317	...	...	NH <sub>2</sub> OH	$\nu_1$
3	3366	3367	3379	3360	3357	...	...	3372	...	NH <sub>3</sub>	$\nu_3$
4	3336	3333	3333	...	...	...	...	...	3332	H <sub>2</sub> O	$\nu_3$
5	3307	3306	...	...	...	...	...	3290	...	NH <sub>3</sub>	$2\nu_4$
6	3248	3249	3244	3250	3256	3332	3261	...	...	NH <sub>2</sub> OH	$\nu_7$
7	3213	3214	3200	3196	3193	3209	3194	...	...	NH <sub>2</sub> OH	$\nu_2$
8	3204	3207	...	...	...	...	...	3212	...	NH <sub>3</sub>	$\nu_1$
9	3109	3107	3163	3154	3149	...	...	...	3151 3107	H <sub>2</sub> O	$\nu_3$ $\nu_1$
10	3024	3023	3072 3004	3074 3002	3070 3000	3074	...	...	...	NH <sub>2</sub> OH	$\nu_2$
11	2963	2963	2917	2912	2910	2943	2899	...	...	NH <sub>2</sub> OH	$\nu_3 + \nu_4$
12	2916	2911	2879	2833	2814	–	...	...	...	NH <sub>2</sub> OH	$2\nu_4$
13	2748	2745	2782	2786	2719	2507	2716	...	...	NH <sub>2</sub> OH	$\nu_3 + \nu_5$
14	2525	2529	2524	2532	2539	...	...	...	...	NH <sub>2</sub> OH	$\nu_4 + \nu_8$

<sup>a</sup> Assignment based on references.

**Table A3.** Deconvoluted peak positions of D3-hydroxylamine (ND<sub>2</sub>OH), D3-water (D<sub>2</sub>O) and D3-ammonia (ND<sub>3</sub>) absorption bands observed in the processed ammonia–oxygen (ND<sub>3</sub>–O<sub>2</sub>) ices as shown in Figure 65.

Band	This work					Literature values (cm <sup>-1</sup> )			Assignment <sup>a</sup>	
	5.5 K	30 K	150 K	175 K	200 K	ref.1 <sup>[191]</sup>	ref.2 <sup>[217]</sup>	ref.3 <sup>[206]</sup>	species	vibration
1	2567	2559	...	2539	2557	...	...	2572	D <sub>2</sub> O	$\nu_1$
2	2522	2522	2527	2524	2529	2482	...	...	ND <sub>2</sub> OD	$\nu_1$
3	2500	2500	2512	2497	2487	...	2503	...	ND <sub>3</sub>	$\nu_3$
4	2474	2476	2465	...	...	...	...	2470	D <sub>2</sub> O	$\nu_3$
5	2350	2352	...	...	...	...	...	...	ND <sub>3</sub>	$2\nu_4$
6	2358	2360	2392	2398	2409	2393	...	...	ND <sub>2</sub> OD	$\nu_7$
7	2346	2342	2364	2364	2358	...	...	...	ND <sub>2</sub> OD	$\nu_2$
8	2323	2323	...	...	...	...	2326	...	ND <sub>3</sub>	$\nu_1$
9	2297	2293	2364	2364	2361	...	...	2370	D <sub>2</sub> O	$\nu_3$
								2305		$\nu_1$
10	2267	2267	2279	2271	2257	...	...	...	ND <sub>2</sub> OD	$\nu_2$
			2218	2223	2219					
11	2248	2249	2190	2192	2183	2184	...	...	ND <sub>2</sub> OD	$\nu_3 + \nu_4$
12	2131	2129	2142	2135	2139		...	...	ND <sub>2</sub> OD	$2\nu_4$
13	2075	2075	2074	2068	2043	2045	...	...	ND <sub>2</sub> OD	$\nu_3 + \nu_5$
14	2027	2020	2011	2005	2003		...	...	ND <sub>2</sub> OD	$\nu_4 + \nu_8$

<sup>a</sup> Assignment based on references.

**Cartesian coordinates of optimized structures and corresponding energies in Hartree****Table A4.** Cartesian coordinates of **S-7b** optimized at the B3LYP-GD3BJ/aug-cc-pVTZ level of theory.

Atomic symbol	x	y	z
C	0.462	-0.814	-0.002
C	0.040	0.548	0.000
C	1.056	1.539	0.001
C	2.394	1.205	-0.001
C	2.785	-0.136	-0.003
C	1.797	-1.136	-0.004
H	-0.274	-1.602	-0.004
H	0.733	2.570	0.001
H	2.101	-2.175	-0.007
C	-1.283	1.041	0.002
C	-2.371	0.010	0.001
F	-3.602	0.553	0.011
F	-2.325	-0.785	-1.107
F	-2.317	-0.803	1.097
H	3.149	1.979	-0.002
C	4.232	-0.518	0.003
H	4.456	-1.196	-0.822
H	4.881	0.351	-0.075
H	4.481	-1.050	0.925

E=-646.87209, ZPVE=0.13523

**Table A5.** Cartesian coordinates of T-7b optimized at the B3LYP-GD3BJ/aug-cc-pVTZ level of theory.

Atomic symbol	x	y	z
C	-0.587	-0.876	-0.008
C	-0.122	0.469	-0.001
C	-1.096	1.502	-0.003
C	-2.440	1.200	-0.008
C	-2.894	-0.124	-0.011
C	-1.937	-1.147	-0.013
H	0.129	-1.685	-0.012
H	-0.765	2.530	-0.003
H	-2.266	-2.179	-0.022
C	1.231	0.766	0.002
C	2.479	0.004	0.003
F	3.552	0.816	0.011
F	2.589	-0.815	1.084
F	2.598	-0.803	-1.086
H	-3.163	2.006	-0.012
C	-4.360	-0.441	0.017
H	-4.701	-0.611	1.042
H	-4.952	0.376	-0.393
H	-4.582	-1.345	-0.550

---

E=-646.87576, ZPVE=0.13480

---

**Table A6.** Cartesian coordinates of **S-7b** optimized at the B2PLYP-GD3BJ/aug-cc-pVTZ level of theory.

Atomic symbol	x	y	z
C	0.453	-0.812	0.000
C	0.036	0.552	0.000
C	1.052	1.543	0.000
C	2.391	1.206	0.000
C	2.779	-0.137	0.000
C	1.789	-1.136	0.000
H	-0.285	-1.597	0.000
H	0.729	2.573	0.000
H	2.092	-2.175	0.000
C	-1.287	1.052	0.000
C	-2.367	0.009	0.000
F	-3.599	0.540	0.000
F	-2.307	-0.792	-1.099
F	-2.307	-0.792	1.099
H	3.148	1.978	0.000
C	4.226	-0.523	0.000
H	4.458	-1.128	-0.877
H	4.875	0.349	0.000
H	4.458	-1.128	0.877

E=-646.40345, ZPVE=0.13606

**Table A7.** Cartesian coordinates of T-7b optimized at the B2PLYP-GD3BJ/aug-cc-pVTZ level of theory.

Atomic symbol	x	y	z
C	-0.573	-0.861	-0.008
C	-0.124	0.482	-0.001
C	-1.097	1.505	-0.002
C	-2.440	1.197	-0.008
C	-2.883	-0.129	-0.011
C	-1.923	-1.144	-0.013
H	0.148	-1.665	-0.013
H	-0.773	2.536	-0.003
H	-2.244	-2.177	-0.022
C	1.238	0.790	0.002
C	2.474	0.003	0.003
F	3.559	0.794	0.007
F	2.568	-0.811	1.083
F	2.572	-0.806	-1.082
H	-3.167	1.998	-0.013
C	-4.348	-0.453	0.017
H	-4.705	-0.538	1.046
H	-4.934	0.324	-0.469
H	-4.552	-1.400	-0.479

---

E=-646.40281, ZPVE=0.13601

---

**Table A8.** Cartesian coordinates of **S-7b** optimized at the B97D-GD3/def2-TZVP level of theory and CCSD(T)/cc-pV(D/T)Z energies.

Atomic symbol	x	y	z
C	-0.438	-0.785	-0.080
C	-0.032	0.590	-0.006
C	-1.070	1.570	0.054
C	-2.408	1.211	0.079
C	-2.783	-0.142	-0.002
C	-1.775	-1.129	-0.095
H	0.319	-1.559	-0.140
H	-0.764	2.612	0.095
H	-2.068	-2.176	-0.162
C	1.289	1.107	0.000
C	2.397	0.095	0.094
F	3.605	0.664	0.326
F	2.251	-0.851	1.090
F	2.503	-0.576	-1.103
H	-3.179	1.976	0.146
C	-4.231	-0.544	-0.020
H	-4.400	-1.439	0.590
H	-4.882	0.260	0.337
H	-4.538	-0.795	-1.046
	$E_{\text{ref}}$	$E_{\text{corr}}$	$E_{\text{tot}}$
cc-pVDZ	-643.14507	-1.83630	644.98137
cc-pVTZ	-643.32970	-2.28398	-645.61368
cc-pV(D/T)Z	-643.32970	-2.47248	-645.80218

**Table A9.** Cartesian coordinates of T-7b optimized at the B97D-GD3/def2-TZVP level of theory and CCSD(T)/cc-pV(D/T)Z energies.

Atomic symbol	x	y	z
C	-0.583	-0.882	-0.008
C	-0.116	0.473	-0.001
C	-1.096	1.511	-0.003
C	-2.447	1.207	-0.009
C	-2.902	-0.126	-0.012
C	-1.940	-1.154	-0.014
H	0.141	-1.691	-0.013
H	-0.764	2.546	-0.003
H	-2.272	-2.191	-0.023
C	1.242	0.764	0.002
C	2.495	0.007	0.003
F	3.574	0.830	0.006
F	2.610	-0.814	1.098
F	2.614	-0.810	-1.094
H	-3.175	2.017	-0.013
C	-4.374	-0.446	0.018
H	-4.731	-0.532	1.055
H	-4.966	0.338	-0.468
H	-4.585	-1.400	-0.479
	Eref	Ecorr	Etot
cc-pVDZ	-643.16343	-1.82213	-644.98557
cc-pVTZ	-643.34833	-2.26666	-645.61499
cc-pV(D/T)Z	-643.34833	-2.45383	-645.80216

**Table A10.** Cartesian coordinates of S-7b···HOH optimized at the B3LYP/aug-cc-pVTZ level of theory.

Atomic symbol	x	y	z
C	2.968	-0.162	-0.001
C	2.113	-1.283	-0.001
C	0.750	-1.132	-0.001
C	0.157	0.169	-0.001
C	1.039	1.286	-0.001
C	2.408	1.119	-0.001
H	2.546	-2.275	-0.001
H	0.118	-2.007	-0.001
H	0.600	2.275	-0.001
H	3.058	1.984	-0.002
C	-1.216	0.473	0.000
C	-2.179	-0.679	0.000
F	-3.462	-0.272	0.000
F	-2.038	-1.470	1.100
F	-2.038	-1.470	-1.100
O	-1.493	3.420	0.001
H	-1.622	2.444	0.000
H	-2.373	3.806	0.000
C	4.452	-0.358	0.002
H	4.764	-0.904	0.895
H	4.763	-0.957	-0.857
H	4.987	0.589	-0.026

B3LYP: E=-723.31752, ZPVE=0.15935

B3LYP-GD3BJ@B3LYP: E=-723.35506, ZPVE=0.15941

B2PLYP-GD3BJ@B3LYP: E=-722.83452, ZPVE=0.16051

**Table A11.** Cartesian coordinates of T-7b...HOH optimized at the B3LYP/aug-cc-pVTZ level of theory.

Atomic symbol	x	y	z
C	3.098	-0.150	-0.008
C	2.296	-1.298	-0.021
C	0.919	-1.221	-0.019
C	0.269	0.046	-0.004
C	1.087	1.210	0.004
C	2.459	1.099	0.001
H	2.767	-2.273	-0.035
H	0.326	-2.124	-0.033
H	0.608	2.179	0.011
H	3.060	2.000	0.003
C	-1.112	0.159	-0.003
C	-2.283	-0.714	0.007
F	-3.423	0.012	-0.056
F	-2.367	-1.479	1.126
F	-2.309	-1.579	-1.041
O	-1.579	3.539	-0.069
H	-2.055	4.084	0.565
H	-2.138	2.766	-0.205
C	4.597	-0.250	0.022
H	4.971	-0.172	1.047
H	4.941	-1.203	-0.379
H	5.061	0.552	-0.552

B3LYP: E=-723.31135, ZPVE=0.15711

B3LYP-GD3BJ@B3LYP: E=-723.34724, ZPVE=0.15716

B2PLYP-GD3BJ@B3LYP: E=-722.82235, ZPVE=0.15869

**Table A12.** Cartesian coordinates of H<sub>2</sub>O optimized at the B2PLYP-GD3BJ/aug-cc-pVTZ level of theory.

Atomic Symbol	x	y	z
O	0.000	0.000	0.117
H	0.000	0.762	-0.469
H	0.000	-0.762	-0.469

E=-76.41493, ZPVE=0.02133

**Table A13.** Cartesian coordinates of **S-7c** optimized at the B2PLYP-GD3BJ/aug-cc-pVTZ level of theory.

Atomic symbol	x	y	z
C	0.47587500	-0.83192800	-0.00001000
C	0.08065300	0.53896200	-0.00000800
C	1.10617800	1.52263700	-0.00001200
C	2.44314900	1.18224600	-0.00000800
C	2.76145600	-0.16942300	-0.00001000
C	1.80589100	-1.18486100	-0.00001300
H	-0.27415400	-1.60589400	-0.00001200
H	0.79220000	2.55554500	-0.00001500
H	2.12931100	-2.21452700	-0.00001700
C	-1.23553900	1.05478500	-0.00001000
C	-2.32949200	0.02550500	0.00001600
F	-3.55349600	0.57241900	0.00005200
F	-2.27702500	-0.77545200	-1.09884400
F	-2.27698600	-0.77549100	1.09884500
H	3.23158700	1.91865400	-0.00000700
F	4.04884400	-0.51940100	-0.00001100

E=-705.6061927, ZPVE=0.1005051

**Table A14.** Cartesian coordinates of T-7c optimized at the B2PLYP-GD3BJ/aug-cc-pVTZ level of theory.

Atomic symbol	x	y	z
C	-0.59838400	-0.87714000	-0.00001800
C	-0.16599700	0.47168100	-0.00014000
C	-1.14438500	1.49083700	0.00001200
C	-2.48865500	1.18255700	0.00000600
C	-2.86684300	-0.15085700	-0.00015600
C	-1.94366000	-1.18409000	-0.00001300
H	0.13181000	-1.67191900	0.00003400
H	-0.82691400	2.52272700	0.00009200
H	-2.28676200	-2.20744000	0.00016900
C	1.19426700	0.79418400	-0.00027200
C	2.43669100	0.01573900	0.00000200
F	3.51469500	0.81402600	0.00005400
F	2.53588600	-0.79465000	1.08252400
F	2.53620600	-0.79489200	-1.08232500
H	-3.24491500	1.95242600	0.00020200
F	-4.17694500	-0.45262400	0.00007900

E=-705.6198897, ZPVE=0.1004062

**Table A15.** Cartesian coordinates of S-7c···H–OH optimized at the B3LYP-D3/def2-TZVP level of theory.

Atomic symbol	x	y	z
C	2.92398300	-0.22963500	-0.00020700
C	2.09056000	-1.34937100	-0.03579600
C	0.73264500	-1.15043900	-0.02481200
C	0.17981000	0.16827100	0.01768700
C	1.08764200	1.26923200	0.05072900
C	2.45216400	1.07564000	0.04377400
H	2.53231400	-2.33567800	-0.07022500
H	0.07305600	-2.00455900	-0.05208900
H	0.67241500	2.26888700	0.08394500
H	3.15389800	1.89753400	0.06911700
C	-1.18568300	0.50121300	0.02455800
C	-2.16583400	-0.63523200	0.00821700
F	-3.44122800	-0.21286900	0.04452800
F	-2.01355300	-1.46473200	1.07863600
F	-2.04645300	-1.38931900	-1.11909700
O	-1.28129200	3.42509300	-0.09220500
H	-2.03234400	3.88911600	0.28879300
H	-1.49715000	2.46471000	-0.04109600
F	4.24083700	-0.43072700	-0.00914500

E=-783.294983, ZPVE=0.124349

**Table A16.** Cartesian coordinates of T-7c···HOH optimized at the B3LYP-D3/def2-TZVP level of theory.

Atomic symbol	x	y	z
C	3.07109900	-0.15375900	0.00000000
C	2.29046200	-1.30308400	-0.00000200
C	0.91667000	-1.17920700	-0.00000200
C	0.30465300	0.10792100	0.00000100
C	1.14572500	1.25498300	0.00000300
C	2.51807900	1.12110600	0.00000200
H	2.77035300	-2.27228800	-0.00000400
H	0.29642400	-2.06497200	-0.00000400
H	0.68135700	2.23184800	0.00000400
H	3.17008200	1.98392200	0.00000300
C	-1.07487100	0.25171200	0.00000200
C	-2.23552200	-0.63618500	0.00000000
F	-3.38623800	0.07603200	-0.00000100
F	-2.27522200	-1.45245100	1.08514700
F	-2.27522000	-1.45245200	-1.08514500
O	-1.59182500	3.21217800	-0.00000200
H	-2.03133100	2.81718300	0.76161300
H	-2.03132400	2.81718600	-0.76162300
F	4.41015400	-0.28126600	-0.00000100

E=-783.2887047, ZPVE=0.1224556

**Table A17.** Cartesian coordinates of H<sub>2</sub>O optimized at the B3LYP-D3/def2-TZVP level of theory.

Atomic symbol	x	y	z
O	0.00000000	0.00000000	0.11687900
H	0.00000000	0.76506800	-0.46751800
H	0.00000000	-0.76506800	-0.46751800

E=-76.4630041, ZPVE=0.0211705

**Table A18.** Cartesian coordinates of *syn-S-7i* optimized at the B3LYP-D3/6-311++G(d,p) level of theory.

Atomic symbol	x	y	z
H	-2.03633000	2.54304600	-0.88015400
C	1.26502500	-0.92300400	-0.00001100
C	1.64439000	0.46245400	-0.00001600
C	0.60018300	1.44102800	-0.00001800
C	-0.71944500	1.05637100	-0.00000800
C	-1.05479500	-0.31781800	-0.00000600
C	-0.05798700	-1.30843500	-0.00001000
H	2.03721600	-1.67957900	-0.00000900
H	0.89916500	2.48281000	-0.00002500
H	-0.32704200	-2.35847400	-0.00001100
C	-1.97890600	1.89358700	0.00000000
H	-2.03632000	2.54303900	0.88016100
C	-3.06928900	0.84796600	0.00000300
C	-4.44847700	1.00760000	0.00000800
C	-5.25722000	-0.13090500	0.00000900
C	-4.69665100	-1.41487700	0.00000500
C	-3.31620000	-1.58280400	-0.00000100
C	-2.50434800	-0.44455400	-0.00000200
H	-4.89420900	1.99621400	0.00001200
H	-6.33576200	-0.02106700	0.00001400
H	-5.34639800	-2.28222000	0.00000600
H	-2.88079900	-2.57549200	-0.00000500
C	2.95596800	0.98800800	-0.00002400
C	4.06752400	-0.01827300	0.00000200
F	5.29187300	0.55207800	-0.00000100
F	4.03971200	-0.83080900	1.10376800
F	4.03973100	-0.83086300	-1.10372200

E= -876.512666, ZPVE= 0.194876

**Table A19.** Cartesian coordinates of *anti-S-7i* optimized at the B3LYP-D3/6-311++G(d,p) level of theory.

Atomic symbol	x	y	z
H	1.17764800	-2.28044000	-0.88020700
C	-0.88786200	2.02053000	-0.00000100
C	-1.67708200	0.82679900	-0.00000100
C	-0.98723600	-0.43300700	-0.00000100
C	0.38374300	-0.45997900	-0.00000100
C	1.13184300	0.74713000	-0.00000100
C	0.49318800	1.99364700	0.00000000
H	-1.43034200	2.95794600	0.00000000
H	-1.55293500	-1.35519900	-0.00000200
H	1.06845000	2.91198300	0.00000000
C	1.32443200	-1.64540100	-0.00000100
H	1.17764700	-2.28044100	0.88020500
C	2.68460500	-0.98843500	-0.00000100
C	3.94633600	-1.56811500	0.00000000
C	5.06832700	-0.73684200	0.00000000
C	4.93379100	0.65781700	0.00000000
C	3.67360700	1.24544500	0.00000000
C	2.54850300	0.41522800	0.00000000
H	4.06321300	-2.64623600	-0.00000100
H	6.05957000	-1.17588400	0.00000000
H	5.82055800	1.28079000	0.00000100
H	3.56736500	2.32420400	0.00000000
C	-3.07433000	1.03640400	-0.00000200
C	-3.91932400	-0.20236500	0.00000100
F	-5.24320800	0.06332700	-0.00000900
F	-3.70096800	-0.98666200	-1.10369800
F	-3.70098200	-0.98665000	1.10371200

E= -876.513030, ZPVE= 0.194853

**Table A20.** Cartesian coordinates of *syn-T-7i* optimized at the B3LYP-D3/6-311++G(d,p) level of theory.

Atomic symbol	x	y	z
H	-2.03166900	2.52210900	-0.88326800
C	1.17934100	-1.02581100	-0.03426100
C	1.58313700	0.35158200	-0.03247600
C	0.57068700	1.36232400	-0.02385300
C	-0.75327300	0.99557600	-0.01460200
C	-1.13371500	-0.36871600	-0.01329700
C	-0.15684500	-1.37359600	-0.02324800
H	1.94188800	-1.79395600	-0.04879400
H	0.86797700	2.40471200	-0.02342000
H	-0.44134700	-2.41991400	-0.02387200
C	-1.98890500	1.87041300	-0.00389000
H	-2.01803400	2.52008300	0.87753600
C	-3.11399200	0.85866400	0.00371700
C	-4.48564900	1.06514000	0.01523100
C	-5.33669200	-0.04420100	0.02086700
C	-4.81687700	-1.34325200	0.01511700
C	-3.44067200	-1.55735900	0.00380300
C	-2.58830200	-0.45025800	-0.00201200
H	-4.89612800	2.06933000	0.01986400
H	-6.41073100	0.10269900	0.02978600
H	-5.49338900	-2.19031400	0.01971500
H	-3.04086200	-2.56520800	-0.00042400
C	2.92323300	0.70103400	-0.04085100
C	4.20459400	-0.00226100	0.01010300
F	5.23712100	0.82557900	-0.25964300
F	4.45352000	-0.55987300	1.22997100
F	4.27001200	-1.03073000	-0.88690700

E= -876.515015, ZPVE= 0.194071

**Table A21.** Cartesian coordinates of *anti*-T-7i optimized at the B3LYP-D3/6-311++G(d,p) level of theory.

Atomic symbol	x	y	z
H	1.28797400	-2.29392600	-0.88039000
C	-0.85428600	1.97417500	-0.00000100
C	-1.60988400	0.75933900	0.00000000
C	-0.90412800	-0.48979100	0.00000000
C	0.46991400	-0.48454500	0.00000000
C	1.20005000	0.72894200	0.00000000
C	0.52612000	1.95815900	-0.00000100
H	-1.39130600	2.91488200	-0.00000100
H	-1.46201100	-1.41853500	0.00000100
H	1.07923700	2.89058400	-0.00000100
C	1.42757100	-1.65743300	0.00000100
H	1.28797400	-2.29392500	0.88039300
C	2.78144900	-0.98216800	0.00000100
C	4.04848200	-1.54684800	0.00000100
C	5.16448200	-0.70456300	0.00000100
C	5.00984100	0.68608300	0.00000000
C	3.74047200	1.25933500	0.00000000
C	2.62375400	0.41956800	0.00000000
H	4.17631600	-2.62412500	0.00000100
H	6.16050700	-1.13252600	0.00000100
H	5.88774400	1.32209200	0.00000000
H	3.62384000	2.33732500	-0.00000100
C	-2.99449000	0.79633200	0.00000000
C	-4.07049200	-0.19474200	-0.00000100
F	-5.28679000	0.39043000	0.00000200
F	-4.02346200	-1.01926300	-1.08778200
F	-4.02346000	-1.01926700	1.08777800

E= -876.515244, ZPVE= 0.194013

**Table A22.** Cartesian coordinates of S-7b···HNH<sub>2</sub> optimized at the B3LYP-D3/def2-TZVP level of theory.

Atomic symbol	x	y	z
C	2.93338000	-0.22755100	-0.00000200
C	2.06732000	-1.33873700	-0.00000400
C	0.70565400	-1.17247600	-0.00000200
C	0.12647200	0.13482800	0.00000200
C	1.01939000	1.24318400	0.00000100
C	2.38809300	1.05899200	0.00000000
H	2.49144500	-2.33601300	-0.00000700
H	0.06269900	-2.04004100	-0.00000500
H	0.59075200	2.23944600	0.00000100
H	3.04792300	1.91778800	0.00000000
C	-1.24641500	0.45251600	0.00000300
C	-2.20025100	-0.70542100	0.00000100
F	-3.48891200	-0.31360200	-0.00000900
F	-2.05288800	-1.49725000	1.10090600
F	-2.05286900	-1.49725800	-1.10089500
C	4.41597300	-0.44378700	0.00000000
H	4.71790200	-1.02142500	-0.87757700
H	4.96532000	0.49635200	-0.00003600
H	4.71790600	-1.02135700	0.87762100
N	-1.23824500	3.75676300	-0.00000100
H	-1.62579100	4.21877000	-0.81529800
H	-1.62579400	4.21877300	0.81529400
H	-1.58031400	2.79407000	0.00000000

E= -703.292055, ZPVE= 0.171995

**Table A23.** Cartesian coordinates of T-7b...HNH<sub>2</sub> optimized at the B3LYP-D3/def2-TZVP level of theory.

Atomic symbol	x	y	z
C	-3.09457900	-0.13160900	0.01588000
C	-2.28645200	-1.27588300	0.02601200
C	-0.91033200	-1.19007200	0.00640100
C	-0.26903800	0.08143300	-0.02176100
C	-1.09170000	1.24121100	-0.02883400
C	-2.46405100	1.12086500	-0.00960400
H	-2.75292000	-2.25405400	0.05034000
H	-0.30787000	-2.08826100	0.01197400
H	-0.60569200	2.20846500	-0.04604200
H	-3.07258300	2.01805800	-0.01247200
C	1.11119100	0.19779700	-0.03945600
C	2.25830900	-0.70492500	-0.00538300
F	3.40648800	-0.04486300	-0.28284000
F	2.15696700	-1.72035000	-0.90567100
F	2.43234100	-1.29765700	1.20587700
C	-4.59295000	-0.24082100	-0.00162500
H	-4.93118400	-1.18535000	0.42626200
H	-5.05868300	0.57422600	0.55495000
H	-4.97260400	-0.19101300	-1.02708800
N	1.67111000	3.35730400	0.01462000
H	1.98369800	3.35620400	0.97904100
H	1.80132400	4.29542900	-0.34741600
H	2.29418700	2.74302300	-0.49794700

E= -703.293051, ZPVE= 0.170302

**Table A24.** Cartesian coordinates of NH<sub>3</sub> optimized at the B3LYP-D3/def2-TZVP level of theory.

Atomic symbol	x	y	z
N	0.00000000	0.00000000	0.11158000
H	0.00000000	0.94295100	-0.26035300
H	-0.81661900	-0.47147500	-0.26035300
H	0.81661900	-0.47147500	-0.26035300

E= -56.551556, ZPVE= 0.034162

**Table A25.** Cartesian coordinates of S-7b···H<sub>2</sub> optimized at the B3LYP-D3/def2-TZVP level of theory.

Atomic symbol	x	y	z
C	-1.85729600	-1.18182000	-0.00002600
C	-0.51460600	-0.89283500	-0.00001600
C	-0.05734000	0.45968000	0.00001600
C	-1.04846900	1.47637800	0.00003600
C	-2.39552500	1.17553900	0.00002400
C	-2.82109000	-0.15620500	-0.00000600
H	-2.18857800	-2.21365000	-0.00005000
H	-0.70480200	2.50190200	0.00005900
H	-3.13057600	1.97070900	0.00003800
C	1.27952400	0.91653500	0.00003300
H	1.42175000	4.49255000	-0.00016600
H	1.51708300	3.75078200	-0.00011500
C	2.33821200	-0.14673000	0.00000500
F	2.26199000	-0.94842700	-1.10175100
F	2.26199300	-0.94847200	1.10172900
F	3.58439700	0.35983900	0.00001300
C	-4.27833100	-0.50609300	-0.00000800
H	-4.52688700	-1.10828200	0.87767900
H	-4.91103700	0.38013900	-0.00007700
H	-4.52686200	-1.10840800	-0.87761400
H	0.20401100	-1.69889200	-0.00003200

E= -647.901265, ZPVE= 0.147737

**Table A26.** Cartesian coordinates of T-7b···H<sub>2</sub> optimized at the B3LYP-D3/def2-TZVP level of theory.

Atomic symbol	x	y	z
C	-2.92767100	-0.14968200	-0.00327000
C	-1.98721400	-1.17560300	0.16073600
C	-0.63160900	-0.93040100	0.11589900
C	-0.14423600	0.39029400	-0.10414200
C	-1.10223100	1.42546300	-0.27239800
C	-2.45158700	1.15035400	-0.22195100
H	-2.33307700	-2.18946400	0.32601700
H	0.07284800	-1.74066800	0.24520600
H	-0.75553500	2.43582000	-0.44283800
C	-3.16133900	1.95826300	-0.35618900
H	1.21422800	0.65853200	-0.15703500
H	2.44754300	-0.12299600	-0.04246200
C	3.53710300	0.66658000	-0.07976500
F	2.57974000	-1.03489100	-1.04215500
F	2.50431100	-0.83127500	1.11772700
F	-4.40077500	-0.42959900	0.08599000
C	-4.75142300	-0.32965700	1.11808000
H	-4.97771500	0.26846100	-0.52217200
H	-4.63534600	-1.44384400	-0.23997500
H	1.35696300	3.81116800	1.40206000
H	1.49555200	3.12802400	1.13935000

E= -647.906096, ZPVE= 0.145969

**Table A27.** Cartesian coordinates of TS(S-7b...H<sub>2</sub>) optimized at the B3LYP-D3/def2-TZVP level of theory.

Atomic symbol	x	y	z
C	-1.86910700	-1.14934700	0.07095100
C	-0.52509400	-0.83321300	0.09076600
C	-0.09493200	0.51163500	-0.01327600
C	-1.09545800	1.50535600	-0.11816600
C	-2.43657100	1.18419700	-0.09423100
C	-2.84810700	-0.15132800	-0.00547900
H	-2.17488200	-2.18735300	0.12655600
H	-0.77576600	2.53420500	-0.22172400
H	-3.18155600	1.96724000	-0.16855700
C	1.26055100	0.96336400	-0.11351000
H	1.75568400	1.57101300	1.87065400
H	1.67298700	1.85849600	1.12933200
C	2.35839900	-0.06154900	-0.04807300
F	2.34682400	-0.72509100	-1.23193300
F	2.29135400	-1.01029400	0.93636900
F	3.57367300	0.49896800	0.08968800
C	-4.30664600	-0.50356600	0.02981100
H	-4.66679600	-0.51177100	1.06325000
H	-4.90720900	0.22318800	-0.51818000
H	-4.49050800	-1.49397200	-0.38738600
H	0.20318400	-1.62658400	0.16617700

E= -647.894662, ZPVE= 0.148682

**Table A28.** Cartesian coordinates of TS(T-7b...H<sub>2</sub>) optimized at the B3LYP-D3/def2-TZVP level of theory.

Atomic symbol	x	y	z
C	-2.90078700	-0.14781300	-0.01213700
C	-1.93522300	-1.16328300	-0.01399900
C	-0.58608800	-0.88076500	-0.00848300
C	-0.12767100	0.46705600	-0.00208500
C	-1.11259300	1.48994600	-0.00379700
C	-2.45543500	1.18091200	-0.00929200
H	-2.25616600	-2.19855700	-0.02194000
H	0.13422200	-1.68683300	-0.01232900
H	-0.79432800	2.52395100	-0.00400100
C	-3.18368100	1.98352500	-0.01350100
H	1.23118600	0.78194300	0.00165800
H	2.41022500	-0.10140500	0.00280400
C	3.55741000	0.60289800	0.00897300
F	2.45004200	-0.91709300	-1.08498300
F	2.44264100	-0.92413100	1.08551500
F	-4.36663400	-0.47394500	0.01882800
C	-4.71963100	-0.56877600	1.05061100
H	-4.96022800	0.30761100	-0.45734200
H	-4.57638000	-1.41903300	-0.48403500
H	1.77120900	3.06030100	0.00939200
H	1.59227500	2.22685800	0.00661900

E= -647.899669, ZPVE= 0.145027

**Table A29.** Cartesian coordinates of radical pair **50**···H optimized at the B3LYP-D3/def2-TZVP level of theory.

Atomic symbol	x	y	z
C	2.86389300	-0.17411600	0.01236600
C	1.88182500	-1.17474700	0.01515500
C	0.53757300	-0.87125800	0.00917400
C	0.09711500	0.47988700	0.00136000
C	1.10018700	1.48599500	0.00218900
C	2.43887600	1.16171400	0.00814000
H	2.18828500	-2.21433200	0.02420000
H	-0.18998300	-1.67031000	0.01373300
H	0.79663100	2.52618500	0.00134000
H	3.17876200	1.95365000	0.01157400
C	-1.25608200	0.85284300	-0.00321900
C	-2.38930700	-0.10506600	-0.00311300
F	-3.57028100	0.54589100	-0.01088400
F	-2.39483100	-0.92178600	1.08376400
F	-2.38621600	-0.93222100	-1.08202100
H	-0.98655300	4.34247300	0.00441200
H	-1.53937100	1.89564600	-0.00739600
C	4.32416600	-0.52369000	-0.01835100
H	4.67144300	-0.64341000	-1.04959200
H	4.93229400	0.25669500	0.44110900
H	4.52097500	-1.46292800	0.50069100

E= -647.914674, ZPVE= 0.147795

**Table A30.** Cartesian coordinates of **47** optimized at the B3LYP-D3/def2-TZVP level of theory.

Atomic symbol	x	y	z
C	2.79486300	-0.00000200	-0.09667300
C	2.10200800	-1.19517500	0.09736600
C	0.76341700	-1.19665900	0.46619600
C	0.07501600	-0.00000300	0.65474200
C	0.76341700	1.19665400	0.46620000
C	2.10200800	1.19517100	0.09736900
H	2.61743600	-2.13881800	-0.03887900
H	0.24828900	-2.13919800	0.60808000
H	0.24828900	2.13919200	0.60808600
H	2.61743600	2.13881400	-0.03887200
C	-1.38280800	-0.00000200	1.03697800
C	-2.31759800	0.00000100	-0.15657500
F	-3.60856300	0.00000400	0.24619100
F	-2.14677600	-1.08574100	-0.93791300
F	-2.14677200	1.08574200	-0.93791400
H	-1.63907000	0.88092600	1.62670700
H	-1.63907200	-0.88093100	1.62670300
C	4.23717700	0.00000500	-0.52850700
H	4.31480800	0.00013700	-1.61960200
H	4.76296700	0.88358700	-0.16393000
H	4.76291400	-0.88369600	-0.16414400

E= -648.051438, ZPVE= 0.160782